InAs Heteroepitaxy on Nanopatterned GaAs(111)A Surfaces

Dissertation

Submitted to the Department of Physics
at the University of Paderborn
for the award of the degree

'Doctor rerum naturalium'

Submitted by
Vinay Kunnathully Sathees Kumar
from India

Paderborn, May 2026

Doctoral Committee

Prof. Dr. Jörg K.N. Lindner

Prof. Dr. Dirk Reuter

Prof. Dr. Arno Schindlmayr

Dr. Viktoryia Zolatanosha

Kurzfassung

Obwohl das InAs/GaAs(111)A-System im Vergleich zu den umfassend untersuchten GaAs(001)-Substraten aufgrund seiner höheren Symmetrie und der höheren Mobilität von In-Adatomen vielversprechende Perspektiven für die Herstellung neuartiger optoelektronischer Nanostrukturen bietet, ist es aufgrund seiner hohen Neigung zur Defektbildung an der Heterogrenzfläche bislang weitgehend unerforscht geblieben .

In diesem Zusammenhang wird eine Technik zur Defektminimierung untersucht, die als Nano-Heteroepitaxie bezeichnet wird und die Substratnachgiebigkeit von Substraten mit nanoskaligen Abmessungen ausnutzt, um die durch Gitterfehlanpassung hervorgerufene Spannung aufzunehmen. Analytische Modelle auf Grundlage dieses Ansatzes weisen darauf hin, dass eine Reduzierung der lateralen Substratabmessungen auf unter 30 nm erforderlich ist, um die 7%ige Gitterfehlanpassung des InAs-GaAs-Systems auszugleichen. Zu diesem Zweck werden die selbstorganisierte Bottom-up-Strukturierung mittels Nanosphärenlithographie (NSL) in Kombination mit dem Top-down-Verfahren des reaktiven Ionenätzens eingesetzt, um nano-pfeilerstrukturierte GaAs(111)A-Substrate mit mittleren Durchmessern von 28 ± 5 bzw. 31 ± 5 nm, mittleren Höhen von 69 ± 8 bzw. 103 ± 3 nm sowie mittleren Pitches von 129 ± 6 bzw. 228 ± 8 nm herzustellen, abhängig von den durch NSL erzeugten Strukturen und den Waferabmessungen.

Anschließend wird das molekularstrahlepitaktische (MBE-)Wachstum von InAs auf derart nano-pfeilerstrukturierten Substraten durchgeführt, wobei die nominell abgeschiedene Schichtdicke, die Wachstumstemperatur und die Wachstumsrate in den Bereichen von 2 - 5 nm, 150–410 °C bzw. 0,011–0,11 nm/s variiert werden. Darüber hinaus wird eine Vorlage für die selektive Bereichs-Heteroepitaxie entwickelt, um das InAs-Heterowachstum während des MBE-Prozesses ausschließlich auf die Spitzen der GaAs(111)A-Pfeiler zu beschränken; hierbei erfolgen die Wachstumsbedingungen in den Bereichen 300 – 450 °C, 0,011 nm/s und 2 nm abgeschiedene Dicke.

Die resultierenden Nanostrukturen werden mittels (Raster-)Transmissionselektronenmikroskopie ((R)TEM) untersucht, um Gitterdefekte zu charakterisieren, die Modellierung von Mechanismen der Gitterspannungsrelaxation durch molekularstatische Simulationen zu unterstützen und diejenigen Prozessbedingungen zu identifizieren, die defektfreie InAs-Inseln auf GaAs(111)A-Nanopfeilern ermöglichen.

Abstract

Although the InAs/GaAs(111)A system offers prospects for fabricating novel optoelectronic nanostructures compared to the widely explored GaAs(001) substrates due to its higher symmetry and In adatom mobility, its high propensity for defect formation at the heterointerface has left it greatly unexplored.

In this context, a defect mitigation technique called Nano-heteroepitaxy which exploits the substrate compliance of substrates with nano-scale dimensions to accommodate lattice misfit strain is explored. Analytical models based on this approach indicate substrate size reduction with lateral dimensions of sub 30 nm to accommodate the 7% lattice misfit of the InAs-GaAs system. Towards this end, the bottom-up self-organized patterning Nanosphere lithography (NSL) in conjunction with the top-down reactive ion etching is used to create nano-pillar patterned GaAs(111)A substrates with average diameters 28 ± 5 or 31 ± 5 nm, average heights 69 ± 8 or 103 ± 3 nm and average pitch 129 ± 6 or 228 ± 8 nm depending on structures created using NSL and wafer dimensions.

Subsequently, the molecular beam epitaxial (MBE) growth of InAs is performed on such nano-pillar patterned substrates, varying nominal deposited thickness, growth temperature and growth rate in the ranges 2 - 15 nm, 150 - 410 °C and 0.011 and 0.11 nm/s, respectively. Further, a selective area hetero-epitaxy template is developed to restrict InAs heteroepitaxy exclusively to GaAs(111)A pillar tops during MBE growth performed in the temperature ranges, growth rate and deposited thickness 300 - 450 °C, 0.011 nm/s and 2 nm, respectively.

The resulting nanostructures are examined using (scanning)transmission electron microscopy ((S)TEM) to characterize the lattice defects, to guide the modelling of lattice strain relaxation mechanisms using molecular statics simulations and to identify the process conditions yielding defect free InAs islands on GaAs(111)A nanopillars.

Table of contents

List of abbreviations

AFM	Atomic force microscope
AHC	Atomic hydrogen cleaning
BEP	Beam equivalent pressure
BF	Bright field
BSE	Backscatter electron
CCD	Charge-coupled device
CMP	Chemical mechanical planarization
DC	Direct current
DL	Double layer
EDS	Energy dispersive spectroscopy
EFTEM	Energy filtered transmission electron microscopy
ESF	Extrinsic stacking fault
FFT	Fast Fourier transform
FIB	Focused ion beam
GPA	Geometrical phase analysis
HAADF	High angel annular dark field
HRTEM	High resolution transmission electron microscopy
ISF	Intrinsic stacking fault
MBE	Molecular beam epitaxy
ML	Monolayer
NHE	Nanoheteroepitaxy
NSL	Nanosphere lithography
OA	Objective aperture
OL	Objective lens

PECVD	Plasma enhanced vapor deposition
PIPS	Precision ion polishing system
PPA	Peak pairs analysis
PS	Polystyrene
QD	Quantum dot
RF	Radio frequency
RIE	Reactive ion etching
ROI	Region of interest
RTB	Rotational tilt boundary
SAH	Selective area heteroepitaxy
SEM	Scanning electron microscopy
STEM	Scanning transmission electron microscopy
TEM	Transmission electron microscopy
UHV	Ultrahigh vacuum
WZ	Wurtzite
ZB	Zinc blende

Chapter 1
Introduction

1.1 Motivation

$In_xGa_{1-x}As/GaAs$ and $In_{1-x}Ga_xAs_yP_{1-y}/GaAs$ semiconductor heterostructure devices have been researched and developed over half a century [1] due to their light emitting abilities in the IR region, at 1.3 and 1.5 μm wavelength of the optical spectrum [2]. Further, their band gaps can be tuned by modifying their stress states, of which InAs quantum dots are a good example [3]. Additionally, III-V semiconductors provide a wide range of possibilities for bandgap engineering by alloying as seen in Fig 1.1. This also reduces the lattice misfit in many cases [4]. InAs/GaAs is one of the heterostructure combinations with a large misfit (≈ 7%) which increases the propensity for forming misfit dislocations to relieve the strain [5]. The formation of 3D quantum dots is a means to relax this strain by surface strain relaxation in InAs/GaAs(001) substrates [6]. Whereas, in the case of GaAs(111)A substrates hexagonal networks of dislocations form and the InAs film grow as 2D layers [7-9]. The present thesis takes up the challenge to realize InAs quantum dots on GaAs(111)A, which has thus far been demonstrated only by employing the droplet epitaxy route [10,11]. The other objective is to study the strain relaxation mechanism in such a high-lattice misfit system when such quantum dots are generated.

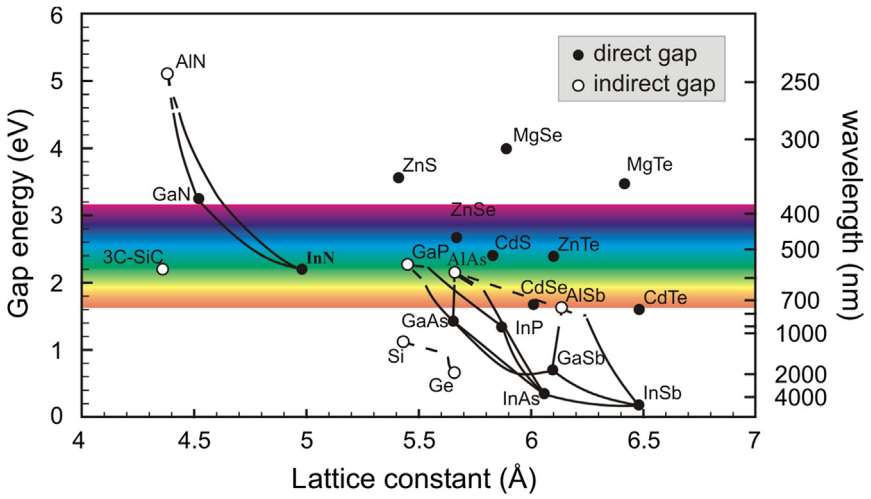

Fig. 1.1. Room temperature bandgaps of various semiconductors versus their lattice constants [4]

1.2 Scope of the thesis

In the present thesis, an effort is made to achieve structurally perfect InAs islands or quantum dots on GaAs(111)A nanopillars by exploiting substrate compliance. Towards this end, InAs deposition on nanopillar patterned GaAs substrates with and without the possibility for selective area heteroepitaxy was probed [12,13]. The former is unique compared to previous studies [14-17] in that it offers possibilities for unconstrained strain partitioning at the pillar tops. Another unique feature of the present study is the use of a cost effective, high-throughput patterning technique called nanosphere lithography. The crystal growth technique molecular beam epitaxy was used to achieve highly pure InAs layers with precisely controlled thicknesses. Finally and importantly, high-resolution transmission electron microscopy was used for studying the defect structures at the heterointerfaces and to model the strain relaxation mechanisms.

The studies carried out in this thesis are organized as follows:

Chapter 1 presents a brief overview of the challenges being addressed in the growth of InAs islands on GaAs(111)A substrates. In **chapter 2** a detailed discussion concerning the fundamentals of the InAs/GaAs(111)A system in terms of crystallography, atomistic surface processes occurring during heteroepitaxy are discussed. Also, the concept of strain partitioning on compliant substrates and models relevant to predictions for achieving dislocation free InAs growth are presented. The characterization techniques necessary to probe such systems with low dimensions are presented in **chapter 3**. The fabrication of two types of nanopatterned substrates is elaborated in **chapter 4**. In **chapters 5 and 6** the results of InAs deposition of nanopillar patterned GaAs(111)A substrates are presented and discussed. Conclusions are compiled and a view into the scope for further research are presented in **chapter 7**.

References

1) M. Fukuda, "Historical overview and future of optoelectronics reliability for optical fiber communication systems", Microelectron Relaib, 40 (2000) 27.

2) B.G. Streetmann and S. Banerjee, Solid state electronics, VII edition, Pearson International (2015).

3) T. Li, M. Dastro and A. Dadgar Eds., III-V compound semiconductors: integration with silicon based microelectronics, CRC press (2011)

4) T. Nishinga and T. Kuech Eds., "Handbook of crystal growth thin films and epitaxy: basic techniques", Elsevier (2015)

5) J. E. Ayers, T. Kujofsa, P. Rago, J. Raphael, "Heteroepitaxy of Semiconductors: Theory, Growth and Characterization", II Edition, CRC Press (2016).

6) U. W. Pohl, "Epitaxy of Semiconductors: Introduction to Physical Principles", Springer (2013).

7) L.A. Zepida-Ruiz, D. Marodus and W. H. Weinberg, "Semicoherent interface formation and structure in InAs/GaAs(111)A heteroepitaxy", Surf. Sci. Lett., 418 (1999) L68

8) H. Yamaguchi, K. Kamisawa, S. Miyashita and Y. Hirayama, "InAs/GaAs(111)A heteroepitaxial systems", Physica E, 23 (2004) 284

9) H. Yamaguchi, J.G. Belk, X.M. Zhang, J.L. Sudijono, M.R. Fahy, T.S. Jones, D.W. Phasley and B.A. Joyce, "Atomic-scale imaging of strain relaxation via misfit dislocations in highly mismatched semiconductor heteroepitaxy: InAs/GaAs(111)A", Phys. Rev. B, 55 (1997) 1337

10) S. Bietti, L. Esposito, A. Fedorov, A. Ballabio, A. Martinelli and S. Sanguinetti, "Characterization and Effect of Thermal Annealing on InAs Quantum Dots Grown by Droplet Epitaxy on GaAs(111)A Substrates", Nanoscale Res. Lett., 10 (2015) 247

11) A. Tuktamyshev, “Droplet epitaxy quantum dots on GaAs(111)A substrates for quantum information applications”, Ph.D. thesis, Università degli Studi di Milano-Bicocca (2020).

12) V. S. Kunnathully, T. Riedl, A. Trapp, T. Langer, D. Reuter and J.K.N. Lindner, “InAs heteroepitaxy on nanopillar-patterned GaAs(111)A”, J. Cryst Growth, 537 (2020) 125597

13) T. Rield, V.S. Kunnathully, A.K. Verma, T. Langer, D. Reuter, B. Brüker, A. Hütten and J.K.N. Lindner, “Selective area heteroepitaxy of InAs nanostructures on nanopillar-patterned GaAs(111)A”, J. Appl. Phys., 132 (2022) 185701

14) P. Zaumseil, G. Kozlowski, Y. Yamamoto, J. Bauer, M.A. Schubert, T.U. Schülli, B. Tillack and T. Schroeder, “Compliant Si nanostructures on SOI for Ge nanoheteroepitaxy—A case study for lattice mismatched semiconductor integration on Si(001)”, J. Appl. Phys., 112 (2012) 043506

15) G. Kozlowaski, “On the compliant behaviour of free-standing Si nanostructures on Si(001) for Ge nanoheteroepitaxy”, Ph.D. thesis, Brandenburgischen Technischen Universität Cottbus (2012)

16) R. Kozak, I. Prieto, Y.A.R. Dasilva, R. Erni, O. Skibitzki, G. Capellini, T. Schroeder, H. von Känel and M.D. Rossel, “Strain relaxation in epitaxial GaAs/Si(001) nanostructures”, Phil. Mag., 97 (2017) 2845

17) R. Kozak, Ph.D thesis, “Integration of GaAs on Si nanostructures: investigation of growth, defects, and interfaces”, ETH Zürich (2018)

Chapter 2
Fundamentals

This chapter introduces the concepts necessary for appreciation of semiconductor heteroepitaxy upon substrates with reduced dimensions. A brief introduction to the technological applications and crystallography of the InAs/GaAs system is made in section 2.1. The various surface processes responsible for morphological evolution during thin film growth are reviewed in section 2.2. Subsequently, two major subsections focusing on the defects formed in zinc blende structures (ZB) and defect mitigation techniques are taken up. Among the defect mitigation techniques, the approach of Nanoheteroepitaxy is presented in greater detail towards the end of the chapter.

2.1 Group III arsenides

III-V arsenide semiconductors are the compounds formed between group III elements such as Ga, In, Al and As belonging to group V. They form an important class of materials due to their role in the fabrication of semiconductor devices such as high-electron-mobility-transistors and quantum well lasers. Such applications can be realized owing to high carrier mobilities, direct bandgaps and bandgap tunability by alloying [1].

Among these compounds, the properties of GaAs and InAs will be described here in greater detail because of their relevance to this thesis. This system shows type I alignment of band edges [2] as depicted in Fig. 2.1 (a) when an InAs layer is embedded between GaAs capping layers. In such a configuration, the charge carriers within the InAs layers are confined to the potential well. Also, energy levels are discretized (E_1, E_2 etc in Fig. 2.1 (a)) when the thickness of InAs is reduced below the de Broglie wavelength (λ) [2] of its charge carriers (≈ 40 nm for electrons at 300 K). $\lambda = h/\sqrt{3m^* k_B T}$, here the variables m^*, T, k_B and h correspond to the effective mass of charge carriers, absolute temperature, Boltzmann constant and Planck's constant, respectively

Such discretized energy levels in a quantum well restrict the electron-hole recombination to specific transitions say between E_1 to E_{h1} [3] in Fig 2.1 (a), resulting in the emission of monochromatic light, an essential requirement for the design of laser light sources. The photon emissions in the InAs/GaAs system specifically correspond to the near IR wavelengths [4].

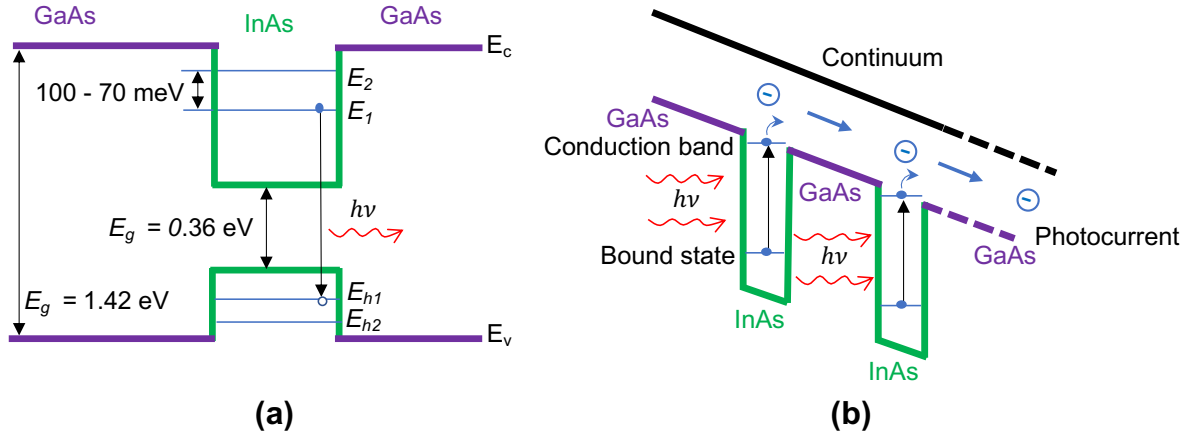

Fig. 2.1. Schematic representation of band edge alignments at the heterojunctions of InAs/GaAs quantum confined structures along with a) electron-hole recombination responsible for photon emission and b) inter sub-band transitions responsible for photocurrent generation in quantum confined GaAs/InAs/GaAs heterostructures. Adapted from [3, 5 and 6]

Another device exploiting the quantum size effects of this system is the IR photodetector. When electrons from the bound state are photo-excited to sublevels close to the continuum energy levels, these electrons contribute to a photocurrent under an applied external field, as schematically described in Fig. 2.1 (b). In this device, the alignment of the upper sub-band slightly beneath the GaAs conduction band edge aids in the efficient transport of charges due to thermal excitement into the continuum of the high mobility GaAs [5].

In the above-described devices, the energy levels of sub-bands can be tuned for specific applications by varying the thickness and/or by reduction of lateral dimensions of the active region (InAs). The latter approach is realized using self-organized InAs quantum-dots (discussed in section 2.2.1.3), where the lattice misfit strain and the three-dimensional charge confinement contribute to band gap modification [7]. Such InA/GaAs quantum well and quantum dot structures are employed for detection of Infra-Red (IR) radiations in the 6-18μm range [6] and for fabrication of lasers with wavelengths in the range 1-1.3 μm [4].

Bulk crystals of GaAs and InAs are known to commonly crystallize in the cubic ZB structure [1] but they also crystallize in the hexagonal wurtzite structure when synthesized under certain conditions far away from equilibrium [2,8]. The ZB structure, shown in Fig. 2.2 (a) belongs to the space group $F\bar{4}3m$ and can be visualized as two interpenetrating FCC lattices of group III (Ga or In) and group V (As) atoms displaced from one another by (¼ a, ¼ a, ¼ a) along the space diagonal of the cubic unit cell, *a* being the lattice constant. Such a crystal structure is built up by stacking alternating close packed double layers of III and V atoms along the [111] direction in an …aAbBcC… stacking of close packed layers as depicted in Fig. 2.2 (b), where equivalent atomic rows are indicated by arrows of the same color. Also, marked in Fig. 2.2 (a) are the important planes and their corresponding normal directions. Within the ZB crystal, each Ga/In atom is tetrahedrally bonded to four As atoms and vice-versa as shown in Fig. 2.2 (c). The bonding is of mixed ionic and covalent nature. This induces a net positive charge on the group III atoms (cations) and negative charge on the group V atoms (anions) [4]. The cation terminated surface is called the A face and the anion terminated face is called the B face, as indicated in Fig. 2.2 (b). Hence, the [111] and $[\bar{1}\bar{1}\bar{1}]$ directions are non-equivalent electronically and atomic constitution wise. This has important implications in terms of surface reconstructions, growth morphologies and etch rates [1]. Similar to the {111} surfaces, the {001} planes too show polarity, the {011} type of planes on the other hand are non-polar meaning that they contain equal number of Ga and As atoms to maintain a net neutrality of charges. These electronically neutral planes with low surface energy are thus the preferred cleavage planes in ZB crystals.

A summary of the structural and electronic properties relevant to the processing and applications of the InAs/GaAs system is presented in Table 2.1. Among these, the effects arising from lattice parameter mismatch and substrate orientation are crucial for morphological control during InAs epitaxy on GaAs and are taken up in the next section.

Table 2.1. Structural and electronic properties of GaAs and InAs at 300 K [1]

Property	**GaAs**	**InAs**
Crystal structure	Zinc blende	Zinc blende
Space group	$F\bar{4}3m$	$F\bar{4}3m$
Lattice constant, Å	5.6535	6.058
Linear thermal expansion coefficient, K^{-1}	5.7×10^{-6}	4.5×10^{-6}
Band gap, eV	1.42	0.36
Electron mobility, $cm^2V^{-1}s^{-1}$	8,000	33,000
Hole mobility, $cm^2V^{-1}s^{-1}$	400	460
Effective mass of electrons, m_e/m_o	0.063	0.023

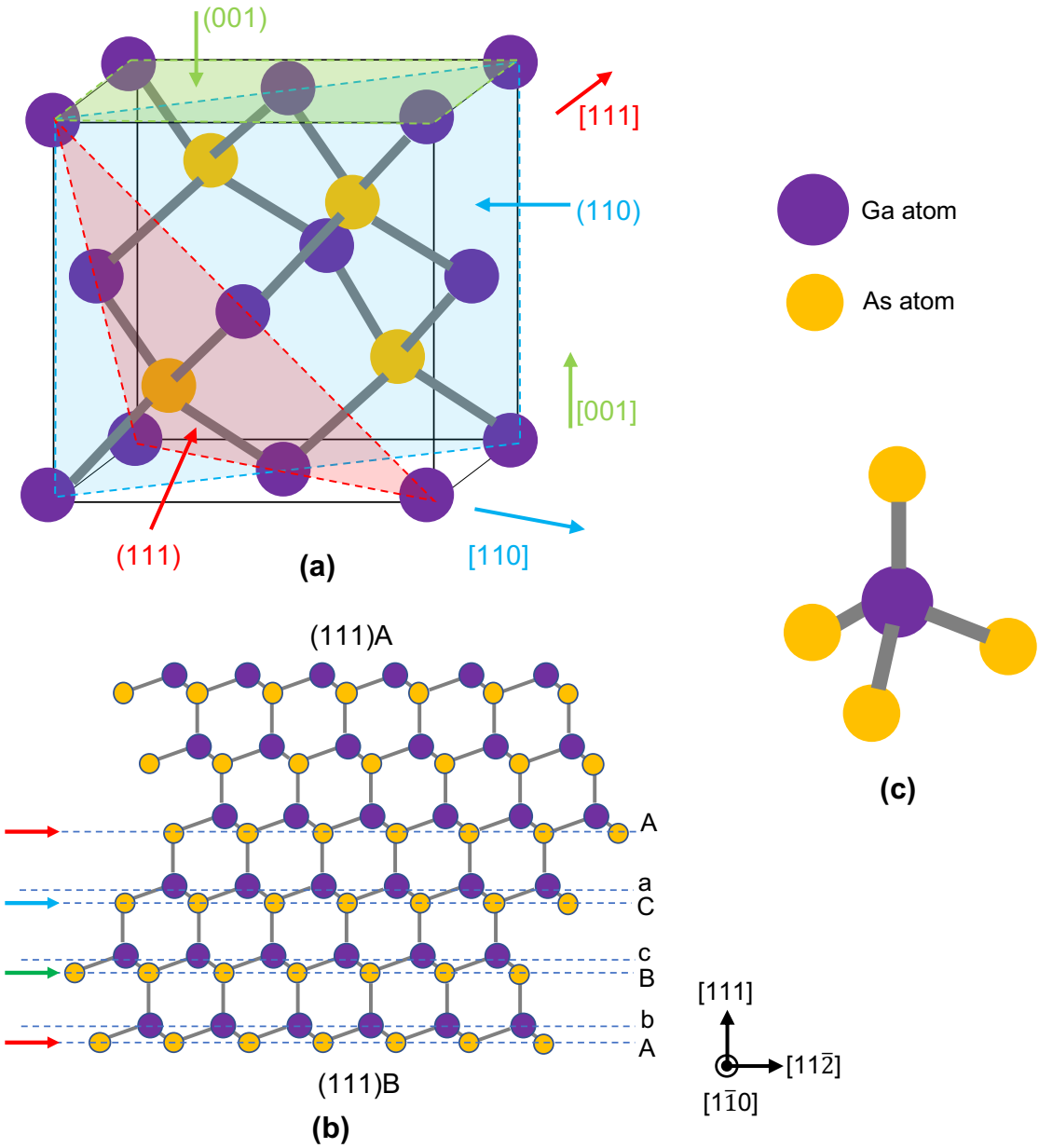

Fig. 2.2. Model of the zinc blende GaAs structure (a) unit cell cube with important crystallographic planes and directions marked, (b) the stacking of close packed (111) atomic layers viewed along [1$\bar{1}$0], layers lying directly above one another are indicated by the same color (c) Ga atom tetrahedrally bonded with four As atoms.

2.2 Epitaxy

The growth of application specific film/substrate combinations is a routine yet demanding step during solid-state device fabrication. In case of crystalline film/substrate systems, the growth process is termed *epitaxy, epi* meaning upon, and taxis refers to the crystalline alignment of the film imposed by the substrate [10,11]. The terms *homoepitaxy* and *heteroepitaxy* are used to distinguish between growth involving constitutionally similar and dissimilar combinations of films and substrates respectively. Molecular beam epitaxy (MBE) and metalorganic vapor-phase epitaxy (MOVPE) are the most widely employed techniques to achieve films with monolayer (ML) precision in thickness. Since MBE was employed in this thesis, epitaxial growth phenomena pertinent only to this technique are discussed further. A detailed description of the MBE set-up will be taken up in section 3.4.

2.2.1 Thermodynamics and kinetic aspects of thin film epitaxy

The interactions between the film forming atoms and the substrate surface under the imposed process conditions determine the morphology of the epitaxial layer (short epilayer. Most of the occurring growth phenomena have been successfully modeled using thermodynamic and kinetic approaches [2]. A brief overview of these models considering the results to be discussed in the subsequent chapters is presented here. An extensive review of these models is presented in the in the book by Pimpinelli and Villian [12].

Atoms *'stick'* and adsorb on the substrate surface if their chemical potential in the gas or vapor phase is larger than their adsorption energy, E_{ads}, (eq. 2.1) and provided they can dissipate the majority of their kinetic energy to the substrate [13,14].

$$E_{ads} = E_{total} - (E_{substrate} - E_{atom}), \qquad 2.1$$

where E_{total} and $E_{substrate}$ are the energies of substrate with and without adatom on the surface respectively and E_{atom} is the energy of an isolated atom. The atoms that do not stick to the substrate surface are desorbed back into the vapor phase. This defines their sticking probability [10], the sticking coefficient, S is quantitatively expressed in equation 2.2 as the fraction of the total number of adhering atoms compared to the number of arriving atoms.

$$S = \frac{N_{ads}}{N_{total}} \quad . \qquad 2.2$$

Once adsorbed on the surface, the atoms migrate as *adatoms*. Thermally activated adatom migration is described by the surface diffusion coefficient [10]:

$$D = \frac{1}{4} \Gamma^2 \nu_d \, , \qquad 2.3$$

where Γ^2 is the mean square distance covered by an adatom during a single jump between two points of minimum energy on the substrate, ν_d is the jump rate and the factor ¼ corresponds to two-dimensional diffusion on a square lattice. The temperature dependence of D enters this equation in the form of ν_d:

$$\nu_d = \nu_o \, e^{\frac{-E_d}{k_B T}} \quad . \qquad 2.4$$

Here, E_d is the energy barrier to be surmounted by the adatom while making a single jump and ν_o is the attempt frequency per jump. An adatom covers a mean distance l, known as the migration length within a duration τ, which spans the length of time between adatom arrival on the surface and its cessation by various possible mechanisms.

$$l = \sqrt{D \, \tau} \qquad . \qquad 2.5$$

Adatom migration is terminated when the adatom encounters other adatom(s) leading to nucleation and cluster formation. The adatom could also incorporate itself in low energy configurations at surface defect sites known as kink positions or reevaporate back to the vapor phase. Each of these possibilities depend mainly upon the substrate temperature T, surface stresses and reconstruction, spacing between individual adatom sinks and adatom flux (F, ML/s) provided by the source. An overview of various processes taking place on a *vicinal* substrate surface along with their corresponding energy barriers is depicted in Fig. 2.3. A vicinal substrate consists of regularly spaced monolayer high steps separated by terraces, realized by inducing a miscut angle $\varphi = \tan^{-1}(h/w)$ with respect to the substrate surface along a specific crystallographic direction, h and w being the step height and terrace width, respectively. If the migration length is greater than the terrace width, the adatoms are incorporated at the kink positions of a step, resulting in its completion and advancement of the terrace, which is known as *step-flow* growth. Nucleation and

growth of 2D islands on terraces occurs if the adatom migration length is shorter than the terrace width. While intra-terrace adatom migration entails a barrier, E_d, as discussed earlier, the inter-terrace migration involves an extra barrier E_{ES} named after Ehrlich and Schwöbel [17], and this has profound implications for the morphological evolution during epitaxial growth.

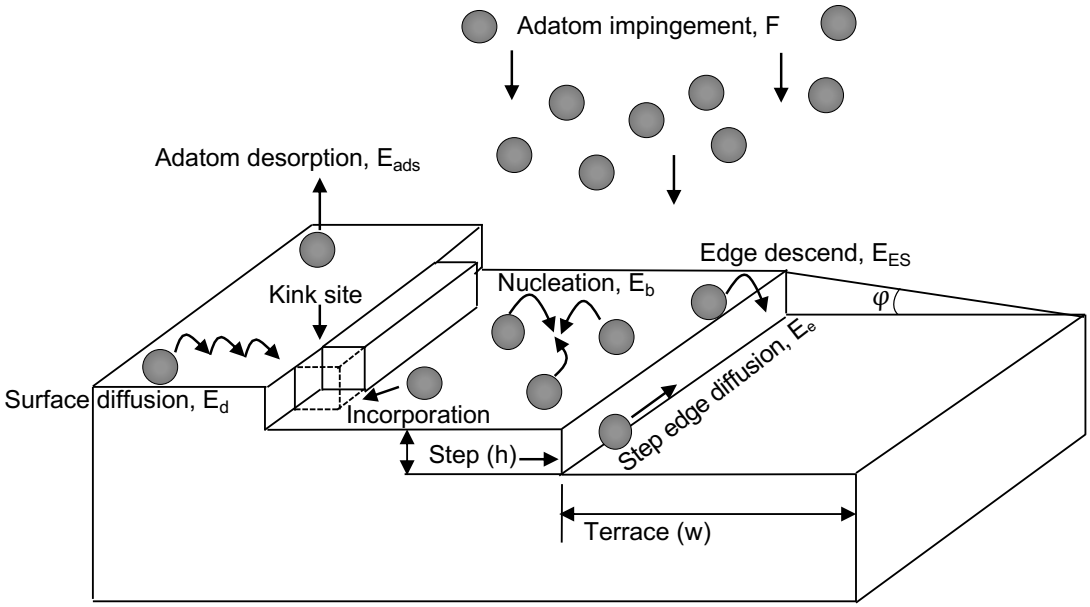

Fig. 2.3. Schematic of atomic processes taking place on a vicinal substrate along with the corresponding energy barriers involved, adapted from [15 and 16].

2.2.1.1 The Ehrlich-Schwöbel barrier and its consequences

An adatom attempting to jump down a step edge experiences an energetically unstable configuration due to reduced coordination with substrate atoms. The excess energy associated with this configuration is called the Ehrlich-Schwöbel (ES) "barrier" [17], since it can reflect adatoms with insufficient energy back to the terrace surface. This phenomenon is depicted in Fig. 2.4, where the adatom B needs an energy E_{ES} in addition to E_d for passing through position D. On making a successful jump, the adatom B is accommodated at the step edge i.e. in coordination with atoms C, E and F, at a position with higher binding energy, E_S. As a result of the ES barrier, a step-down motion of adatoms is hindered whereas the accommodation of adatoms migrating on lower terraces at step edges is favored. Morphological instabilities such as step-bunching, hillock formation and step-meandering are a result of the ES barrier. Among these, step-meandering shall not be discussed further.

An ideal vicinal surface consists of equally spaced steps as shown in Fig. 2.5 (a). If for some reason a step lags behind the others, step B in Fig. 2.5 (b) for example, the corresponding terrace receives lesser number of adatoms on its surface. In the absence of ES barrier one half of the total adatoms distribute themselves at the upper and the other at lower edges of the terraces.

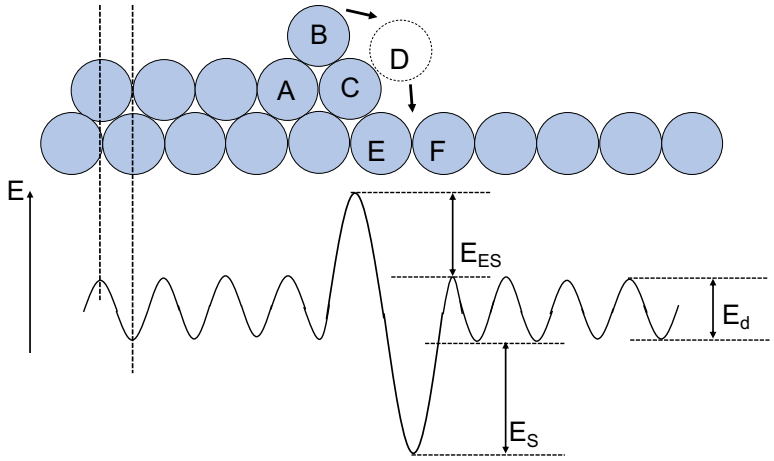

Fig. 2.4. An illustration of atomic positions and the corresponding theoretical potential distribution corresponding to adatom migration across a step. E_d, E_{ES} and E_S are the diffusion barrier, ES barrier and the binding energy at the step edge respectively [2].

Consequently, the terrace of step B shrinks further in width and that of step A broadens and this step also gains in velocity since $r_{step} \propto (w_{upper} + w_{lower})$ [2], where r_{step}, w_{upper} and w_{lower} are the step growth velocity and terrace widths of upper and lower terraces, respectively. Consequently, the terrace ahead of step A is shortened a bit and this process when continued creates bunches of steps separated by long terraces as shown in Fig. 2.5 (c) also known as *step-bunching*. In the presence of a positive ES barrier however, since the adatoms gathered by terrace A are repelled by the barrier and they tend to accommodate themselves at the edge of step B resulting in the broadening of terrace B and thus restoring the regular arrangement of steps as in Fig. 2.5 (a). Multi-atomic super steps formed on vicinal GaAs surfaces have been exploited to fabricate quantum wires [18] and quantum dot arrays [19]. On surfaces which are perfectly oriented along a low index plane, 2D or 3D islands are formed by nucleation and growth.

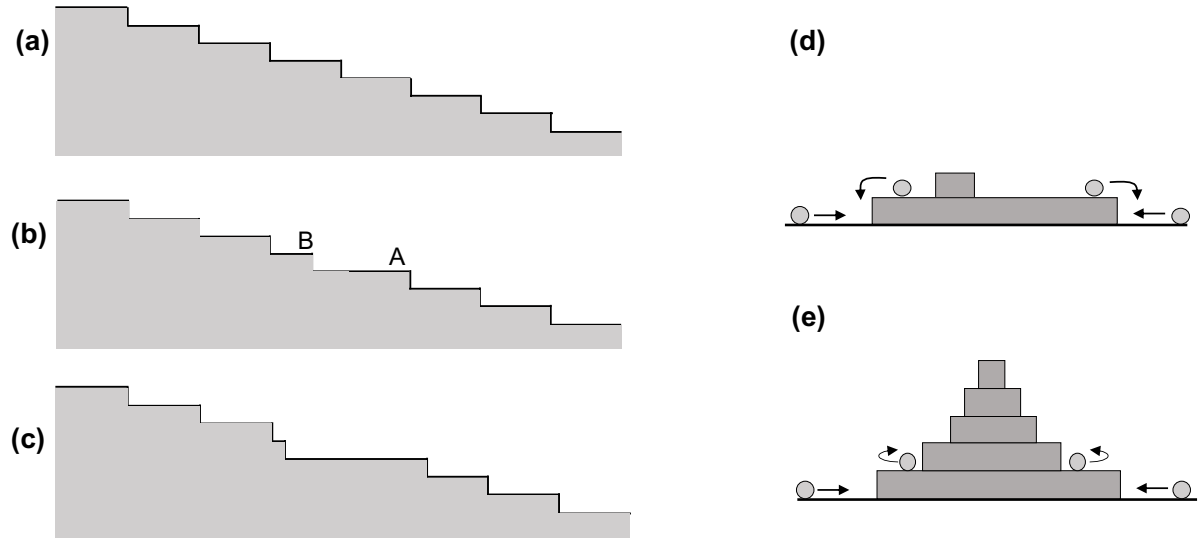

Fig. 2.5. (a) Vicinal surface under stable step-flow when ES barrier is present, (b) step B lagging behind step A, (c) formation of step bunches in the absence of ES barrier (d) step-flow mode with ES barrier absent and (e) hillock formation with ES barrier present in the case of singular surfaces. Adapted from [2, 12 and 23]

These islands grow laterally by accommodation of arriving adatoms at their step edges, a second layer can form in parallel on top of the first one. The probability of second layer nucleation is low if the adatom migration length is larger than the size of the 2D islands and ES barriers at the edges of the first layer are absent, as illustrated in Fig. 2.5 (d). However, if a positive ES barrier is present at the step edge, the adatoms diffusing on the first layer are repelled at the edge and start forming the second layer. When repeated on successive monolayers this process results in the formation of *hillocks* as shown in Fig. 2.5 (e). In the case of singular GaAs(111)A substrates, a positive ES barrier at the step edges results in the formation of pyramidal hillocks, which increase the surface roughness during buffer layer growth and degrade the electronic properties of nanostructures grown upon it [20, 21]. The height of the ES barrier in the case of vicinal GaAs(001) with misorientation towards the [010] direction has been estimated by comparing Monte-Carlo simulations to the experimentally measured surface step profiles to be 0.175 eV [22]. A complete understanding of the epilayer's morphological evolution requires not only the consideration of the rate limiting kinetic barriers discussed thus far, but also the structural and thermodynamic aspects need to be considered. This shall be dealt with in the next sections.

2.2.1.2 Strain in heteroepitaxial films

In the initial stages of heteroepitaxy on an infinitely thick planar substrate, the epilayer grows as a defect free 2D layer maintaining lattice coherency at the interface. This layer could be strained or strain free depending upon the magnitude of lattice mismatch between the two materials and the deposited thickness. Such a growth is termed *pseudomorphic* [1]. For a coherent growth in the absence of lattice defects, the *lattice misfit or lattice mismatch*, is defined as [2]:

$$f = 2 \cdot \frac{a_e - a_s}{a_e + a_s} \quad . \tag{2.6}$$

Here, a_e and a_s are the unstrained lattice parameters of the epilayer and the substrate, respectively. The lattice misfit for InAs/GaAs is 7%. In systems with $a_e \neq a_s$, the in-plane lattice parameter at the heterointerface assumes an intermediate value, $a_\parallel$ resulting in a compressively strained epilayer and tensely strained substrate when $a_e > a_s$. This lattice configuration is depicted in Fig. 2.6 (a). Here the vertical lattice parameter of the epilayer $a_{e\perp}$is larger than a_e to preserve the volume of the lattice, resulting in a *tetragonal distortion* of lattice. The magnitude of the resulting vertical lattice strain $\varepsilon_\perp$ is expressed as:

$$\varepsilon_\perp = \varepsilon_{zz} = -R_B \varepsilon_\parallel = -\frac{2C_{12}}{C_{11}} \varepsilon_\parallel \ , \tag{2.7}$$

where, $\varepsilon_\perp = \varepsilon_{zz}$ and $\varepsilon_\parallel = \varepsilon_{xx} = \varepsilon_{yy}$ denote the strain in the vertical direction and the in-plane biaxial strain, respectively, ε_{xx}, ε_{yy} and ε_{zz} being the normal strain components along the x, y and z axes. C_{12} and C_{11} are the material dependent stiffness constants and R_B is the biaxial relaxation constant of the epilayer, as defined in Appendix-1. The in-plane stress, $\sigma_\parallel$ resulting from the in-plane biaxial strain $\varepsilon_\parallel$ is:

$$\sigma_\parallel = \sigma_{xx} = \sigma_{yy} = 2\,G\,\frac{1+\nu}{1-\nu}\,\varepsilon_\parallel = E'\varepsilon_\parallel \ , \tag{2.8}$$

where, G and ν are the shear modulus and poison ratio, and E′ is the biaxial modulus. And the out of plane stress, $\sigma_\perp = \sigma_{zz} = 0$ for biaxially strained layers. Now, the elastic strain energy per unit volume in the epilayer, which accumulates with increasing deposited thickness, is quantified as:

$$E_V = \frac{E_s}{At_e} = 2\,G\,\varepsilon_\parallel^2\,\frac{1+\nu}{1-\nu} = Y\,\varepsilon_\parallel{}^2 \quad . \tag{2.9}$$

E_V, E_s, t_e and A are the strain energy density, strain energy, epilayer thickness and the area of the heterointerface, respectively. A more convenient measure of lattice strain

is the areal density of elastic strain, $E_s/A = E_A$, which is quadratically dependent upon the lattice misfit and linearly on the deposited thickness t_e [2]:

$$E_A = 2\,G\,\varepsilon_{\parallel}^2\,\frac{1+\nu}{1-\nu}\,t_e \quad . \qquad 2.10$$

Although the contribution of lattice misfit is sizeable, it is fixed, whereas that of the deposited thickness is a variable, with significant consequences.

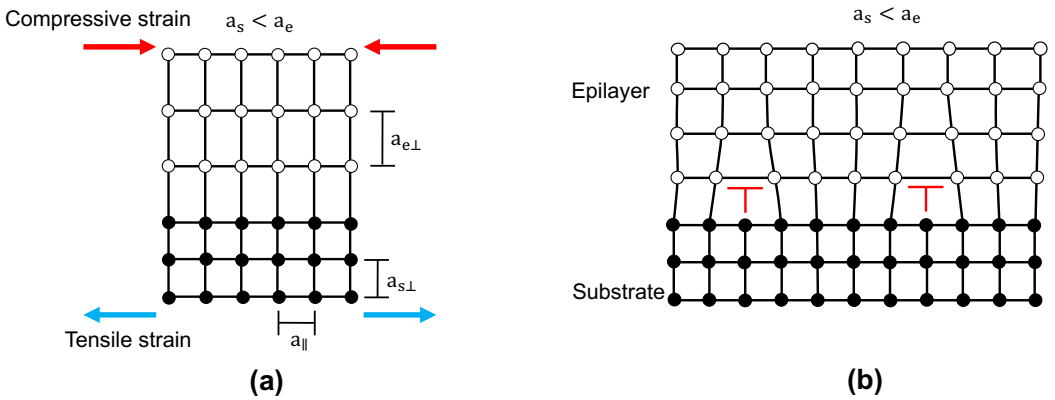

Fig. 2.6. A schematic illustration of the heterointerface during (a) heteroepitaxy with $a_s < a_e$ and $t_e \leq t_c$, showing tetrahedral distortion of lattice (b) heteroepitaxy under $a_s < a_e$ and $t_e > t_c$ showing the presence of misfit dislocations (⊥). Here the lattice parameter in the vertical direction for epilayer and substrate are denoted as $a_{e\perp}$ and $a_{s\perp}$ respectively adapted from [24].

When the epilayer thickness exceeds a critical value, t_c, the strain is plastically relieved by forming misfit dislocations (MDs) (detailed description in section 2.3.1) as illustrated in Fig. 2.6 (b). Therefore, the total misfit f can written as equation 2.11:

$$f = \varepsilon_{\parallel}\ \text{(in-plane elastic strain)} + \delta\ \text{(plastic strain)} \quad . \qquad 2.11$$

Reducing the lateral and or vertical dimensions of the substrate to dimensions comparable to the epilayer makes it compliant. In such a case, the lattice elastic strain is partitioned between the two layers (elaborated in section 2.4). Most of the descriptions used in this section have been adapted from [1 and 2].

2.2.1.3 Growth modes

There are three morphological forms in which the epitaxial layers manifest on the substrate surface corresponding to the mode of film growth, namely, Frank-Van der Merwe (FM), Volmer-Weber (VW) and Stranski-Krastanov (SK), schematically represented in Fig. 2.7. The criteria for film formation by either of these modes are based purely on thermodynamic equilibrium arguments, considering the surface energies γ_e, γ_i and γ_s corresponding to the free energy per unit area at epilayer-

ambient, epilayer-substrate and substrate-ambient interfaces, respectively [5] and the contribution of lattice strain energy [11,18] in the form of E_A.

If γ_s is small compared to the sum of γ_e, γ_i and E_A i.e.

$$\gamma_s < \gamma_e + \gamma_i + E_A \ , \qquad 2.12$$

the system is stable when the area exposed by the deposit-ambient surface is minimized, forcing the deposit to adopt a three-dimensional (3D) island morphology. This is the VW mode. This mode is observed in systems with large lattice misfit (typically > 10%) [7] and large differences in surface energies between substrate and epilayer. Such 3D islands, although initially coherent, become highly defective upon growth and further defects form when adjacent islands coalesce as growth progresses [25, 18]. But if

$$\gamma_s > \gamma_e + \gamma_i + E_A \ , \qquad 2.13$$

the system is stable when the epilayer coverage of the substrate is maximized, resulting in layer-by-layer growth of epilayers which is the characteristic of the FM mode. Strong interfacial bonding between the epilayer and substrate, high growth temperatures aiding step flow growth, low supersaturation to prevent 3D islands [26] and $f_m < 10\%$ [25] promote this type of growth. In this mode, the film is *pseudomorphically* strained up to a certain *critical thickness*, beyond which, the lattice strain is relieved by the formation of *misfit dislocations.*

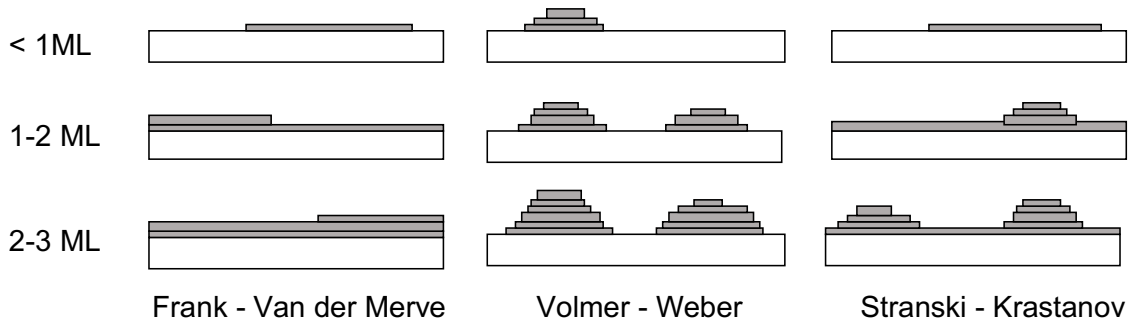

Fig. 2.7. Schematic illustration of the three growth modes as a function of deposited epilayer thickness, adapted from [2]

The SK mode is the intermediate case between FM and VW where, initially the epilayer grows layer-by-layer and thereafter forms 3D islands on the 2D layers when its thickness exceeds a critical value t_{cw}, $t_{cw} < t_c$. This switch in growth mode is triggered by the elastic strain energy that builds up with increasing epilayer thickness or a high enough barrier for misfit dislocation formation [27]. After exceeding t_{cw}, the 2D layer

reorganizes itself into 3D islands plus a wetting layer (WL), as seen in the schematic in Fig. 2.7. This morphology is chosen because the surface energy increase due to 3D island formation is outweighed by the release of strain energy [28]. The thermodynamic criterion for SK island formation is captured in eq. 2.14 [28] which estimates the difference between the total energies of the two possible configurations during further growth upon a 2D epilayer of thickness θ_{WL}:

$$\Delta E = \frac{1}{k}\left[\gamma(\theta_{WL}) - \gamma(\theta_0)\right] + \left[\gamma_s A_1 V^{2/3} - \gamma(\theta_{WL}) A_2 V^{2/3}\right] - \omega A_3 \varepsilon_0^2 V \quad . \qquad 2.14$$

Here, k is the areal density of 3D islands on the wetting layer, $\omega = M(1+\upsilon)/(1-\upsilon)$ where M is the Young's modulus of the epilayer, V, $\gamma(\theta_{WL})$, $\gamma(\theta_0)$ are the volume of 3D islands and surface energy densities of the wetting layer and of an epilayer with thickness θ_0 [29], respectively, γ_s is the surface energy density of the 3D island's side facets and A_1, A_2, A_3 are shape factors , which depend on the geometry of the 3D island. The first term is the difference in energy of wetting layers in the two modes, the second term shows to corresponding surface energy change and the last term the strain energy of the 3D island. The transition of growth mode from FM to SK as a function wetting layer thickness for the Ge/Si(001) system is exemplified with calculations in Fig. 2.8 [28, 30]. Such estimates were made at a fixed island density.

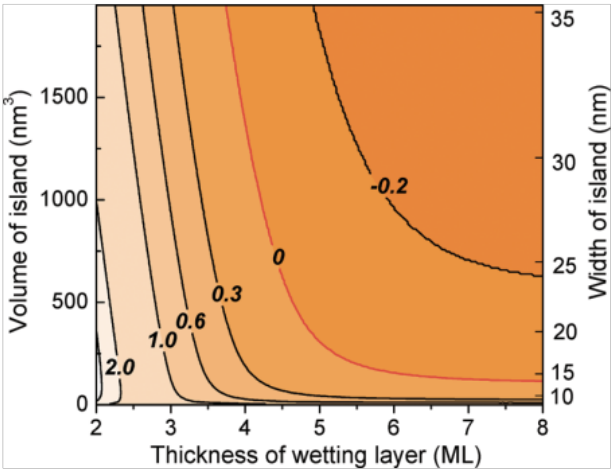

Fig. 2.8. The energy difference between SK and FM modes per unit volume of Ge Island on Si(001) [28]

In the initial stages of growth, the slope of the curve in Fig. 2.8 is larger compared to that at later stages/larger WL thicknesses, it is also positive. Meaning, at lower WL thicknesses, the 2D film is favored and as the WL thickens, the SK 3D island plus WL morphology takes over. Such a transition between growth modes ($\Delta E = 0$) is driven by a balance between surface energy of WL, which is thickness dependent ($\gamma(\theta_0)$), and

the release of strain energy due to 3D island formation [29]. The critical WL thickness for Ge/Si (001) system is estimated and corroborated by experimental findings to be 3.5-4 ML [31,32], in case of InAs/GaAs(001) this value is in the range 1.5-1.7 ML [2,32,33]. Such 3D islands, also known as quantum dots (QDs), initially form as pyramids which transition to domes with multiple side facets [32,34]. Hence, facet and facet edge energies are the additional terms that contribute to the total energy of QDs [35]. These are accounted for in the total energy calculations of eq. 2.15 [36]:

$$E^{QD} = E^{elastic} + E^{facet} + E^{edge} \quad . \qquad 2.15$$

The SK mode is favored in heteroepitaxial combinations with intermediate misfits 2.5%-10% [7]. This mode is widely employed to fabricate self-organized InAs QDs in the InAs/GaAs(001) system [2, 18, 37]. Such self-organized structures having uniform size and shape distribution with sizes in the range of a few nanometers behave optically like artificial atoms and have the potential to yield recombination spectra with low peak broadening [35].

Thermodynamic and kinetic aspects of growth considered up to now are the major factors determining the morphology of heteroepitaxially grown structures. Yet, there are other factors such as surface orientation, growth ambient and substrate compliance which can significantly alter the growth morphology, especially in the InAs/GaAs system [38].

2.3 Extended defects in the InAs/GaAs system

Extended defects or structural deviations from the perfect crystal structure are classified based on the dimensions in which they are extended as volume, surface, and line defects [39]. The extended defects formed during InAs/GaAs heteroepitaxy as reported in literature and in this work are dislocations, stacking faults, twin boundaries and polytypism [40]. Among these, dislocations are the commonly observed kind and shall be taken up first. Most of the information presented below has been adapted from reference [41].

2.3.1 Dislocations: basics

Dislocations are line defects or one-dimensional lattice defects characterized by a displacement of one part of the crystal lattice (with respect to the perfect crystal) in a region along a line, the dislocation line. It may not always be straight as represented by line SME in Fig. 2.9 (a). The crystal lattice is heavily distorted around this line also

known as the core of the dislocation where local atomic coordination is lost due to broken bonds. Dislocations are classified based on the angle θ between their line vector $\vec{l}$ and the *Burgers vector* $\vec{b}$ as either edge ($\theta = 90°$), screw ($\theta = 0°$) or mixed type ($0° < \theta < 90°$). These configurations are demarcated as points E, S and M in Fig. 2.9 (a). An edge dislocation can be visualized as an extra half plane inserted into the lattice, highlighted as a blue rectangular plane adjoining point E in Fig. 2.9 (a). By convention an edge dislocation is represented by ⊥ where the long arm of the inverted T shows the direction of extra half plane in case of an edge dislocation. A screw dislocation on the other hand can be envisaged as a single helicoid structure where the atoms are arranged in a helical pattern around $\vec{l}$. The Burgers vector $\vec{b}$ indicates the amount and direction of the lattice displacement and is determined by constructing a loop around the dislocation line in the undistorted crystal, following the right-hand / finish-start convention. Such a construction is made by choosing an arbitrary starting point, point S in the case of Fig. 2.9(c) around the dislocation core. A clockwise loop is then constructed around the core, maintaining equal number of points in the horizontal and vertical directions. The presence of the extra half plane results in the closure of the circuit at point F instead of S. The extra vector, $\vec{b}$ is the Burgers vector, obtained by connecting the finish and start points i.e., F and S respectively in Fig. 2.9 (c). The magnitude of $\vec{b}$ remains a constant for the plane containing $\vec{b}$ and $\vec{l}$, known as the *slip plane,* marked in gray color, Fig. 2.9 (a). In case of mixed dislocations, the screw and edge components are determined by resolving $\vec{b}$ along the tangent to the point of interest on the dislocation line, XY in case of Fig. 2.9 (b). The Burgers vector $\vec{b}$ can be split into its screw (parallel to XY) and edge components (normal to XY), $\overrightarrow{b_2}$ and $\overrightarrow{b_1}$ respectively with magnitudes corresponding to $b\cos\theta$ and $b\sin\theta$. Vectorially speaking, $\overrightarrow{b_2} + \overrightarrow{b_1} = \vec{b}$. The presence of a dislocations causes an elastic distortion of lattice which can in general be expressed as eq. 2.16. Here, E_d^{θ}/L is the dislocation energy per unit length of a mixed dislocation, R and b are the outer and inner cutoff radii of the dislocation. In semiconductor heteroepitaxy, R is usually taken as the deposit height and $|\vec{b}|$ is the magnitude of the Burgers vector. The parameter β is included to account for the non-Hookian elastic energies and dangling bonds at dislocation core β values ranging from 1 to 4 have been adopted in literature [41, 42]. The line energy is in general of the form $E \propto b^2$. A corollary of this result is the *Frank's*

rule according to which, a dislocation of magnitude $|\mathrm{b}_1|$ can split into $\overrightarrow{\mathrm{b}_2}$ and $\overrightarrow{\mathrm{b}_3}$ if $|b_1|^2 > |b_2|^2 + |b_3|^2$.

$$\frac{\mathrm{E}_\mathrm{d}^\theta}{L} = \frac{\mathrm{G}\cdot \mathrm{b}^2\,(1-\upsilon\cos^2\theta)}{4\pi(1-\upsilon)}\ln\left(\beta\frac{R}{\mathrm{b}}\right) \qquad 2.16$$

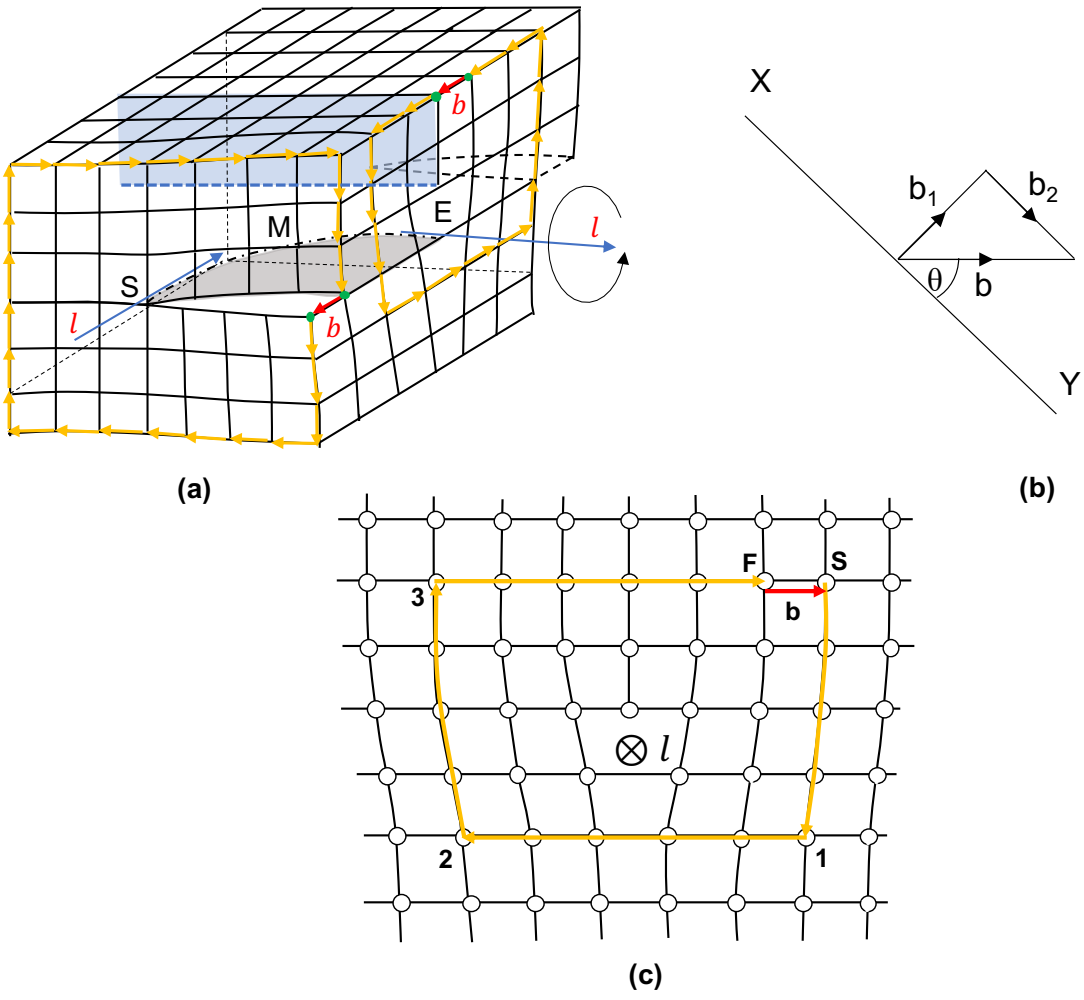

Fig. 2.9. Configuration of dislocations in a crystal (a) A curved dislocation segment SME with pure edge, screw and mixed portions at E, S and M respectively. (b) The components of Burgers vector $\vec{b}$ resolved into its screw and edge components along XY. (c) The RH/FS rule for determination of Burgers vector $\vec{b}$ in the case of an edge dislocations. Adapted from [40 and 41].

2.3.2 Dislocations in III-V Zinc Blende crystals

Dislocation motion by *glide* in III-V semiconductor crystals occurs on the same slip planes as in the face centered cubic crystals, namely the close packed {111} planes, and with the shortest lattice translations of the type $1/2\ \langle 110\rangle$. Such dislocations are termed *perfect dislocations* because their Burgers $1/2\ \langle 110\rangle$ vector is a perfect lattice translation. The multiplicity of these specific planes and directions yields twelve slip systems in total for the $a/2\ \langle 110\rangle\{111\}$ combination. Perfect dislocations of the edge (90°), screw 0° and the 60° type are the frequently observed configurations in ZB crystals. Among these, the 60° dislocations, depicted in Fig 2.10 (a) are the most prevalent because of the high core energy of the edge type and the inability of the screw type to relax tetrahedral distortions [2, 42]. Due to energetic reasons perfect dislocations split into two partial dislocations [41] with Burgers vectors that are not perfect lattice translation vectors. The *Frank* (FPD) and *Shockley* (SPD) partials dislocations are the most important ones in f.c.c. crystals. Dislocation splitting reactions are governed by the Frank's rule and in f.c.c. crystals have the general from:

$$\frac{a}{2}\,[011] \rightarrow \frac{a}{6}\,[121] + \frac{a}{6}\,[\bar{1}12] \qquad 2.17$$

$$\frac{a^2}{2} > \frac{a^2}{6} + \frac{a^2}{6} \qquad 2.18$$

The energetic feasibility of reaction 2.17 is confirmed by eq. 2.18 using vector magnitudes. Perfect 60° dislocations for example split into an *extended dislocation* consisting of 90° and 30° SPDs , as illustrated in Fig. 2.10 (c). As seen in Fig. 2.10 (c), the local atomic stacking in between the two partials (denoted with T) differs from the perfect crystal on the extreme left and right. It changes from aBbCcAaBbC to aBbCc|BbCcA, the missing Aa planes create a layer of h.c.p. lattice (BbCcBbCc) in between the regions of the perfect lattice. Such areas with locally altered stacking sequence are called *stacking faults.* A general representation of this configuration in f.c.c. crystals is exemplified by Fig. 2.10 (b) with an edge dislocation and its associated partials and the resulting stacking fault, lying on the $(\bar{1}\bar{1}\bar{1})$ plane [43]. Further classification of stacking faults in ZB crystals is provided in section 2.3.4.

The AaBbCc stacking of the {111} planes in ZB crystals results in two possible slip planes for undissociated dislocations. They are called as *shuffle* or *type I* and *glide* or *type II sets*, as indicated in Fig. 2.11 (a). Their associated dislocation models are shown

in Fig. 2.11 (b) and (c). Among these two possible configurations, the glide set is favored due to the relatively lower core energy of partials [44]. Another argument posed in literature favoring the glide set is the high energy of stacking faults resulting from the splitting of perfect shuffle dislocations [45]. The glide and shuffle dislocations in AB type compounds semiconductors are further classified into α or β type depending on dislocation core occupancy by A or B atoms respectively [1]. Among these two types, the α dislocations are abundant due to the lower activation energy for their formation and a higher mobility on glide planes [46].

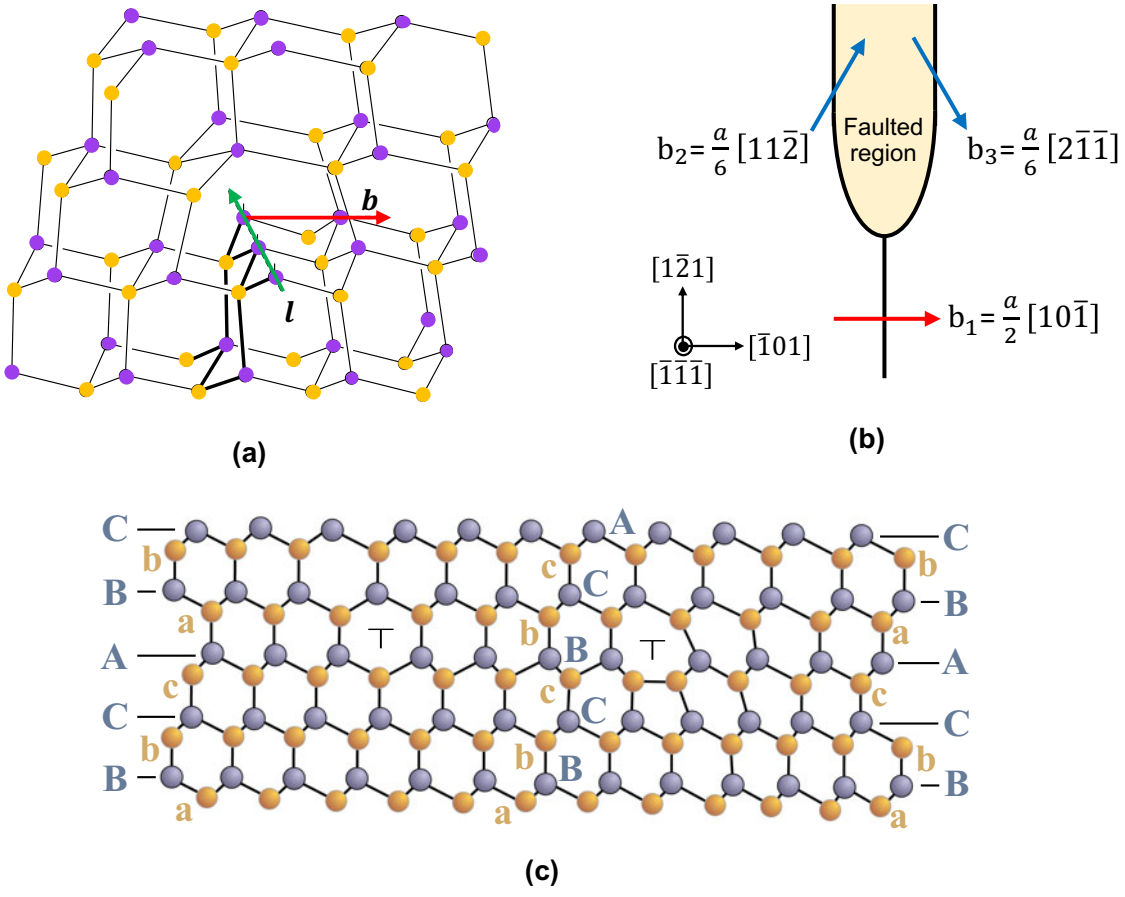

(a) (b)

(c)

Fig. 2.10. (a) A ball and stick model of a perfect 60° dislocation. The extra half-plane is depicted by the darker connecting sticks to the bottom [39] (b) A schematic illustration of a perfect dislocation splitting into partials and a stacking fault in an f.c.c. lattice [43] (c) atomic core configurations of 30°, 90° partials and their separating stacking fault viewed along $\langle 1\bar{1}0 \rangle$ type zone axis in a ZB crystal [2].

2.3.3 Dislocation sources in epitaxial layers and the critical thickness

As pointed out in section 2.2.1.2, dislocations nucleate during epitaxy on planar substrates when strain accommodation mode switches from elastic to plastic at $t > t_c$. There are three major modes of plastic strain relief namely, i) grown-in threading dislocations (TDs) ii) half-loop formation iii) interfacial misfit dislocations (IMF) [1]. Mechanisms i) and ii) are depicted in Fig. 2.12 (a) [45] as A and B, respectively. Apart from these three mechanisms, additional dislocations are generated during misfit dislocation interactions [45-47], shown as C in Fig. 2.12 (a). Grown-in threading dislocations are extensions of substrate dislocations and are energetically the easiest to from. Once nucleated, they may bend and glide over the slip plane under elastic strain. The heterogenous nucleation and expansion of dislocation half-loops is the next most favored mechanism. Both mechanisms i) and ii) ultimately produce misfit segments as the dislocation expands and reaches the interface (process 1→ 2, Fig. 2.12 (a)). The *glissile* 60° dislocations gliding on adjacent {111} planes as half-loops combine to form 90° *sessile* dislocations when they meet at the interface. Additionally, splitting of perfect dislocations into partials is favored in i) and ii) due to lowering of energy and increased mobility of extended dislocation cores. A schematic representation of misfit dislocations in relation to the threading segments is shown in Fig. 2.12 (b).

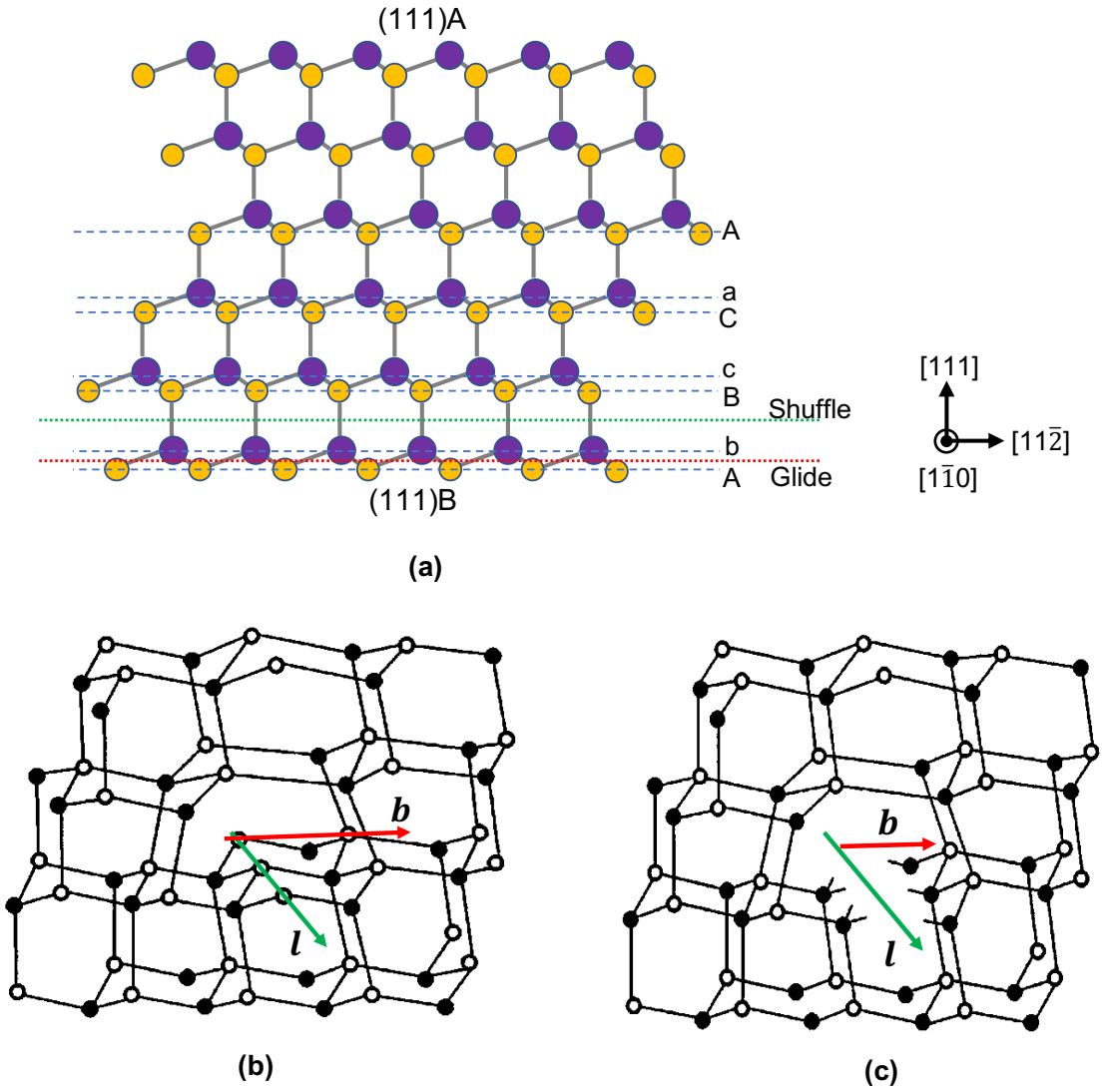

Fig. 2.11. Glide and shuffle set of (111) planes in ZB semiconductors viewed along the [1$\bar{1}$0] zone axis (a), (b) and (c) are respectively the ball and stick models of 60° perfect dislocations belonging to the glide and shuffle in these crystals [1,48].

Furthermore, Fig. 2.12(b) indicates the forces acting on a dislocation i.e. the resolved isotropic elastic strain driving dislocation glide (F_G) and its opposing forces, the line tension (F_l) and Peierls-Nabarro frictional drag force (F_p) [46].

Mechanism (iii) of plastic strain relaxation is characterized by formation of regular arrays of misfit dislocations at the interface. This mode is distinguished by the spontaneous formation of regular edge dislocation arrays at the heterointerface, in absence of an initial pseudomorphic layer. Moreover, such arrays are independent of interactions between 60° dislocations. Detailed studies of the GaSb/GaAs (001) system

point to the skipped Ga-Sb bonds on the GaAs surface as the sites for initiating edge dislocations. Such skipped bonds are the result of the large size difference between the covalent radii of Sb and Ga atoms. The edge character of IMF dislocations prevents slip on {111} planes of the epilayer and thus threading segments are absent in this mode. Selection of strain relaxation by this mode is very sensitive to surface reconstructions of the substrate and growth parameters employed.

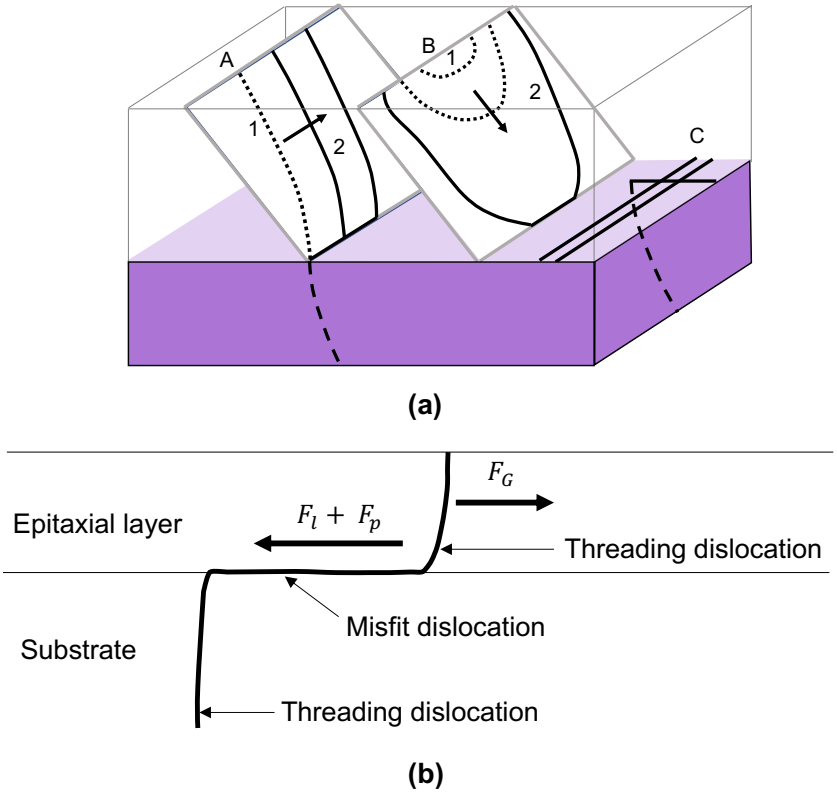

Fig. 2.12. (a) Schematic illustration of misfit dislocation generated at the heterointerface because of A grown-in threading dislocations and B nucleation of surface half-loops, C are the misfit segments produced due by processes A and B. The splitting of perfect 60° dislocations into partials during slip is indicated by the process 1 → 2 [44] (b) shows the misfit dislocation segment of a threading dislocation bent under the influence of elastic strain along with the forces acting upon it [49].

The critical thickness, t_c marking the transition from the pseudomorphic to metamorphic state has been successfully modeled by two thermodynamic approaches, energy minimization and force balance [42,1]. In the energy minimization approach, t_c is derived by the criterion $\partial(E_A + E_d) / (\partial\varepsilon) = 0$ with $E_d = E_d^{\theta}/S$ and S being the separation between dislocations in a square array. Whereas in the force balance

approach the opposing forces F_G and F_l, described in Fig. 2.12 (b) are equated to arrive at an expression for t_c, with the forces $F_G = \sigma_{\parallel} \cdot b \cdot t_e \cdot \cos\lambda$ and $F_l = E_d^{\theta}$. Among these two approaches, the force balance model originally introduced by Matthew and Blakeslee (MB) [50] is widely adopted in literature [1,2,51]. The expression for t_c based on this approach is

$$t_c = \frac{b\,(1-\upsilon\,\cos^2\alpha)\left[\ln\frac{t_c}{b}+1\right]}{8\,\pi\,f\,(1+\upsilon)\,\cos\lambda} \quad . \qquad 2.19$$

The variables υ,b, α,f and t_c in equation 2.19 are the same as previously defined. Here, λ is the angle between the Burgers vector and the line in the film plane, which is perpendicular to the intersection of the glide plane with the specimen surface. However, equation 2.19 has been shown to underpredict the critical thickness due to kinetic effects. More accurate models considering kinetic effects such as Peierls-Nabarro friction force, dislocation interaction and multiplication and stress dependent activation energy for dislocation glide have been developed [45, 47]. Few other shortcomings of the MB approach are the assumption of isotropic elasticity, the dependence of t_c on the value of the core parameter β being assumed. These shortcomings are handled by ab-initio based models which also incorporate effects arising from surface reconstruction, surface strain relaxation and elastic anisotropy [52, 53].

Beyond critical thickness, the efficiency of strain relieved by a misfit dislocation depends upon its component along the heterointerface. This is quantified by the amount of effective Burger's vector b_{eff} , which relieves a plastic strain δ amounting to $\delta = b_{eff}/S$. This relation holds true for planar epitaxial films. In the case of strained islands, it assumes the form $\delta = N \cdot b_{eff}/w$ where N is the number of interfacial misfit dislocations along the island's width w [54]. The magnitude of b_{eff} for 60° misfit dislocations at InAs/GaAs(111)A heterointerfaces is $\sqrt{6}a/4$. This value is obtained by resolving the $a/2\,\langle\bar{1}10\rangle$ Burgers vector along the $\langle1\bar{1}2\rangle$ direction of the heterointerface [55].

2.3.4 Stacking faults and twin boundaries

An *intrinsic stacking fault* (ISF) results when a part of a lattice plane or an entire lattice plane is missing, as is the case of a partial C plane in Fig. 2.13 (a), transforming the

perfect f.c.c. stacking to CAB | ABC. ISFs are formed by splitting of perfect dislocations into partials or due to condensation of vacancies on close packed planes during crystal growth. However, if an extra atomic plane is inserted, it results in an *extrinsic stacking fault* (ESF) as illustrated by the extra A layer in Fig. 2.13 (b). The Burgers vectors of SPDs' bounding an ISF or ESF lie in the {111} plane and are glissile, but those of FPD with Burgers vector $1/3\langle 11\bar{2}\rangle$ are sessile. A comparison between Fig.2.13 (a) and (b) reveals that an ISF causes disturbance in one atomic plane whereas an ESF causes disturbance in two.

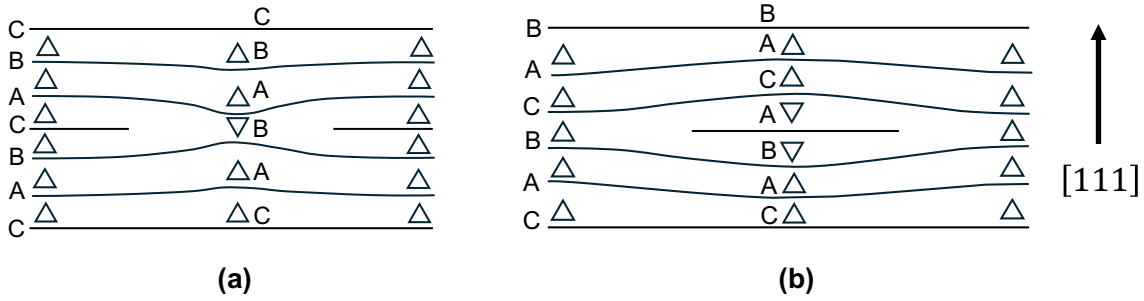

Fig. 2.13. Schematic illustration of stacking faults in f.c.c. structures (a) an intrinsic stacking fault and (b) an extrinsic stacking fault. △ and ▽ denote correct and wrong stacking sequences of close packed planes. In ZB crystals the A, B and C layers correspond to double layers Aa, Bb and Cc, created by cation-anion pairs. Adapted from [41].

The area along which two differently oriented crystals of the same material intersect is termed as a grain boundary and if this plane constitutes a mirror plane for the two crystals, it is called a twin boundary. When there is perfect one-to-one matching between the planes across the twin boundaries it is called a coherent twin boundary (CTB). CTBs' in case of ZB crystals are further classified into a mirror and rotational twin boundary (RTB) based on the polarity of atoms across the boundary. In the mirror twins shown in Fig. 2.14 (a), the two crystals are mirror images of one another across the boundary line. They show an angular separation of 60º about the [111] rotation axis. When an additional 180° rotation is provided to the mirror twin about the $[1\bar{1}0]$ axis, it results in an RTB. As seen in Fig. 2.14 (a) mirror twins show homopolarity, which is why they are less commonly observed in ZB semiconductors due to the high energy cost of repulsive interactions. A twin boundary showing no perfect matching of lattice planes across the defect plane is called an incoherent twin boundary (ITB). An ITB consists of rings of atoms arranged periodically across the interface. These twin boundaries shall not be discussed further in view of their non-relevance to the results of this thesis.

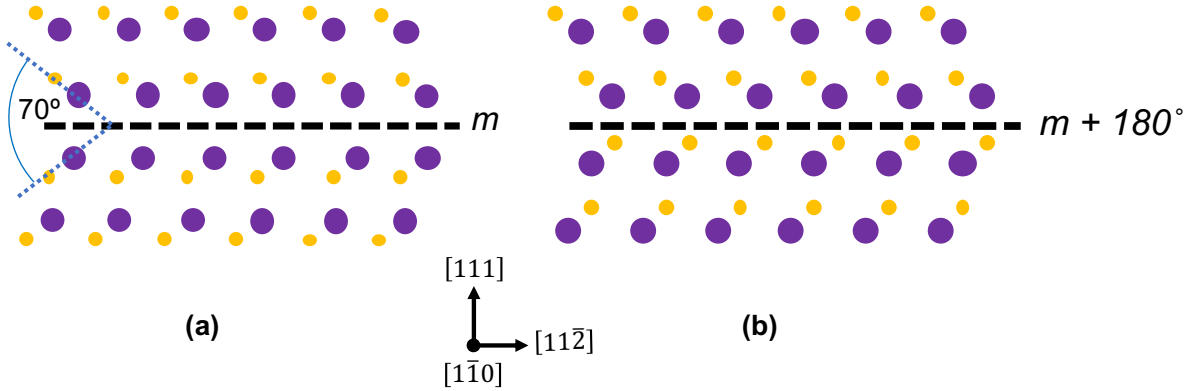

Fig. 2.14. A schematic representation of atomic columns in a ZB crystal viewed along the [1$\bar{1}$0]direction showing the mirror twin and the rotational twin boundaries in (a) and (b), respectively. Adapted from [40].

2.3.5 Polytypes

Polytypes are crystals with the same stoichiometry existing in different lattice structures. Wurtzite (WZ) and ZB are the commonly observed polytypes in III-V semiconductors. Stable bulk forms of III-V arsenides, antimonides and phosphides crystallize in the ZB phase, whereas nitrides form preferably in the WZ phase [56]. However, when the dimensions of these materials are reduced to the nanoscale, the dominance of surface energy can result in a phase switch. When ZB semiconductors are synthesized as nanowires, the WZ phase with its lower fraction of dangling bonds compared to the ZB phase is thermodynamically stable [57]. Hence, below a critical nanowire diameter, the WZ phase is stabilized although its bulk cohesive and electrostatic energy values are larger compared to the ZB phase [39]. In the case of III-V semiconductors, the difference in energy between ZB and WZ is less than 25 meV per III-V atom pair [2,58], increasing the propensity for mixed phase formation. The critical diameter for InAs nanowires is estimated to be ≈ 20 nm [57], ignoring kinetic effects.

Amongst the defects described in this section, dislocations are the most frequently observed and the most deleterious. Dislocations break the local crystal symmetry which alters the electronic states in their vicinity. The broken bonds at their cores and their strain fields create local charge traps and recombination centers. These effects have direct impact on the charge carrier density and performance of devices [39]. The industrially acceptable dislocation density in III-V arsenide devices is 10^2-10^3/ cm^2 [2]. Twins and stacking faults on the other hand are known to induce scattering of charge carriers and phonons at the boundaries [57]. And lastly, the bandgap and optical properties of nanostructures containing mixed ZB/WZ polytypes are affected when their proportions are not carefully controlled [59].

The next section will deal with methods to reduce defects in epitaxially grown structures, specifically misfit and threading dislocations.

2.4 Defect reduction strategies

A variety of defect mitigation techniques driven by the need for enabling integration of III-V semiconductors on Si(001) platforms have been developed over the last decades. Amongst them, the use of lattice matched *buffer layers* between the device and substrate layer has been widely explored. The simplest variant is the *uniform buffer layer* where a layer with a fixed composition and lattice parameter matched to the device layer is incorporated. This technique relies on the annihilation of TDs upon mutual interaction [1,2]. Such interactions are especially probable at the buffer/substrate interface where the threading dislocation densities (TDDs) reach 10^9-10^{10} cm^{-2} [60], depending on the mismatch. Buffer layers with thickness in the range of a few microns are commonly employed in this method. Introduction of a composition gradient in the buffer layers promotes dislocation glide and maximizes strain relaxation via an increase in MD segment length [61]. This method uses a *linearly graded buffer*. Yet another type of buffer layer approach involves the use of layers with alternating positive and negative signs of stress to create *strained layer superlattices* (SLS). Here, the alternating sinks of stresses force the bending of TDs on passing from one layer to another, ultimately resulting in their coalescence and annihilation [61]. The buffer layer approaches discussed thus far can produce *virtual substrates* (VS) with TDs in the range 10^6-10^8 cm^{-2}, depending on the system. Most buffer layer approaches also involve intermediate annealing steps which, in addition to their large thicknesses,

make the formation of buffer layers a time-consuming process. An additional drawback of this method is the susceptibility of buffer layers for crack formation due to thermal expansion coefficient mismatches with the Si substrate [62]. Another defect reduction method for heteroepitaxy on planar substrates is the use of multiple *quantum dot layers.* In this method, successive layers of QDs are deposited over III-V buffer layers grown over Si substrates. However, this defect reduction approach involves multiple buffer layer fabrication steps, making this technique less attractive. Strain fields created by QDs bend the TDs propagating from the buffer layer due to Peach-Koehler forces. This approach has been shown to produce GaAs with etch pit densities in the order of $9x10^5$ cm^{-2} [63-65].

A totally different way of addressing defect reduction is through *Selective area growth* (SAG) methods. In SAG approaches, the epilayer is deposited on the substrate through openings in a patterned dielectric mask. Openings, mostly in the form of trenches have been widely reported, arrays with square and round growth sites have also been explored. Here the dielectric masks play the role of trapping TDs at the walls as the epilayer propagates outwards during deposition. Growth conditions favoring selective growth within the mask openings and preventing parasitic nucleation over them are employed [62]. Epitaxial lateral overgrowth (ELO) and aspect ratio trapping (ART) are two of the most extensively explored SAG strategies for realizing a virtual substrate. In ELO, conditions promoting a high epilayer growth rate in the lateral direction are adopted with the objective of achieving merging of film fragments growing from adjacent mask openings [66]. A drawback of this technique is the high TDD in the film directly above the mask openings due their escape. Formation of coalescence boundaries upon merging of epilayer fragments from adjacent openings is another issue. The shortcoming of dislocation escape into the device layer is addressed with ART, using mask openings with aspect ratios (height to width ratios) typically > 1.43 [67]. A high enough aspect ratio (AR) helps in restricting the motion of 60° dislocations gliding over the {111} planes at the mask walls. One of the major drawbacks of ART is its inability to block partial dislocations which glide along a {111} plane oriented perpendicular to the trench direction [68]. The ELO and ART approaches are able to produce epilayers with TDDs in the order of 10^6 cm^{-2} on Si(001). Successful demonstrations of III-V/Si integration and device applications have also been reported using these two approaches [69,70].

The defect reduction strategies discussed thus far can restrict the TDD at the active region up to a range of 10^5 cm^{-2} at best [1,68,71], mainly due to the confinement of elastic strain relaxation to the vertical direction. This obstacle is overcome by performing heteroepitaxy on substrates with reduced growth areas which allows strain relief in all three dimensions. A major advantage of this approach is the ability to prevent the formation of dislocations at the very beginning of growth. The strain relief mechanisms involved and the kernel of the theoretical approaches enabling the estimation of critical substrate dimensions are discussed in the next section.

2.4.1 Growth on substrates with reduced growth areas

An again totally different defect reduction technique involves heteroepitaxy on substrates with reduced growth areas, since the total the number N of TDs' available for strain relaxation at the heterointerface depends on the growth area A and substrate dislocation density D due to the relation N = DA. A reduction in growth area A proportionally reduces the number of TDs. Additionally, a lower A facilitates migration of TDs to sample edges when annealed. This possibility was initially envisaged by Matthews in 1970 [47].

The efficacy of the concept was demonstrated by Fitzgerald in the $In_xGa_{1-x}As/GaAs(001)$ system using compositions that resulted in low misfits (<2%) [46]. The theoretical background for heteroepitaxy on rigid nanopatterend substrates as a means for complete mitigation of dislocations was proposed by Luryi and Suhir [72]. This was further modified by Zubia and Hersee [73] by including the effect of substrate compliance. They named their theory "*nanoheteroepitaxy*", abbreviated as NHE. The strain relaxation mechanisms and the predictions for critical substrate and epilayer dimensions by NHE and other models/approaches are discussed in the next sections.

2.4.1.1 Nanoheteroepitaxy (NHE)

During heteroepitaxy on planar substrates, the mismatch strain is relieved by vertical lattice deformation of the epilayer or by forming threading dislocations, depicted in Fig. 2.15 (a) *(i)* and *(ii)*, respectively. In contrast to this, Zubia and Hersee propose in NHE a three-dimensional strain relief due to lateral and vertical deformation of the nanoscale substrate and epilayer, illustrated by mechanisms *i* , *iii*, *iv* and *v* in Fig. 2.15

(b) [73]. Additionally, even MDs that might form at the heterointerfaces in systems with large lattice mismatch can easily glide towards edge when annealed, aided by dislocation image forces [1] and create a step as indicated as *vi* in Fig. 2.15 (b). The full potential of NHE is realized by using square or round seed pads with lateral dimensions in the 10-100 nm range [1, 74], separated by large enough distances to guarantee growth selectivity. The theory behind these models is detailed in Appendix-2, whereas only their most salient aspects shall be discussed here.

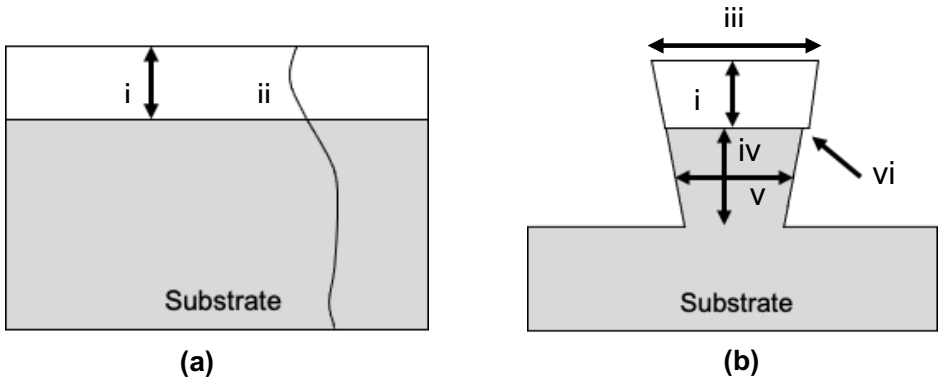

Fig. 2.15. A schematic of the stress relief mechanisms operative during heteroepitaxy on (a) planar substrates and (b) nanopillar patterned substrates. Adapted from [73].

Luryi and Suhir formulated expressions describing the evolution of epilayer stress along the film thickness, assuming a "rigid" contact at the epilayer-seed pad interface and that the strain energy of epilayer concentrated along its center [72]. The in-plane strain distribution is of the form

$$\sigma_{\parallel} = \frac{\mathrm{Y}_{epi}}{1-\upsilon_{epi}}\, \varepsilon_{epi}\, \chi(y,z) e^{-\pi z/2l} \,. \qquad 2.20$$

Here, an important relation is the exponential decay of stress with diameter, 2l of the seed pad, indicating the impact of nanoscale dimensions on strain relief along the epilayer thickness. Here, Y_{epi}, ε_{epi} and υ_{epi} are the Young's modulus, strain and Poisson ratio of the epilayer. The lateral stress distribution is described by the function $\chi(x,y)$ (elaborated in Appendix-2). The authors go on to predict the critical thickness, $h_c^l(f)$, needed for triggering plastic relaxation as

$$h_c^l(f) = h_c\, [\phi\, (l/h_c^l) f] \quad , \qquad 2.21$$

where h_c is the critical thickness predicted for conventional planar substrates using either the People and Bean model [75] or the Matthews and Blakeslee expression [50].

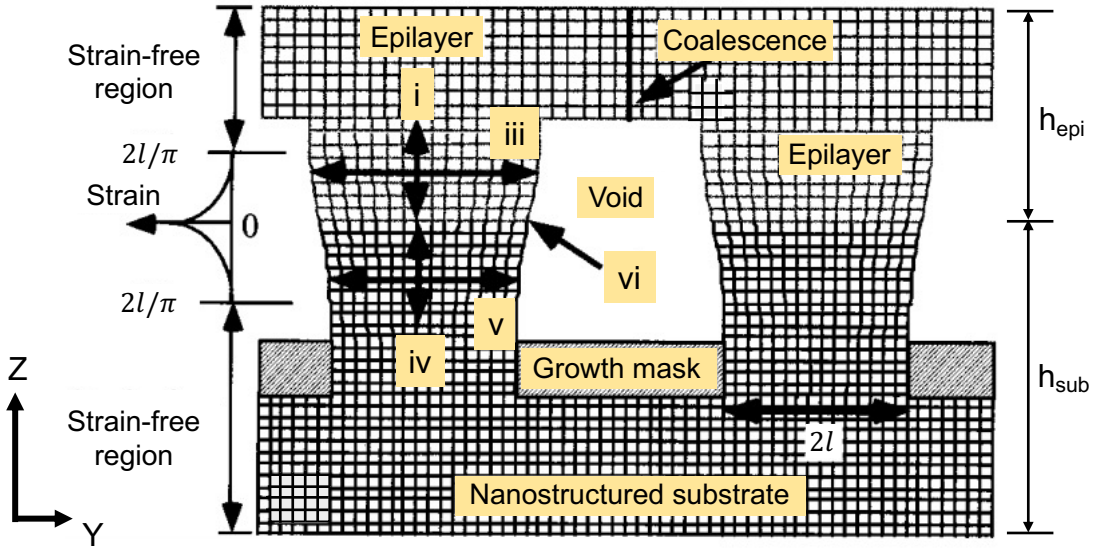

Fig. 2.16. A schematic representation of the NHE growth model proposed by Zubia and Hersee [76].

By including the substrate compliance effect to the above theory, Zubia and Hersee estimated the extent of strain partitioning between the epilayer and substrate. This is indicated by the exponential decay of strain away from the heterointerface on both the epilayer and the substrate as shown in Fig. 2.16. Additionally, the strain relaxation mechanisms (i)-(vi) described earlier aiding in are also indicated. However, the features such as epilayer coalescence and the resulting void region have been retained from the Luryi and Suhir model (Fig. A2-1, Appendix-2).

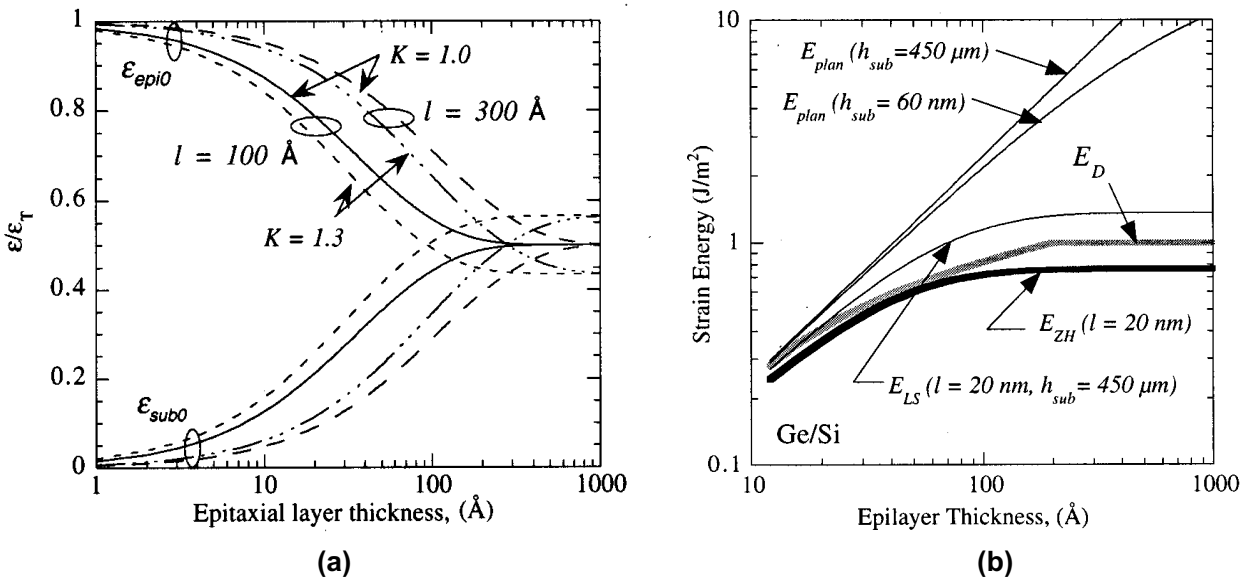

Fig. 2.17. (a) Interfacial strain partitioning as a function of deposited epilayer thickness for seed pads with diameters 100 and 300 Å at K values 1 and 1.3 (b) Dependence of strain energy on epilayer thickness in the Ge/Si system for planar and nanopatterned substrates, estimated using ZH and LS models [73].

During a typical NHE growth, the majority of lattice misfit strain in the initial stages is accommodated by the epilayer but as thickness increases, the portion of strain accommodated by the substrate increases. This effect is termed *"strain partitioning"*. Figure 2.17 (a) is a graphical representation of this phenomenon, the value on the y-axis represents the strain relative to lattice misfit strain *f*, represented here as ϵ_T. Also noticeable from this graph is the dependence of strain partitioning on the diameter 2l of seed pads used and on the value of K

$$K = \frac{\mathrm{Y_{epi}}}{(1-\upsilon_{epi})}\frac{(1-\upsilon_{sub})}{\mathrm{Y_{sub}}}, \qquad 2.22$$

where Y and υ are the Young's modulus and Poisson ratio, respectively, with subscripts corresponding to epilayer or substrate as the case might be. It can also be inferred that a higher K value corresponding to a stiffer epilayer enhances the extent of strain partitioning, considering that $\upsilon \approx 0.3$ for most semiconductor materials.

The most important outcome of the model by far is an expression for the total areal strain energy $E_{coh.}^{Total}$:

$$E_{coh.}^{Total} = E_{epi} + E_{sub} = \frac{Y_{epi}}{1-\upsilon_{epi}} \varepsilon_{epi,0}^2 h_{epi}^{eff} + \frac{Y_{sub}}{1-\upsilon_{sub}} \varepsilon_{sub,0}^2 h_{sub}^{eff} \quad . \qquad 2.23$$

By equating this total areal strain energy to the areal strain energy to formation energy of a mixed dislocation, the critical epilayer thickness for plastic relaxation can be estimated:

$$\frac{Y_{epi}}{1-\upsilon_{epi}} \varepsilon_{epi,0}^2 h_{epi}^{eff} + \frac{Y_{sub}}{1-\upsilon_{sub}} \varepsilon_{sub,0}^2 h_{sub}^{eff} = \frac{1}{5} \frac{G_{sub}G_{epi}b}{2\pi (G_{sub}+G_{epi})} \left(\cos^2\theta + \frac{\sin^2\theta}{1-\upsilon_{dep}}\right) \left(1 + \ln\frac{R}{b}\right). \quad 2.24$$

In their estimates for critical thickness, Zubia and Hersee however used the areal strain energy expression of a screw dislocation, expressed as

$$E_{Disloc.} = \frac{Gb^2}{4\pi(1-\upsilon)W_D} \ln\left(\frac{R}{b}\right) \quad . \qquad 2.25$$

A comparative plot of strain energies for the Ge/Si system ($f = 4.2\%$) with planar and nanostructured substrates and $E_{Disloc.}$ (equation 2.25), as a function of epilayer thickness, made by Zubia and Hersee [73] is presented in Fig. 2.17 (b). The plots indicate that Ge deposits on compliant Si structures with diameters 40 nm or below can grow dislocation free for infinite thicknesses.

Experimental results of NHE growth performed on silicon-on-insulator (SOI) substrates [77-79] by Zubia and Hersee demonstrated the reduction in defect density in GaAs/Si and GaN/Si systems away from the heterointerface. The authors also demonstrated the compliancy effect resulting from the softening of Si nanopillars due to melting point reduction. Ge/Si is another system of technological significance which was heavily researched by Schroeder et. al., who have been able to prove the glide of threading dislocations out of the Ge epilayer upon annealing [80]. The authors also demonstrate the synthesis of fully relaxed Ge crystals with MDs confined to the heterointerface [81] and even defect free [82]. However, the SiO_2 selective area growth masks used during their growth experiments impeded the realization of strain partitioning [83].

2.4.1.2 Other theories

Nanowires (NWs) with their high aspect ratio and specific surface areas open many possibilities for synthesis of strain free heterostructures. This is made possible by the

very efficient strain relaxation along the sidewalls. Axial nanowires, radial nanowires, nanowires on bulk substrates and quantum dots on nanowire surfaces (top and/or sidewalls) are the morphologies made possible employing nanowire substrates [84]. Among these mentioned variants, focus will be paid on strain relaxation in axial nanowires due to its congruity with NHE. The models dealing with coherent relaxation of axial NWs assume coherency at the heterointerface and force cancellation on all free surfaces of the epilayer. Moreover, the large aspect ratio of the NW substrate ensures that its strain state remains unaffected by the bulk substrate underneath. Linear elastic approaches are best suited for describing the strain distribution of such systems and one of the early models were proposed by Ertekin et al. [85]. In this work, the authors propose expressions describing the strain field, vary certain parameters in them until the strain expressions yield minimum total elastic energy. Their work produced analytical expressions that predict the critical diameter for achieving an infinitely long coherent NW epilayer. However, the basic strain expressions used in this model called the variational approach is not based on solutions of elasticity. This renders the results unreliable for quantitative estimates and they also do not result in lateral free surfaces. A more precise analytical solution for this problem was derived by Frank Gals [86], employing modified Barton's solution for an infinitely long cylindrical bar subjected to a uniform pressure [87]. Conditions such as finite epilayer thickness and the existence of free lateral and top surfaces were superimposed to simulate a strain free epilayer. The calculations reveal the attainment of a strain free state in the epilayer at thickness $h \geq 2r_0$, r_0 being the radius of the NW epilayer, as shown in Fig. 2.18 (a). Hence, the material deposited beyond this thickness assumes its bulk lattice parameter. This effect is quantified by the ratio $f_v(\rho) = W_e/W_{2D}$ [88]. Here W_e and W_{2D} are the total strain energies of the epilayer-NW system shown in Fig. 2.18 (a) and that of an epilayer of an same volume deposited on a flat substrate of identical elastic parameters and lattice misfit ,respectively and ρ the aspect ratio the epilayer. Essentially, the term $f_v(\rho)$ captures the extend of surface strain relaxation dependent upon ρ. A good approximation for its value is $f_v(\rho) = 1/(1 + A_v\rho)$, A_v= 27.3±0.55 for $\upsilon = 0.33$. Frank Glas was able to theoretically demonstrate a 75% decrease in surface strain relaxation $f_v(\rho)$ even for $\rho \cong 0.1$.

As an extension to these calculations, Frank Gals incorporated the transition towards plastic relaxation by inserting a pair of orthogonal dislocations along a NW's diameter. The average distance of the dislocation pair to the lateral surface was

averaged as $\bar{d}=\beta r_0$ with $\beta = 2/\pi$ and the average distance $\bar{h}$ between the dislocation and free surface was defined as $\bar{h} = h$ if $h \leq \beta r_0$ and $\bar{h} = \beta r_0$ if $h \geq \beta r_0$. An effective misfit, defined as $f_{eff} = f - n\,4b_{eff}/(\pi D)$ with n = 0, 1, 2…denoting the number of interfacial dislocation pairs was used in the estimation of residual elastic strain energy. The difference between elastic strain energy and dislocation energy $\Delta W(r_0, h)$ is considered for estimating the critical thickness h_c. When ΔW >0, the system is coherent and when ΔW <0 , dislocations are introduced. Equation 2.26 when solved iteratively yields the value of h_c for a given r_0.

$$\Delta W(r_0, h) = \frac{Yr_0}{1-\upsilon}\left[f_\upsilon\left(\frac{h}{2r_0}\right)\pi r_0 h\left(\frac{\alpha^2 b_{eff}}{4r_0^2} - \frac{\alpha b_{eff}}{r_0}f\right) + C\left(1 + \ln\frac{\bar{h}(r_0,h)}{b}\right)\right],$$

with $\alpha=4/\pi$ and $C = (1-\upsilon\cos^2\theta)b^2/[2\pi(1+\upsilon)]$ 2.26

A plot showing the variation of critical thickness as a function of misfit strain according to this approach is shown in Fig. 2.18. The data presented in Fig. 2.18 are specific to 60° dislocations with θ=30° and $b_{eff} = b/2$, the value of b being 0.4 nm. The h_c vs r_0 plot of Fig. 2.18 conveniently separates the (r_0, h) plane into coherent (left, below) and relaxed (right, above) states. Most importantly, the vertical asymptotes in this figure indicate substrate radii that result in infinitely thick dislocation free NW epilayers. The verification of the predictions shown in Fig. 2.18 against experimental data from various coaxial NW systems such as InAs/InP [89], GaP/GaAs [90] and GaP/$GaAs_{1-x}P_x$/GaP [91] showed good agreement.

By following finite element method (FEM) based solutions for the equations of elasticity in axial NWs, with and without dislocations, Ye et al. [92,93] estimated the critical diameter of NWs and the position of dislocations at the interface. Most importantly, the interaction between the coherency strain of epilayer and dislocations were captured using the Peach-Kohler [94] approach, resulting in more precise values.

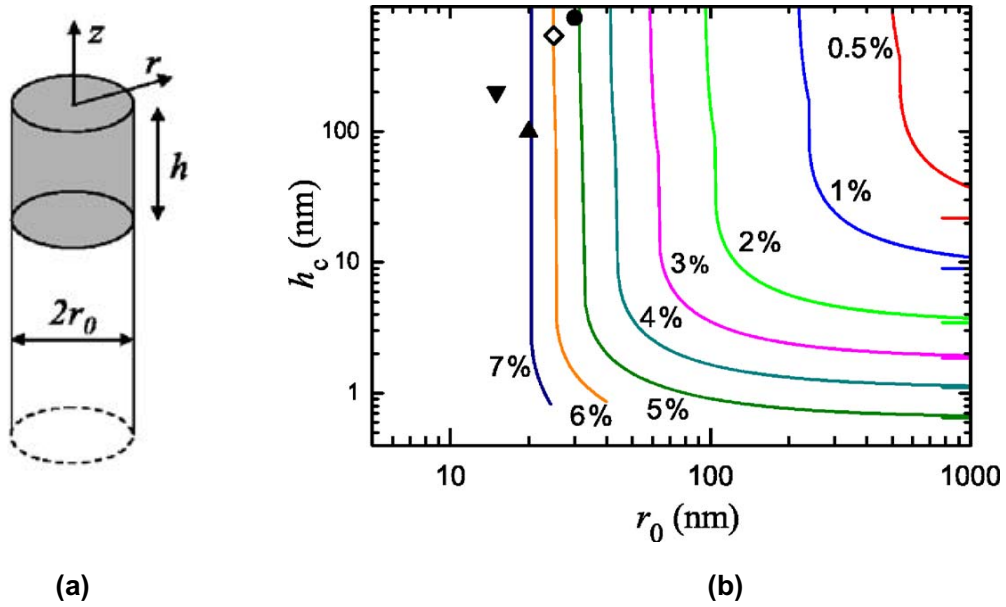

Fig. 2.18. (a) A schematic representation of the semi-infinite NW substrate (white) and NW epilayer (grey) of height h with common diameter $2r_0$ considered in Frank Gas's model. (b) The colored lines, corresponding to the marked misfits show the variation of critical thickness h_c as a function of NW substrate radii r_0. The open and closed symbols demarcate the epilayer thicknesses corresponding to coherent and dislocated configurations, respectively [84].

2.4.1.3 Comparison of predictive models for critical nanowire dimensions

The determination of critical dimensions of epilayer and nanoscale substrate that prevent plastic relaxation have been approached using analytical and numerical methods in literature [8,72,73,84,85,92,93,95]. While the substrate geometries considered in analytical approaches are limited, their generality and simplicity compensate for it. Numerical approaches on the other hand such as FEM provide the flexibility of including detailed substrate geometries, but such exact solutions are very much system specific [84]. Hence, a comparison of the results based on the analytical approaches formulated by Zubia and Hersee, Frank Glas and Ertekin et. al. shall be made here. Most of the inferences presented in this section are based on [95] where predictions of these models are made considering υ=0.33, $Y_{epi} = Y_{sub}$= 100 GPa for 60° and 90° dislocations. The estimate of the critical diameter below which an infinitely thick epilayer, free from dislocations as a function of misfit is considered first, mainly because the model by Ertekin et al. assumes $h_{epi} \rightarrow \infty$ [85]. A comparison of the critical NW diameter values below which infinitely thick epilayers can be deposited is plotted

as a function of misfit in Fig. 2.19 (a). The plots show a clear separation between the curves of Zubia and Hersee, which is based in the energy areal density criterion and Frank Glas and Ertekin's total energy criterion. These discrepancies can be attributed to the assumption of maximum strain energy density along the nanowire axis in the Zubia and Hersee model and the neglection of residual misfit strain.

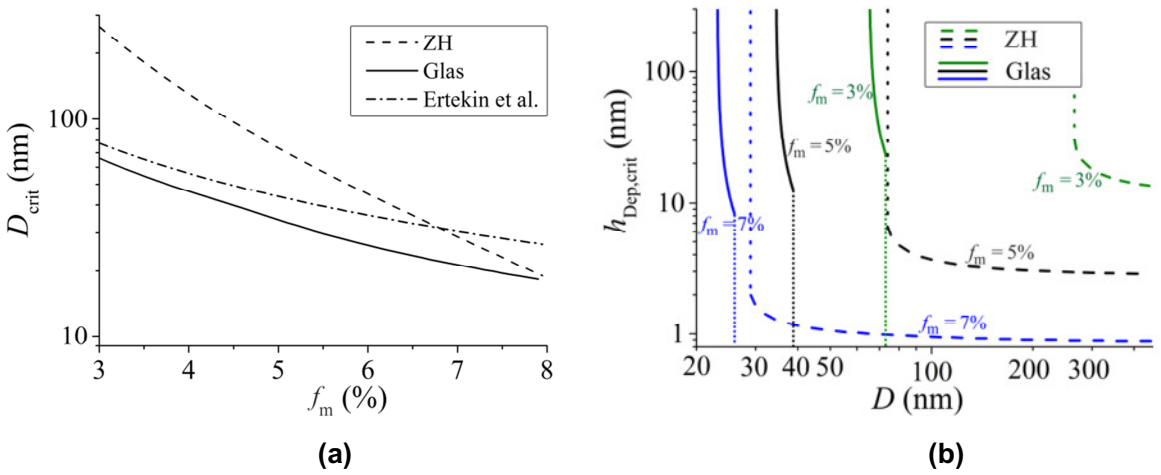

Fig. 2.19. Predictions of (a) Critical nanowire diameter D_{crit} as a function of lattice misfit f_m (b) Critical epilayer thickness $h_{Dep,crit}$ as a function of nanowire diameter D [93].

The influence of such assumptions is also evident in Fig. 2.19 (b) showing the dependence of critical deposit thickness $h_{Deposit}$ on the nanowire thickness in the Zubia and Hersee and Frank Glas models. The deviation in the plots for critical deposit thickness as a function of NW diameter increases at low misfits, like in Fig. 2.19 (a). Nevertheless, for the misfit value relevant to the InAs/GaAs system (f_m = 7%), the predicted critical diameters amount to 23 and 28 nm, for the FG and Zubia and Hersee models respectively. Such theoretical estimates provide valuable guidelines for choosing the fabrication process for NW or nanopillar substrates upon which coherently strained epilayers can be realized. It must be noted that predictions made using the models thus far are based purely on thermodynamic equilibrium considerations, ignoring kinetic barriers for defect nucleation.

References

1) J. E. Ayers, T. Kujofsa, P. Rago, J. Raphael, "Heteroepitaxy of Semiconductors: Theory, Growth and Characterization", II Edition, CRC Press (2016).

2) U. W. Pohl, "Epitaxy of Semiconductors: Introduction to Physical Principles", Springer (2013).

3) N. Holonyak Jr., R. M. Kolbas, R. D. Dupuis and P. D. Dapkus, "Quantum-well heterostructure lasers", IEEE J Quantum Electron, QE-16, 170 (1980).

4) A.Y. Liu, R.W. Herrick, O. Ueda, P.M. Petroff, A.C. Gossard, and J.E. Bowers, "Reliability of InAs/GaAs Quantum Dot Lasers Epitaxially Grown on Silicon", IEEE J Quantum Electron, 21, 690 (2015).

5) S.D. Gunapala, S.V. Bandara, J.K. Liu, E.M. Luong, S.B. Rafol, J.M. Mumolo, D.Z. Ting, J.J. Bock, M.E. Resseler, M.W. Werner, P.D. LeVan, R. Chehayeb, C.A. Kukkonen, M. Levy, P. LeVan and M.A. Fauci, "Quantum Well Infrared Photodetector Research and Development at Jet Propulsion Laboratory", Sens. Mater. ,12, 327 (2000).

6) J. Phillips, P. Bhattacharya, S.W. Kennerly, D.W. Beekman, and M. Dutta, "Self-Assembled InAs–GaAs Quantum-Dot Intersubband Detectors", IEEE J Quantum Electron, 35, 936 (1999).

7) K.E. Sautter, K.D. Vallejo and P.J. Simmonds, "Strain-driven quantum dot self-assembly by molecular beam epitaxy", J. Appl. Phys. 128, 031101 (2020).

8) F. Glas, J.-C. Harmand and G. Patriarche, "Why Does Wurtzite Form in Nanowires of III-V Zinc Blende Semiconductors?", Phys. Rev. Lett., 99, 146101 (2007).

9) J.A. Stroscio and W.J. Kaiser (Eds.), "Methods in Experimental Physics", Vol. 27, Academic Press Inc., (1993).

10) Thomas Michely and Joachim Krug, "Islands, Mounds and Atoms", Springer Series in Surface Sciences, Band 42, Springer, (2003).

11) M.L. Royer, "Experimental research on the epitaxy or mutual orientation of crystals of different species", Bull. Soc. Fr. Min., 51, 7 (1928).

12) A. Pimpinelli and J. Villain, "Physics of Crystal Growth", Cambridge University Press (1998).

13) T. Ito, N. Ishimure, T. Akiyama and K. Nakamura, "Ab initio-based approach to adsorption–desorption behavior on the InAs(111)A heteroepitaxially grown on GaAs substrate", J. Cryst. Growth, 318, 72 (2011).

14) T. Ito and T. Akiyama, "Recent Progress in Computational Materials Science for Semiconductor Epitaxial Growth", Crystals, 7, 42 (2017).

15) H. Brune, "Epitaxial growth of thin films", In: Surface and Interface Science, Vol. 4, K. Wandelt (Ed.), Wiley -VCH Verlag GmbH (2014).

16) T. Nishinga and T. F. Kuech (Eds.), "Handbook of Crystal Growth Thin Film and Epitaxy: Basic Techniques", Vol. 3, Part A, Elsevier (2014).

17) R.L Schwoebel and E.J. Shipsey, "Step motion on crystal surfaces", J. Appl. Phys., 37, 3682 (1966).

18) F. Hatami and O. Bierwagen, "Growth of low-dimensional semiconductor structures", In: "Comprehensive Semiconductor Science and Technology", Vol. 1, P. Bhattacharya, R. Fornari and H. Kamimura (Eds.), Elsevier (2011).

19) R. Nötzel, Z. Niu, M. Ramsteiner, H.-P. Schönherr, A. Tanpert, L. Däweritz, K.H. Ploog , "Uniform quantum-dot arrays formed by natural self-faceting on patterned substrates", Nature, 392, 56 (1998).

20) L. Esposito, S. Bietti, A. Fedorov, R. Nötzel, S. Sanguinetti, "Ehrlich-Schwöbel effect on the growth dynamics of GaAs(111)A surfaces", Phys. Rev. Mater., 1,024602 (2017).

21) J. Ritzmann, R. Schott, K. Gross, D. Reuter, A. Ludwig and A.D. Wieck, "Overcoming Ehrlich-Schwöbel barrier in GaAs(111)A molecular beam epitaxy", J. Cryst. Growth, 481, 7 (2018).

22) P. Smilauer and D. D. Vvedensky, "Step-edge barriers on GaAs(001)", Phys. Rev. B, 48, 17603 (1993).

23) N.A.K. Kaufmann, L. Lahourcade, B. Hourahine, D. Martin and N. Grandjean, "Critical impact of Ehrlich–Schwöbel barrier on GaN surface morphology during homoepitaxial growth", J. Cryst. Growth, 433, 36 (2016).

24) H. Brune and K. Kern, "Heteroepitaxial metal growth: the effects of strain", In: The chemical physics of solid surfaces, Vol. 8, D. A. King and D.P. Woodruff (Eds.), Elsevier (1997).

25) D.W. Pashley, "Epitaxy growth mechanisms", Mater. Sci. Technol., 15:1, 2 (1999).

26) W. Siefert, N. Carlsson, M. Miller, M-E Pistol, L. Samuelson and L.R. Wallenberg, "In-situ growth of quantumdot structures by the Stranski–Krastanow growth mode", Prog. Cryst Growth. Charact. Mater., 33, 422471 (1996).

27) T. Ito, T. Akiyama and K. Nakamura, "Growth mode in heteroepitaxial system from nano- and macro- theoretical viewpoints", J. Cryst. Growth, 512, 41 (2019).

28) X. Li and G. Yang, "Strain self-releasing mechanism in heteroepitaxy on nanowires", J. Phys. Chem. C, 113, 12402 (2009).

29) X. Li and G.W. Yang, "Theoretical determination of contact angle in quantum dot self-assembly", Appl. Phys. Lett., 92, 171902 (2008).

30) X.L. Li, C.X. Wang and G.W. Yang, "Thermodynamic theory of growth of nanostructures", Prog. Mater. Sci., 64, 121 (2014).

31) A. Vailionis, B. Cho, G. Glass, P. Desjardins, D.G. Cahill and J.E. Greene, "Pathways for the strain-driven two-dimensional transition during growth Ge on Si(001)", Phys. Rev. Lett., 85, 3672 (2000).

32) G. Constantini, A. Rastelli, C. Manzano, P. Acosta-Diaz, G. Kastsaros, R. Songmuang, O.G. Schmidt, H.v. Känel, K. Kern, "Pyramids in the InAs/GaAs(001) and Ga/Si(001) systems", J. Cryst. Growth, 278, 38 (2005).

33) B.A. Joyce and D. D. Vvedensky, "Heteroepitaxial growth modes and morphologies on GaAs surfaces", In: Thin films: Heteroepitaxial systems, Vol. 15, W. K. Liu and M. B. Santos (Eds.), World scientific publishing Co. Pte. Ltd. (1999).

34) A. Rastelli and Hans von Känel, "Surface evolution of faceted islands", Surf. Sci., 515, L493 (2002).

35) N. Moll, M. Scheffler and E. Pehlke, "Influence of surface stress on the equilibrium shape of strained quantum dots", Phys. Rev. B, 58, 4566 (1998).

36) X.L. Li, G. Ouyang and G.W. Yang, "A thermodynamic theory of self-assembly of quantum dots", New. J. Phys.,10, 043007 (2008).

37) D. Bimberg, "Semiconductor Nanostructures", Springer (2008).

38) B.A. Joyce and D.D. Vvedensky, "Quantum dots in the InAs/GaAs system: An overview of their formation", In: Quantum dots: fundamentals, applications and frontiers, B.A. Joyce, P.C. Kelires, A.G. Naumovets and D.D Vvedensky (Eds.), NATO science series, Springer (2003).

39) D.B. Holt and B.G. Yacobi, "Extended defects in semiconductors", Cambridge university press (2007).

40) Y.A.R. Dasilva, R. Kozak, R. Erni and M.D. Rossell, "Structural defects in cubic semiconductors by aberration-corrected scanning transmission electron microscopy", Ultramicroscopy, 176, 11 (2017).

41) D. Hull and D.J. Bacon, "Introduction to Dislocations", Butterworth-Heinemann (2011).

42) E.A. Fitzgerald, "Dislocations in strained-layer epilayer: theory, experiment and applications", Mater. Sci. Rep., 7, 87 (1991).

43) G.E. Dieter, "Mechanical Metallurgy", III Edition, McGraw-Hill publishers (1989).

44) C-Z. Wang, J. Li, K-M Ho and S. Yip, "Undissociated screw dislocation in Si: glide or shuffle?", Appl. Phys. Lett., 89, 051910 (2006).

45) P.M. J. Maree, J.C. Barbour, J.F. van der Veen, K.L. Kavanaugh, C.W.T. Bulle-Lieuwma and M.P.A. Viegers, "Generation of misfit dislocations in semiconductors", J. Appl. Phys., 62, 4413 (1987).

46) E.A. Fitzgerald, G.P. Watson, R.E. Proano, D.G. Ast, P.D. Kirchner, G.D. Pettit and J.M. Woodall, "Nucleation mechanisms and the elimination of misfit dislocations at mismatched interfaces by reduction in growth area", J. Appl. Phys., 65, 262110 (1989).

47) J.W. Matthews, S. Marder and T.B. Light, "Accommodation of misfit across the interfaces between crystals of semiconducting elements or compounds", J. Appl. Phys., 41, 3800 (1970).

48) Z. Bougrioua, J.L. Faevaceque and D. Ferre, "Efffects of dislocations on transport properties of two-dimensional electron gas. I. Transport at zero magnetic field", J. Appl. Phys., 79, 1536 (1996).

49) E.A. Fitzgerald, "The effect of substrate growth area on misfit and threading dislocation densities in mismatched heterostructures", J. Vac. Sci. Technol. B, 7, 782 (1989).

50) J. W. Matthews and A.E. Blakeslee, "Defects in epitaxial multilayers: I Misfit dislocations", J. Cryst. Growth, 27, 118 (1974).

51) R. Hull and J.C. Bean (Eds.),"Germanium Silicon: physics and materials science", Semiconductors and semimetals, Vol. 56, Academic press (1999).

52) T. Ito, T. Akiyama and K. Nakamura, "Growth mode in heteroepitaxial systemsfrom nano- and macro- theoretical viewpoints", J. Cryst. Growth., 512, 41 (2019).

53) L.A. Zepedia-Ruiz, D. Maroudas and W.H. Weinberg, "Theoretical study of the energetics, strain fields and semicoherent interface structures in layer-by-layer semiconductor heteroepitaxy, J. Appl. Phys., 85, 3677 (1999).

54) M. Lentzen, D. Gerthsen, A. Förster and K. Urban, "Growth mode and strain relaxation during the initial stage of InxGa1-xAs growth on GaAs(001)", Appl. Phys. Lett., 60, 74 (1992).

55) T. Riedl, V.S. Kunnathully, A. Trapp, T. Langer, D. Reuter and J.K.N. Lindner, "Size-dependent strain relaxation in InAs quantum dots on top of GaAs(111)A nanopillars", Adv. Mater. Interfaces., 9, 2102159 (2022).

56) T. Ito, "Simple criterion for wurtzite-zinc blende polytypism in semiconductors", Jpn. J. Appl. Phys., 37, 1217 (1998).

57) T. Akiyama, K. Sano, K. Nakamura and T. Ito, "An empirical potential approach to wurtzite-zinc blende polytypism in group III-V semiconductor nanowires", Jpn. J. Appl. Phys., 45, 275 (2006).

58) P. Caroff, J. Bolinsson and J. Johansson, "Crystal phases in III-V nanowires: from random towards engineered polytypism", IEEE J. of Sel. Top. Quantum Electron., 17, 829 (2011).

59) L. Güniat, P. Caroff and A.F. i Morral, "Vapor phase growth of semiconductor nanowires: key developments and open questions", Chem. Rev., 119, 8958 (2019).

60) Y. Du, B. Xu, G. Wang, Y. Miao, B. Li, Z. Kong, Y. Dong, W. Wang and H.H. Radamso, „ "Review of highly mismatched III-V heteroepitaxy growth on (001) Si", Nanomaterials,12, 1741 (2022).

61) B. Kunert, Y. Mols, M. Baryshniskova, N. Waldron, A. Schulze and R. Langer, "How to control defect formation in monolithic III/V hetero-epitaxy on (001)Si? A critical review on current approaches", Semicond. Sci. Technol., 33, 093002 (2018).

62) T. Riedl and J.K.N. Lindner, "Heteroepitaxy of III-V zinc blende semiconductors on nanopatterned substrates", In: "Nanoscaled films and layers", L. Nanai (Ed), InTechOpen (2017).

63) D. Huang, M.A. Reshchikov, F. Yun, T. King, A.A. Baski and H. Morkoc, "Defect reduction with quantum dots in GaN grown on sapphire substrates by molecular beam epitaxy", Appl. Phys. Lett., 80, 216 (2002).

64) J. Yang, P. Bhattacharya and Z. Mi, "High-performance $In_{0.5}Ga_{0.5}As/GaAs$ quantum-dot lasers on silicon with multiple-layer quantum-dot dislocation filters", IEEE Trans. Electron. Devices, 54, 2849 (2007).

65) H. Hu, J. Wang, Y. He, K. Liu, Y. Liu, Q. Wang, X. Duan, Y. Huang and X. Ren, „Modified dislocation filter method: towards growth of GaAs on Si by metal organic chemical vapor deposition", Appl. Phys. A, 122, 588 (2016).

66) Z.R. Zytkiewicz, "Laterally overgrown structures as substrates for lattice mismatched epitaxy", Thin Solid Films, 412, 64 (2002).

67) J.-S. Park, J. Bai, M. Curtin, B. Adekore, M. Carroll and A. Lochtefeld, "Defect reduction of selective Ge epitaxy in trenches on Si(001) substrates using aspect ratio trapping", Appl. Phys. Lett., 90, 052113 (2007).

68) B. Kunert and K. Volz, "Monolithic III/V integration on (001) Si substrate", In: Metalorganic vapor phase epitaxy (MOVPE): growth, materials properties and applications", S. Irvine and P. Capper (Eds.), John Wiley and Sons Ltd. (2020).

69) J.G. Fiorenza, J.-S. Park, J.M. Hydrick, J. Li, J.Z. Li, M. Curtin, M. Carroll and A. Lochtefeld, "Aspect ratio trapping: a unique technoogy for integrating Ge and III-Vs with Si CMOS", ECS Trans., 33, 963 (2010).

70) D.J. Ironside, A.M. Skipper, A.M. Garcia and S.R. Bank, "Review of lateral epitaxial overgrowth of buried dielectric structures for electronics and photonics", Porg. Quant. Electron., 77, 100316 (2021).

71) G. Wang, R. Loo, E. Simoen, L. Souriau, M. Caymax, M.M. Heyns and B. Blanpain, "A model of threading dislocation density in strain-relaxed Ge and GaAs epitaxial films on Si(100)", Appl. Phys. Lett., 94, 102115 (2009).

72) S. Luyri and E. Suhir, "New approach to the high-quality epitaxial growth of lattice mismatched materials", Appl.Phys. Lett., 49, 140 (1986).

73) D. Zubia and S.D. Hersee, "Nanoheteroepitaxy: The applicaton of nanostructuring and substrate compliance to the heteroepitaxy of mismatched semiconductor materials", J. Appl. Phys., 85, 6492 (1999).

74) A. Fischer and H. Richter,"Elastic misfit stress relaxation in heteroepitaxial SiGe/Si mesa structures", 61, 2656 (1992).

75) R. People and J.C. Bean, "Calculation of critical thickness versus lattice mismatch for Ge_xSi_{1-x}/Si strained-layer heterostructures", Appl. Phys. Lett., 47, 322 (1985).

76) D. Zubia, S.H. Zaidi, S.D. Hersee and S.R. J. Brueck, "Nanoheteroepitaxy: Nanofabrication route to improved epitaxial growth", J. Vac. Sci. Technol. B, 18, 3514 (2000).

77) D. Zubia, S.H. Zaidi, S.R.J. Brueck and S.D. Hersee, "Nanoheteroepitaxial growth of GaN on Si by organometallic vapor phase epitaxy", Appl. Phys. Lett., 76, 858 (2000).

78) D. Zubia, S. Zhang, R. Bommena, X. Sun, S.R.J. Brueck and S.D. Hersee, J. Electron. Mater., ," Initial nanoheteroepitaxial growth of GaAs on Si(100) by OMVPE", 30, 812 (2001).

79) S.D. Hersee, D. Zubia, X. Sun, R. Bommena, M. Fairchild, S. Zhanng, D. Burckel, A. Frauenglass and S.R.J. Brueck, "Nanoheteroepitaxy for the integration of highly mismatched semiconductor materials", 38, 1017 (2002).

80) J. Bauer, Y. Yamamoto, P. Zaumseil, O. Fursenko, K. Schulz, G. Kozlowski, M.A. Schubert, T. Schroeder and B. Tillack, "Nanostructured silicon for Ge nanoheteroepitaxy", Microelectron. Eng., 97, 169 (2012).

81) G. Kozlowski, Y. Yamamoto, J. Bauer, M.A. Schubert, B. Dietrich, B. Tillack and T. Schroeder, "Selective Ge heteroepitaxy on free-standing Si(001) nanopatterns: A combined raman, transmission electron microscopy, and finite element method study", J. Appl. Phys., 110, 053509 (2011).

82) G. Niu, G. Capellini, M.A. Schubert, T. Niermann, P. Zaumseil, J. Katzer, H-M. Krause, O. Skibitzki, M. Lehmann, Y-H. Xie, H. von Känel and T. Schroeder, "Dislocation-free Ge nano-crystals via pattern independent selective Ge heteroepitaxy on Si nano-tip wafers", Sci. Rep., 6, 22709 (2016).

83) P. Zaumseil, Y. Yamamoto, A. Bauer, M.A. Schubert and T. Schroeder, "X-ray characterization of Ge epitaxially grown on nanostructured Si(001) wafers", J. Appl. Phys., 109, 023511 (2011).

84) F. Glas, "Strain in nanowires and nanowire heterostructures", In: Semiconductor and semimetals, Vol. 93, "Semiconductor nanowires I: growth and theory", A. F. I Morral, S.A, Dayeh and C. Jagadish (Eds), Academic press (2015).

85) E. Ertekin, P.A. Greaney, D.C. Chrzan and T.D. Sands, "Equilibrium limits of coherency in strained nanowire heterostructures", J. Appl. Phys., 97, 114325 (2005).

86) F. Glas, "Critical dimensions for the plastic relaxation of strained axial heterostructures in free-standing nanowires", Phys. Rev. B, 74, 121302-1(2006)

87) M.V. Barton, "The circular cylinder with a and of uniform pressure on a finite length of the surface", J. Appl. Mech., 8, A97 (1941).

88) F. Glas and B. Daudin, "Stress-driven Island growth on top of nanowires", Phys. Rev. B, 86 174112 (2012)

89.) M.T. Björk, B.J. Ohlsson, T. Sass, A.I. Pearsson, C. Thrlander, M.H. Magnusson, K. Deppert, L.R. Wallenberg and L. Samuelson, "One-dimensional steeplechase for electrons realized", Nano. Lett., 2, 87 (2002).

90) M.A. Verheijen, G. Immink, T. de Semet, M.T. Borgström and E.P.A.M Bakkers, "Growth kinetics of heterostructured GaP-GaAs nanowires", J. Am. Chem. Soc., 128, 1353 (2006).

91) C.P.T. Svensson, W. Seifert, M.W. Larsson, L.R. Wallenberg, J. Stangl, G, Bauer and L. Samuelson, "Epitaxially grown GaP/$GaAs_{1-x}P_x$/GaP double heterostructure nanowires for optical applications", Nanotechnology 16, 936 (2005).

92) H. Ye and Z. Yu, "Plastic relaxation of mixed dislocation in axial nanowire heterostructures using Peach-Koehler approach", Phys. Status Solidi Rapid Res. Lett., 8, 445 (2014).

93) H. Ye, P. Lu, Z. Yu, Y. Song, D. Wang and S. Wang, "Critical thickness and radius for axial heterostructure nanowires using finite-element method", Nano Lett., 9, 1921 (2009).

94) M. Peach and J.S. Koehler, "The forces exerted on dislocations and the stress fields produced by them", Phys. Rev.80, 436 1950)

95) T. Riedl and J.K.N. Lindner, "Comparison of theoretical approaches predicting the coherent-semicoherent transition in nanoscale axial heterostructures", MRS proceedings, 1664, 7 (2014).

Chapter 3
Characterization methods

This chapter describes the various tools employed in the present thesis for accessing the structural perfection of the synthesized materials. These are essential for aiding process control and prediction of mechanisms related to strain relaxation of nanostructures discusses in the subsequent chapters.

3.1 Light optical microscopy

Light optical microscopic investigations of Polystyrene (PS) spheres deposited GaAs substrates was performed in bright field and differential interference contrast (DIC) mode using a Zeiss Axio Scope A1 light microscope. In DIC, a polarizer splits light from the source into orthogonally polarized components. These components are reflected differently from inclined surface areas and thus their interference leads to images containing inclination dependent contrasts.

3.2 Scanning electron microscopy (SEM)

A scanning electron microscope (SEM) is nowadays a routinely used tool for imaging the surface morphology of materials. In a SEM an electron beam produced by a thermionic of field emission source is turned into a fine probe using a series of lenses. The probe is rastered over the sample surface and the resulting signals such as secondary electrons (SE), backscatter electrons, characteristic x-rays etc. are processed to create respective images [1]. A schematic of a SEM is shown in Fig. 3.1. In the present thesis the in-lens mode was extensively used for imaging due to its very high sensitivity to surface topography. An in-lens detector consists of an SE detector embedded into the polepiece of the objective lens. The sample surface is brought close to the magnetic field of the objective lens by reducing the working distance (sample to pole piece distance). The so called SE1 electrons which are produced exclusively by the interaction of the impinging electrons and the sample, from the sample i.e. without excitation by backscatter electrons, are accelerated into the pole piece and are detected by the in-lens SE detector as shown in Fig. 3.1. Such a configuration gives the best resolution. In the present work, a Raith Pioneer (Raith 150-2 series) SEM was used for SEM imaging. An acceleration voltage of 15 kV was used for InAs/GaAs(111)A and

SiN_x, whereas polymers such as the PS spheres were imaged at a lower voltage of 5 kV to prevent beam induced damage. A low working distance of 4.5 mm was used to exploit the full potential of the in-lens mode.

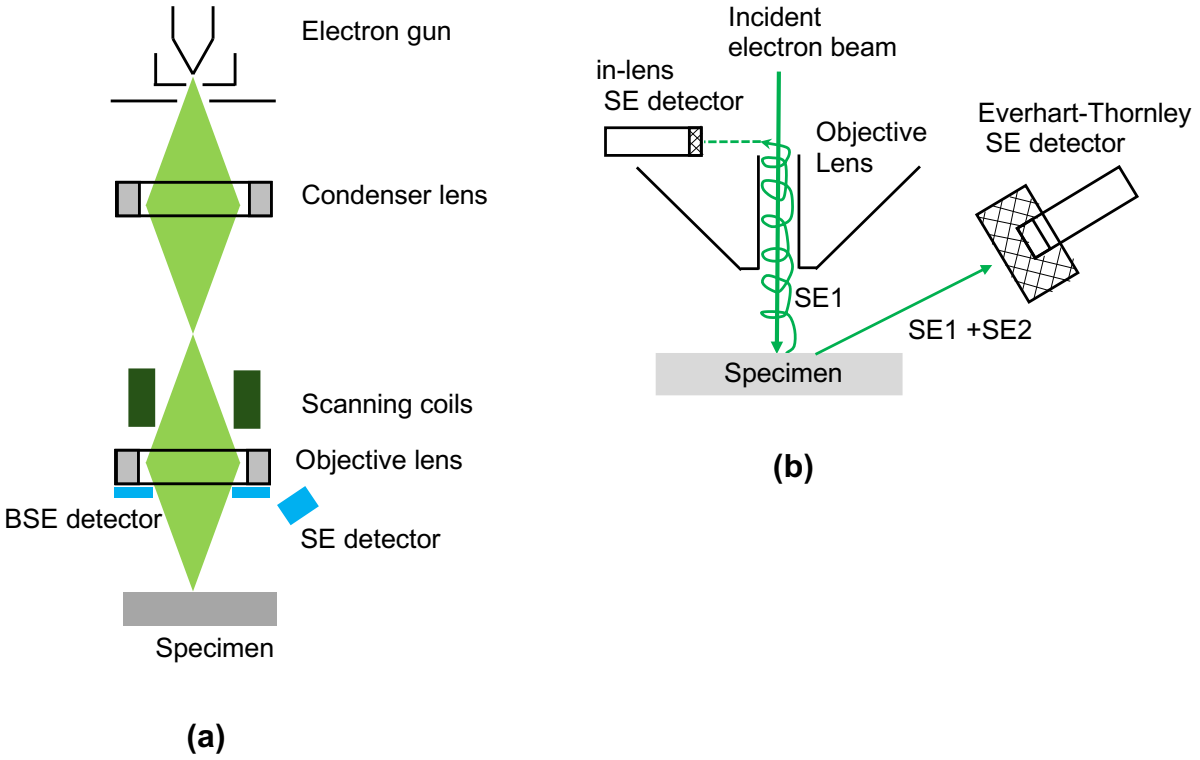

Fig. 3.1. A schematic illustration of an SEM's basic components is shown in (a), (b) shows the basic geometry of an in-lens detector. (a) and (b) are adapted from [2 and 3], respectively.

3.3 Scanning/Transmission electron microscopy

Scanning transmission electron microscopy (STEM) and Transmission electron microscopy (TEM) are extensively used tools for the investigation of materials with very small dimensions mainly because it enables the direct visualization of atomic configurations. The high lateral resolution of the (S)TEM is attributed to the rather small wavelengths that can be achieved by accelerating electrons. An electron accelerated by a voltage U has a wavelength λ which can be calculated using relativistic corrections with the relation

$$\lambda = \frac{h}{\sqrt{2m_0 eU\left(1+\frac{eU}{2m_0c^2}\right)}} \quad , \qquad 3.1$$

where, h, m_o and c are the Planck's constant, rest mass of the electron and velocity of light, respectively [4]. Hence, an electron accelerated to 200 kV has a relativistic wavelength of 2.51 x 10^{-12} m. This wavelength value when evaluated with the Rayleigh criterion for resolution δ of an optical instrument which relates the wavelength of an instrument to the refractive index μ of a medium and collection semi-angle of the lens β, stated as

$$\delta = \frac{0.61\,\lambda}{\mu \sin(\beta)} \quad , \qquad 3.2$$

[4] yields a value of a 2.7 pm. This value is not practically achieved due to lens aberrations. The best resolution achievable by the instrument used in this thesis, the JEOL ARM-200F with Cs-correction is 80 pm in STEM mode and 190 pm in TEM mode. Hence, the detection and quantification of misfit dislocations and local chemistry in the present case is rendered possible only using this technique. This section describes the various (S)TEM based techniques that were employed for the qualitative and quantitative analysis of the InAs/GaAs(111)A heterointerfaces in terms of structural perfection, lattice strain and chemistry. All (S)TEM measurements were performed on JEOL ARM-200F Cs-corrected TEM. Specimens were prepared using both conventional precision ion polishing (PIPS) and focused ion beam milling (FIB). (S)TEM data were acquired using the bright field (BF), high-angle annular diffraction (HAADF) , energy dispersive X-ray spectroscopy (EDS) and the energy filtered transmission electron microscopy (EFTEM) mode. The raw (S)TEM data was analyzed using DigitalMicrograph [5] software and lattice strain was evaluated using geometrical phase analysis (GPA) plugging provided by HREM research [6].

3.3.1 Microscope set-up

Fig. 3.2 (a) shows a schematic diagram of the JEOL ARM-200F TEM/STEM [7]. The instrument's set-up consists of three essential parts, namely the illumination system, the sample stage and objective system and the imaging system. These are marked in Fig. 3.2 (a). The illumination system comprises the electron source, which in the present case is a cold field emission gun. Electrons thus generated can be accelerated in the rage of 30 – 200 kV, and 200 kV was used in this work. The electrons then pass through condenser lenses which form the beam and scan coils which are needed for rastering the beam in the STEM mode. Also important for defining the STEM probe

are the condenser apertures. Two sets of apertures C1 and C2 with four aperture sizes each are provided. In between the condenser lens and the condenser apertures is the ASCOR Cs-corrector manufactured by CEOS GmbH which can correct lens aberrations of upto the 5th order. After this, the electrons pass through the condenser mini lens which controls the parallelity of the electron beams in the TEM mode. Thereafter, the electron interacts with the specimen which is placed in a holder in the goniometer with the possibility of translation along the X, Y and Z axes, and tilting about up to two axes.

The electron-specimen interaction produces a range of signals as shown in Fig. 3.2 (b). Amongst these, the elastically scattered electrons and direct beam are relevant for (S)TEM based imaging techniques, characteristic x-rays for STEM-EDS and inelastically scattered electrons for EFTEM.

The electrons emerging from the exit surface of the specimen are focused by the objective lens to create diffraction patterns (DP) in the back focal plane of the objective lens. These rays recombine to form an image in the image plane of the objective lens. DPs of images can be observed by changing the strength the intermediate lens. The ray diagrams shown in Fig. 3.3 (a) and (b) illustrate this. The bright-field (BF) and high-resolution transmission electron microscopy (HRTEM) imaging and EFTEM modes using the broad beam were used in this thesis, whereas HAADF-STEM was performed using the converged beam.

The electron beam then passes through three intermediate lenses and one projector lens which magnify the image before it arrives at the viewing screen or a 4k x 4k CMOS camera. Prior to this, a HAADF detector is placed after the projector lens for STEM imaging. A GATAN GIF- Quantum ER energy filter equipped with a GIF CCD camera placed under the TEM column enables EFTEM and EELS measurements. Additionally, for EDS measurements a JEOL SDD is provided.

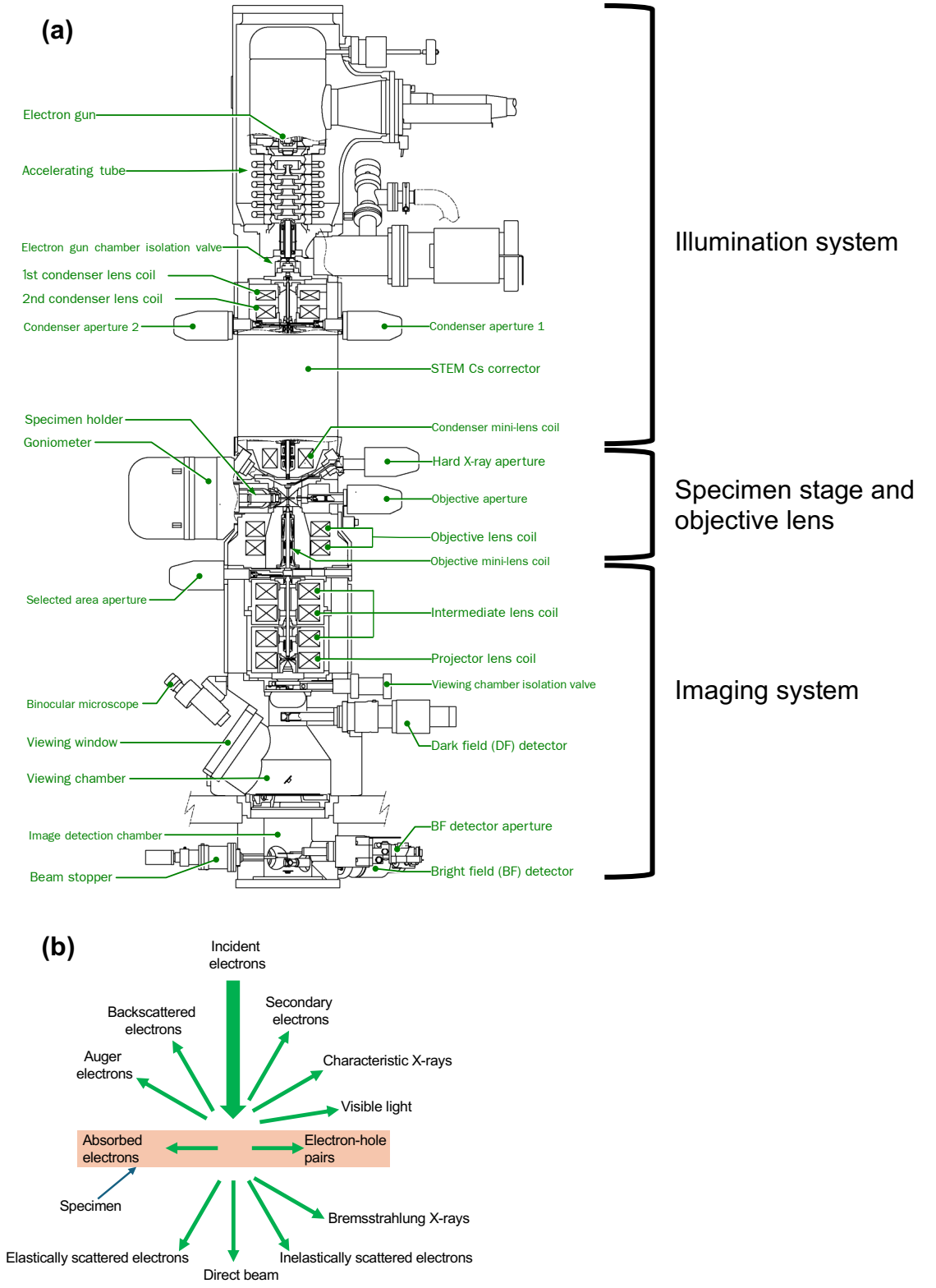

Fig. 3.2. (a) A schematic illustration of the JEOL ARM 200-F TEM/STEM [7]. (b) Various signals produced by beam-specimen interaction in a TEM [4].

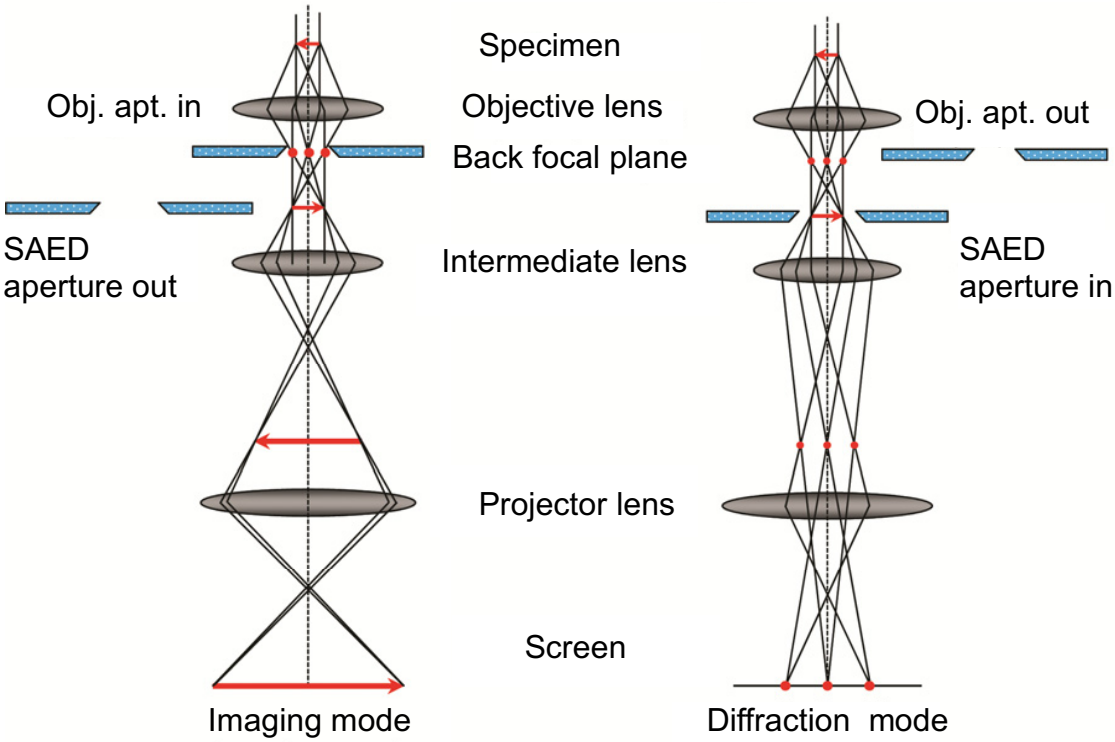

Fig. 3.3 (a) and (b) show ray diagrams illustrating the imaging and diffraction modes of a TEM respectively [8].

3.3.2 Imaging and analytical techniques

3.3.2.1 TEM-BF and HRTEM imaging

A bright field (BF) image is produced when the first intermediate image formed beyond the back focal plane of the objective lens (OL) is brought to the object plane of the intermediate lens (Fig. 3.3). In a BF image, only electrons along the microscope axis contribute to the imaging. Hence, an objective aperture (OA) restricting the off-axial beams can be placed at the back focal plane to prevent off-axial beams form contributing to the image, yielding an image with improved contrast with lower intensity (Fig. 3.3(a). Image contrast in BF-TEM images arise either due to mass-thickness contrast or diffraction contrast. In the former case, regions in the sample with heavier atoms or larger thickness suffer a larger extent of Rutherford elastic scattering, the electron beam is scattered off-axis, and these regions appear dark in the image. The combined contribution of both these factors is called mass-thickness contrast. Similarly, diffraction by favorably oriented crystal planes in the certain

regions of a specimen result in them appearing darker and is termed diffraction contrast.

3.3.2.2 HRTEM imaging

HRTEM images result from the interference between the direct and diffracted beams in the back focal plane of the OL. Their phase difference results in alternating dark and bring fringes and spots which correspond to the lattice periodicity. An essential condition for achieving such images is a low specimen thickness (ideally below 20 – 30 nm), to prevent plural scattering of beams. Additionally, the beam direction must be oriented along a low-index zone axis for achieving good resolution of fringes, the $\langle 1\bar{1}0 \rangle$ type zone axis was chosen during HRTEM imaging to render the dislocations visible [9].

3.3.2.3 HAADF-STEM

In the STEM mode, images are formed by scanning a fine probe over the specimen and recording them serially, dot by dot. The probe is formed using the condenser lenses, maintaining it parallel to the optical axis throughout the scan. This is achieved by using two pairs of double deflector scan coils which create a pivot point in the front focal plane of the third condenser lens. A schematic illustration of the process is shown in Fig. 3.4 (a). The elastic scattering of electrons within the specimen results in a convergent beam electron diffraction pattern in the back focal plane of the objective lens. Images using scattered electrons by various degrees can be created with electron detectors shown in Fig. 3.4 (b). Amongst them, the annulus shaped HAADF detector is highly sensitive to the atomic number of atoms. Atoms with higher atomic number (Z) scatter the electrons to a greater extent and appear brighter in HAADF-STEM images. The intensity shows a $Z^{2-\delta}$ dependence with a small δ, which depends on the exact experimental conditions. This enables a straightforward interpretation of images and qualitative determination of elements. Additionally, the tolerance towards minor local specimen thickness variations compared to HRTEM makes it a technique of choice for lattice strain mapping.

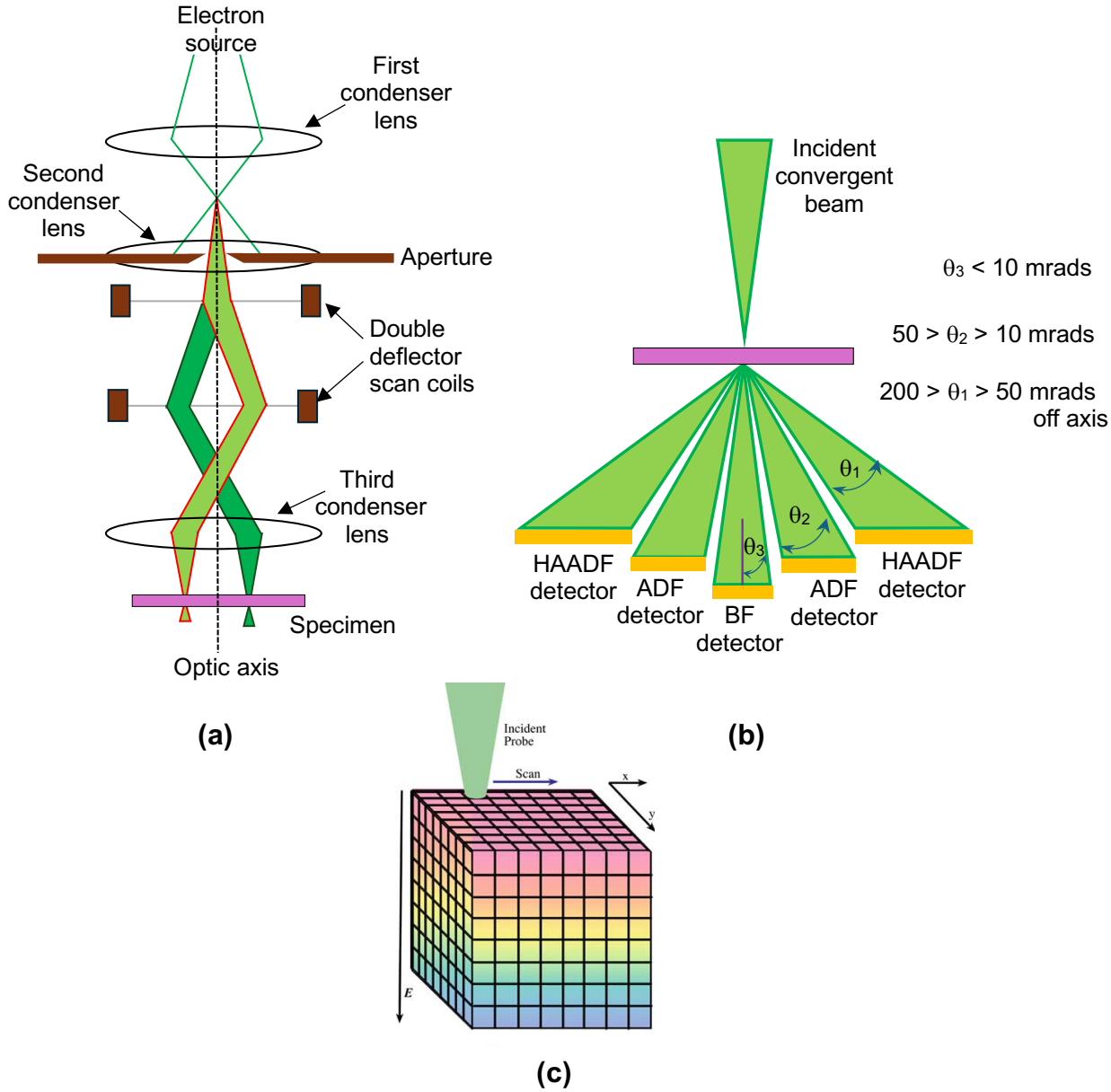

Fig. 3.4 (a) shows the probe formation mechanism while operating the microscope in the STEM mode (b) illustrates the various electron detectors and their placement with respect to the various angles of scattered beam, adapted from [4]. (c) A schematic of a 3D data cube generated during STEM-EDS mapping in the x-y plane [4].

3.2.2.4 Energy dispersive X-ray spectroscopy (EDS)

Fast moving electrons knock out inner shell electrons of atoms within the specimen upon impact and lose up to 20 keV of energy doing so. The missing shell electrons leave the atom in an excited state, leading to electronic transitions that release characteristic X-rays. The X-ray energies are element specific and can be used for qualitative and quantitative detection of elements in the specimen. STEM-EDS line scans were performed to detect In traces on GaAs pillars and SiN_x hard masks. The acquisition of EDS data in the STEM mode enables the collection of EDS spectrum at every pixel. The resulting data is stored in the form of a 3D data cube for an area EDS map, schematically shown in Fig. 3.4(c). For a line scan the cube reduces to a slice with the width along the x-axis of the cube reduced to the size of a single pixel.

3.2.2.5 Energy filtered transmission electron microscopy (EFTEM)

EFTEM is one of the techniques based on the use of inelastically scattered electrons emerging from the specimen. Incident electrons undergo energy losses due to various processes. A measurement of these losses can be used to determine properties such as bonding states, band gap and specimen thickness to name a few. The instrumentation consists of an energy filter placed below the column which magnetically disperses electrons based on their energy. By choosing a specific energy window, images can be made with electrons which have undergone a certain amount of energy loss. The quadrupole and hexapole lenses behind an energy selective slit focus these images onto the GIF camera where they are registered. This is illustrated in Fig. 3.5. EFTEM-BF images have better contrast due to the lack of inelastically scattered electrons. These images can also be used to create relative thickness maps. This is done by taking a logarithm of intensities from unfiltered and zero-loss or elastic images. The relative thickness is calculated as

$$\frac{t}{\lambda} = -\log\frac{I_o}{I_t} \quad ,$$

where t/λ [10] is the sample thickness relative to the mean free path of the electrons, I_o and I_t are the intensities of the unfiltered and zero-loss peak electrons, respectively. In the present case, a slit width of 10 eV centered at the zero-loss peak was used to generate the elastic images.

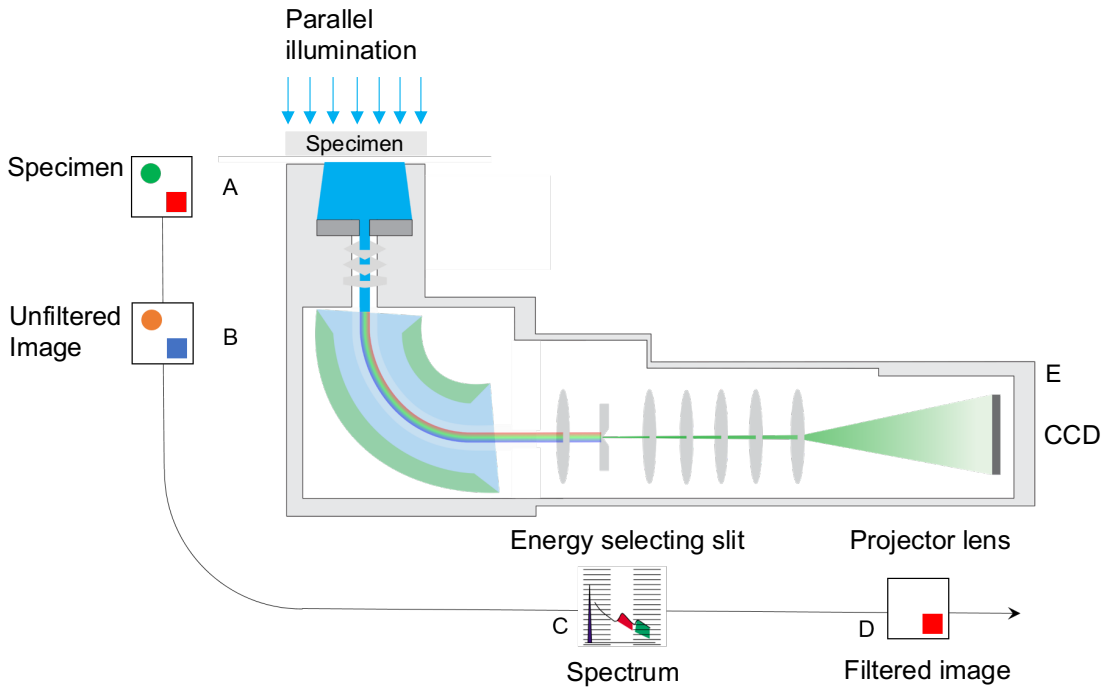

Fig. 3.5 Schematic of a conventional EFTEM with post-column energy filter, energy selecting slit and CCD detector for imaging. The energy filter (C) transforms the unfiltered image (B) of the specimen (A) into a spectrum, choosing a filter of appropriate energy range results in a filtered image (D) which is projected onto a CCD camera (E) [11]

3.3.3 Specimen preparation

3.3.3.1 Conventional cross-section specimen preparation

Conventional specimen preparation of cross-sectional TEM specimens involve various steps. These are illustrated in Fig. 3.6. Initially, two wide 2 mm stripes are cut using a slow speed saw (Fig. 3.6 (a)). These cuts are made along the $[1\bar{1}0]$ direction in the sample plane. The sample surfaces of interest are coated with epoxy glue and pasted one on top of the other as shown in Fig. 3.6 (b). The glue is hardened by annealing in air in a box furnace maintained at 130°C. This results in a sandwich of sample surfaces with glue in between. Next, the sandwich structure is sliced into ≈ 900 µm wide pieces and are individually glued into the slots of a CuZn-grid having a diameter of 3 mm (Fig. 3.6 (c) and (d)). This assembly is further thinned by grinding over SiC coated papers until a final thickness of ≈ 100 µm is reached. Further thinning of the discs at the center is performed using a dimple grinder (Model 656 from Gatan). The dimpling process is terminated to leave a thickness of ≈ 30 µm at the center of the

sample (Fig. 3.6 (e)). This remaining amount of material is thinned down using Ar ions using a Gatan Model 691 precision ion polishing system (PIPS). Two guns operating in turns mill the sample's surface by attacking at predefined angles and energies, which can be independently varied Fig. 3.6 (f). An accelerating voltage of 4.5 keV and incidence angles of +3 and -4.5 degrees were used for the milling at a vacuum of ≈ 5 x 10^{-5} Torr. The milling is terminated when a small hole forms at the center of the sample.

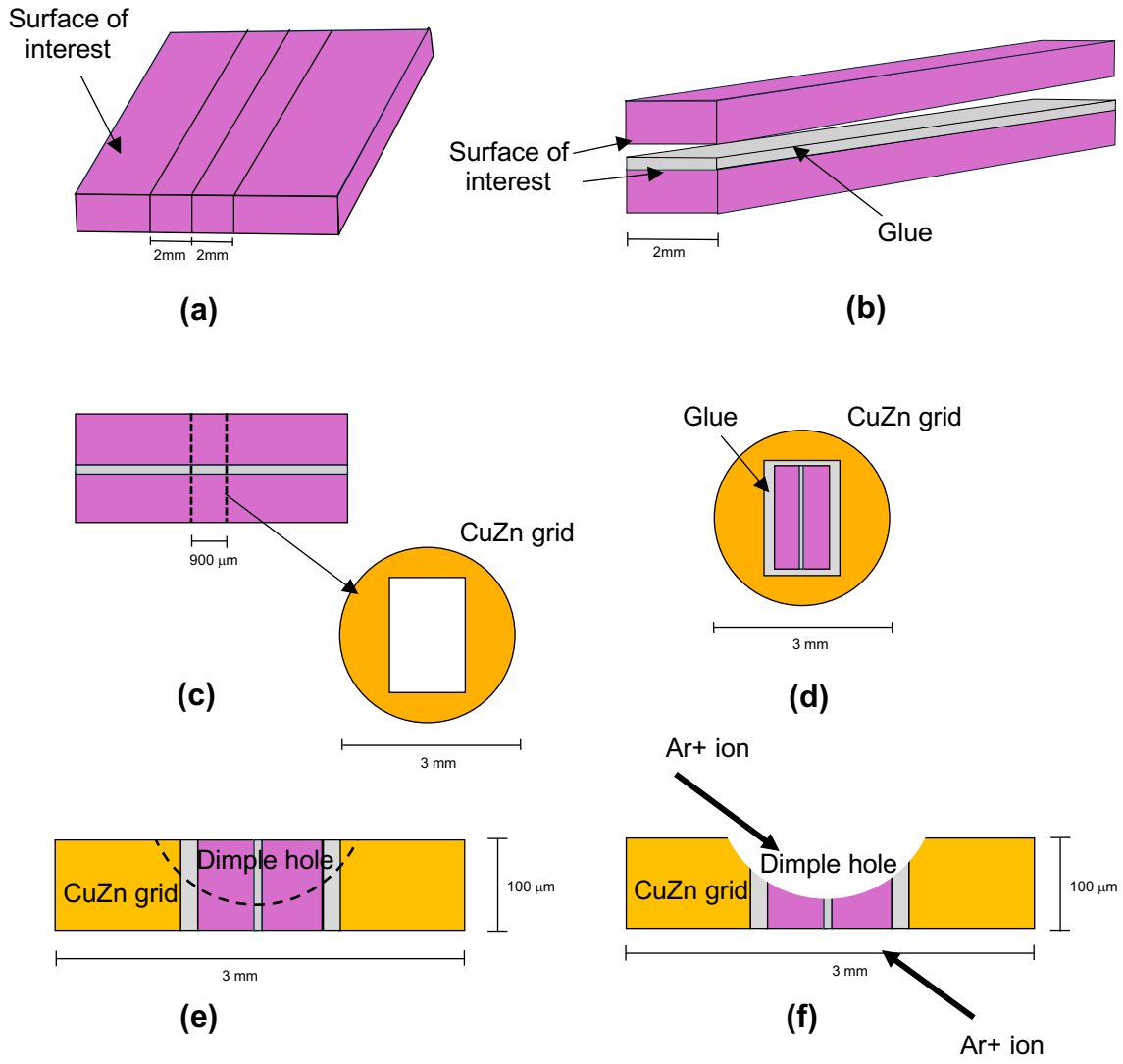

Fig. 3.6 Schematic illustrations of the essential steps involved in conventional cross-section TEM specimen preparation (a) cutting sample into stipes (b) glueing together sample surfaces (c) cutting slices into smaller slices after curing (d) introduction of smaller slices into slot of CuZn grids (e) Dimpling of samples contained in the grids (f) Precision ion polishing of samples

3.3.3.2 Focused ion beam preparation

Focused ion beam (FIB) based TEM lamella preparation offers the possibility of site-specific specimen preparation. In the present case, this method was necessary to exclusively preform the TEM characterization of InAs islands formed at monolayer patterned areas of the selective area heteroepitaxy template (discussed in chapter 3 and 6). FIB TEM lamellas were prepared using the FEI Helios NanoLab Dualbeam SEM at the Bielefeld Institute for Biophysics and Nanoscience (BINAS), University of Bielefeld, by Dr. Björn Brüker.

Initially, ≈ 140 nm of carbon is deposited onto the samples using a Leica EM ACE600 carbon sputter coater. SEM top view image of a sample in this state is shown in Fig. in Fig. 3.7 (c). The sample is introduced into the FIB-SEM and a row of GaAs nanopillars normal to the $[1\bar{1}0]$ direction with highest linear density is chosen for Pt layer deposition, schematically shown in Fig. 3.7 (b). Here, the sample edges were used for reference of crystallographic directions, see Fig. 3.7 (a). The Pt layer was deposited on the chosen row of pillars using Ga ion beam on an area of 12 μm x 2 μm. A total of 800 nm of Pt was deposited, (52° tilted view in Fig. 3.7 (d). A trench was then cut out around the Pt deposited area using Ga ions (Fig. 3.7 (e)). Following this, a J-cut of the resulting slice was performed (Fig 3.7 (f)). A Pt layer was then welded to a micro manipulator needle to make a contact to the sample. The slice is now detached (lifted-out) from the sample with a final cut and attached to a FIB lift-off grid shown in Fig. 3.7 (h). Further thinning of the slice was done to reduce the sample thickness. After the fine polishing step, an electron transparent sample with a thickness of ≈ 60 nm resulted, as evidenced by the GaAs nanopillars observable in Fig. 3.7(k) between the carbon layer and GaAs(111)A substrate. Figs. 3.7 (c) – 3.7 (k) are snapshots of the above-mentioned steps and table 3.1 summarizes the ion beam parameters used for FIB-TEM lamella preparation.

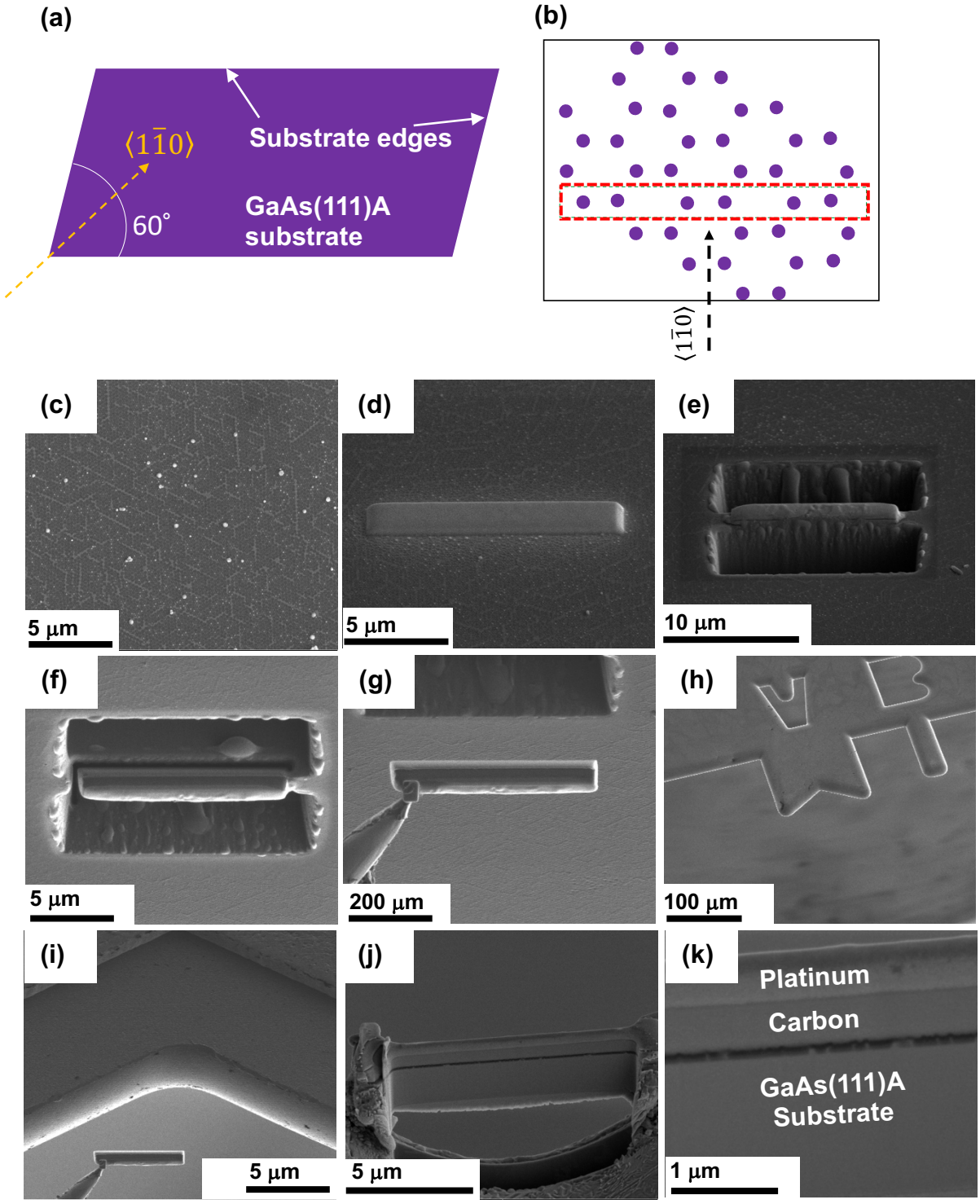

Fig. 3.7 (a) is a schematic showing the position of ⟨1$\bar{1}$0⟩ direction with respect to wafer edges (b) Criterion for choosing a row of GaAs nanopillars for FIB. (c) to (k) SEM image sequences, showing the various stages of FIB TEM lamella preparation as explained in the text.

Table 3.1. Ion beam parameters used for FIB-TEM lamella preparation

Process	**Voltage**	**Probe Current**
Pt deposition	30kV	70pA
Trench creation	30kV	2.8nA
J-cut	30kV	54nA
Ion Polishing	30kV	55pA
Fine polishing	5kV	74pA

3.3.4 Geometrical phase analysis

Geometrical phase analysis (GPA) is a method for determining lattice strain variations using the geometric phase information present in HRTEM and HRSTEM images [12]. This is made possible by representing such lattice images in terms of Fourier series. Based on the formalism of GPA [12], the intensity I(r) of a lattice image at a location **r** in a perfect lattice can be described using a Fourier sum as

$$\mathrm{I(r)} = \sum_g H_g(r) exp\ \{2\pi i \boldsymbol{g}.\boldsymbol{r}\}, \tag{3.1}$$

$$H_g(\boldsymbol{r}) = A_g(\boldsymbol{r}) exp\{iP_g(\boldsymbol{r})\}, \tag{3.2}$$

where, $\boldsymbol{g}$ is a reciprocal lattice vector, H_g are Fourier components which describe the local lattice image contrast in terms of amplitude (A_g) and phase (P_g).
The initial step in GPA involves the application of a Bragg filter on two chosen $\boldsymbol{g}$ vectors ($\boldsymbol{g_1}$and $\boldsymbol{g_2}$) from the FFT pattern of the lattice image and creating an inverse transform. $\boldsymbol{B_g}$, the intensity of Bragg filtered image can be expressed as

$$B_g(\boldsymbol{r}) = 2A_g(\boldsymbol{r}) cos\{2\pi \boldsymbol{g}.\boldsymbol{r} + P_g(\boldsymbol{r})\}. \tag{3.3}$$

The effect of lattice distortions can be incorporated in 3.3 as

$$B_g(\boldsymbol{r}) = 2A_g(\boldsymbol{r}) cos\{2\pi \boldsymbol{g}.\boldsymbol{r} - 2\pi \boldsymbol{g}\ \boldsymbol{u}(\boldsymbol{r})\}, \tag{3.4}$$

where $\boldsymbol{u}(\boldsymbol{r})$ is the displacement field since the phase is related to the displacement field as

$$P_g(\boldsymbol{r}) = -2\pi \boldsymbol{g}\, \boldsymbol{u}(\boldsymbol{r}) \quad . \tag{3.5}$$

Hence, the displacement field of the lattice image made using vectors $\boldsymbol{g_1}$ and $\boldsymbol{g_2}$ can be written as

$$\boldsymbol{u}(\boldsymbol{r}) = -\frac{1}{2\pi}\left[P_{g1}(\boldsymbol{r})a_1 + P_{g2}(\boldsymbol{r})a_2\right] \quad . \tag{3.6}$$

Here, a_1 and a_2 are the real space lattice vectors corresponding to the reciprocal vectors $\boldsymbol{g}_1$ and $\boldsymbol{g}_2$, respectively.

The lattice distortion e is described in terms of the gradient of distortion field as matrix. This is also related to the resolved lattice parameters along the x, y axes for the two g vectors as

$$e = \begin{pmatrix} e_{xx} & e_{xy} \\ e_{yx} & e_{yy} \end{pmatrix} = \begin{pmatrix} \frac{\partial u_x}{\partial x} & \frac{\partial u_x}{\partial y} \\ \frac{\partial u_y}{\partial x} & \frac{\partial u_y}{\partial y} \end{pmatrix} = -\frac{1}{2\pi}\begin{pmatrix} a_{1x} & a_{2x} \\ a_{1y} & a_{2y} \end{pmatrix}\begin{pmatrix} \frac{\partial P_{g1}}{\partial x} & \frac{\partial P_{g1}}{\partial y} \\ \frac{\partial P_{g2}}{\partial x} & \frac{\partial P_{g2}}{\partial y} \end{pmatrix} \quad . \tag{3.7}$$

Using these relations, the in-plane and out-of-plane strains, ε_{xx} and ε_{yy} and the mean dilatation strains can be determined. The in-plane strain ε_{xx} and mean dilatation, Δ_{xy} are relevant measures of misfit strain at the heterointerfaces. These quantities are described mathematically as

$$\varepsilon_{xx} = \frac{\partial u_x}{\partial x},\ \varepsilon_{yy} = \frac{\partial u_y}{\partial y} \text{ and } \Delta_{xy} = \frac{1}{2}(\varepsilon_{xx} + \varepsilon_{yy}) \quad . \tag{3.8}$$

The GPA analysis was carried out on the DigitalMicrograph software using the GPA plug-in provided by HREM Inc. A cosine mask of size ≈ 0.0316 pixel^{-1} was applied on the $\boldsymbol{g}_{111}$ and $\boldsymbol{g}_{\bar{1}11}$spots in the FFT pattern, using an area of ≈ 4 nm x 4 nm in the GaAs lattice as reference.

3.4 Atomic force microscopy (AFM)

Atomic force microscopy (AFM) is a scanning probe-based technique used primarily for surface topography mapping. It can also yield other information such as magnetic and piezoelectric domain maps, stiffness, phase imaging etc. In AFM a tip with very small radius of curvature (usually < 20 nm) is brought close to the surface of interest. This can result in either an attractive, repulsive or a mixed interaction (see Fig. 3.8 (a)). These interactions are exploited by various operation modes to map out surface properties. In the present thesis, the AFM is primarily used to generate surface topography maps. The set-up consists of an ultra-fine tip mounted at the end of a cantilever attached to an ultrasensitive piezo crystal, which can be driven it in the x-, y- or z-directions. A solid-state laser beam is directed on the cantilever and the beam reflection on a split photodiode detects the cantilever deflection as it moves over the sample surface (Fig. 3.8 (b)). Thus, the split-photodiode converts the deflection at the AFM tip into voltage. A topographic map is thus created as the tip traverses the sample surface. When the tip approaches the sample surface, it enters the repulsive regime. Here, the magnitude of the repulsive force at the AFM tip is mapped out as a function of distance travelled laterally on the sample, keeping the tip height fixed. Alternatively, the height needed to maintain a constant repulsive force can be monitored to map height variations. This constitutes the contact mode of operation. In the tapping mode, the tip is oscillated at its resonance frequency and made to approach the sample surface. Tip-specimen interactions induce changes in the resonance frequency, amplitude and phase of the oscillating tip. These phase changes resulting from differences in elastic properties of materials create maps showing material contrast [13].

Three different AFMs were used in this thesis for topographic imaging. A NANOSURF MOBILE S system manufactured by Nanosurf AG was operated in static mode with a tip load of 18 nN. This instrument was operated in contact mode with a pyramidal Si tip of < 7 nm radius, 30 nm thick Al coating for reflection, provided by PPP-CONTR from NANOSENSORS GmbH, Ltd. was used. Also a Bruker Dimension Icon and Dimension Icon 3100 series were used in tapping mode with a HQ:CSC17/Al BS, Si tip with radius < 8 nm and resonance frequncy 13 kHz.

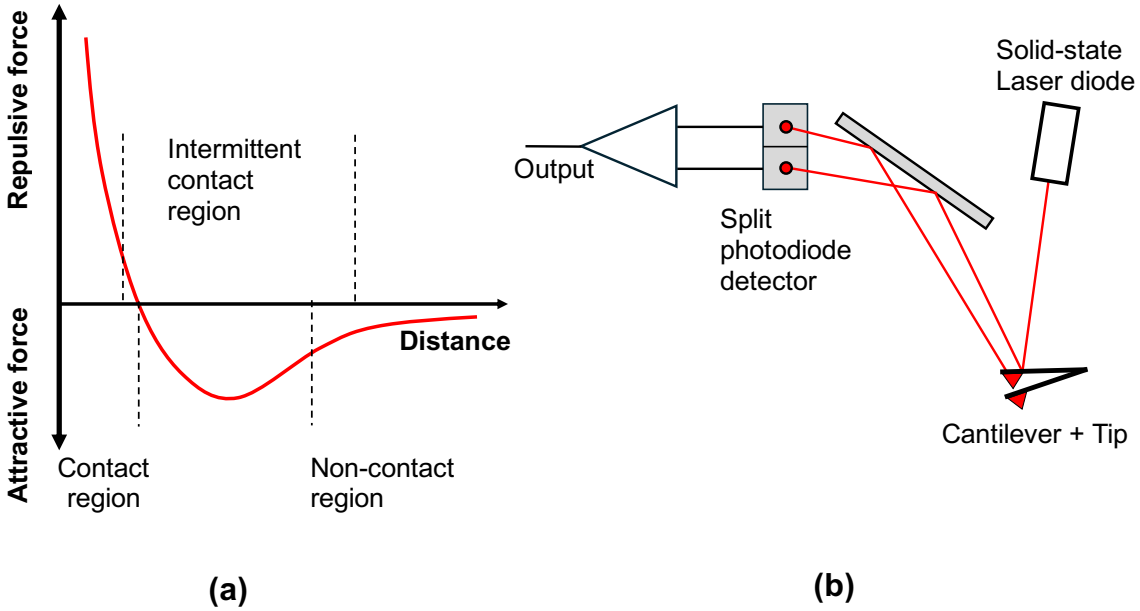

Fig. 3.8. (a) The three regimes of operation of AFMs, based on the interaction behavior between tip and specimen. (b) Working principle of an AFM is for operating in the topography mode, where the motion of the cantilever-tip arrangement is monitored using a split photodetector. Adapted from [13]

References

1) J.I. Goldstein, D.E. Newbury, J.R. Michael, N.W.M. Ritchie, J.H.J. Scott and D.C. Joy, "Scanning electron microscopy and X-Ray microanalysis", IV edition, Springer (2018)

2) Electron microscopy- ETH Zürich: https://www.microscopy.ethz.ch/sem.htm

3) W. O. Gordon, "Metal Oxide Nanoparticles: Optical Properties and Interaction with Chemical Warfare Agent Simulants", Ph.D. Thesis, Virginia Polytechnic Institute and State university (2006)

4) D. B Williams and B.C. Carter, "Transmission electron microscopy: A textbook for electron microscopy", Springer (2009)

5) Gatan Inc., DigitalMicrograph software: https://www.gatan.com/products/tem-analysis/digitalmicrograph-software

6) HREM Research Inc., Geometrical Phase Analysis plug-in for DigitalMicrograph: https://www.hremresearch.com/gpa/

7) Instructions manual, JEM-ARM200F atomic resolution analytical microscope, JEOL Ltd.

8) Z. Luo, "A practical guide to transmission electron microscopy : Fundamentals", Momentum Press, LLC (2016)

9) Y.A.R. Dasilva, R. Kozak, R. Erni and M.D. Rossell, "Structural defects in cubic semiconductors by aberration-corrected scanning transmission electron microscopy", Ultramicroscopy, 176, 11 (2017).

10) K. M. Krishnan, "Principles of materials characterization and metrology", Oxford press (2021)

11) Gatan Inc., EELS.info: https://eels.info/about/techniques/eftem

12) M. J. Hÿtch, E. Snoeck and R. Kilaas, Ultramicroscopy, "Quantitative measurement of displacement and strain fields from HREM micrographs", Ultramicroscopy, 74 (1998) 131.

13) W.D. Kaplan and D. Brandon, "Microstructural Characterization of Materials", Wiley publications (2008)

Chapter 4
Sample Fabrication

4.1. Substrate nano-pillar patterning

GaAs(111)A nanopillar arrays with two different arrangements and dimensions are created on $1/6^{th}$ and $1/3^{rd}$ of 3" GaAs(111)A wafers, by combining nanosphere lithography (NSL), hard mask deposition, polystyrene (PS) sphere layer lift-off and substrate reactive ion etching (RIE). These processes are schematically represented in Fig. 4.1 and are described in detail in the sections that follow.

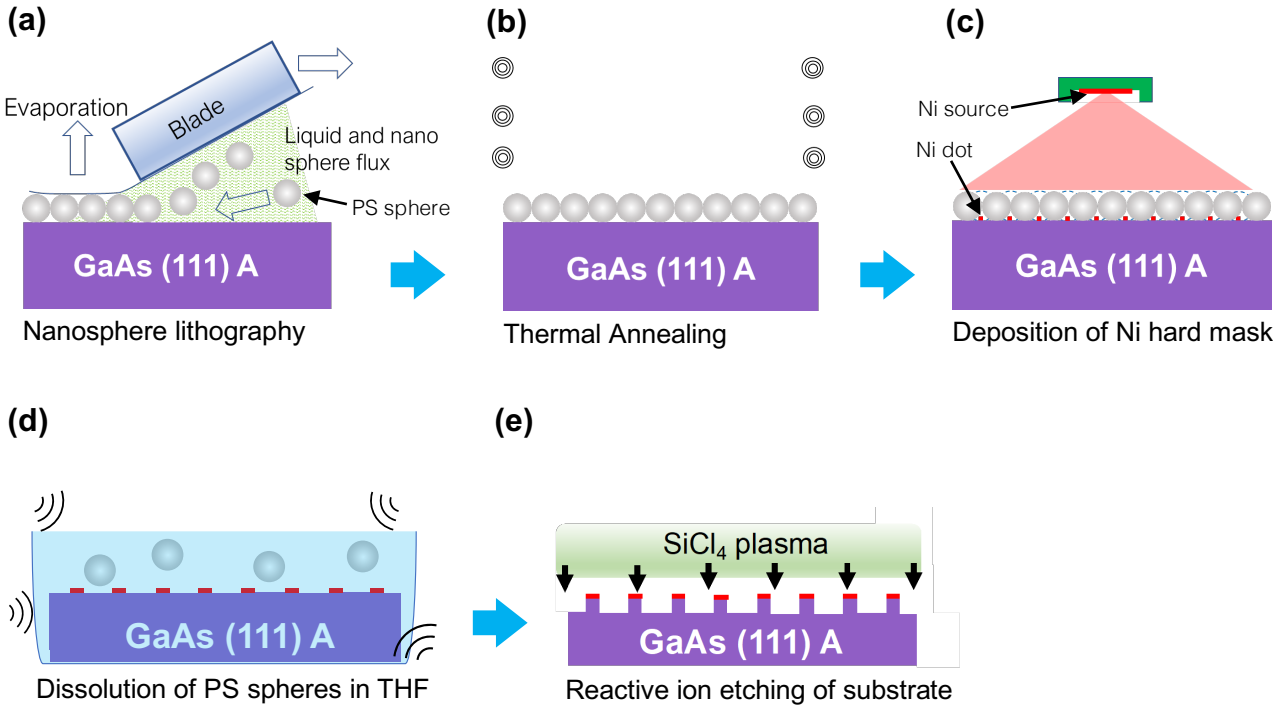

Fig. 4.1. A side-view sketch of the main process steps involved in fabricating GaAs(111)A nanopillar arrays (a) Deposition of PS mono and double layers (b) Controlled thermal annealing of PS spheres (c) Deposition of Ni on the substrate through PS sphere interstices (d) PS sphere layer lift-off by ultrasonication in tetrahydrofuran (THF) (e) RIE of substrate after PS lift-off.

4.1.1 Nanosphere lithography (NSL)

Nanosphere lithography (NSL) is a low-cost, high-throughput method capable of producing a wide range of periodic nanostructures [1,2]. The fabrication of nano-mesh structures with uniform pore arrays is especially attractive in lithographic applications for the use as shadow masks [3]. Essentially, NSL involves the self-organization of polymer spheres over a substrate surface, e.g. exploiting the phenomenon of convective self-assembly. In convective self-assembly, colloidal particles are transported from a liquid suspension towards the growing colloidal crystal driven by the evaporation flux of suspension fluid at the triple phase boundary between substrate, suspension and gas phase of the processing chamber [4,5]. These processes are schematically represented in Fig. 4.2 (a). Polystyrene (PS) spheres with a diameter of 220 nm (PS 220) in an aqueous suspension are employed as colloidal particles in the present work.

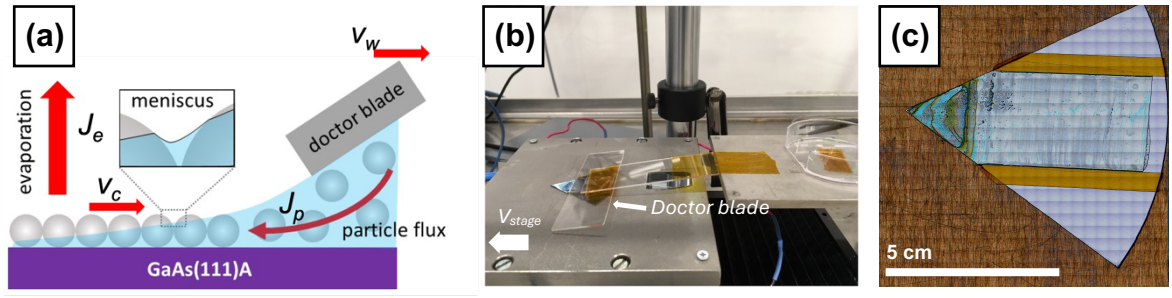

Fig. 4.2. (a) A schematic detailing the various fluxes involved during convective self-assembly of colloidal particles at the triple phase boundary of a colloidal suspension on a solid surface. (b) A photograph of the doctor blade set-up used for depositing PS sphere mono and double layers. (c) An actual image of a 1/6 of GaAs(111)A 3'' wafer after deposition of 220 nm PS spheres.

A controlled deposition of such colloidal crystals on substrate surfaces can be realized using various techniques such as spin coating, dip coating or the doctor blade method [6,7]. Amongst these, the doctor blade technique is adopted in this thesis. A simple analytical expression for the growth velocity of the colloidal crystal (v_c) based on material flux balance was proposed by Dimitrov and Nagayama [5] for such a set-up:

$$v_c = \frac{\beta j_e l \varphi}{h(1-\epsilon)(1-\varphi)} \quad . \qquad 4.1$$

Based on the above expression, the colloidal crystal growth velocity depends on suspension properties such as the particle volume fraction φ in the suspension, the height h of the film at the triple phase. Here, the parameters dependent on the processing conditions are, l the length of the evaporation zone (here the sphere diameter) and the porosity ϵ of the colloidal layer (0.395 for a hexagonally close packed array of colloidal particles). The evaporation flux j_e depends on the suspension and the gas phase characteristics (humidity and temperature) in the vicinity of the triple phase β is a coupling parameter giving the ratio between average sphere velocity and liquid velocity. It is evident form equation 4.1 that the growth velocity (v_c) of PS sphere layers depends on the process chamber ambient and concentration of PS sphere in the suspension. Controlling these, the sphere layer configuration in mono or multilayers can be set. In practice, by matching withdrawal velocity (v_w) of the doctor blade to the crystal growth velocity one can generate colloidal crystals with the desired structures. This possibility is exploited with the help of a home-made doctor blade set-up, a photograph of which is shown in Fig. 4.2(b). Here, the blade withdrawal velocity is precisely controlled by a stepper motor driven stage against a fixed doctor blade.

Doctor blading of GaAs(111)A substrates begins by plasma assisted surface hydrophilization in an Oxford Plasma Lab 100 reactive ion etcher to enhance substrate surface wettability [7]. The following process parameters were used. chamber pressure 75 mTorr, gas flow rates of O_2 and Ar, 2 and 8 sccm respectively, RF power 50 W, duration 180 s and DC bias 172 V. Then, two stripes of 2 mm wide and 70 μm thick brown Kapton tapes are glued to the substrates for defining the area to be patterned, as seen in Fig. 4.2 (c). The substrate is positioned on the stage and 10 μl of PS 220 suspension is transferred onto the substrate surface in between the tapes. Next, the doctor blade which is hydrophobized with octadecyl trichlorosilane, is used to spread the PS 220 suspension on the Kapton tape confined areas by gently placing the blade on the suspension and driving the stage with a defined velocity. The stage movement is terminated when the blade reaches the other end of the Kapton tape confinement, and the residual suspension is immediately flushed off with a nitrogen gun to prevent the flow back of the remaining PS 220 suspension onto the PS deposited areas. Two important parameters in addition to the blade velocity affecting the growth velocity of PS sphere layers are the chamber

humidity and the substrate temperature because they directly influence the evaporation rate of the suspension. These parameters are regulated by performing the NSL in a glove box and heating the substrate using a Peltier-heating system attached to the stage. A table summarizing the optimum conditions for NSL of PS 220 spheres is shown below.

Table 4.1. Optimized process parameters for NSL of PS 220 nm spheres on GaAs(111)A.

Supplier (Art. No.)	**Solid content (w%/v)**	**CV* (%)**	**Sphere diameter (nm)**	**Relative humidity (%)**	**Substrate temperature (°C)**	**Blade velocity (μm/s)**
Thermo Scientific Inc. (5022A)	10	< 3	220	45 - 50	25	110 - 120

*CV is the coefficient of variance of the sphere diameter distribution

Patterned areas with rectangular and rhombus shapes are produced depending on the area bound by the Kapton tapes, which amounts to 2.5 x 4.5 cm^2 and 3.2 x 3.2 cm^2 for wafer 1/3rd and 1/6th respectively.

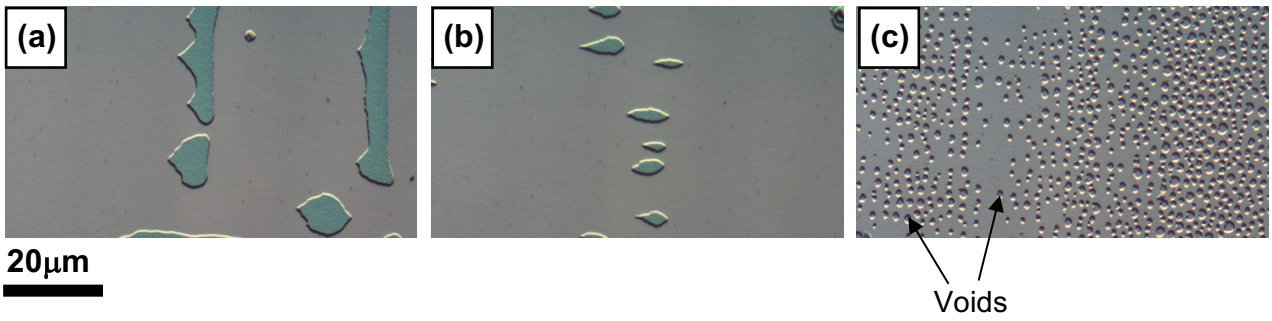

Fig. 4.3. (a), (b) and (c) are DIC light microscopy images for of PS 220 deposited on 1/6 or 1/3 of a 3'' wafer blade velocities 85, 100 and 110 μm/s respectively, respectively. The scale bar indicated is the same for all the three images.

Furthermore, the patterned areas consisted of mostly PS sphere monolayers (ML) and voids as seen in Fig. 4.3(e) along with few stripes of double layer (DL) regions (Fig. 4.3 (b) and (c)). They are distinguished by their colors resulting from interference when examined using polarized light. Monolayers appear grey, whereas double layers appear turquoise in color and the voids appear darker gray and rounded in shape.

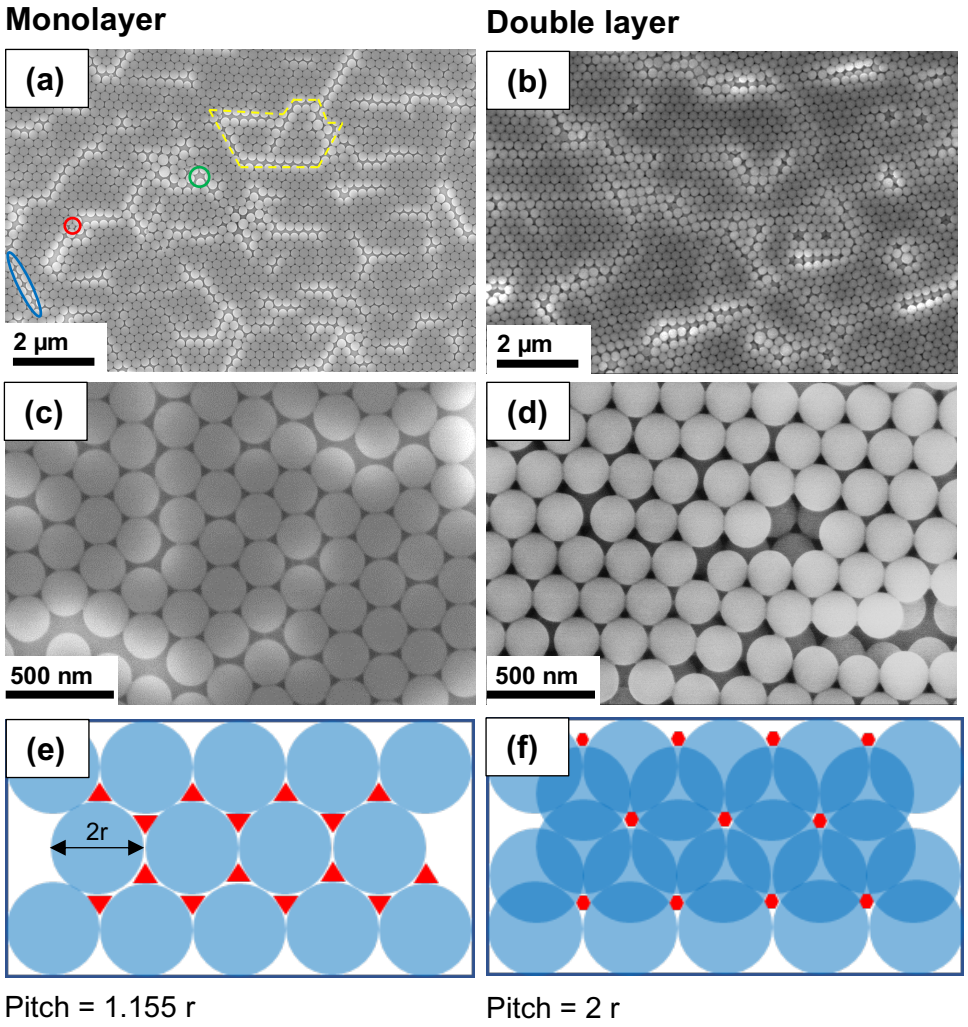

Fig. 4.4. PS sphere arrangement in the as-deposited condition for ML and DL on a wafer 1/6 of a 3" wafer are shown in (a) and (b) respectively, additionally the various types of defects present in these films are indicated in (a). (c) and (d) are the higher magnification images of (a) and (b) respectively. Sphere interstice modification after annealing and plasma cleaning, of ML and DL are observable in (e) and (f) respectively.

The perfect 2D hexagonal arrangement of PS 220 spheres in the deposited films is occasionally disturbed by the formation of defects such as voids, dislocations and grain boundaries [8] demarcated using shapes with green, blue and yellow colors in Fig. 4.4 (a). Their formation is attributed to impurities on the substrate surface or spheres with exceptional size in the suspension [9]. Also observable in Figs. 4.4 (a)-(d) are the differences in sphere arrangement, resulting in irregular interstice shape and deviation of pitches in ML and DL regions compared to the ideal arrangements [10] schematically shown in Figs. 4.4 (e) and (f), respectively.

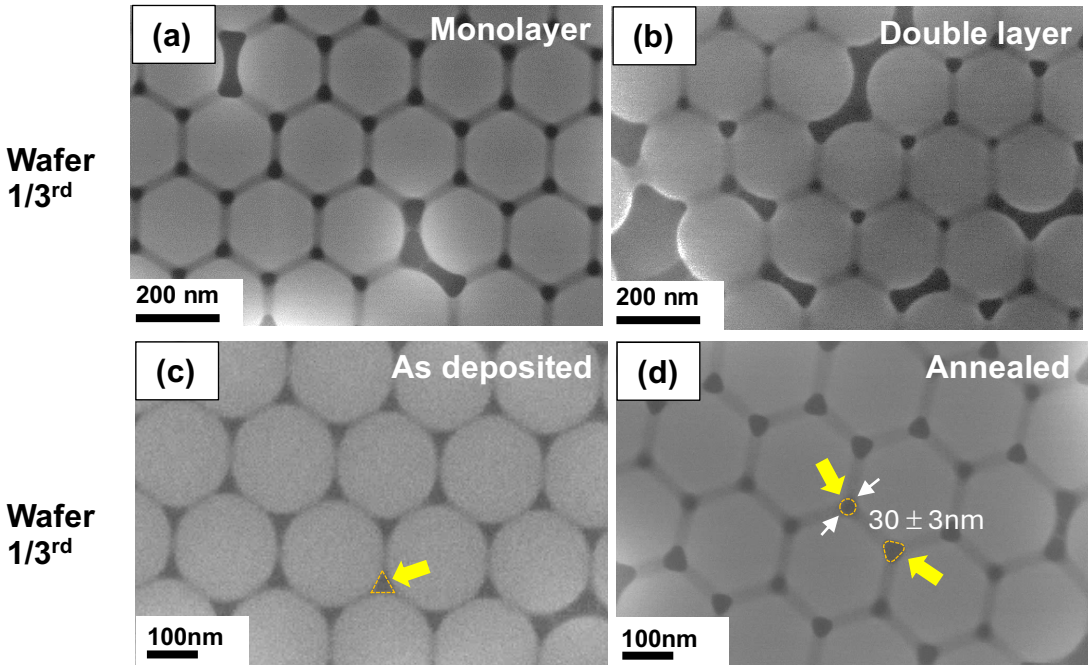

Fig. 4.5. PS sphere arrangement in the ML and DL regions after PS sphere annealing in (a) and (b) respectively for a wafer $1/3^{rd}$. A comparison between the triangular interstice of the as-deposited state to the annealed state for a wafer $1/3^{rd}$ is made in (c) and (d). The insets in (c) and (d) compare indicate the interstice shapes for the respective conditions.

Next, the PS sphere layers deposited on the substrates are subjected to thermal annealing in air ambient using a box furnace maintained at 105°C. The annealing was performed in three steps with durations of 6.5, 5 and 2.5 mins and 5, 5 and 5 mins for 1/6 and 1/3 of 3" wafers. Annealing durations were optimized to yield interstices which are either circular or rounded triangles in shape and have a size of approximately 30 nm (Fig. 4.5 (d)). A closer examination reveals the merging of PS spheres at the points of contact. This is indicative of temperature driven material transport leading to pore shrinkage which reduces the overall surface energy of the PS spheres [9]. The efficacy of pattern transfer using such PS sphere interstices is examined in section 4.2.

In the next step, 99.98% pure Ni from wire pieces provided by ChemPur Feinchemikalien und Forschungsbedarf GmBH was thermally evaporated on the GaAs substrates covered with PS sphere masks at a rate of 0.1 nm/s. A total thickness of 30 nm was deposited.

The thermal evaporation experiments were performed in a home-made set-up whose chamber pressure was maintained at $1x10^{-6}$ mbar. Prior to the thermal evaporation step the hydrocarbon layer on the GaAs substrate surface within the sphere interstices was removed using plasma etching in a PlasmaLab 100 to improve the adhesion between Ni and the GaAs substrate. The parameters used were chamber pressure 75mTorr, oxygen gas flow rate 15sccm, RF power 15W and duration 20s which resulted in a DC bias value of 118V. The Ni coated PS mask on GaAs substrates were removed by ultrasonication in a tetrahydrofuran solution for 30 minutes to completely dissolve the PS spheres. The Ni dot patterned substrates are subjected to reactive ion etching (RIE) for creating GaAs nanopillar arrays as described in the next section. Here, Ni is chosen specifically due to its high etch selectivity and resistance to attack against ions when employed as RIE hard mask [11].

4.1.2 Reactive ion etching (RIE)

Reactive ion etching (RIE) is a widely employed dry-etching technique for pattern transfer from mask to the substrate [12]. A major advantage of such a dry-etching process is the faithful transfer of mask pattern onto the substrate [13]. A RIE apparatus comprises a vacuum chamber with two (parallel) plate electrodes across which an AC voltage is applied at a radio frequency (RF) of 13.56 MHz. The reactive chamber gases ionize under the RF field, resulting in the formation of a glow discharge and sheath layer between the plates. Specimens to be reactively ion etched are placed on the bottom electrode, which assumes a negative potential because it is connected to a blocking capacitor. Additionally, the region between the plates splits into a glow discharge plasma and sheath region due to the mass differences of ions and electrons, as depicted schematically in Fig. 4.6. A potential difference (V_{dc}), known as DC-bias, created between the plasma and the sheath layer is responsible for the impingement of ions on the sample placed on the lower electrode [14]. The magnitude of the DC-bias depends upon the RF power and the chamber pressure [15]. Larger DC-bias values and lower chamber pressures reduce ion scattering within the sheath region and promote normal incidence of ions onto the substrate surfaces. Such ion trajectories induce directionality to the etching, which is termed *anisotropic etching*. RIE based dry-etching as such involves surface activation of substrate atoms by direct kinetic energy transfer by the ions. Once activated, the substrate

surfaces are readily etched by adsorbed free radicals formed by ionization of reactive gases in the chamber. The volatile compounds formed by such reactions desorb and expose a fresh layer to be etched [14].

All plasma assisted surface modification experiments in this thesis were performed using an Oxford Instruments PlasmaLab 100, equipped with both capacitively coupled or inductively coupled power sources (CCP or ICP respectively for short). The substrates to be processed were placed on a 150 mm diameter p-type boron doped Si(100) wafer to prevent charging effects during RIE. Samples are transferred into the process chamber maintained at 10^{-4} mTorr base pressure, using a load lock system. A variety of process gases (CF_4, $SiCL_4$, SF_6, O_2 and Ar) are made available at desired flow rates using mass flow controllers to produce the desired reactive species. To ensure a uniform etch during RIE, the substrate is cooled by introducing helium between the electrode and substrate. This also ensures a good contact between these two surfaces.

Various types of plasma assisted surface modifications such as hydrophilization, plasma cleaning and reactive ion etching were performed in this thesis. Process parameters relevant to each of these processes are elaborated where necessary.

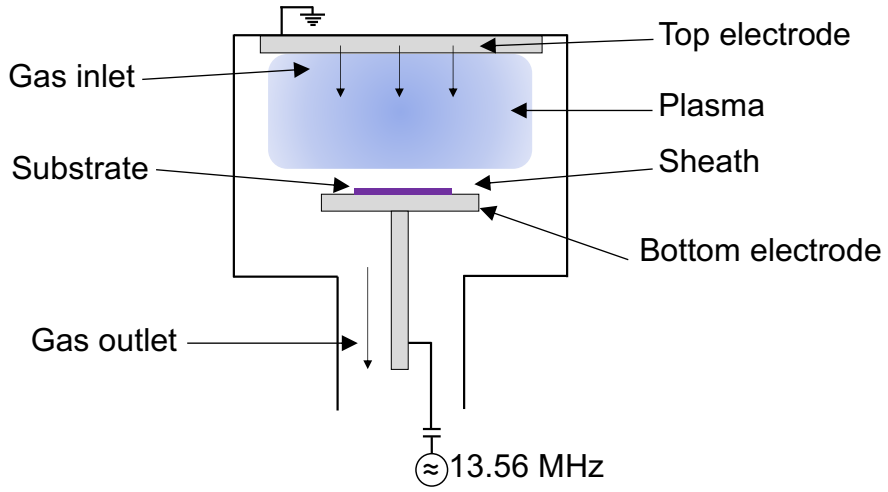

Fig. 4.6. A schematic representation of a the RIE apparatus used. Adapted from [16]

GaAs(111)A substrates with Ni-dot patterns atop (as described in section 4.1.1) were subjected to RIE for fabricating nanopillars. The process parameters employed were 195 W RF power, 3.5m Torr chamber pressure, 5 sccm $SiCl_4$ gas flow rate for a duration of 65 s. A relatively large DC bias value of 715V was recorded for the above conditions, indicating a high etch anisotropy. Here, by employing $SiCl_4$ as the etch gas, a smoother dry-etch and a residue free surface is achieved, compared to when using pure Cl_2 gas or fluorine based etch gases [15]. Additionally, the adsorption of the less volatile $GaCl_2$ species compared to $GaCl_3$ helps in sidewall passivation during the RIE process, yielding nanopillars with nearly perfect sidewalls as seen in Fig. 4.7 (b), (e) and (f). The exact values of sidewall inclination with respect to the wafer surface measured from cross-sectional SEM images amounts to 88±0.8° and 87±1.1° for pillar arrays fabricated using ML and DL PS sphere masks, respectively.

The pillars resulting from the RIE process have either circular or rounded triangle cross-sections at ML regions and circular or oval shaped cross-sections DL regions, when viewed from top (see Fig. 4.7(c) and (d)). Such rounded profiles after RIE, when compared with the slightly triangular edges of Ni hard masks remaining after PS liftoff seen in Fig. 4.7(a) are indicative of Ni mask erosion during the RIE process. This reasoning is also corroborated by the observation rounded Ni masks atop the GaAs nanopillars (Fig. 4.7 (b)). A consequence of mask erosion is the deviation from the perfect 90° sidewall angle of these pillars.

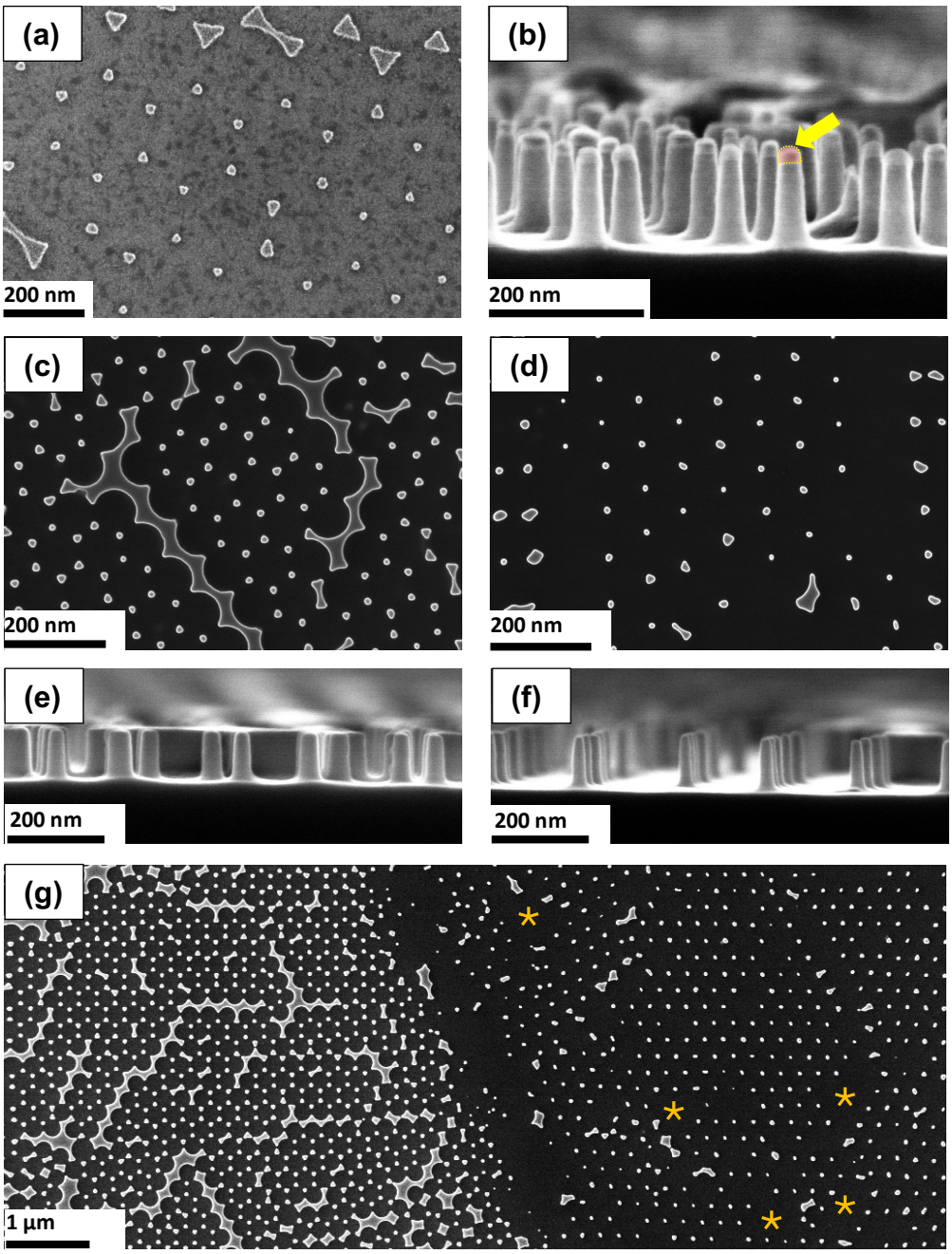

Fig. 4.7. (a) The Nanodot pattern formed by thermal evaporation of Ni using a PS220 ML mask. GaAs nanopillars with intact Ni hard mask particles on top after the RIE process are seen in (b), where a Ni cap on a selected pillar top is highlighted and indicated using an arrow. (c) and (d) are top-view images of GaAs nanopillars formed using PS220 ML and DL masks. Their corresponding side view images are shown in (e) and (f), respectively. (g) is a top-view image captured at the border separating nanopillars at ML and DL patterned areas, showing the differences in shape and size of the two patterned regions. Some locations with more than one missing Ni dot are indicated by the * symbol.

Various characteristics quantifying the pillar arrays from ML and DL sphere masks are summarized in Table 4.1. The most noticeable difference amongst them is the areal density. ML regions yield more than double the number of pillars compared to DL regions and are spaced about 1.8 times closer. Another prominent feature of the pillar arrays is the presence of defects consisting in pillars with irregular shapes, line defects of interconnected or missing pillars originating from dislocations in the sphere masks or from domain boundaries of sphere layers. They occupy approximately 11% and 1.1% of the area at ML and DL regions, respectively, resulting in a reduction of the areal density by 40% and 45%, respectively, for these regions compared to their defect free versions. The decrease is more pronounced for pillars formed at DL regions resulting in areas with missing pillars as indicated by the '*' symbol in Fig. 4.7 (g). A reason for this is the transfer of defects from the lower to the upper PS layers in the DL areas [11].

The dimensional aspects of the pillars such as verticality with respect to substrate plane, height and diameter are comparable for the two patterns/regions. The most critical pillar dimension, the diameter is found to be below the 30 nm limit necessary to realize the full potential of NHE in the InAs/GaAs(111)A system (see section 2.4.1.3). The results discussed so far refer to nanopillars produced on wafer one-thirds. The RIE processing of wafer one-sixths yields shorter nanopillars with an average height of 69±8 nm and diameter 31±nm respectively, compared to 103±2 and 28±5 nm for the smaller GaAs pieces. This reduction in nanopillar aspect ratio from approximately 3.6 to 2.2 is attributed to the larger consumption rate of etch gases because of the doubling GaAs wafer area, also known as loading effect [17]. Alternatively stated, the doubling of wafer surface area to be reactive ion etched increases the gas consumption resulting in pillars with smaller height. Still, nanopillars on the one-sixth wafers are by far tall enough to be used for nanoheteroepitaxy experiments.

Table 4.2. Summary of characteristics of RIE fabricated GaAs nanopillars

Sphere Layer arrangement	**Pillar Diameter (nm)**	**Pitch (nm)**	**Areal density ($x10^9/cm^2$)**	**Pillar Height (nm)**	**Sidewall angle (degrees)**
Monolayer	28±5	129±6	2.9	103±2	88±0.8
Double layer	23±5	228±8	1.1	105±1	87.5±1.1

4.2 Substrate preparation for molecular beam epitaxy

4.2.1 Wet chemical cleaning

The remanent Ni hard mask atop the GaAs pillars after RIE were dissolved by immersing the substrates in a solution of H_2SO_4 in deionized (DI) water (H_2SO_4 (96%): DI water = 1:10) for a duration of 5 minutes. After this, the specimens were transferred to a beaker containing pure DI water to desorb the H_2SO_4, rinsed in pure DI water to remove any remnants of the etching medium and later dried using a jet of N_2 gas.

As part of the final wet chemical cleaning step, the substrates were cleaned using a solution of 10 wt.% HF made using a 49% HF stock solution by immersion for 10 mins. This cleaning step removes the native oxide and traces of undesired surface impurities. After the cleaning step the specimens were immersed in pure DI water for 30 mins to desorb traces of HF, later rinsed with fresh DI water and dried using a jet of N_2 gas. For selective area heteroepitaxy (SAH) templates (discussed in section 4.3), a HF concentration of 0.5 wt.% and a duration of 15 s were used as a cleaning step prior to introduction into the MBE chamber.

4.2.2 Atomic hydrogen cleaning

Atomic hydrogen cleaning (AHC) is a benign yet effective process of removing the native oxide present on GaAs nanopillar tops, mainly because it is performed at low temperatures (300 – 400 °C for GaAs). The nascent H atoms impinging on the sample surface are selectively reactive towards As-O and Ga-O amorphous oxides compared to the bulk GaAs crystal. The As-O molecules are reduced to volatile As and Ga_2O_3 is reduced to volatile Ga_2O leaving a very clean surface GaAs surface [18,19]. A commercial atomic hydrogen beam source manufactured by MBE Komponenten GmbH was used for this purpose. Atomic hydrogen is produced by cracking H_2 molecules at 1800°C within a tungsten capillary tube. A process efficiency > 70% is achieved by this process [20]. The atomic hydrogen beam source is installed in the molecular beam epitaxy system (section 4.4), used such that cleaned samples are kept under ultra-high vacuum conditioions until epitaxy is performed. AHC was performed at T_{sub} = 350°C and duration 3 mins for

optimum surface preparation. More details on the choice of the duration is explained in section 5.1 of chapter 5.

4.3 Fabrication of selective area heteroepitaxy templates using SiN_x masks

In this subsection, an approach to create a masked substrate that enables the site-specific InAs/GaAs(111)A epitaxy is discussed. The major challenges concerning the realization of nanopillars with unconstrained tops that enable strain partitioning are discussed and the a few critical practical aspects are detailed in Appendix-3. The process flow of the steps involved is shown in Fig. 4.8.

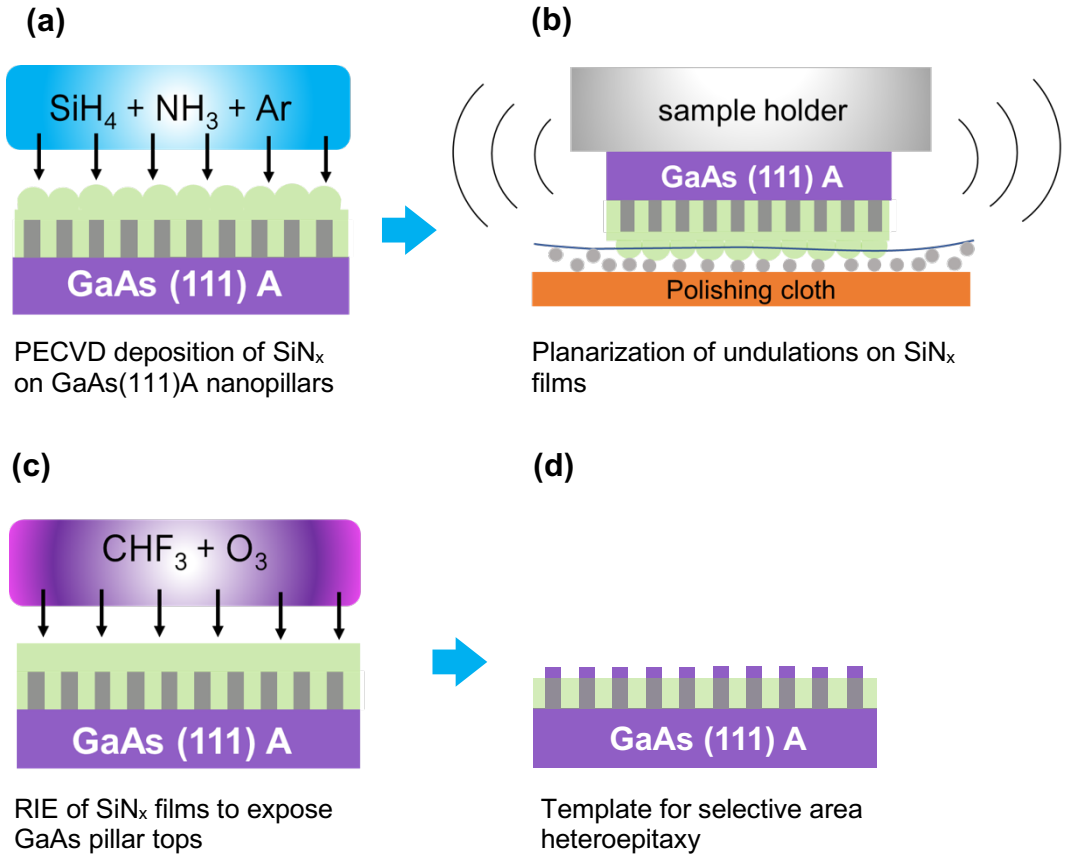

Fig. 4.8. A side-view sketch of the main process steps involved in the fabrication of SiN_x/GaAs(111)A nanopillar substrates for selective are a heteroepitaxy. (a) PECVD deposition of SiN_x films on nanopillar patterned GaAs(111)A substrates from the process chain detailed in Fig. 4.1. (b) planarization of undulations on SiN_x film surface using vibratory polishing. (c) RIE of planarized SiN_x films to expose GaAs(111)A nanopillar tops. (d) Selective area heteroepitaxy template with GaAs(111)A nanopillars exposed.

4.3.1 PECVD of SiN_x on nanopillar patterned GaAs(111)A substrates

Plasma enhanced chemical vapor deposition (PECVD) is a thin-film deposition technique which employs both a plasma and heat to activate the film forming precursors [21]. A major benefit of this technique is the reduced process temperature for film deposition compared to chemical vapor deposition (CVD). This is highly beneficial for preventing substrate damage during thin-film deposition on temperature sensitive III-V semiconductors such as GaAs(111)A. A wide variety of passivation film materials such as nitrides, carbides and oxides of Si and Ti can be deposited using this method [21].

Amorphous silicon nitride (SiN_x) films are widely employed in the semiconductor fabrication to form conformal passive coatings on topological structures such as vias, trenches and high-aspect ratio channels [22]. SiN_x films were chosen as mask material in this work to reduce the chances of oxygen contamination in the MBE chamber when compared to using SiO_2 masks. It must be noted that the PECVD silicon nitride mentioned here is amorphous and off stoichiometric in composition compared to bulk silicon nitride (Si_3N_4) synthesized at high temperatures. The synthesis reaction of silicon nitride films can be stated as:

$$3SiH_4\,(g) + 4NH_3\,(g) \rightarrow Si_3N_4\,(s) + 12H_2\,(g) \qquad (4.1)$$

All PECVD experiments in the present study were conducted in an Oxford Instruments PlasmaLab 80plus machine, a schematic view of which is shown in Fig. 4.9. The reaction chamber is as such similar to the RIE chamber described in section 4.1.2, consisting of two parallel plate electrodes that generate plasmas of precursor gases using 13.5 MHz RF microwave power (400 W max). However, in a PECVD system. the lower electrode on which samples are placed is grounded and has provision for heating up to 400°C. A wide variety of precursor gases such as NH_3, N_2, N_2O, CF_4 and (98% SiH_4 +2%Ar) can be chosen from to deposit the film material of choice.

PECVD deposition of SiN_x films on nanopillar patterned GaAs(111)A substrates was performed by generating a plasma of Ar diluted SiH_4 gas (98% SiH_4 +2%Ar) and NH_3 at flow rates of 400 and 20 sccm, respectively, using 20W RF power for a duration of 16 minutes. Such films usually contain entrapped hydrogen which reduces the density and

etch rate [23]. This drawback is remediated by plasma annealing the films in a N_2 ambient which converts the Si-H and N-H bonds to crosslinked Si-N-Si bonds, thus promoting H_2 desorption [24]. Plasma annealing or film densification was performed by passing N_2 at a flow rate of 40 sccm and RF power 50W. Both film disposition and densification steps were conducted in succession, without interrupting the chamber pressure and table temperature, the vales of which amounted to 1 Torr and 370°C, respectively. The choice of the highest accessible chamber pressure and temperature for PECVD promotes isotropic film deposition and lateral migration of active species, both of which are essential for gap filling in nanopatterned structures.

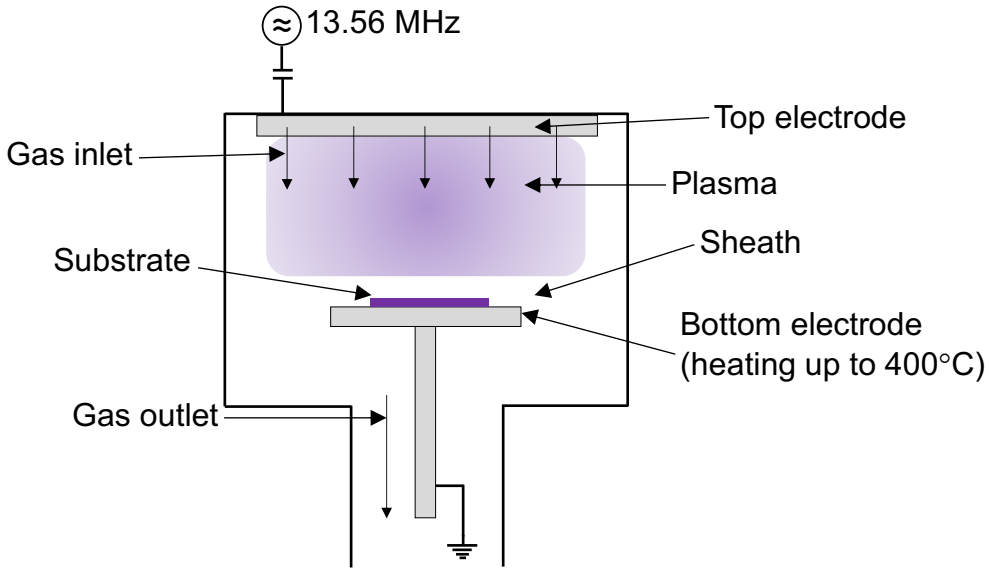

Fig. 4.9. A schematic representation of the PECVD apparatus used. Adapted from [16]

Top view images of the deposited SiN_x films such as Fig. 4.10(a) show GaAs nanopillars and defects buried under these films. They also reveal the presence of triangular lines with dots at their vertices, indicated using green and yellow arrows in Fig. 4.10(a), respectively. A cross sectional view of these films (Fig. 4.10(b)) allows to estimate the deposited thickness which amounts to ≈ 285 nm when measured from the pillar base to the top of the film. Also noticeable are the undulations on the film's surface, the crests of which align with the locations of pillars and the trough form in between the pillars, indicated using orange and blue arrows. The amplitude of these undulations amounts to ≈ 90 nm and is marked in Fig. 4.10(b). Additionally, an EFTEM relative thickness map

(Fig. 4.10 (e)) and corresponding unfiltered (Fig. 4.10 (c)) and zero loss peak (Fig. 4.10 (d)) images of the deposited films, clearly indicate the presence of pores and boundaries at positions where SiN_x growth fronts have met. Such locations with low mass-thickness contrast are indicated with yellow arrows in Fig. 4.10 (d) and (e). As an example, the dip in the relative thickness along a region ion of interest (ROI) with a pore is plotted in Fig. 4.10(f).

SEM images captured at the intermediate stages of SiN_x film growth show the initial conformal nature of film growth on the patterned substrates (Fig. 4.10). Starting form triangular pillars (Fig. 4.11(a)), the pillars first get conformally embedded with SiN_x (Fig. 4.11(b)). Upon longer SiN_x deposition (Fig. 4.11(c), (e) and (g)) the edges of the SiN_x shells surrounding the pillars get rounded until they merge (Fig. 4.11(d)). The films growing on neighboring pillars then form boundaries upon impingement which appear as lines (indicated by a yellow arrow in Fig. 4.11(d)) and collectively as a triangular grid (see Fig. 4.10(a)). In Fig. 4.10(d) the intermediate state of this feature is indicated using a green arrow. Cross-sectional and 45° tilted view images of this state, Figs. 4.10(f) and (h) respectively reveal the presence of gaps at this position.
In the final state i.e. after 16 mins of deposition and densification these positions form vertical cavities as inferred from Figs. 4.10(d) and (e).

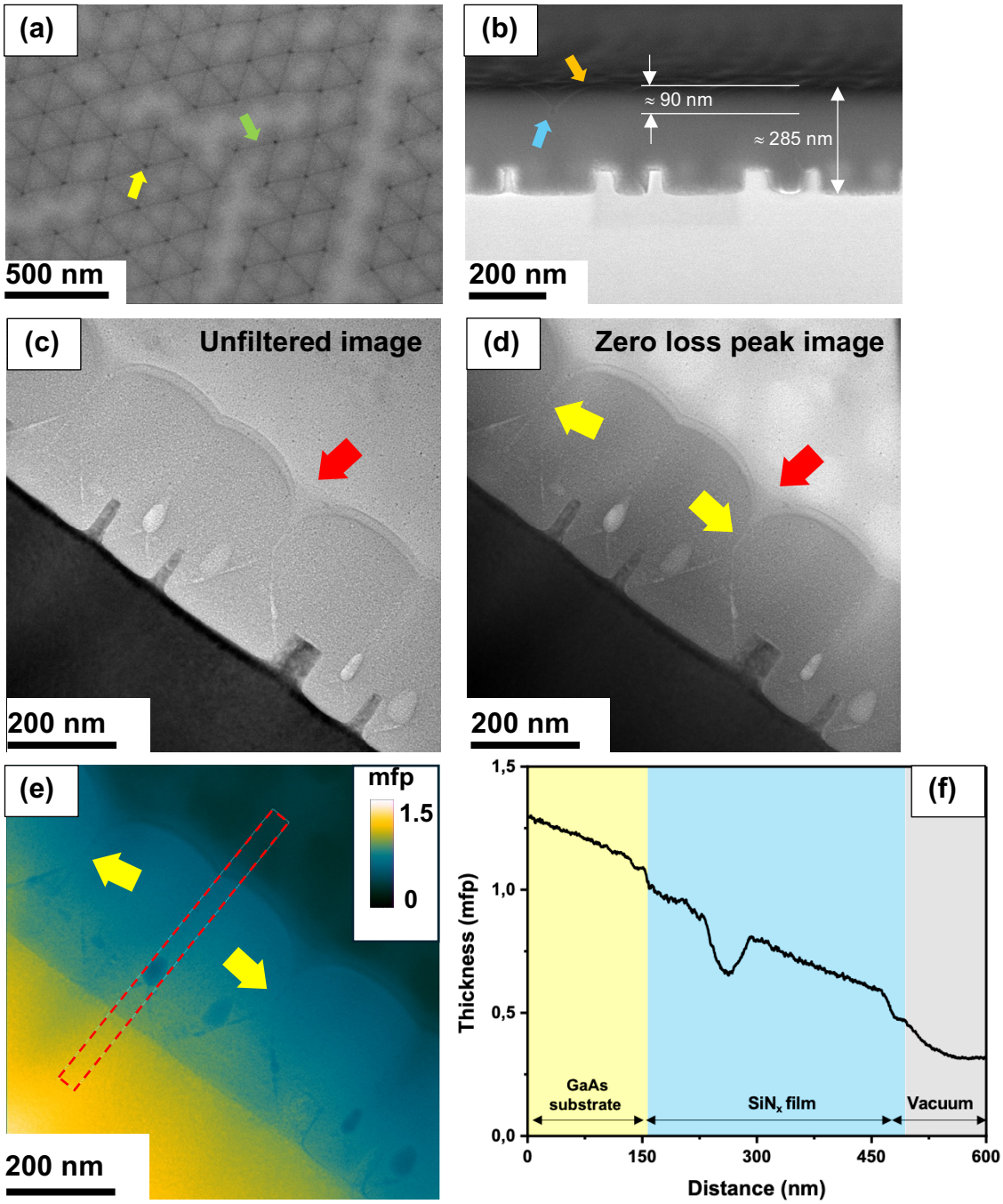

Fig. 4.10. (a), (b), (c) and (d) are top-view images of SiN_x films deposited on nanopillar patterned GaAs(111)A substrate for durations 0, 1, 4 and 8 minutes respectively. The cross-sectional views of substrates with films deposited for durations 4 and 8 mins are shown in (e) and (f), their corresponding 45 tilted view images are shown in (g) and (h) respectively.

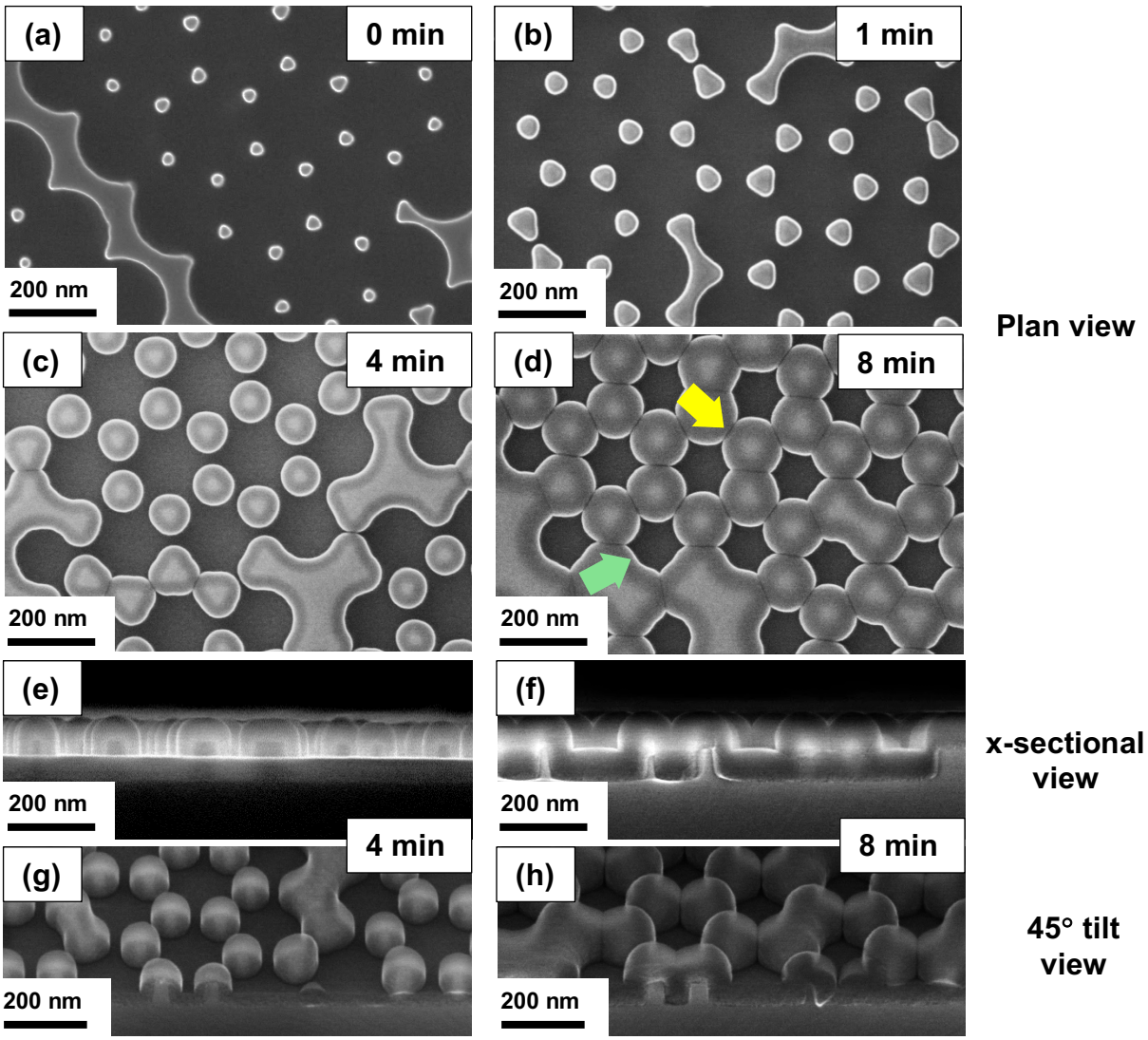

Fig. 4.11. (a), (b), (c) and (d) are top-view images of SiN_x films deposited on nanopillar patterned GaAs(111)A substrate for durations 0, 1, 4 and 8 minutes respectively. The cross-sectional views of substrates with films deposited for durations 4 and 8 mins are shown in (e) and (f), their corresponding 45 tilted view images are shown in (g) and (h) respectively.

Such films when subject to RIE* for releasing pillar tops using a CHF_4+O_2 plasma (details in section 4.3.3) formed circular cavities at the center of honeycomb arrays as seen in Fig. 4.11(a). The side view image of the same state in Fig. 4.11(b) reveals the attack of the SiN_x film by the ions. Upon closer examination of TEM images Figs. 4.10(c) and (d), the meeting point of adjacent SiN_x growth fronts are found to create recesses that connect with the boundaries. These are assumed to be the locations for ingress of reactive ions

and widening of the preexisting cylindrical cavities. A prolongation of RIE upon such films could create holes that expose the GaAs substrate surface without exposing nanopillar tops. As a remedy, the planarization of such undulations was performed, the details of which are discussed in the next section.

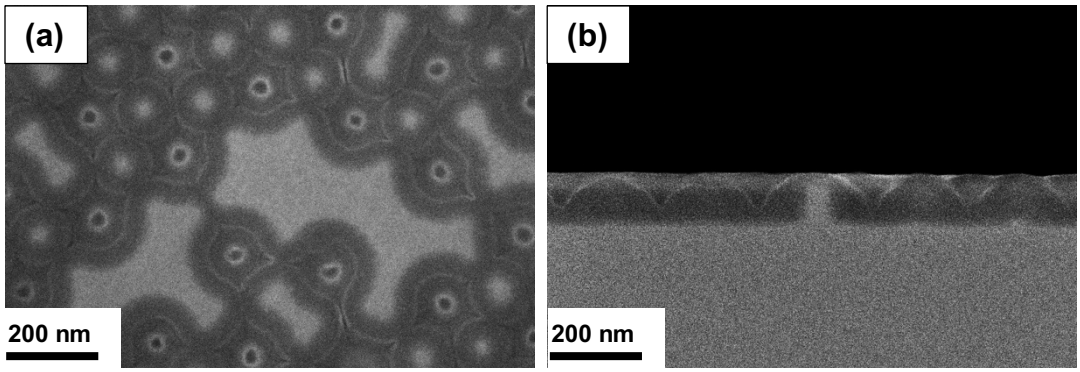

Fig. 4.12. (a) and (b) are respectively the top view and cross-sectional view images of SiN_x film deposited on nanopillar patterned GaAs(111)A substrate after RIE using CHF_3 and O_2 plasma for 9 minutes.

4.3.2 Surface planarization of SiN_x films

Chemical mechanical polishing (CMP) is a technique widely used in the semiconductor industry to level the surface topography of complex device morphologies. More details regarding this technique and its applications can be read in [25,26]. The undulations of the SiN_x film surface in the present case are mitigated using vibratory polishing. In this technique, the substrate is attached to a load, the surface to be planarized is placed on a polishing bowl containing a cloth at its center, filled with a colloidal suspension. By superposing vertical and torsional vibrations, the sample moves in a circular path within the bowl. The polishing action as such is achieved by a combination of surface attack due to the basic pH of the colloidal suspension and the mechanical removal of reaction products by particles in the suspension [27]. Here the load attached to the sample determines the speed of rotation and intensity of horizontal vibration determine the material removal rate. Vibratory polishing in the present case was performed using a Vibromet2 (Fig. 4.13(a) manufactured by Buehler Inc which has a horizontal vibration frequency of 120 Hz. A colloidal suspension consisting of 55 nm SiO_2 particles with 50% active content and pH in the range 10 – 11, produced by Kurt Obermeier GmbH under the commercial name Levasil CS50-34P was used as the main polishing medium. This

solution was diluted with water (1:5 = suspension: water) and spread over a long napped synthetic rayon cloth, marketed under the name MicroCloth by Buehler Inc. The samples to be polished were attached to a stainless steel 316L block weighing 600g and placed on the bowl as shown in Fig. 4.13(b) and a vibration intensity of 30% of maximum was used. These parameters result in a controlled material removal rate of 1nm/min for PECVD SiN_x. Hence vibratory polishing was performed for a duration of 90 mins to level the ≈ 90 nm tick undulations. Following the planarization step the substrate surface is cleaned using a water diluted soap solution to prevent SiO_2 colloidal particles from sticking to the surface. SEM images of the resulting planarized SiN_x films are shown in Figs. 4.14 (a) and (b). The top-view image (Fig. 4. 14 (a)) reveals the GaAs pillars embedded within the SiN_x (see Fig. 4.14 (b)) due to the ≈ 2 μm deep interaction volume, calculated using Monte Carlo electron trajectory simulations with Casino software version 2.48, developed by McGill electron microscopy research group [28].

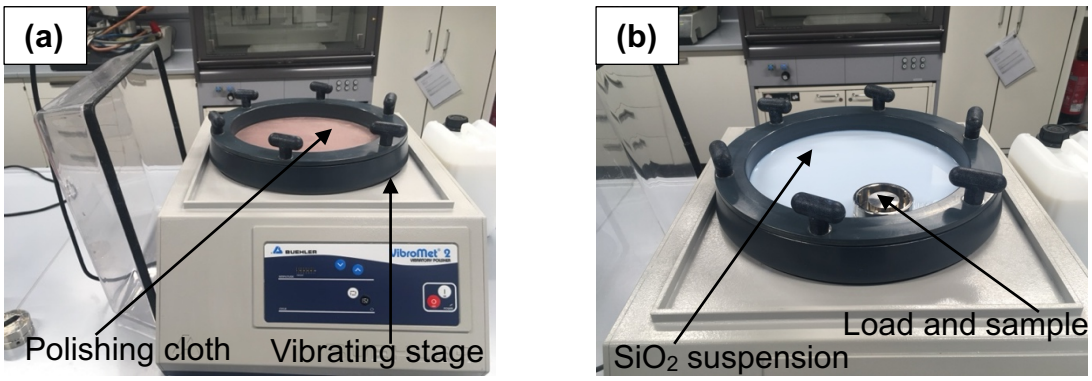

Fig. 4.13. (a) and (b) Pictures of the Vibromet2 vibratory polisher showing the salient features of the machine.

4.3.3 Releasing GaAs(111)A pillar tops

The planarized SiN_x films were subjected to RIE in an Oxford PlasmaLab 100 reactive ion etcher employing the following parameters. RF power 40 W, chamber pressure 30 mTorr, gas flow rates of CHF_3 and O_2 25 and 1 sccm, respectively. A RIE etch rate of 0.55 nm/s was achieved for SiN_x with the above conditions. The RIE was performed until the pillar tops were exposed as seen in Figs. 4.14 (c) and (d). A duration of approximately 5 mins was needed to achieve this. As a final cleaning step, the substrates were dipped in 0.5

wt% HF for 15 s to remove residues left from the RIE process and the native oxide. An example of the resulting SAH template is shown in Fig. 4.14 (e) and (f) in top-view and 45° perspective view. These images reveal the remnants of an SiN_x shell that initially forms around the pillars. Also the flat regions surrounding them are seen in Fig. 4.14 (f).

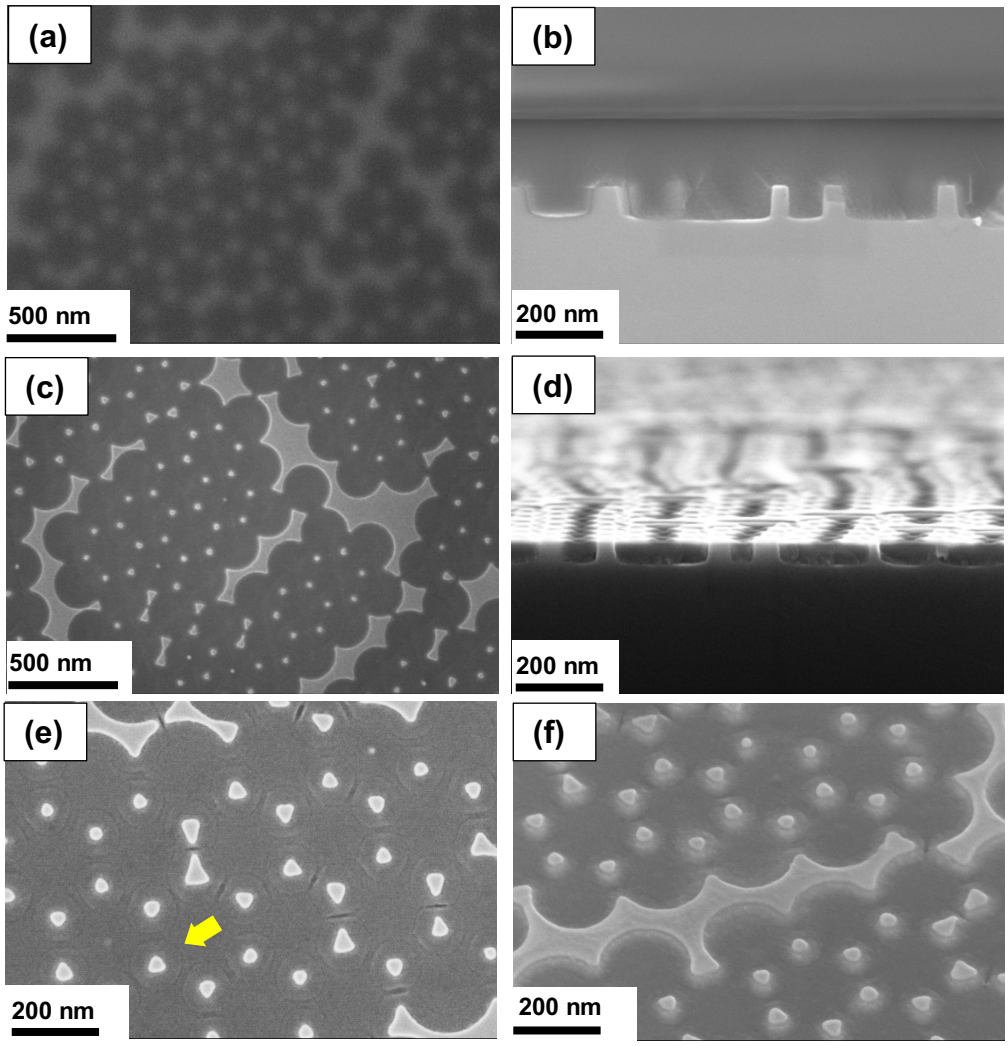

Fig. 4.14. (a) and (c) are top-view and cross-sectional view images of SiN_x film deposited on nanopillar patterned GaAs(111)A substrate after surface planarization and RIE. The cross-sectional views corresponding to these states are shown in (c) and (d). (e) and (f) show the top-view and a 45° tilted view of a SAH template after final cleaning with dilute HF solution. Here, the yellow-colored arrow points towards the SiN_x shell which initially forms around the pillars

The PECVD SiN_x formed at the DL pillar patterned areas (Fig. 4.15 (a)) are much more compact compared to that formed at ML patterned areas (Fig. 4.10 (a)) due to the larger pillar to pillar separation which reduces the occurrence of cavities. Such areas are therefore suitable for estimating the surface roughness of the SiN_x film after RIE and wet chemical etching. A quick comparison between Fig. 4.14 (e) and 4.15 (b) clearly reveals the absence of cavities formed between the SiN_x shells surrounding the pillars, in case of the former. An average RMS value of 0.97±0.18 nm measured using multiple ROIs with average area ≈ 4843 nm^2 was obtained using AFM topography scans performed at such DL patterned areas such as Fig. 4.15 (c).

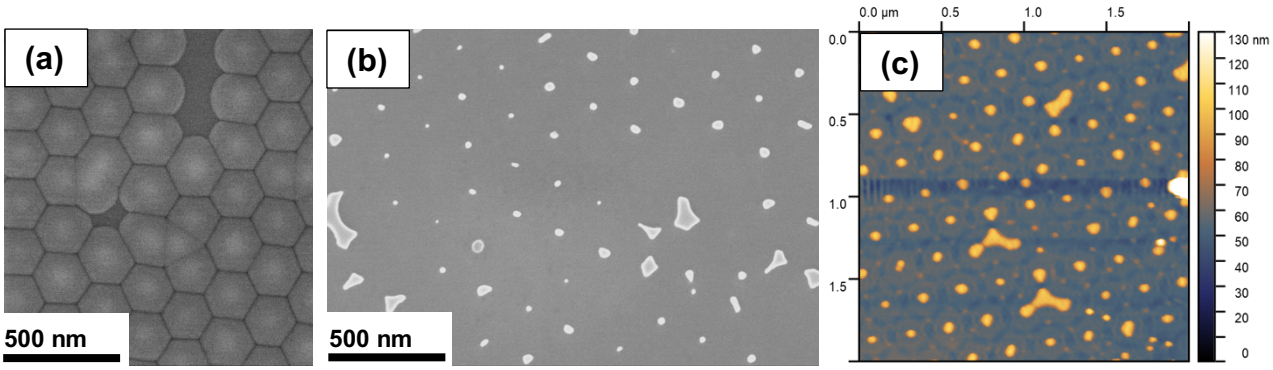

Fig. 4.15. (a) is a top-view SEM image of a nanopillar patterned GaAs(111)A substrate overgrown by PECVD SiN_x film at DL patterned area. (b) and (c) top-view SEM and AFM topography scan images of SAH template also at the DL patterned areas.

4.4 Molecular beam epitaxy (MBE)

Molecular beam epitaxy is an advanced crystal growth technique used for growing high purity semiconductor heterostructures with sharp interfaces under precisely controlled growth rates. In this method, beams of atoms or molecules of the desired material(s) are vaporized and made to incident upon the substrate of choice. Growth of high-purity materials is achieved by performing the deposition in the high vacuum regime at a working pressure $< 1 \times 10^{-4}$ mbar while the base pressure is maintained in the ultra-high vacuum (UHV) regime, $< 1 \times 10^{-9}$ mbar. One of the major disadvantages of this technique is the very low achievable growth rates of typically ≈ 1 μm/h [29].

The MBE growth runs reported in this thesis were performed by the Optoelectronic Materials and Devices group (OMD) lead by Prof. Dirk Reuter at the Paderborn University in a III-V MBE system from Dr. Eberl MBE-Komponenten GmbH. A schematic illustration of this system is depicted in Fig. 4.16 [30]. It consists of four main chambers 1. growth chamber 2. preparation chamber 3. transfer chamber and 4. load-lock. Gate valves separate each of these chambers. The high vacuum levels of $\approx 1 \times 10^{-10}$ mbar are maintained within the MBE chamber with the help of a cryo pump, a liquid nitrogen cooled titanium sublimation pump, an ion gettering pump and a liquid nitrogen filled cryo shroud that surrounds the source cells and sample. Additionally, chamber purity is monitored with a quadrupole mass spectrometer.

In the chamber molecular beams of various III group source materials such as Ga, In, Sb, Al, Si and C can be generated using effusion cells. Of these, the Al, Ga and In are contained in pyrolytic boron nitride crucibles of the effusion cells, whereas the group V sources such as As and Sb are produced using cracker cells that generate well defined ratios of As_2 and As_4. Mechanical shutters which can be shut within fraction of seconds are used to control the amount of material being deposited. Material flux is controlled by heating the cells to the appropriate temperatures. Actual estimates of beam fluxes are made using beam flux monitors (BFM) which measure the beam equivalent pressure (BEP) of materials using an ion gauge. The growth rate of resulting films is determined using RHEED oscillations from reference growth runs performed on flat substrates, un-patterned. Substrate temperatures were estimated using the temperature of the heating

elements placed behind the substrate. Samples were rotated at a speed of 10 rpm to maintain uniformity of deposited material and temperature.

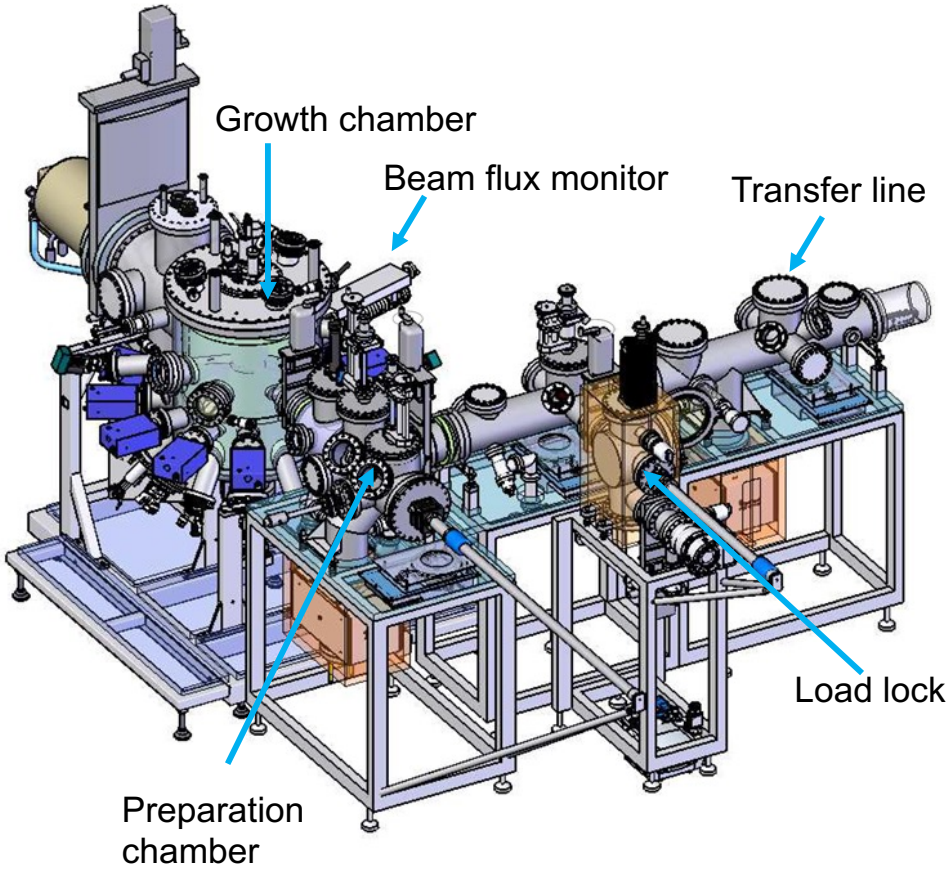

Fig. 4.16. A schematic of the III-V MBE system at AG Reuter, Paderborn University [30].

The basic substrate materials used for nanopillar patterning and MBE growth were 3 inch GaAs(111)A wafers with a deviation of ±5° to the normal. The wafers were provided in epi-ready condition by MaTeck (Material-Technologie & Kristalle GmbH) and Semiwafer Inc. with a Si dopant concentration of 1 x 10^{18} /cm^{-3}. The AFM measured rms roughness of these samples amounted to 0.5 nm. For MBE, patterned and cleaned sixths of 3 inch wafers were placed upside down into Mo holders of the load-lock, held in position by gravity. The load-lock enables the entry and exit of samples without breaking the UHV

of the MBE. Turbopumps maintain the pressure in the load-lock chamber at 5 x 10^{-8} mbar. A six-way magazine enables the loading of up to six samples to be loaded at a time.

The following sequence of steps was performed in the MBE growth of samples:

1.) Samples are introduced into the load-lock. The chamber is pumped to a vacuum level of 10^{-7} – 10^{-8} mbar. Condensed water molecules and hydrocarbon impurities on the wafer are degassed by heating up to 120°C for 8h. The sample are transferred to the transfer chamber upon reaching a chamber pressure of 10^{-8} mbar.

2.) After cooling down of the samples and achieving a chamber pressure < 10^{-7} mbar, the substrates are transferred to the preparation chamber via the transfer chamber.

3.) The samples are heated up to 200°C in the heating station of the preparation chamber to remove further contaminants for 2h.

4.) Samples are cleaned by atomic hydrogen cleaning. More details regarding this step are given in section 4.2.2.

5.) A transfer of specimens is made from the preparation chamber to the growth chamber when they are both at pressures below 10^{-9} mbar. All fluxes in the growth chamber at this point are null and the growth manipulator has a temperature below or equal to 300°C.

6.) The substrate is heated to the desired temperature. Then the substrate is exposed to an As flux ≈ 2.5 x 10^{-5} mbar to stabilize the GaAs surface, In shutter is opened and the required In flux to achieve the desired III/V ratio is provided.

7.) After the In beam is shut the As flux is provided for an extra 5 minutes after the In beam is shut, to crystallize any remaining In clusters or droplets.

8.) The sample is transferred back to the load-lock system and retrieved.

A summary of the InAs growth conditions used in this thesis is presented in Table 4.3. The In cell inclination during initial growth runs was maintained normal sample surface or an inclination of 40° with respect to the sample normal was used. SEM based morphological investigations were performed to confirm the reproducibility of InAs growths between the two used In incidence angles. The growth sheets corresponding to the growth runs listed in Table 4.3 are presented in Appendix-4, this helps to trace back the wafers used and the growth parameters of the growth runs.

Table 4.3. Sample codes and growth conditions used for MBE of InAs

S. No.	Growth sheet	Sample Code	Temp. (°C)	Growth rate (nm/s)	Deposited thickness (nm)	In cell inclination (degrees)
1	A0618	W3_S4	410	0.011	15	0
2	A0643	W3_S2	350	0.011	15	0
3	A0668	W6_S2	300	0.011	15	0
4	A0698	W6_S3	300	0.11	15	0
5	A0740	W7_S3	150	0.011	15	0
6	A0771	W8_S4	150	0.011	5	0
7	A0793	W8_S6	150	0.011	2	0
8	A0874	W10_S5	300	0.011	15	40
9	A0904	W12_S6	150	0.011	5	40
10	A1100	W15_S4	150	0.011	2	40
11	A1120	W14_S1	200	0.011	15	40
12	A1132	W15_S6	250	0.011	15	40
13	A1216	W14_S2-3	300	0.011	2	40
15	A1271	W16_S2-3	450	0.011	2	40
16	A1338	W17_S3-2	400	0.011	2	40
17	A1697	SW2_S3-2	425	0.011	2	40

References

1) P. Colson, C. Henrist and R. Cloots, "Nanosphere Lithography: A powerful method for the controlled manufacturing of nanomaterials", J. Nanomater., 2013 (1), Article 948510 (2013)

2) C. L. Haynes and R. P. Van Duyne, "Nanosphere lithography: A versatile nanofabrication tool for studies of size-dependent nanoparticle optics", J. Phys. Chem. B, 105, 5599 (2001)

3) T. Qiu, E. M. Akinoglu, B. Luo, M. Konarova, J-H. Yun, I. R. Gentle and L. Wang "Nanosphere Lithography: A Versatile Approach to Develop Transparent Conductive Films for Optoelectronic Applications", Adv. Mater., 34, 2103842 (2022)

4) B. G. Prevo, D. M. Kuncicky and O. D. Velev, "Engineering deposition of coatings from nano- and micro-particles: A brief review of convective assembly at high volume fraction", Colloids Surf. A: Physicochem. Engg. Asp., 311, 2 (2007)

5) A. S. Dimitrov and K. Nagayama, "Continuous convective assembling of fine particles into two-dimensional arrays on solid surfaces", Langmuir, 12, 1303 (1996)

6) X. Ye and L. Qi, Na, "Two-dimensionally patterned nanostructures based on monolayer colloidal crystals: Controllable fabrication, assembly, and applications", Nano today, 6, 608 (2011)

7) K. Brassat, F. Assion, U. Hilleringmann and J. K. N. Lindner, "Self-organization of nanospheres in trenches on silicon surfaces", Phys. Status Solidi ,210, 1485 (2013)

8) M. Bekeris, T. Truong, S. Carron, Z. Karimi, H. Feng, U. Nze, M. Beeman, R. D. Sochol and R. Warren, "Rapid quantification of nanosphere lithography packing defects using scanning electron microscopy edge defects", Phys. Status Solidi RRL, 14, 2000328 (2020)

9) V. Canalejas-Tejero, M. Ibisate, D. Golmayo, A. Blanco and C. Lopez, "Qualitative and quantitative analysis of crystallographic defects present in 2D colloidal sphere arrays", Langmuir, 28, 161 (2011)

10) C. Brodehl, S. G-Weber and J.K.N. Lindner, "Fabrication of nanoantennas on large areas for plasmonic devices", Mater. Toda: Proc., 4, S44 (2017).

11) T. Rield and J.K.N. Lindner, "self-organized fabrication of periodic arrays of vertical, ultra-thin nanopillars on GaAs surfaces", Phys. Status Solidi A, 211, 2871 (2014)

12) Nicolas Posseme (Ed.), "Plasma Etching Processes for CMOS device realization", Elsevier (2017)

13) F. Karouta, "A practical approach to reactive ion etching", J. Phys. D: Appl. Phys., 47, 233501 (2014)

14) Kazuo Nojiri, "Dry etching technology for semiconductors", Springer (2014)

15) R.J. Schul and S.J. Pearton (Eds.), "Handbook of advanced plasma processing techniques", Springer (2012)

16) Operation and maintenance manual, PlasmaLab 80 plus, Oxford Instruments Plasma Technology, Oxford Instruments plc.

17) H. Jansen, H. Gardeniers, M. de Boer, M. Elwenspoek and J. Fluitman, "A survey on the reactive ion etching of silicon in microtechnology", J. Micromech. Microeng. 6, 14 (1996)

18) M. Yamada and Y. Ide, "Direct observation of species liberated from GaAs native oxides during atomic hydrogen cleaning," Jpn. J. Appl. Phys., 2, (1994) 671

19) P. Tomkiewicz, A. Winkler and J. Szuber, "Comparative study of the GaAs(1 0 0) surface cleaned by atomic hydrogen," Appl. Surf. Sci., 33, (2006) 7647.

20) Nandlal Sharma, "Molecular beam epitaxy of tailored (In,G)As/GaAs quantum dot heterostructures", Ph.D. thesis, Uiversität Paderborn (2017)

21) H.O. Pierson, "Handbook of chemical vapor deposition: principles, technology and applications", II Edition, Noyes publications, New York (1999)

22) A. E. Kaloyeros, F.A. Jove, J. Goff and B. Arkles, "Review- silicon nitride and silicon nitride-rich thin film technologies: trends in deposition techniques and related applications", ECS J. Solid State Technol., 6, 691 (2017)

23) C.H. Ling, C.W. Kwok and K. Prasad, "Silicon nitride films prepared by plasma enhanced chemical vapour deposition (PECVD) of $SiH_4/NH_3/N_2$ mixtures: some physical properties", Jpn. J. Appl. Phys., 25, 1490 (1986)

24) J. Ning, C. Niu, Z. Tang, Y. Sun, H. Yan and D. Zhou, "Optimization of the PECVD process for stress-controlled silicon nitride films: enhancement of tensile stress via UV curing and layered deposition", coatings, 15, 708 (2025)

25) A.Y.C. Nee (Ed.), "Handbook of manufacturing engineering and technology", Springer London (2015)

26) G. Ginami, D. Canali, D. Fattori, G. Girardi, P. Scintu, L. Tarchini and D. Tricarico, "Survey on flash technology with specific attention to the critical process parameters related to manufacturing", Proc. IEEE, 91, 503 (2003)

27) O. Engler, S. Zaefferer, and V. Randle, "Introduction to texture analysis: macrotexture, microtexture and orientation mapping", e3, CRC Press (2024)

28) McGill Electron Microscopy Research Group, , McGill University, Montreal, Canada, Casino v2.8: https://www.memrg.com/programs-download

29) M.A. Hermann, W. Richter and H. Sitter, “Epitaxy: physical principles and technical implementation”, Springer (2004)

30) MBE-Komponenten GmbH, UHV-system komplett Reuter PB, Freigabezeichnung (2014)

Chapter 5
InAs heteroepitaxy on nano-pillar patterned GaAs(111)A substrates

This chapter deals with the identification of MBE parameters necessary for isolating InAs growth to nano-pillar tops and with the strain misfit strain accommodation by the resulting InAs Islands on the nanopillars. Towards this end, the influence of growth parameters such as temperature and growth rate were probed. Further, the mechanisms concerning the misfit strain at the resulting heterostructures as a function of InAs island size are studied by varying the deposited InAs film thickness.

5.1 Influence of substrate temperature

The influence of growth temperature is investigated first to realize InAs heteroepitaxy on GaAs pillar tops. Growth experiments were conducted at substrate temperatures T_{sub} of 410°C, 350°C, 300°C, 250°C, 200°C and 150°C. A constant growth rate of 0.011 nm/s was maintained for all these conditions. Deposited InAs thicknesses of 15, 5 and 2 nm were explored for T_{sub} = 150°C.

Top-view SEM images of GaAs nanopillar patterned substrates with monolayer ML patterned areas, overgrown by InAs at various temperatures are shown in Fig. 5.1. Growth was performed until a film thickness of 15 nm would have been reached, called the nominal film thickness. Their corresponding cross-sectional images are shown in Fig. 5.2. A feature common to all growth conditions is the presence of pyramidal InAs hillocks with truncated corners at the base of GaAs nanopillars visible both in Fig. 5.1 and 5.2. This is attributed to the availability of step edges at the pillar bases which easily accommodate incoming adatoms. Step edges at the base of one such pillar embedded in a SiN_x film after MBE growth are shown in Fig. 5.3 at low and high resolution. More details regarding this specimen are outlined in chapter 6. The presence of such step edges evinces the hillock formation via a step-flow type of growth mechanism. Although the formation of such pyramidal hillocks is widely reported in literature for singular 111 surfaces [1-3], the ones observed here are distinct in the sense that they are restricted to pillar bases. The bases of pillars such as the one shown in Fig. 5.3 act as adatom sinks because their concave edges reduce the local chemical potential [4].

Another noticeable feature form top view SEM images (Fig. 5.1 (a-f)) is the coalescence of pyramids upon increasing the growth temperature from 150°C to 410°C. Along with this, the facets of pyramids become better defined, and the exposure of GaAs substrate increases (demarcated using white arrows). However, after an increase in lateral individual hillock size from 150°C to 300°C, a size decrease is observed between 350°C and 410°C. This can be attributed to the increased adatom mobility with increased temperatures, which enhances incorporation at the preexisting pyramids and coalescence. Due to the same reason, the pyramids at 410°C decrease in size and separation. Here, the InAs growth is concentrated mainly around pattern defects (Fig. 5.1(a)). Cross-sectional SEM images for this condition also indicate a possible erosion of GaAs at the pillar tops, see Fig. 5.2 (a). The possibility of melting temperature suppression due to the reduced dimensions of GaAs pillars [5] was verified using the Gibbs-Thompson equation $\Delta T = T_m - T_r = 2\gamma\Omega/r\Delta S$ [6]. Here, T_m is the melting temperature of bulk GaAs and T_r is the melting temperature of GaAs nanopillar with a radius of curvature r =15 nm for a 30 nm diameter nanopillar. Under As stabilized conditions GaAs(111)A surface energy γ = 0.82 J/m^2 [7], $\Delta S = L/T_m$ = 69,5 J/m considering, latent heat L = 80.30 kJ/kg for Ga [8] , and melting temperature of GaAs T_m = 1511 K [9]. This yields ΔT = 43 K, which is too small explain the erosion of pillar tops. Hence, the 15 minutes long AHC used for this sample was considered a possible cause for eroding the pillar tops. Hence, the duration of AHC was reduced to 3 minutes for all subsequent growth runs.

The edges of the pyramids lying on the substrate plane are found to be aligned along the $\langle 1\bar{1}0 \rangle$ type directions and their normals are aligned along the $\langle 11\bar{2} \rangle$ type of directions. Arrows indicating these important in-plane directions are marked in the legends of top-view images for reference. A more detailed insight into the formation of pyramids shall be discussed when considering InAs growth at DL patterned areas.

With decreasing T_{sub} one observes an enhancement of substrate surface coverage, hillocks with poorly defined edges and the formation of InAs islands on GaAs pillar tops (See Figs. 5.1 (c)-(f)). These observations can be correlated with the exponential decrease in adatom migration length and enhanced As incorporation rate [10], both of which are temperature related effects. The influence of sluggish migration leading to the InAs island formation is clearly seen by comparing the side view images Figs. 5.2 (d)-(f). Here,

the initially bare GaAs pillars at T_{sub} = 250°C develops a film on top at 200°C and at 150°C distinguishable InAs islands form. At T_{sub} = 200°C, InAs growth on top of adjacent GaAs pillars is found to coalesce and show signs of small InAs clusters formation, indicated in Fig. 5.1 (e) using blue arrow. This condition is a clear intermediate step between T_{sub} = 250°C and T_{sub} = 150°C which shows the formation of an enveloping InAs film on the pillars, which later grows thicker and more irregular at T_{sub} = 150°C.

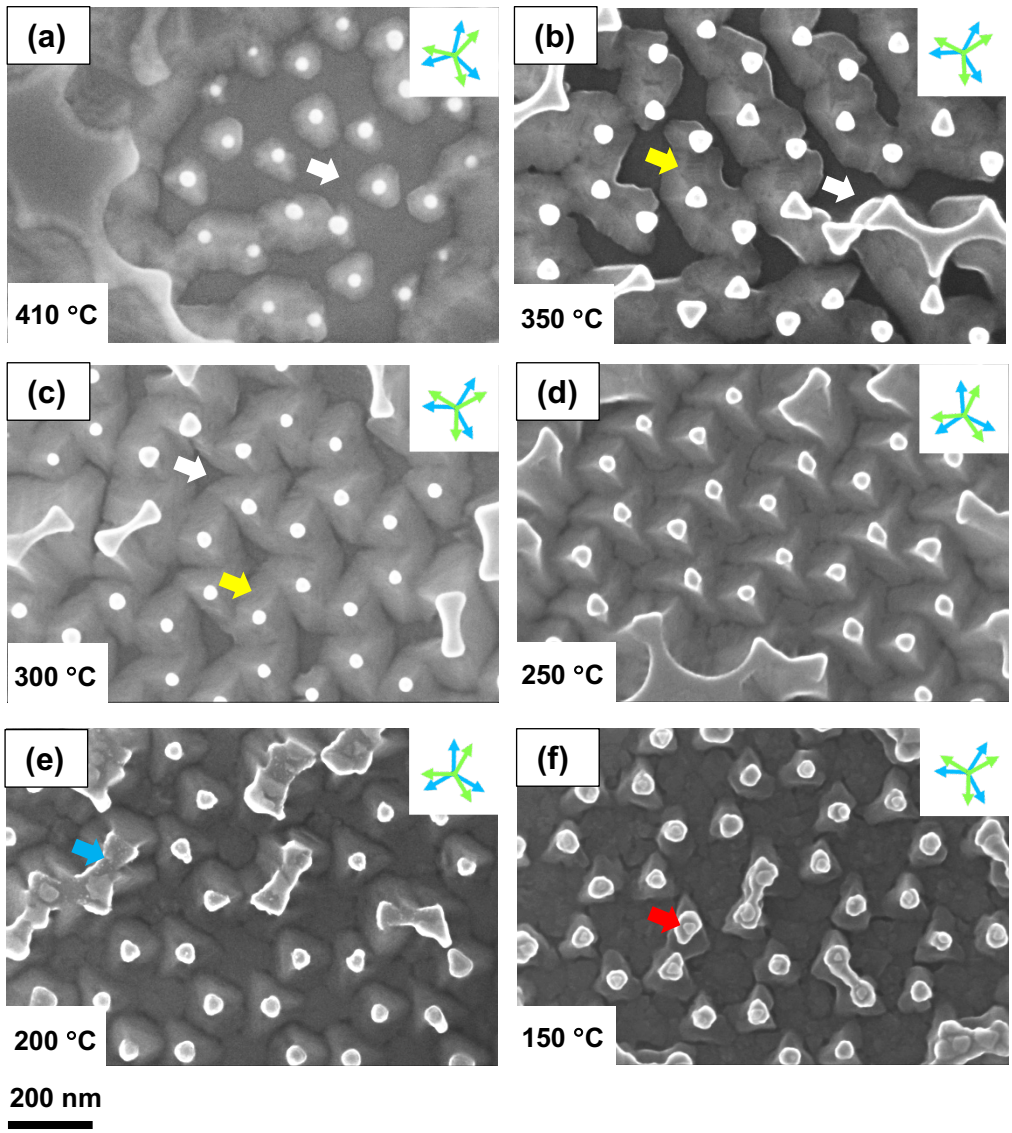

Fig. 5.1. (a -f) are Top-view SEM images of nanopillar patterned GaAs substrates overgrown with nominally deposited 15nm InAs at various temperatures. The blue and green arrows show the $\langle 1\bar{1}0 \rangle$ and $\langle 11\bar{2} \rangle$ directions, respectively, on the GaAs(111)A substrate surface. Additionally, the blue, yellow, white and red arrows indicate the small clusters, step-bunches, GaAs(111)A substrate and InAs islands, respectively. The scale bar shown is the same for all images.

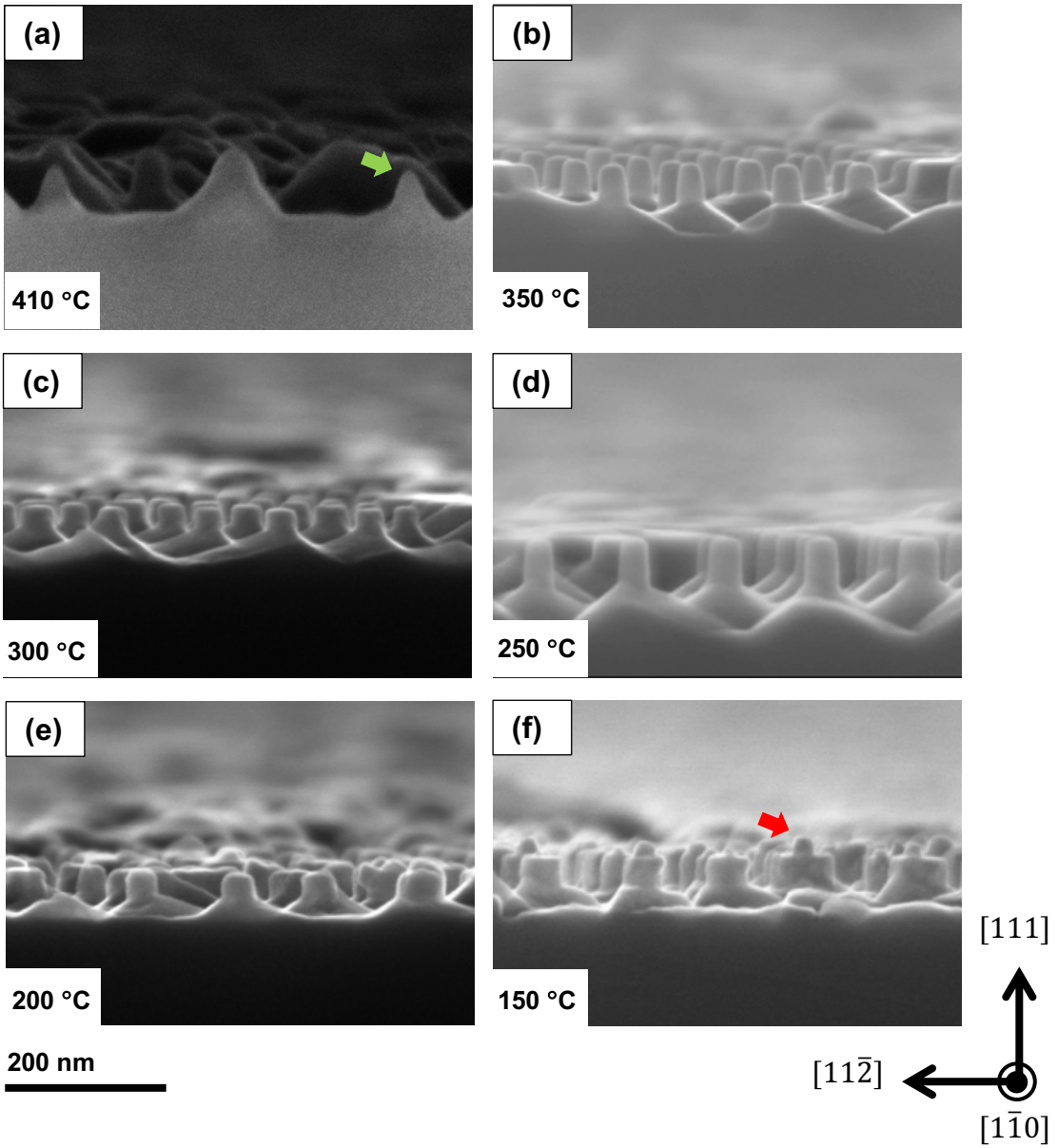

Fig. 5.2. (a -f) Cross-sectional view images of GaAs nanopillar patterned GaAs(111)A overgrown with nominally deposited 15 nm of InAs at various temperatures. The green and red arrows point towards the eroded GaAs nanopillar tops and InAs islands, respectively. Crystallographic directions relevant to these images are shown for reference. The scale bar shown is the same for all images.

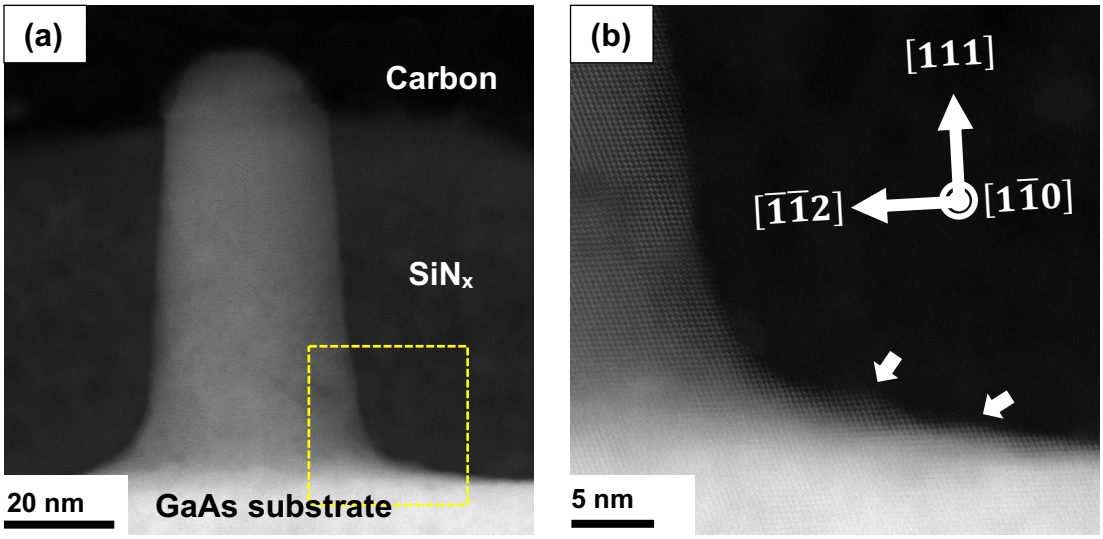

Fig. 5.3. (a) is a HAADF-STEM image of a GaAs nano-pillar embedded within SiN_x and carbon layers, imaged along the [1$\bar{1}$0] zone axis. (b) is a magnified image of the region of interest marked in (a) with the yellow box. The white arrows point to the step-edges at the pillar base.

5.2 Influence of InAs deposit thickness

Based on the result of section 5.1, smaller InAs deposit thicknesses were explored for the substrate temperature of T_{sub} = 150°C to further reduce InAs island size. Towards this end, InAs thicknesses of 5 and 2 nm were deposited on nano-pillar patterned substrates. Islands of much smaller dimensions and in greater number density compared to 15 nm thick deposits were obtained (see Fig. 5.4). Also noticeable is the reduced InAs coverage on the substrate surface between the pillars and the smaller size of InAs deposits at the pillar bases. (S)TEM was used to further probe the structural order and size of such small islands deposited at rather low temperatures compared to conventional InAs/GaAs(001) [11-13] and InAs/GaAs(111)A [14-16], QD structures.

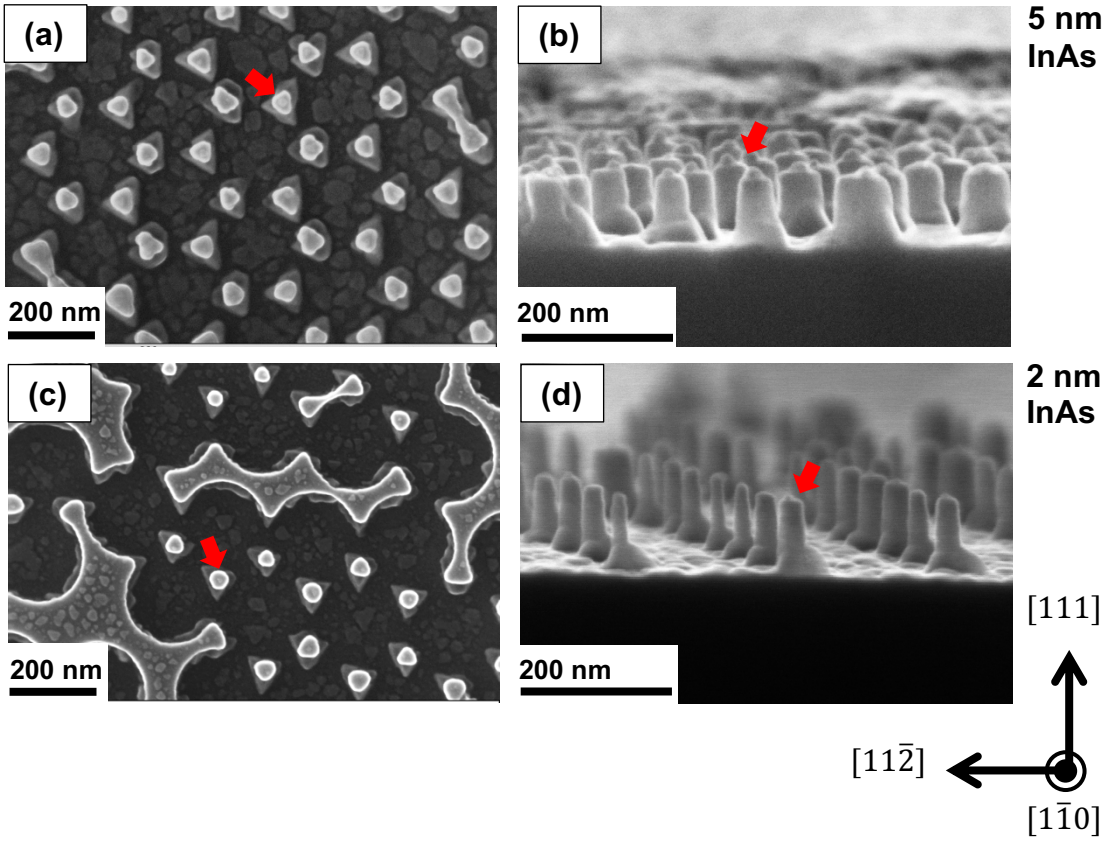

Fig. 5.4. Top view images of nanopillar patterned GaAs(111)A substrates after deposition of 5 and 2nm of InAs T_{sub} = 150°Care shown in (a) and (c), their respective side view images are shown in (b) and (d). Crystallographic directions relevant to the side-view images is shown for reference. The red arrows point towards the InAs islands sitting on top of the GaAs nanopillars.

5.3 Pyramidal hillock formation

An investigation of InAs growth at the NSL-DL patterned areas offers an insight into the mechanisms governing the hillock formation. Here, the relatively larger separation between the pillars reduces the influences of adjacent pyramids, thus preserving their true structures.

SEM examination of these structures reveals their surface to be bound by three major and six minor facets, clearly observable in Fig. 5.5 (a) and (b). Fig. 5.5 (c and d) shows AFM images of such pyramidal hillocks together with an AFM line profile in Fig. 5.5 (e), and they are schematically represented in Fig. 5.5 (f). These features are clearly observable for growths performed at 300 and 350°C compared to lower growth temperatures. AFM

topographic scans of the sample grown at 350°C (Fig. 5.5 (c)) was quantitatively analyzed to index the facets. The detailed images of such scans are shown using the corresponding derivative plot (Fig. 5.5 (d)). An average inclination of 35.5°±1.4° was measured along the $\langle 11\bar{2} \rangle$ direction as seen in Fig. 5.5 (e). This value matches the theoretically estimated angle of 35.26° between the ⟨110⟩ type facet and [111] substrate normal. This facet has also been shown to form during InAs heteroepitaxy on planar GaAs(111)A substrates in the literature [17-19]. The minor facet inclinations yield average values of 31.2°±1.8° and 39.6°±1.8° with respect to substrate normal. However, due to the wide variation in the measured values the facets could not be distinctly assigned to low-index lattice planes.

The formation mechanism of pyramids or hillock type of structures on fcc (111) surfaces has been studied well in literature based on simple atomistic models neglecting surface reconstruction [20-22]. For a hexagonal crystal forming on the GaAs(111)A surface there exists six $\langle 1\bar{1}0 \rangle$ step edges with $\langle 11\bar{2} \rangle$ type of normals. Amongst them, the $[11\bar{2}], [1\bar{2}1]$ and $[\bar{2}11]$ have type-B edges and $[2\bar{1}\bar{1}]$, $[\bar{1}\bar{1}2]$ and $[\bar{1}2\bar{1}]$ have type-A. The type-A edges have two dangling bonds whereas type-B has only one. This asymmetry promotes a higher adatom incorporation rate at type-A edges which causes type-A edges to shrink [19]. This results in the formation of triangular monolayers at pillar bases, upon which subsequent layers grow due to the ES barrier at the step edges [19]. A closer observation of the pyramid surfaces reveals bunching of steps. A likely reason for this is the elastic interaction between the steps that are strained due to lattice mismatch [24-26] and the ES barrier. These step-bunches disappear at lower temperatures due to the increased InAs nucleation rate on them [23], as also evident from Figs. 5.1 (d)-(f). AFM topography scans of the pyramids revealing the presence of step bunches both qualitatively and quantitatively are shown in Fig. 5.6. The line profile demarcated by yellow dotted line along the $\langle 11\bar{2} \rangle$ direction spanning both the GaAs substate and a {110} type major facet in Fig. 5.6 (a) is plotted in Fig. 5.6(d). Fig. 5.6 (b) is the derivative plots of 5.6 (a), Fig. 5.6 (c) is a magnified image of the region of interest (ROI) marked in Fig. 5.6 (b). Bunches of

steps separated by (111) terraces that are 10.4 nm wide are observed. The terrace separation along the [111] direction is 4.8 nm, each step has a height of 3.5 Å, hence this height corresponds to approximately 30 steps. Alternatively, considering the {110} type of terraces, the (111) terrace width can be considered to consist of 7 {110} planes.

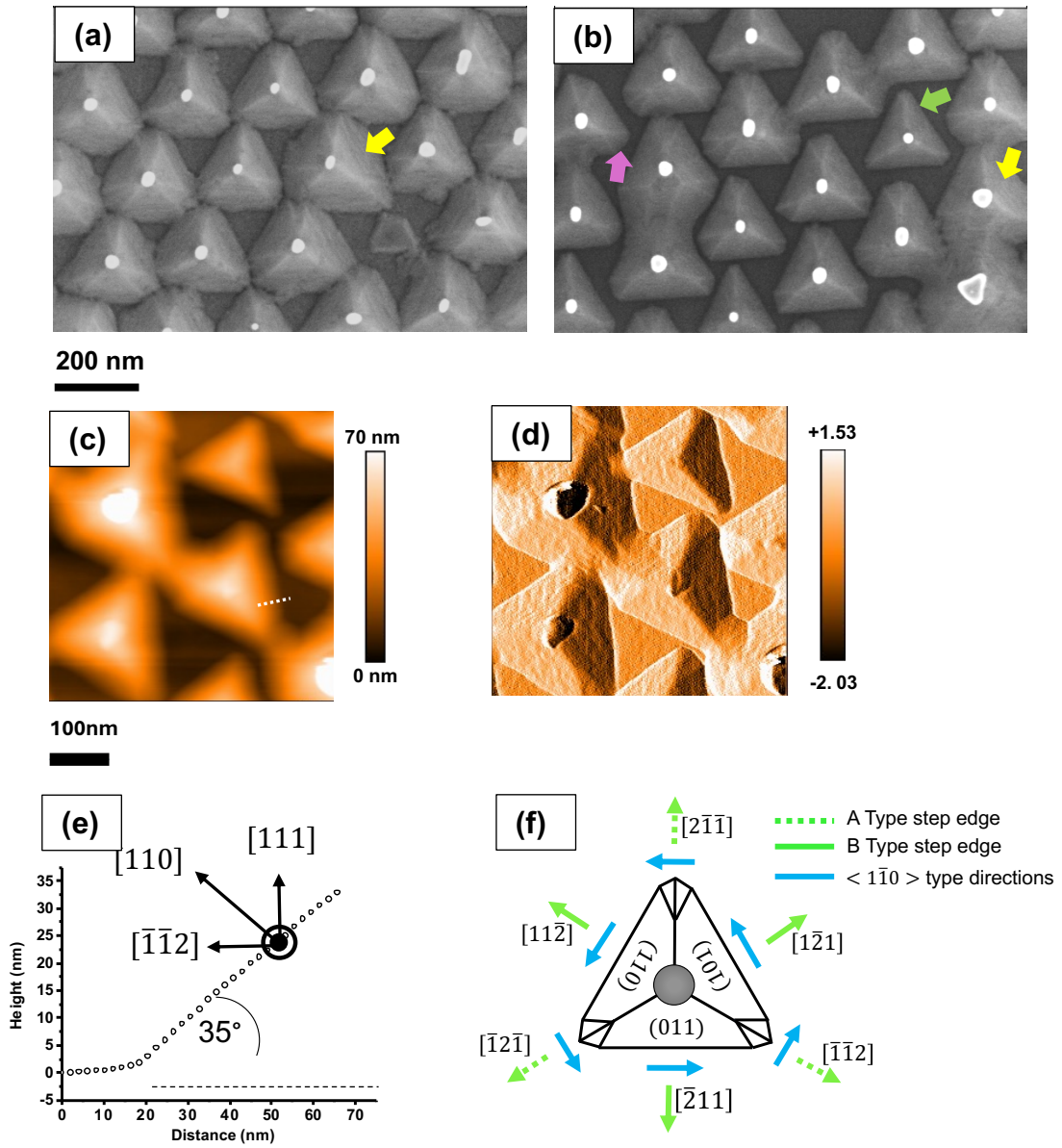

Fig. 5.5 (a) and (b) are the SEM top-view images of InAs pyramidal hillocks formed at the DL patterned areas at T_{sub} = 300 and 350°C, respectively at a growth rate of 0.011 nm/s. (c) is a raw AFM image of pyramidal hillocks formed at 350°C and 0.011 nm/s, (d) is the derivative plot of (c). Line height profile along the yellow dotted line marked in (c) is shown in (e). (f) is a schematic of the of InAs pyramids along with relevant crystallographic directions marked

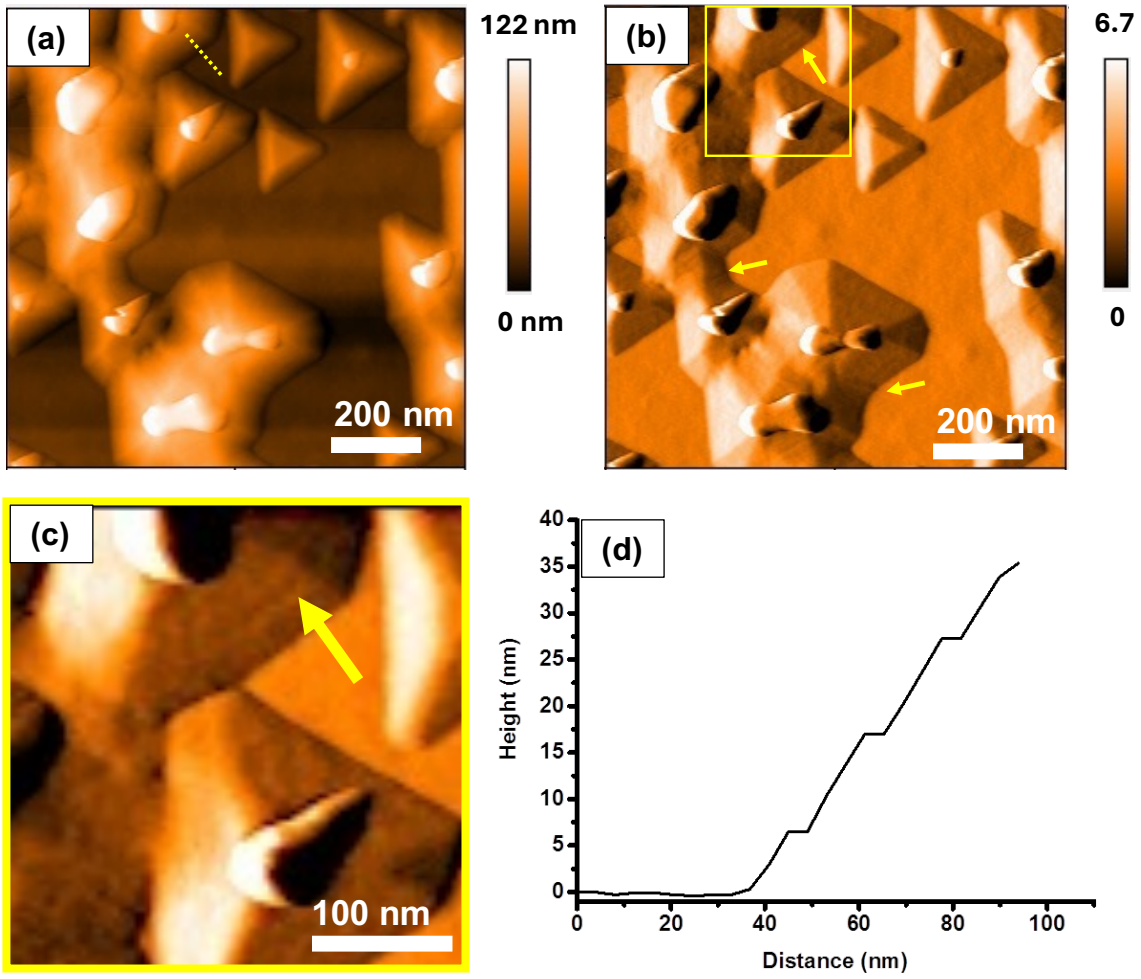

Fig. 5.6 AFM height profile of sample with 15 nm InAs deposited at $T_{sub} = 350°C$ and at a growth rate of 0.011nm/s (a) raw height data and (b) derivative plot of (a). Yellow arrows in (b) indicate locations on InAs structures where step bunches are formed. (c) is a close-up view of the yellow rectangular box shown in (b). (d) shows the height profile corresponding to the yellow dotted line in (a).

5.4 Defects in InAs islands

TEM investigations of samples with InAs deposited at T_{sub} = 150°C were performed to determine the inner structure and morphology of the islands. The low-magnification BF-TEM x-sectional image in Fig. 5.7 (a) for a nominally deposited thickness of 15 nm reveals the formation of InAs on pillar walls as films and on pillar tops as islands. These observations are in line with those made using SEM imaging, see Fig. 5.2 (f). The higher magnification image of a selected GaAs pillar in Fig. 5.6 (b) shows the formation of Moiré fringes on the pillar walls due to the superposition of the GaAs lattice with the one of InAs. The height and width of this island amounts to 16 nm and 24 nm, respectively, and the pillar diameter is 40 nm. At still higher magnification, the HRTEM image of the InAs island/GaAs pillar shows the presence of stacking faults within the island. The bright areas at the interface indicated with white arrow show regions of lower mass-thickness contrast, most likely resulting from a surface oxide layer on the GaAs pillars. The HAADF-STEM images of the same InAs island in Fig. 5.7(d,e) show the presence of 60° misfit dislocations and stacking faults. The Burgers vector of these dislocations was determined to be $\vec{\boldsymbol{b}} = \frac{1}{2}[\bar{1}01]$ using the RHFS Burgers circuit analysis as indicated by the inset in Fig. 5.7(e). [24,29]. An amorphous oxide layer can also be observed surrounding the island.

The HRTEM images for a sample with a smaller deposited thickness of t_{dep} = 5 nm but otherwise identical growth conditions in Figs. 5.8 (a) and (b) reveal details similar to the sample above with t_{dep} = 15 nm, such as the presence of InAs on GaAs pillar walls and the existence of a native amorphous oxide layer. An additionally observable feature are defects such as stacking faults and dislocations at the pillar base where InAs is deposited Fig. 5.8(a). InAs width and height of 11 nm and 7 nm, respectively, are measured and the GaAs pillar top diameter amounts to 30 nm. Fig. 5.8 (c) shows a low-magnification HAADF-STEM image of the same pillar with an InAs island on top, which is presented in a high-resolution HAADF-STEM image in Fig. 5.8 (d). It demonstrates the presence of a stacking fault and one 60° misfit dislocation, the core of which is marked with a red ⊤ in Fig. 5.8(d).

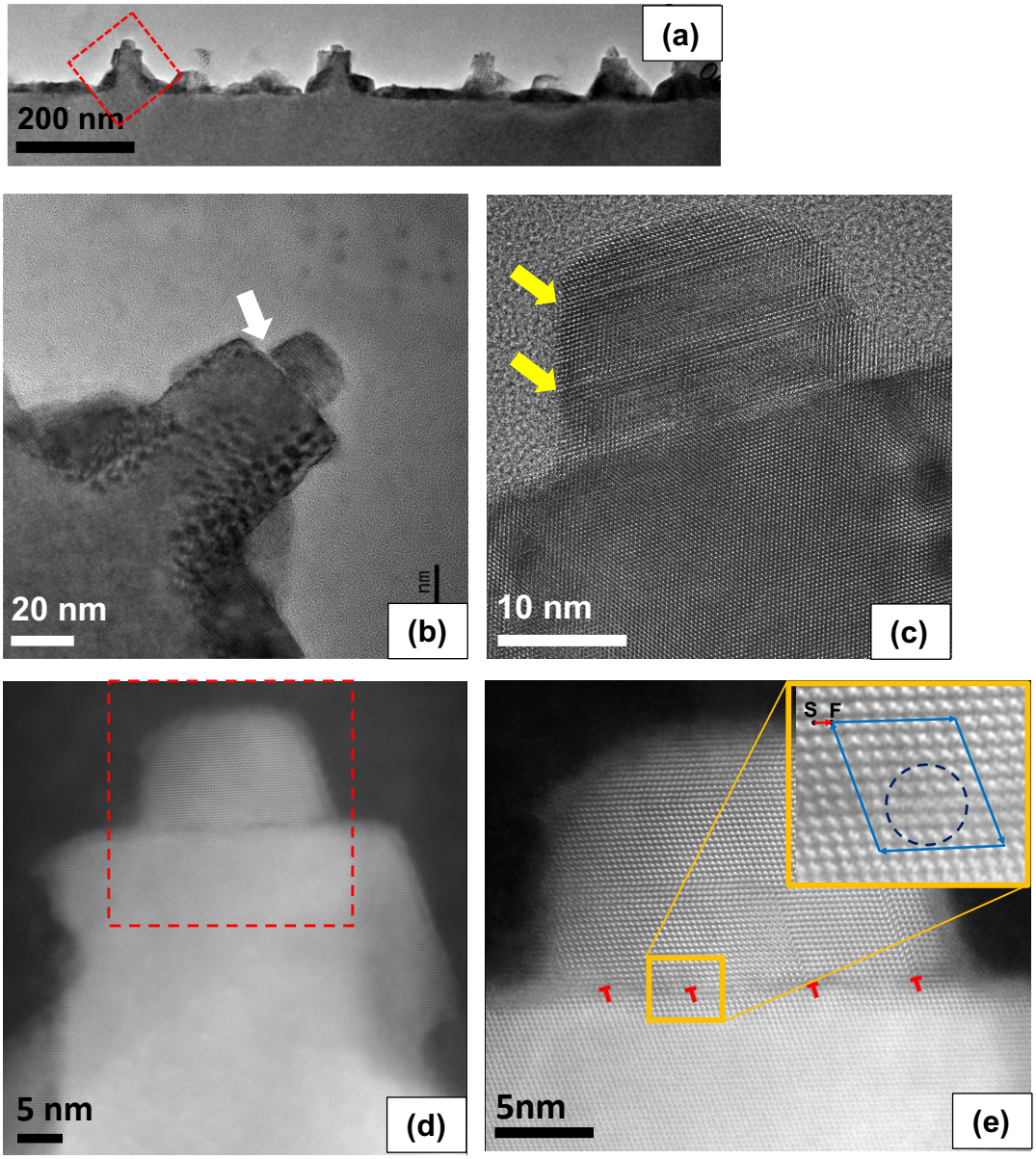

Fig. 5.7. TEM-BF image showing a row of GaAs pillars after InAs deposition carried out at T_{sub} = 150°C, t_{dep} = 15 nm and growth rate 0.011 nm/s. (b) is a HRTEM image of the nanopillar marked with a red square in (a). The InAs island sitting on top of this pillar is shown in (c). The same pillar is imaged using HAADF-STEM in (d). A higher magnification image of (d) with dislocations marked is shown in (e). The inset shows the RHFS method of Burgers vector determination.

At further reduced deposited thickness of t_{dep} = 2 nm and again otherwise the same fabrication conditions, the pillar walls are found to be devoid of InAs films as no Moiré fringes were observable, as seen in Fig. 5.9 (a). The absence of such a film compared to the SEM images (Fig. 5.4(d)) for the same growth conditions due to the very low thickness of InAs film, which completely lattice matched to the GaAs pillar. In this case, an InAs island with a height and width of 6 nm both is observed to form on a GaAs pillar with pillar top diameter of 25 nm (Fig. 5.9 (b) and (d)). HAADF-STEM image of this island in Fig. 5.9 (d) shows the absence of any misfit dislocations. Only the presence of numerous stacking faults on the (111) planes is observed.

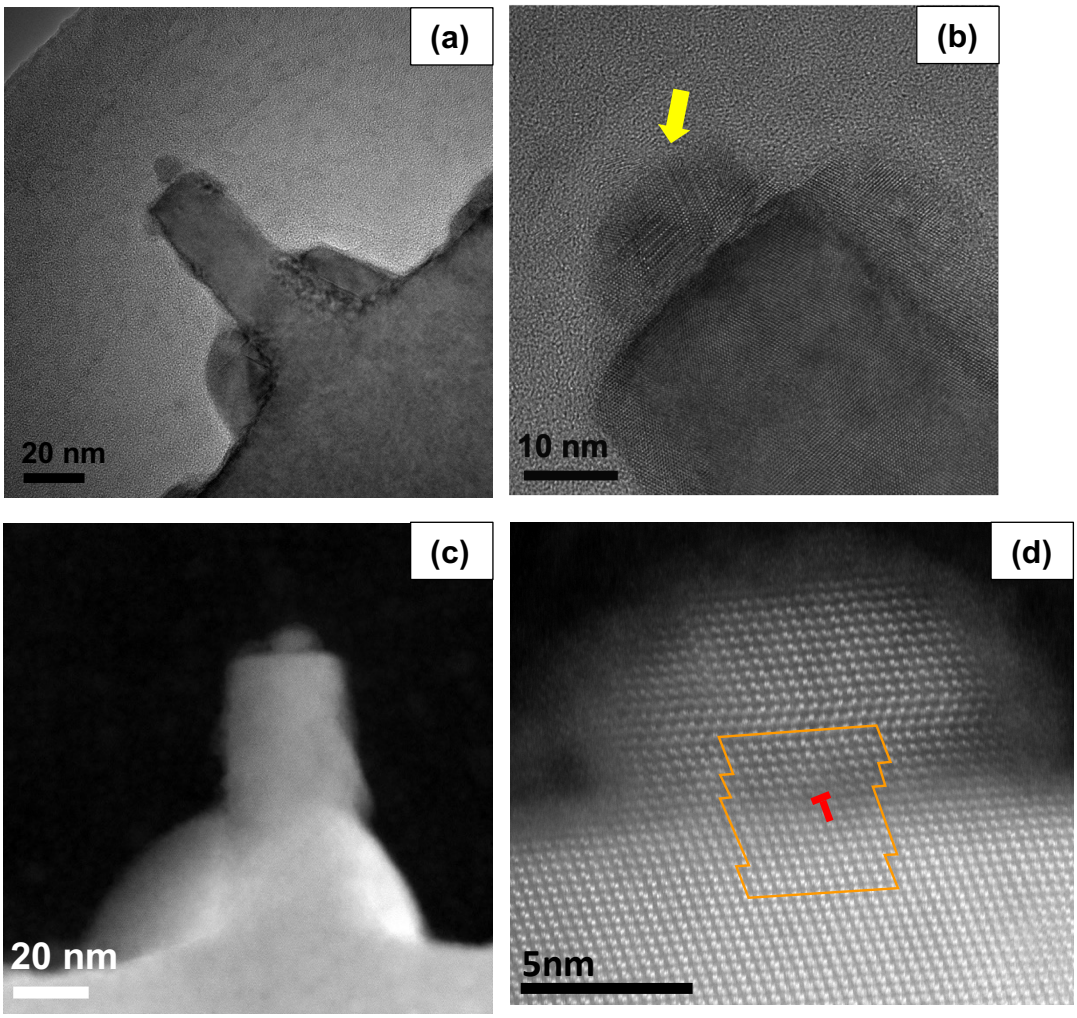

Fig. 5.8. (a) TEM-BF image of a GaAs pillar after InAs deposition carried out at T_{sub} = 150°C, growth rate 0.011 nm/s and t_{dep} = 5 nm (b), HRTEM image of the InAs island sitting on top of the GaAs nanopillar. (e) HAADF-STEM image showing the same nanopillar as in (a). (d) The InAs island sitting on top of the GaAs pillar, with the position of a misfit dislocation and Burgers circuit.

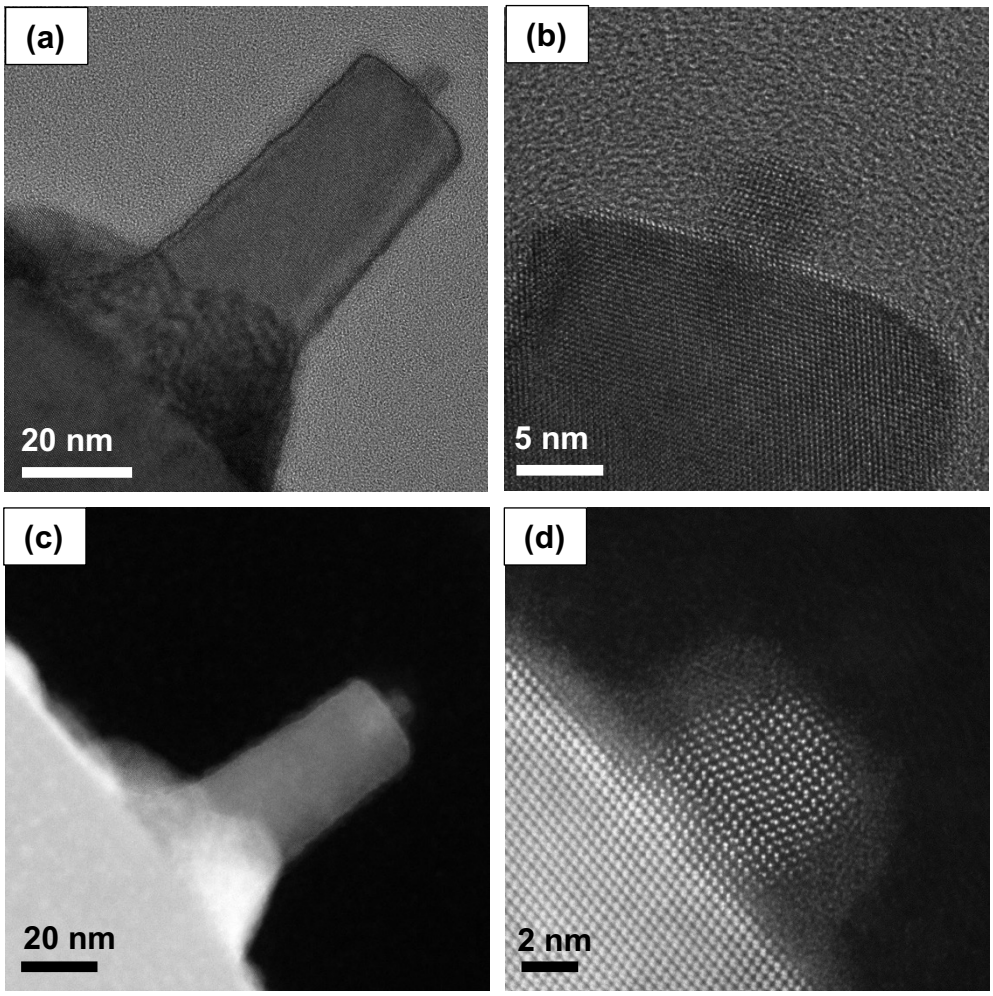

Fig. 5.9. (a) shows a TEM-BF image of the GaAs pillars after InAs deposition carried out at T_{sub} = 150°C, growth rate 0.011 nm/s and t_{dep} = 2nm (b) is a HRTEM image of the InAs island sitting on top of the GaAs nanopillar. (c) HAADF-STEM image showing the same nanopillar as in (a) (d) Higher resolution HAADF-STEM image of (b) showing that the InAs island is dislocation free.

5.5 Wetting layers on GaAs nanopillars

The same GaAs pillar with the InAs island on top as in Fig. 5.9 is presented once more in Fig. 5.10 (a) for a more detailed analysis of GaAs near surface region in the areas marked. Integrated intensity profiles across the walls of the HAADF-STEM images show weak local maxima as indicated in Figs. 5.10 (b) to (d). They correspond to the three regions of interest (ROIs) marked in Fig. 5.10 (a). As the contrast in HAADF-STEM is proportional to roughly the squared atomic number ($Z^{1.7}$), the presence of these maxima is an indication of an InAs wetting layer. Another evidence for the presence of such wetting layers also for higher deposition temperatures comes from STEM-EDS and HAADF-STEM measurements made across a GaAs pillar after InAs growth at 350°C. The composition profile in Fig. 5.10 (f), corresponding to the dashed line in Fig. 5.10 (e), clearly shows an enhancement of the In concentration at the edges of the GaAs pillar.

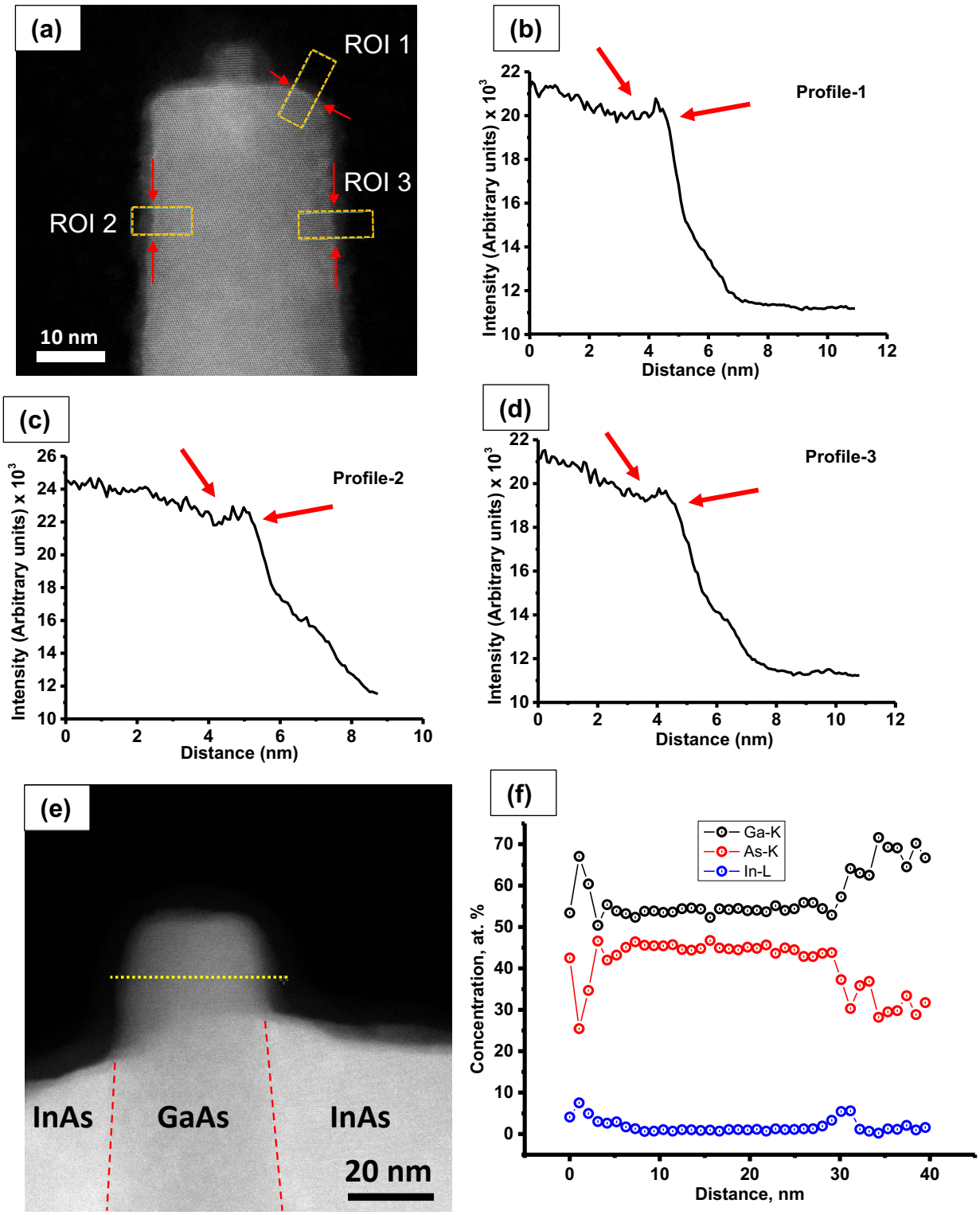

Fig. 5.10. Shows various evidence for the presence of an InAs wetting layer on GaAs pillars (a) HAADF-STEM image of a GaAs nanopillar with InAs deposited at T_{sub} = 150°C, growth rate 0.011 nm/s and t_{dep} = 2 nm. Integrated intensity values corresponding to the areas marked in (a) are plotted in (b), (c) and (d). HAADF-STEM image of GaAs nanopillar overgrown with InAs at T_{sub} = 150°C, growth rate 0.011 nm/s and t_{dep} = 15 nm (f) STEM-EDS composition profiles of Ga, In and As indicating a wetting layer rich in indium at the periphery.

5.6 Influence of growth rate

The enhancement of InAs nucleation rate to promote island formation on GaAs pillar tops was explored by increasing the In flux by a factor of 10, resulting in a growth rate of 0.11 nm/s. A substrate temperature of T_{sub} = 300°C and deposited thickness of t_{dep} = 15 nm was chosen for this results are displayed in Fig. 5.11. A noticeable morphological difference with respect to the sample grown at lower growth rate is the absence of coalescent hillocks (Fig. 5.1(c) vs 5.11 (a)). The hillocks are also found to sometimes not fully covering the pillar bases (indicated using yellow arrows). In the present case, the higher In flux promotes InAs formation on pre-existing InAs hillocks at pillar bases. Additionally, the reduced migration length stemming from the higher nucleation rate restricts new InAs islands to pre-existing hillocks [28]. This can explain the InAs morphology seen in Fig. 5.11 (a). In 5.11 (b), the substrate areas between the hillocks in NSL-DL patterned areas show a rough InAs layer (indicated using a green arrow), also resulting from the higher growth rate. Additionally, because of the enhanced nucleation rate, the major facets measure an angle of 38.9 ± 1.7° with the GaAs(111)A substrate surface, which is slightly larger than the 35° for samples grown at 0.011 nm/s. The side view SEM image of the resulting InAs growth in Fig. 5.10(c) shows the absence of InAs island formation on top of the pillars. A further investigation of InAs growth at growth rates higher than 0.11nm/s, such as the present case was not pursued further due to the larger process window resulting from both temperature and In flux as variables. InAs growth at higher fluxes leading to growth restricted to pillar bases, however, holds prospects for fabricating nano-ring structures around GaAs nanopillars.

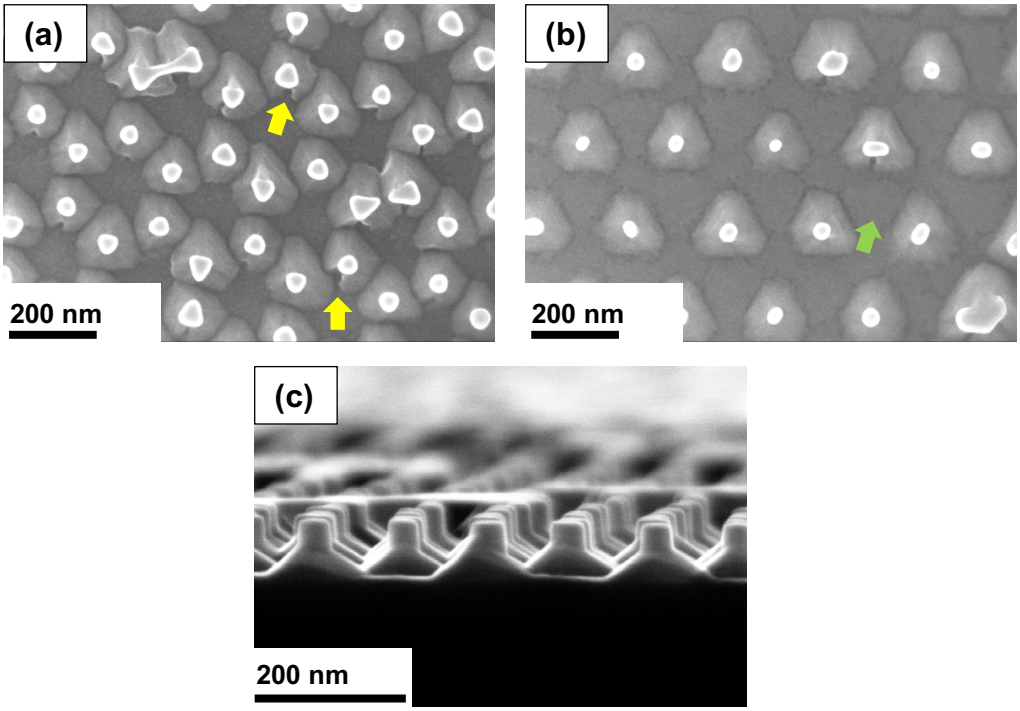

Fig. 5.11. (a) and (b) SEM top-view images of nanopillar patterned GaAs after InAs deposition at T_{sub} = 300°C, growth rate 0.11 nm/s and t_{dep} = 15 nm for ML and DL pattered areas ,respectively. (c) Cross-sectional SEM view of a ML patterned area under the same condition

5.7 Size dependent strain relaxation of InAs islands

In this section, a systematic analysis of strain accommodation by InAs island formation on GaAs(111)A nanopillar tops is discussed. The atomistic simulations performed to correlate and explain the (S)TEM based observations were performed by Dr. Thomas Riedl at AG Lindner (Nanostrukturierung-Nanoanlytik-Photonische Materialien), Paderborn University and published in [29]. The InAs island-GaAs nanopillar configurations, the (S)TEM images of which were presented in section 5.4 are chosen for this, to examine the influence of InAs island size as a function of deposited thickness.

A Burger circuit analysis following the RHFS convention [27] was performed on each of the HAADF-STEM images to determine the location and nature of misfit dislocations. The Burger analysis showed that the misfit dislocations are of the 60° edge type, with

sense vector $[0\bar{1}1]$ and Burgers vector $\vec{\boldsymbol{b}} = a/2[\bar{1}01]$. The amount of plastic strain accommodated by the dislocations was computed for each island using the formula

$$\varepsilon_{pl} = \frac{Nb_{eff}}{w_{InAs}} \ , \qquad 5.1$$

where N is the number of dislocations, b_{eff} is the magnitude of the effective Burgers vector and w_{InAs} is the width of the InAs island at the heterointerface [30]. Here, $b_{eff} = \sqrt{6}/4\, a$ for the edge component of $\vec{\boldsymbol{b}}$ [31]. Strain mapping of the InAs islands on pillars was performed using GPA (discussed in section 3.4.3) [32] and peak-pairs analysis (PPA) to extract the strain maps. In this technique, the intensity maxima of Bragg filtered high resolution TEM or STEM images detected by comparing each pixel with eight nearest neighbors. Such maxima are directly correlated to atomic column positions. A strain free region of the image is selected to determine two non-collinear basis vectors that define the reference lattice. The deviations from the peak positions of the strained with respect to the basis vectors are used to calculate the displacement fields at atomic positions. Subsequently, the strain fields can be derived from the displacement fields as described in section 3.3.4. While GPA works in the Fourier space, the PPA is based on real space information [33,34].

The ε_{xx} or in-plane strain component was mapped in all cases. GPA strain maps, with lattice variations along the $[\bar{2}11]$, denoted as $\Delta d/d_{GaAs} = (d - d_{GaAs})/d_{GaAs}$, were extracted from the GPA maps. An example is shown in Fig. 5.12(b). The $(\bar{2}11)$ planes being chosen here are normal to the $[\bar{2}11]$ in-plane strain direction [29].

The resulting strain analysis data was correlated to molecular statics calculations for the deposited InAs thicknesses of 5 and 2 nm. Self-written scripts for the DigitalMicrograph software [35] were used to generate atomistic models of InAs islands atop GaAs nanopillars. A cylindrical shape was assumed for the InAs islands and GaAs pillars due to the expected lower stability of triangular islands at small sizes. The model is shown in Fig. 5.12 (a) and (b) in coherent and dislocated states, respectively. 60° edge dislocations were created by removing an inclined InAs $(\bar{1}11)$ half plane intersecting the nanopillar axis and placing it on the top (111) surface of the island, as seen in Fig. 5.12 (c). The gap thus formed in InAs is closed by relaxing this lattice using a molecular static simulation as shown in Fig. 5.12(c) and (d). A thin section of the dislocated InAs island on GaAs pillar is shown in Fig. 5.11 (d). A shuffle-set type of dislocation which has a Ga terminated

core was assumed due its better reproduction with the potential used for the simulations. The iterative relaxation of the structures was done using the conjugate gradient approach of the LAMMPS software [36] Tersoff potential [37] in the parameterization of Hammerschmidt [38,39] was used which considers the interaction energies of atom triples and thus includes the effects of atomic coordination on bond strength. The parametrization used yields lattice constants a_{GaAs} = 5.653 Å and a_{InAs} = 6.050 Å for GaAs and InAs, respectively, and the corresponding misfit is $f \approx 6.8\%$, which is slightly lower than the experimentally reported misfit value of $f \approx 6.9\%$ calculated using bulk lattice parameters of a_{GaAs} = 5.653 Å and a_{InAs} = 6.058 Å [40,41]. A relative energy difference of $< 10^{-9}$ was chosen as the stopping criterion between successive steps. Self-written scripts for DigitalMicrograph are used to extract the atomic coordinates of the relaxed structures. The InAs wetting layer found on pillar tops was neglected during the calculations.

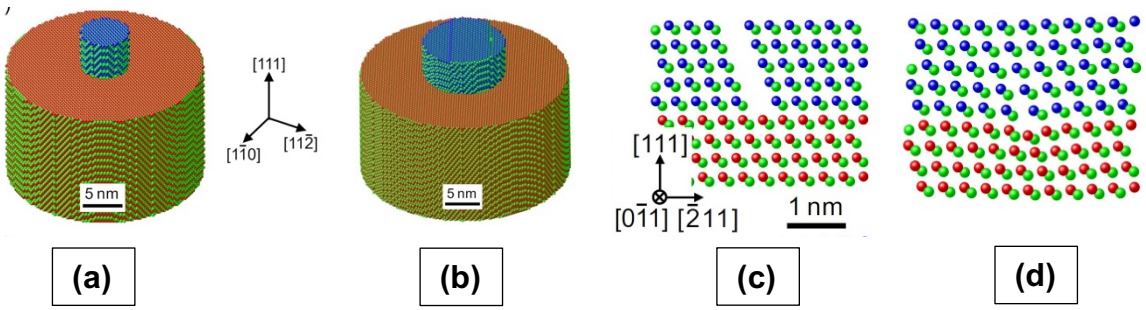

Fig. 5.12. Atomic representation of InAs QDs on GaAs(111)A nanopillars. (a) and (b) represent the coherent and dislocated states, respectively. (c) illustrates the atomic columns at the heterointerface with an atomic layer removed along the InAs ($\bar{1}$11) half plane and (d) with the gap replaced by a 60° misfit-dislocation after relaxation. Ga, In and As atoms correspond to the red, blue and green beads, respectively [29]

As shown in Fig. 5.13(a) the 24 nm wide and 16 nm high InAs island resulting from 15 nm of deposited thickness sitting on a 40 nm diameter GaAs pillar has four 60° dislocations which accommodate ≈ 90% of lattice misfit. This indicates that 10% of remaining lattice strain is accommodated elastically.

A corresponding map of the GPA map of the lattice strain is shown in image 5.13 (b). It indicates that the GaAs and InAs lattices are completely relaxed. Lattice strain profile across the interface along the [111] direction A transition zone of 0.4 nm at the heterointerface is observed.

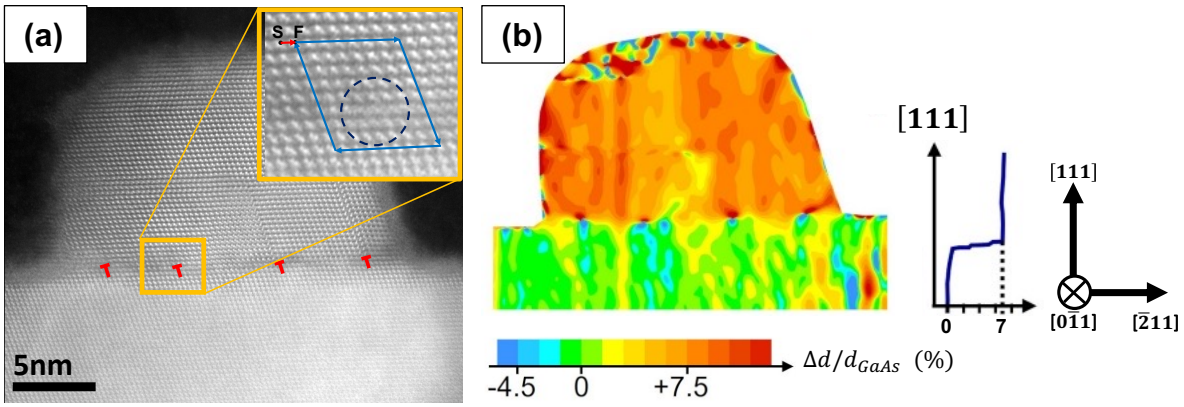

Fig. 5.13. (a) HAADF-STEM image of a 24 nm wide, 16 nm high InAs QD sitting on top of a 40 nm diameter GaAs(111)A nanopillar, with positions of misfit-dislocations marked. The inset in (a) shows the Burgers circuit analysis of the region marked in (a) indicating the presence of a 60° misfit-dislocation. (b) is a GPA derived map of the strain $\Delta d/d_{GaAs}$ of (a) along with the strain profile in [111] direction corresponding to the region marked in (a). The growth conditions employed were T_{sub} = 150°C, growth rate 0.11 nm/s and t_{dep} = 15 nm.

The case of 5 nm nominally deposited InAs on a 30 nm diameter pillar is investigated in Fig. 5.14. Here, an InAs island of 11 nm width and 7 nm height is observed in Fig. 5.14 (a). One 60° dislocation accommodates ≈ 56% of lattice misfit in the crystalline part, neglecting the surrounding amorphous region (Fig. 5.14 (a)). (Ga,In)/As HAADF intensity ratios of the [0$\bar{1}$1] atomic columns were plotted along the [111] growth direction to exactly determine the location of the interface and the relative distance of the misfit dislocation core. The resulting atomic number sensitive intensity profile is shown in Fig. 5.14 (b). It indicates that the dislocation core is located exactly at the heterointerface. A reduction in intensity observable on the GaAs side ≈ 2 nm away from the interface could be due to an As enrichment arising from the decomposition of AsH_3 during the HF cleaning step [36,37] and atomic hydrogen cleaning or due to the native oxide layer. Fig. 5.14 (d) shows a map of the local strain in [$\bar{2}$11] direction, derived by GPA from the HAADF-STEM image in Fig. 5.14(a). The misfit dislocation at the heterointerface is clearly visible by compressive/tensile strain dipole at the center of the interface. For comparison, the strain distribution obtained by a molecular statics

simulation if Fig. 5.14(c) with a 60° misfit dislocation in the middle of the InAs/GaAs interface has a very similar shape and magnitude.

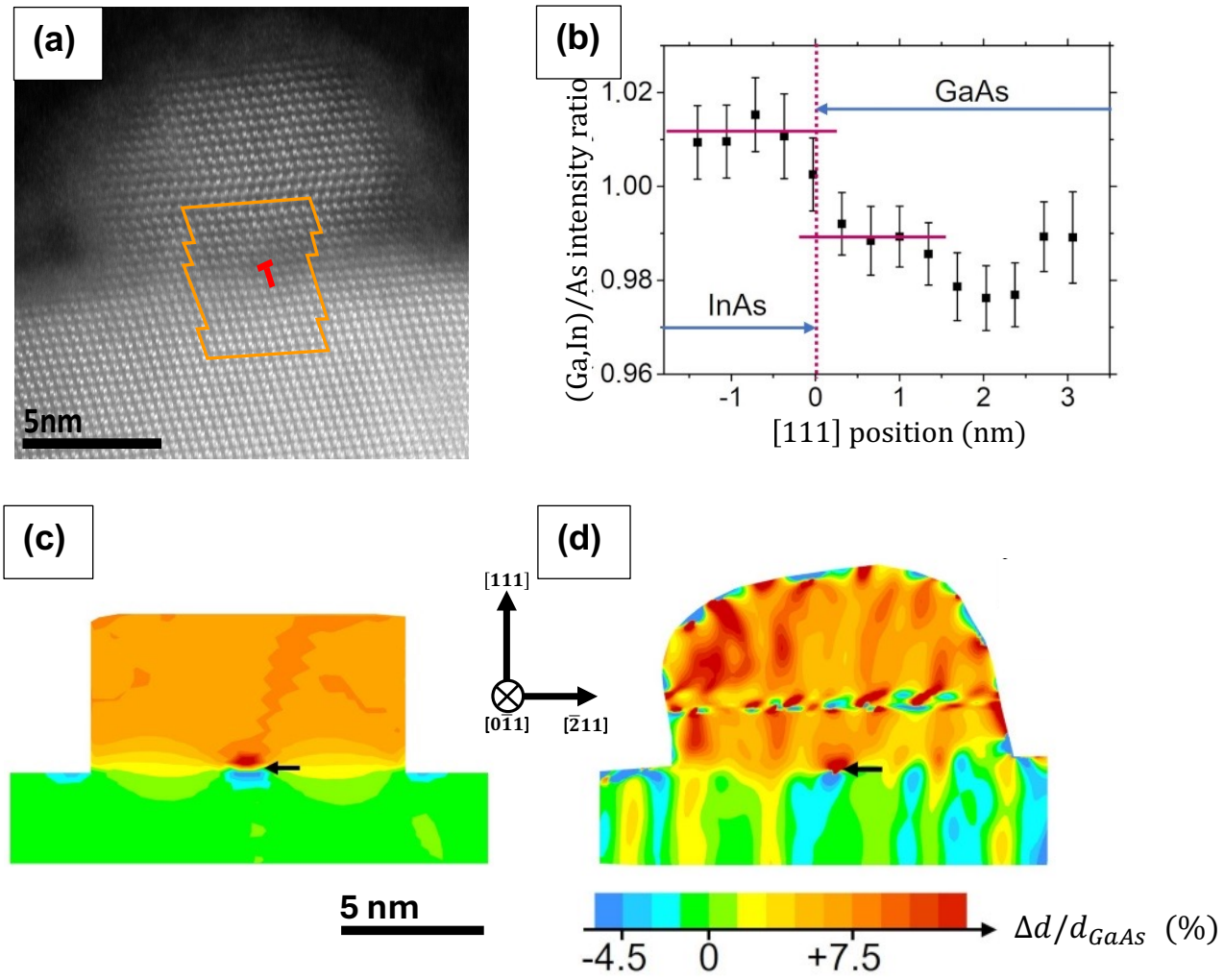

Fig.5.14. a) HAADF-STEM image of a 11 nm wide, 7 nm high InAs QD sitting on top of a 30 nm diameter GaAs(111)A nanopillar with one misfit dislocation at the marked position. (b) and (c) are $\Delta d/d_{GaAs}$ strain maps of (a) obtained by GPA of the image (a) and by molecular statics simulations, respectively. The arrows indicate the position of a 60° MD. (d) Average (In,Ga)/As atomic column HAADF intensities along the [111] growth direction. The growth conditions employed were T_{sub} = 150°C, growth rate 0.11 nm/s and t_{dep} = 5 nm.

An InAs island with a width and height of 6 nm on a GaAs pillar with a diameter of 25 nm is observed for the 2 nm thick deposit at T_{sub} = 150°C (Fig. 5.15 (a). This island is found to be dislocation free. However, it contains many stacking faults as seen in Fig. 5.15 (a). Due to this reason, atomic column positions were extracted by fitting 2D Gaussians to atomic

intensity maxima, and PPA was then performed to create the lattice strain map in Fig. 5.15 (b). A molecular statistics simulation of this configuration is displayed in Fig. 5.15(c) and shows disregarding the absence of noise good agreement to the experimental result observed between the experimental and simulated lattice strain profiles along the [111] direction in Fig. 5.15 (d). The 20-80% interfacial width from the experimental and simulated profiles amounted to 1.2 and 1.1 nm respectively. The large data scatter in the strain profile of within the InAs island (Fig. 5.15 (d)) is a result of the thick oxide layer formed during FIB milling of the specimen.

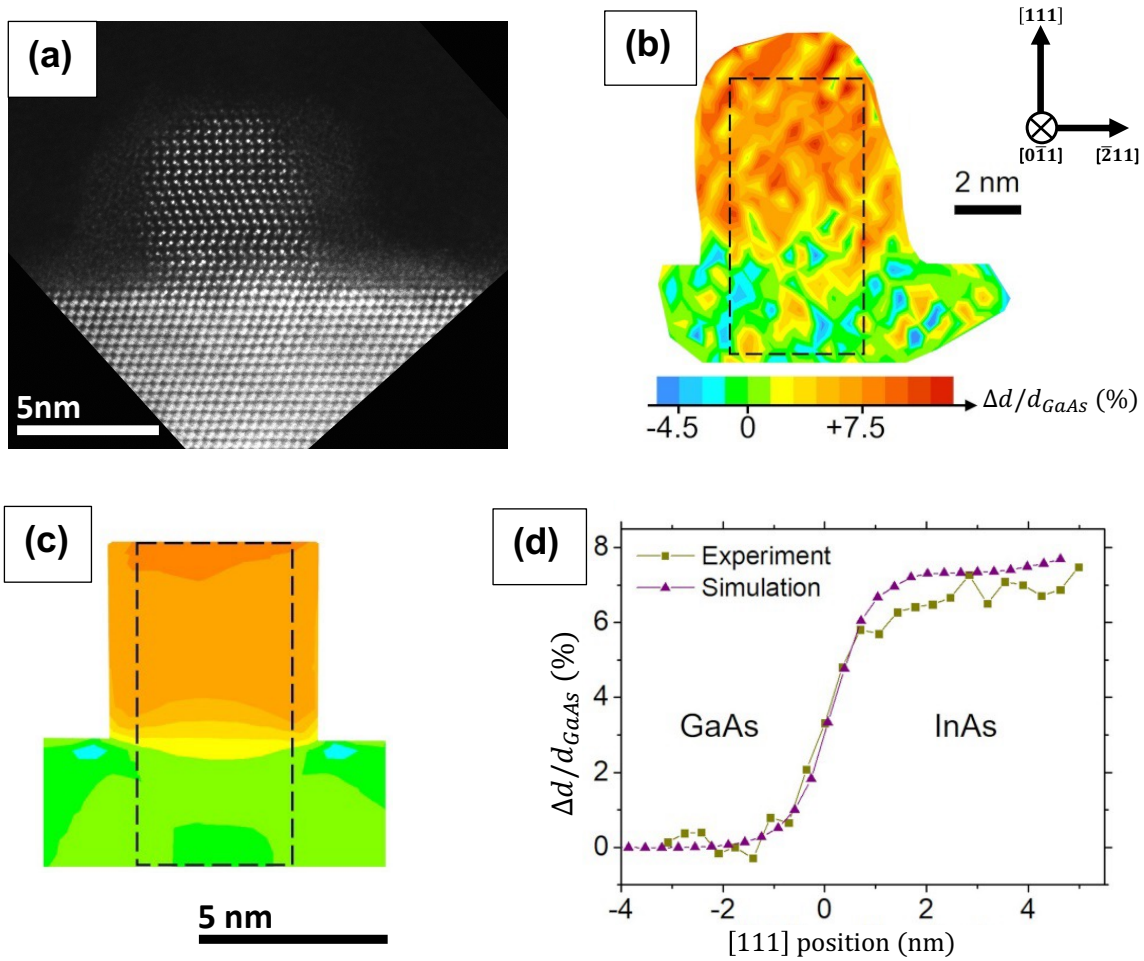

Fig. 5.15. a) HAADF-STEM image of a 6 nm wide and 6 nm high coherently strained InAs QD on top of a 25 nm diameter GaAs(111)A nanopillar . (b) and (c) are $\Delta d/d_{GaAs}$ strain maps (a) obtained by PPA from the image in (a) and by molecular statics simulations respectively. (d) compares $\Delta d/d_{GaAs}$ profiles along the [111] growth directions averaged across the regions marked in (b) and (c). The growth conditions employed were T_{sub} = 150°C, growth rate 0.11 nm/s and t_{dep} = 2 nm.

The impact of finite substrate diameters on strain partitioning is further examined by comparing the simulated strain maps of the 6 nm wide and 6 nm high InAs island on GaAs pillars with the same diameter 6 nm. 25 and larger 42 nm). Example are shown in Fig. 5.16(a) and (b). Extracted line profiles in [111] direction averaged in the marked regions are plotted in Fig. 5.16(c). Obviously, the strain profiles for the two cases where the pillar diameter is much larger than the diameter of the quantum dot are identical. However, the dilatational strain on the GaAs side and the compressive strain on the InAs side are significantly larger when the quantum dot and the nanopillar have the same diameters. These are clear indications of strain partitioning. The observed narrow strain transition zone is a clear proof for efficient elastic strain relaxation at the interface. Additionally, the transition from a dislocation free state to dislocated state happens for InAs islands in the present case between 6 to 11 nm. This observation is in line with the predictions made by Ye and Yu [44] for critical diameters of NW growth on bulk substrates, which is 9 nm for 7% lattice misfit.

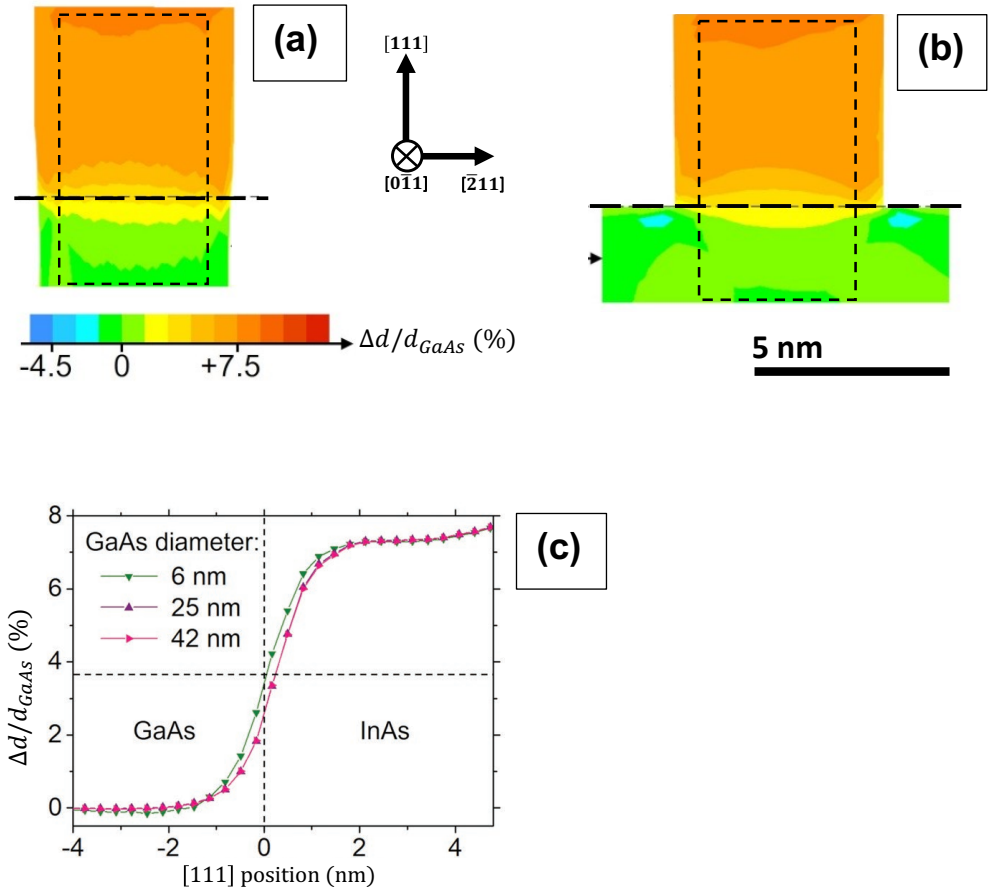

Fig. 5.16. $\Delta d/d_{GaAs}$ maps obtained from molecular statics simulations of a 6 nm wide and high InAs island sitting on (a) a 6nm and (b) a 42 nm diameter GaAs(111)A pillar top. (c) Comparison of the simulated $\Delta d/d_{GaAs}$strain profiles of (a) and (b and a pillar of 25 nm diameter. Averaging regions corresponding to the plots in (c) are marked in (a) and (b).

5.8 Position dependent strain relaxation of InAs islands on GaAs pillars

Yet another consequence of strain energy and minimization is visible in the location of InAs islands on the GaAs pillar top surfaces. InAs islands are observed to form on the pillar tops at locations either aligned with the pillar-axis or form at the edge as observed in the insets of Fig. 5.17(a). TEM images of the nanopillars with InAs islands on top, fabricated under the same conditions are seen in Figs. 5.17(b,c). The energetic basis favoring the occurrence of either of these configurations were examined in collaboration with Dr. Thomas Riedl, more details regarding this work can be found in [45].

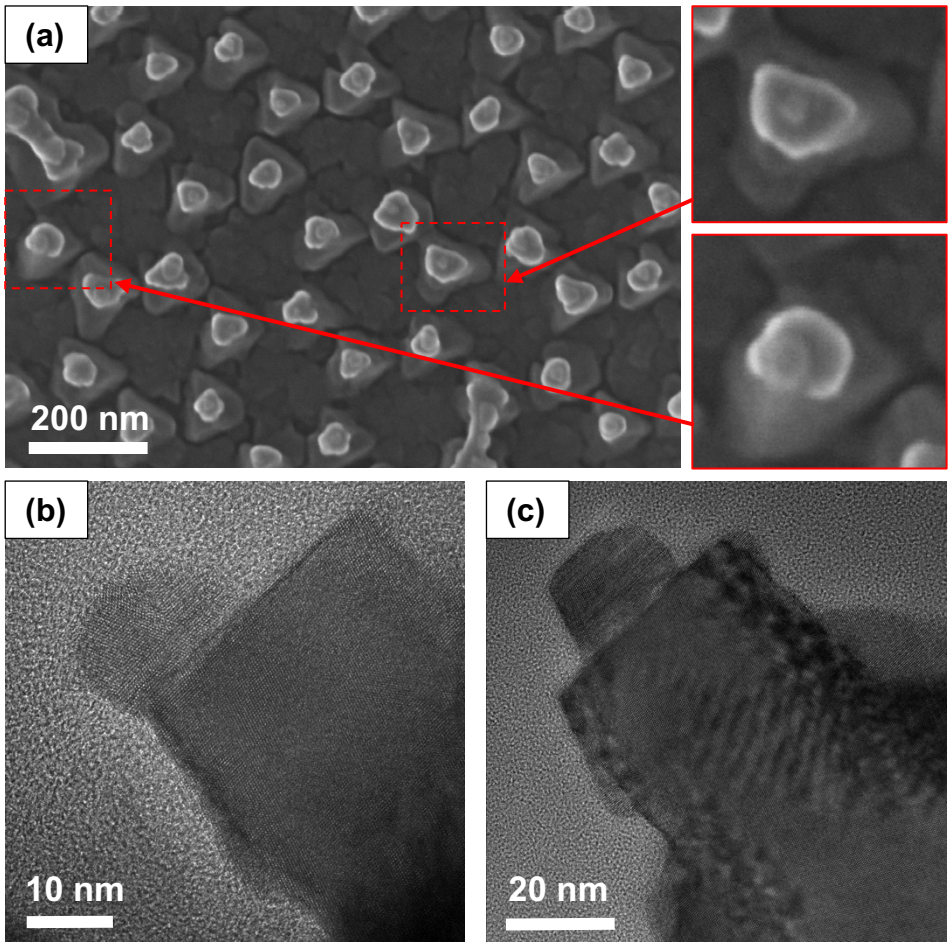

Fig. 5.17. SEM top-view images of a nanopillar patterned GaAs(111)A substrate overgrown with InAs despoted at T_{sub} = 300°C, growth rate 0.11 nm/s and t_{dep} = 15 nm is shown in (a). The insets show InAs islands on two GaAs pillars, one aligned with nanopillar axis and other towards the edge. TEM images showing examples of InAs islands formed the on pillar tops at the pillar edges and along the pillar axis and are shown in (b) and (c), respectively.

The simulations were performed using the schemes discussed earlier. In addition to this, strain energy estimates were made using the following material constants, Young's moduli 85.5 and 51.4 GPa and Poisson ratios of 0.31 and 0.35 for GaAs [46] and InAs [47], respectively. InAs islands with triangular-prismatic islands with $\{11\bar{2}\}$ sidewall facets were considered, as seen in Fig. 5.18(a) because they approximately replicate the experimentally observed InAs islands.

First, the equilibrium configurations of centered InAs islands with different aspect ratios were considered. The in-circle radius of these islands, i.e. the radius of the largest circles filling the triangular face (Fig. 5.18(a)) was used to represent the aspect ratio. The lowest energy states of the islands were determined by varying their aspect ratios (configurations A and B in Fig. 5.18(b) and (c)), maintaining the volume constant. Two lowest energy reference states characterized by flat, step-free GaAs(111)A top surfaces but differing in aspect ratios were identified. Islands with incircle radii of 4.8 nm and 6.2 nm and with heights of 8 and 5 monolayers were determined as reference states 1 and 2, respectively, and are indicated by arrows in Fig. 5.18(d), showing the enhancement of the total energy upon a change of the InAs incircle radius. The atomic configurations and $\varepsilon_{11\bar{2}}$ strian maps for the two different states A and B are displayed in Fig. 5.18 (b) and (c), where the centre of InAs islands sit on the axis of a 25 nm diameter pillar. In state B, the edge of the triangular InAs islands just touch the circumference of the GaAs islands. As one can see in Fig. 5.18(e), a reduction of the InAs incircle radius would lead to an increase of the total number of broken bonds at the GaAs and InAs top surface while the averaged $\varepsilon_{11\bar{2}}$ strain magnitude (distribution plotted in Fig. 5.18(b) would decrease. In other words, a high aspect ratio entails the penalty of larger number of broken bonds of surface atoms whereas at lower aspect ratios, the in-plane lattice strain dominates.

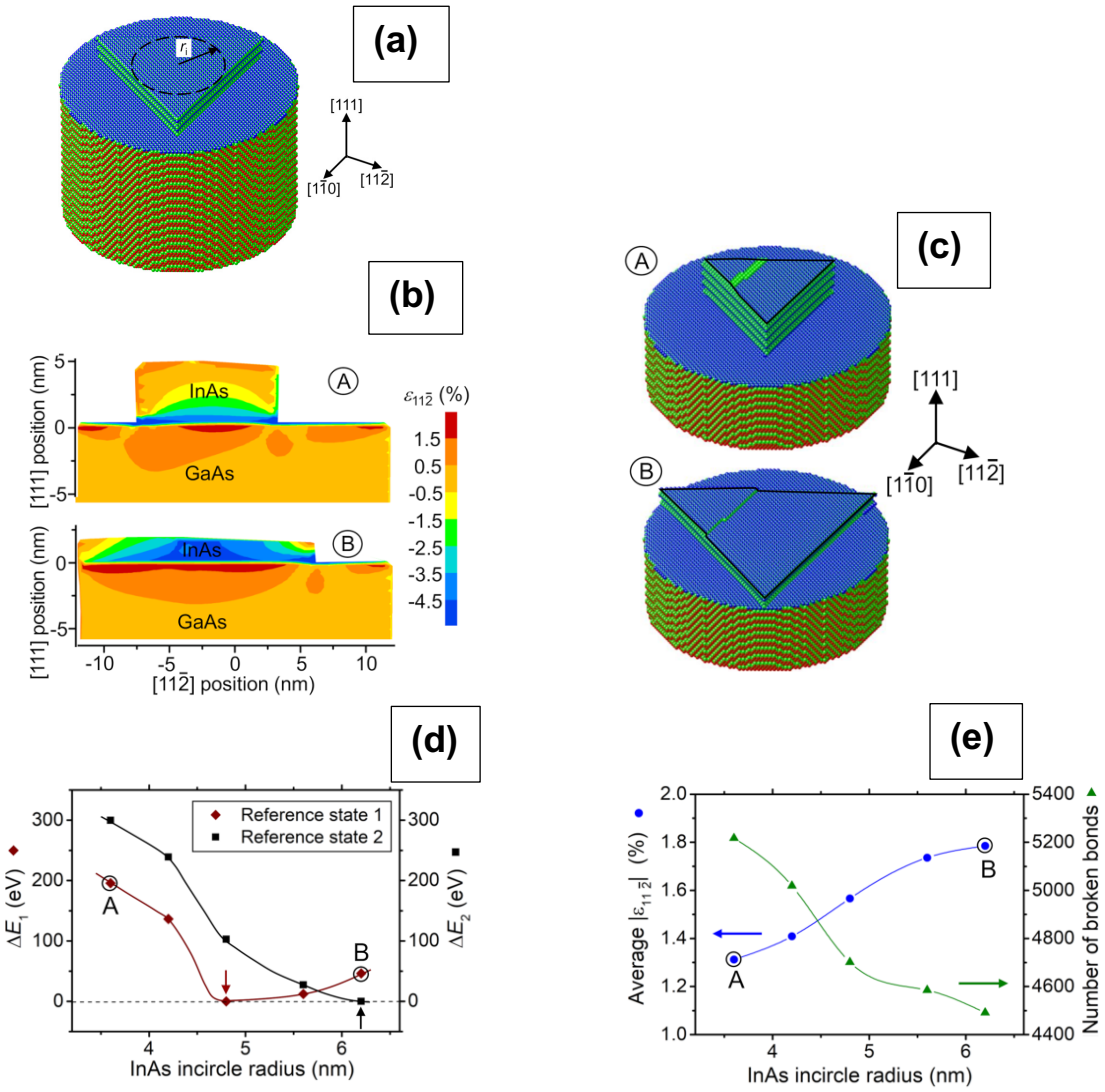

Fig. 5.18. (a) Atomistic model of an InAs island sitting on top of a 25 nm diameter GaAs pillar with a one ML coverage of an InAs wetting layer. The Ga atoms are coloured red, In blue and As green. Strain maps of $\varepsilon_{11\bar{2}}$ for island dimensions A and B shown in (c) are plotted in (b). (d) Total energy deviation from the energy states marked by arrows is .Average value of strain and the number of broken bonds at the InAs surfaces and the GaAs top surface for different InAs aspect ratios is shown in (e)

Further, the position of an InAs island with an incircle radius of 4.8 nm and aspect ratio of 0.27 was varied along the [11$\bar{2}$] direction on the GaAs pillar top face. The total energy decreases upon displacing the island from the center (position C) towards the edges due to a lowering of strain energy, as can be inferred from Fig. 5.19 (a). Positions marked A and B correspond to these energy minima. Fig. 5.19(b) shows that, if the islands are displaced further, and made to hang over the edges, the energy rises due to the broken bonds. Fig. 5.19(c) compares the integrated strain energy of GaAs and InAs for the

islands at positions A, B and C. The lower strain energy observed at positions A and B originates from elastic strain relaxation at pillar walls, as discernable from the strain maps. Amongst these two configurations, the position B has a slightly lower energy. At B, the proximity of the InAs island to the edge promotes a more rapid strain decay from the heterointerface, observable in Fig. 5.19(d). Hence, it can be concluded that InAs island formation at pillar edges energetically favored over centered islands.

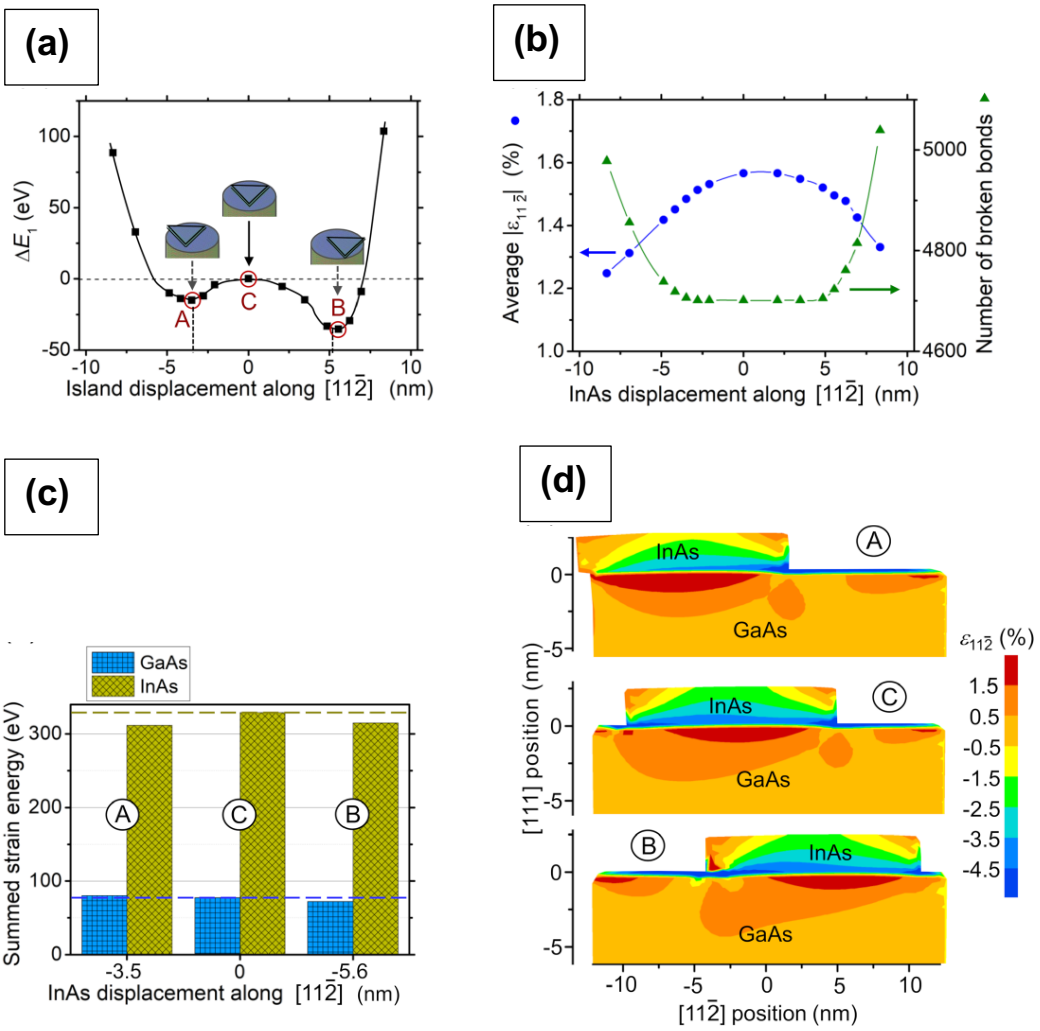

Fig. 5.19. (a) Deviation of the total energy from the reference state 1 for various InAs island positions. The variation of average strain $\varepsilon_{11\bar{2}}$ and number of broken bonds as a function of InAs island position is shown in (b). (c) shows the $\varepsilon_{11\bar{2}}$ total strain energy in GaAs and for InAs islands at positions A, B and C. (d) Map showing strain distribution within InAs and GaAs for positions A, B and C, viewed in cross section.

5.9 Summary

1.) MBE deposition of InAs was carried out on nanopillar patterned GaAs(111)A with pillars of 25 to 30 nm diameter, 72 to 75 nm height and inter-pillar distances of either 129 or 228 nm at substrate temperatures in the range of 150 to 410°C and at growth rates 0.011 and 0.11 nm/s and with a deposited thicknesses of 2, 5 and 15 nm.

2.) Microstructural observations reveal that InAs growth takes place preferentially at the GaAs pillar bases for all probed conditions due to ease of incorporation at the kink positions available there. As a result, GaAs pillar bases get embedded by epitaxially grown InAs pyramids dominated by {111} type facets.

3.) InAs island formation on top of the GaAs pillars is observed only when substrate temperatures are lowered considerably below usual growth temperatures for flat, non-patterned substrates, i.e. to 150°C leading to a reduced adatom migration length.

4.) (S)TEM investigations reveal that the contribution of plastic strain relaxation scales directly with InAs island size. Dislocation free InAs islands with a width and a height of 6 nm are formed atop GaAs(111)A pillars when the deposited thickness is reduced to 2 nm nominally. For larger thicknesses of 5 or 15 nm, 60° misfit dislocations with Burgers vector of $\vec{\boldsymbol{b}} = a/2[\bar{1}01]$ are observed. Pillars overgrown with InAs at T_{sub} = 150°C are covered with a coherent InAs wetting layer.

5.) Molecular statics simulations reveal the efficacy of surface strain relaxation of small dislocation free InAs islands. The calculations also confirm that the InAs pillar tops behave similar to a bulk substrate and hence rule out the possibility of substrate compliance.

6.) InAs islands are observed to preferably occupy off-pillar axis positions. Molecular static simulations confirm that positions near the pillar edges provide energetically favorable growth conditions where the total energy contributions of strain and broken bonds at the surface are minimized, based on based on a balance between strain energy and surface energy.

References

1) T. Uehara, T. Iwai, I. Yoshiba, Y. Horikoshi, "Area-Selective Epitaxial Growth of GaAs on GaAs(111)A Substrates by Migration-Enhanced Epitaxy" , Jpn. J. Appl. Phys. 46 (2007) 496.

2) H. Brune, in: K. Wandelt (Eds.), Surface and Interface Science, vol. 4, Wiley-Verlag, (2014).

3) C.D. Yerino, B. Liang, D.L. Hu aker, P.J. Simmonds, M.L. Lee, "Review Article: Molecular beam epitaxy of lattice-matched InAlAs and InGaAs layers on InP (111)A, (111)B, and (110)", J. Vac. Sci. Technol. B 35 (2017) 010801.

4) E. Colas, G.C. Nihous, D.M. Hwang, "Nonplanar step and terrace configurated surfaces as templates for crystal growth dynamics studies", J. Vac. Sci. Technol. A 10 (1992) 691.

5) J.C. Hulteen, D.A. Treichel, M.T. Smith, M.L. Duval, T.R. Jensen and R.P. Van Duyne, "Nanosphere Lithography: Size-Tunable Silver Nanoparticle and Surface Cluster Arrays", J. Phys. Chem. B, 103 (1999) 3854 .

6) D.A. Porter and K.E. Easterling, " Phase transformations in metals and alloys", 3rd Edition, CRC press (2009) .

7) N. Moll, A. Kley, E. Pehlke and M. Scheffler, "GaAs equilibrium crystal shape from first principles", Phys. Rev. B, 54 (1996) 884.

8) Y. Yao, T. Zhou, D. Huang, S. Mao and H. Zhang, "Thermophysical properties of liquid gallium: A review", Ann. Nucl. Ehergy, 234 (2026) 112322.

9) Thermal properties of GaAs, Ioffe Institute: http://www.ioffe.ru/SVA/NSM/semicond/GaAs/thermal.html

10) E.S. Tok, T.S. Jones, J.H. Neave, J. Zhang and B.A. Joyce, "Is the arsenic incorporation kinetics important when growing GaAs(001), (110), and (111)A films?", Appl. Phys. Lett., 71 (1997) 3278.

11) F. Patella, F. Arciprete, M. Fanfoni, A. Balzarotti and E. Pladidi ,"Apparent critical thickness versus temperature for InAs quantum dot growth on GaAs(001)", Appl. Phys. Lett., 88 (2006) 161903.

12) T.J. Krzyzewski, P.B. Joyce, G.R. Bell and T.S. Jones, "Wetting layer evolution in InAs/GaAs(001) heteroepitaxy: effects of surface reconstruction and strain", Surf. Sci., 517 (2002) 8.

13) P.N. Fawcett, B.A. Joyce, X. Zhang and D.W.Phasley, "Interface structure of InAs grown on GaAs(001) surfaces by molecular beam epitaxy", J. Cryst. Growth, 116 (1992) 81.

14) A. Ohtake, M. Ozeki and J. Nakamura, "Strain Relaxation in InAs GaAs 111 A Heteroepitaxy", Phys. Rev. Lett., , 84 (2000) 4665.

15) L.A. Zepeda-Ruiz, B.Z. Nosho, R.I. Pelzel, W.H. Weinberg and D. Maroudar, "Kinetics of strain relaxation through misfit dislocation formation in InAs/GaAs(111)A heteroepitaxy", Surf. Sci., 411 (1999) L911.

16) H. Yamaguchi, M.R. Fahy and B.A. Joyce, "Inhibitions of three dimensional island formation in InAs films grown on GaAs (111)A surface by molecular beam epitaxy", Appl. Phys. Lett., 69 (1996) 776.

17) J.-S. Lee, K. Kazuhiro, N. Shigeru, Y. Akimasa, M. Yunosuke and T. Kuniaki, "The initial growth stage of the in as quantum well structures on variously oriented gaas substrates", Jpn. J. Appl. Phys., 32 (1993) 4889.

18) J. Lee, K. Kudo, K. Tanaka, Y. Makita, and A. Yamada,"Formation of InAs microstructures on variously oriented GaAs substrates", J. Cryst. Growth., 115 (1991) 164.

19) M. Jo, T. Mano, M. Abbarchi, T. Kuroda, Y. Sakuma and K. Sakoda,"Self-Limiting Growth of Hexagonal and Triangular Quantum Dots on (111)A", Cryst. Growth. Des., 12 (2012) 1411.

20) J. Lee, K. Kudo, S. Kuniyoshi, K. Tanaka, Y. Makita and A. Yamada, "Formation of InAs microstructures on variously oriented GaAs substrates", J. Cryst. Growth, 115 (1991) 164.

21) M.H. Xie, S.M. Seutter, W.K. Zhu, L.X. Zheng, H. Wu and S.Y. Tong, "What causes step bunching—negative Ehrlich–Schwoebel barrier versus positive incorporation barrier", Surf. Sci., 515 (2002) L459.

22) T. Michley, M. Hohage, M. Bott and G. Comsa, "Inversion of growth speed anisotropy in two dimensions", Phys. Rev. Lett., 70 (1993) 3943.

23) L. Esposito, S. Bietti, A. Fedorov, R. Nötzel and S. Sanguinetti, "Ehrlich-Schwöbel barrier effect on the growth dynamics of GaAs(111)A surfaces", Phys. Rev. Mater., 1 (2017) 024602.

24) J. Tersoff, "Step- bunching instability of vicinal surfaces under stress", Phys. Rev. Lett., 75 (1995) 2730.

25) T. Marschner, S. Lutgen, M. Volk, W. Stolz, E.O. Göbel, N.Y. Jin-Phillipp and F. Phillipp, "Strain-induced changes in epitaxial layer morphology of highly-strained III/V-semiconductor heterostructures", 12 (1994) 183.

26) T. Kikkawa, K. Makiyama, H. Ochimizu, K. Kasai and J. Komeno, "Effect of strained InGaAs step bunching on mobility and device performance in n-InGaP/InGaAs/GaAs pseudomorphic heterostructures grown by metalorganic vapor phase epitaxy", J. Crsyt. Growth, 145 (1994) 799.

27) Y.A.R. Dasilva, R. Kozak, R. Erni and M.D. Rossell,"Structural defects in cubic semiconductors characterized by aberration-corrected scanning transmission electron microscopy", Ultramicroscopy, 176 (2017) 11.

28) N.A.K. Kaufmann, "Investigation indium-rich InGaN and kinetic growth regime of GaN", Ph.D. Thesis, EPFL (2013).

29) T. Riedl, V.S. Kunnathully, A. Trapp, T. Langer, D. Reuter and J.K.N. Lindner, "Size-Dependent Strain Relaxation in InAs Quantum Dot on Top of GaAs(111)A Nanopillars", Adv. Mater. Interfaces, 9 (2022) 2102159.

30) M. Lentzen, D. Gerthsen, A. Förster and K. Urban, "Growth mode and strain relaxation during the initial stage of $In_xGa_{1-x}As$ growth on GaAs(001)", Appl. Phys. Lett., 60 (1992) 74.

31) D. Hull and D.J. Bacon, "Introduction to Dislocations", Butterworth-Heinemann (2011).

32) M. J. Hÿtch, E. Snoeck and R. Kilaas, Ultramicroscopy," Quantitative measurement of displacement and strain fields from HREM micrographs", Ultramicroscopy, 74 (1998) 131.

33) P. Galindo, J. Pizzaro, S. Molina and K. Ishizuka, " High resolution peak measurement and strain mapping using peak pairs analysis", Microsc. Microanal., March (2009) 24.

34) P L Galindo, S Kret, AM Sánchez, J-Y Laval, A Yáñez, J Pizarro, E Guerrero, T Ben and S .Molina, "The Peak Pairs algorithm for strain mapping from HRTEM images", Ultramicroscopy 107 (2007) 1186.

35) Gatan Inc., Gatan Microscopy Suite Software, www.gatan.com/products/tem-analysis/gatan-microscopy-suite-software (accessed: September 2021).

36) J. Plimpton, "Fast Parallel Algorithms for Short-Range Molecular Dynamics", J. Compt. Phys., 171 (1995) 1.

37) J. Tersoff, "New empirical approach for the structure and energy of covalent systems", Phys. Rev. B, 37 (1988) 6991.

38) T. Hammerschmidt, P. Kratzer and M. Scheffler, "Analytic many-body potential for InAs/GaAs surfaces and nanostructures: formation energy of InAs quantum dots", 77 (2008) 235303.

39) T. Hammerschmidt, P. Kratzer and M. Scheffler, "Erratum: analytic many-body potential for InAs/GaAs surfaces and nanostructures: formation energy of InAs quantum dots [Phys. Rev. B 77, 235303 (2008)]", 81 (2010) 159905.

40) D. J. Dunslan, in Properties of GaAs (Eds: M. R. Brozel and G. E. Stillman), Institution of Electrical Engineers (IEE), London (1996).

41) O. Madelung, U. Rössler and M. Schulz, Semiconductors: Group IV Elements, IV-IV and I. I. I.-V.Compounds. Part a – Lattice Properties, Vol. 41A1a, Springer, Berlin (2001).

42) A. Chanda, S. Verma and C. Jacob, "Etching of GaAs substrates to create As-rich surface", Bull. Mater. Sci., 30 (2007) 561.

43) N. J. Smeenk, J. Engel, P. Mulder, G. J. Bauhuis, G. M. M. W. Bissels, J. J. Schermer, E. Vlieg, J. J. Kelly "Arsenic Formation on GaAs during Etching in HF Solutions: Relevance for the Epitaxial Lift-Off Process", ECS J. Solid State Sci. Technol., 2 (2013) 58.

44) H. Ye and Z. Yu, "Plastic relaxation of mixed dislocation in axial nanowire heterostructures using Peach–Koehler approach", Phys. Status Solidi, 8 (2014) 445.

45) T. Riedl, V.S. Kunnathully, A. Trapp, T. Langer, D. Reuter and J.K.N. Lindner, "Strain-driven InAs island growth on top of GaAs(111) nanopillars", Phys. Rev. Mater., 4 (2022) 014602.

46) J. S. Blakemore, "Semiconducting and other major properties of gallium arsenide", J. Appl. Phys., 53 (1982) R123.

47) Yu. A. Burenkov, S. Yu. Davydov, and S. P. Nikanorov, Elastic properties of indium arsenide, Sov. Phys. Solid State, 17 (1975) 1446.

Chapter 6
Selective area heteroepitaxy of InAs

In this chapter a process technology resulting in the growth of InAs islands restricted to GaAs(111)A nanopillar tops is presented. It is therefore called a selective area heteroepitaxy (SAH) technology. Morphological and structural characterization results shedding light on the growth mechanisms and structural perfection of the resulting InAs islands are discussed.

6.1 Influence of substrate temperature

Based on the growth study of chapter 5, a growth rate of 0.011 nm/s and a nominal deposited film thickness of 2 nm were chosen for all experiments. InAs growth in the range 300°C to 450°C was done on SAH templates (Fig. 4.8) fabricated as detailed in chapter 4. SEM was employed as the main tool for morphological characterization and HAADF-STEM was used for the structural characterization of the resulting InAs islands. The results presented here have been published in [1].

The substrates used were prepared by monolayer/double layer nanosphere lithography and exhibit GaAs pillars of approximately 31 nm diameter protruding out of the SiN_x matrix. As seen in Fig. 6.1 (a) – (d), InAs islands form both on the SiN_x hard mask and on the nanopillars for $T_{sub} \leq 400°C$. Importantly, the nucleation of InAs islands on pillar edges is observed at all temperatures, in line with the predictions of [2] discussed in section 5.3. The areal density and diameter of InAs islands on the SiN_x mask at $T_{sub} = 300°C$ were estimated using ImageJ software [3] to be 2.02×10^3 μm^{-2} and 10 ± 2 nm, respectively. For $T_{sub} = 400°C$ they are much less dense but larger amounting to 2.13×10^2 μm^{-2} and 15 ± 5 nm, respectively. Additionally, InAs island size distribution charts for these growth conditions are shown in Fig 6.2 (a) and (b), which indicate a broader distribution for 400°C. N = 686 and N = 309 particles have been evaluated for these temperatures, respectively. The higher InAs island density at 300°C results from a lower In adatom desorption rate and migration length. At 400°C, the conditions are reversed, the larger In adatom mobility results in larger islands with a broader size distribution. These two growth conditions are examples for nucleation

vs growth dominated regimes. By assuming a conical or cylindrical shape of the islands, the volume deposited per area of mask can be described as $V/A = c_1 c_2 \sum_i D_i^3/A$, where c_1 is the geometry factor, $\pi/12$ for a cone or $\pi/4$ for a cylinder, c_2 is the proportionality factor relating cone or cylinder's height to its base diameter D, i is the index running across the individual islands being considered. The calculations show that V/A for 400°C is only 43% of that at 300°C due to the higher rate of adatom desorption, which is widely reported in literature for SiO_2 and SiN_x masks [4-6].

At 425°C, the islands grow exclusively at nanopillar tops (see Fig. 6.1 (c)), here the SiN_x mask is devoid of islands due to the enhanced migration and desorption. The higher desorption of In adatoms from the mask is expected because of its lower sticking coefficient on SiN_x. A common feature observed for all InAs islands is their extension towards the in-plane $\langle 11\bar{2} \rangle$ direction which is indicated using arrows in each of the images in Fig. 6.1. The relevance of this feature to the crystallography aspects of InAs island's growth are discussed later in this section.

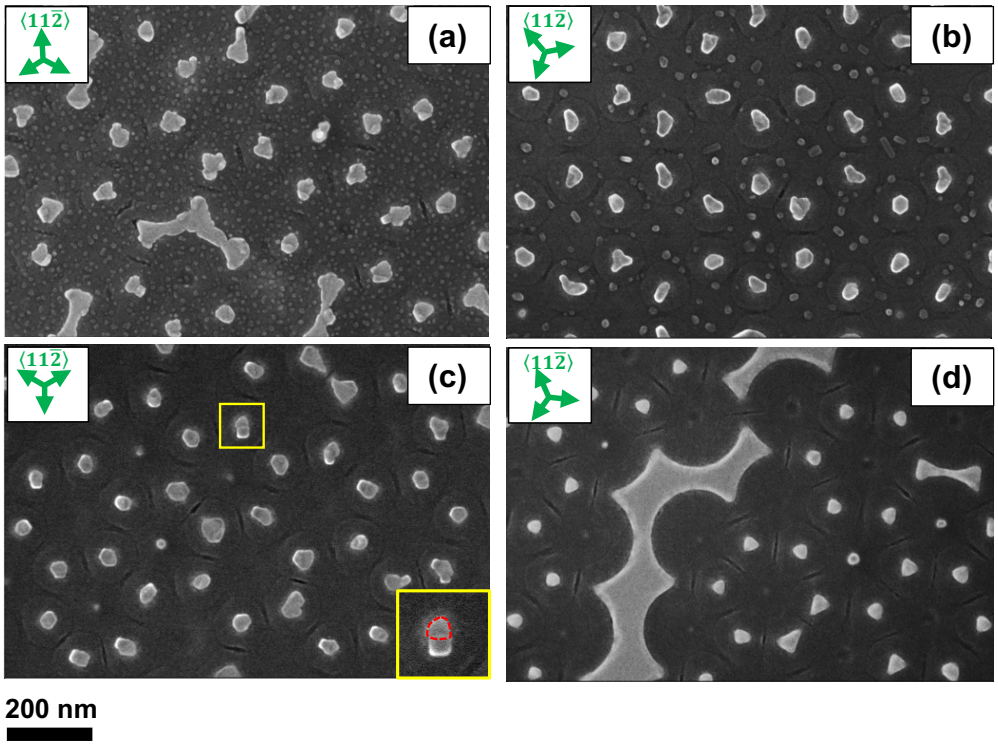

Fig. 6.1. Top view SEM images of SAH templates after depositing 2 nm of InAs at a growth rate of 0.011 nm/s. Images for growth temperatures of 300°C, 400 °C, 425°C and 450°C are presented in (a), (b), (c) and (d), respectively, along with the in-plane $\langle 11\bar{2} \rangle$ directions at the substrate surface. The inset in (c) highlights the outer profile of a GaAs pillar upon which an InAs island grows off-centre.

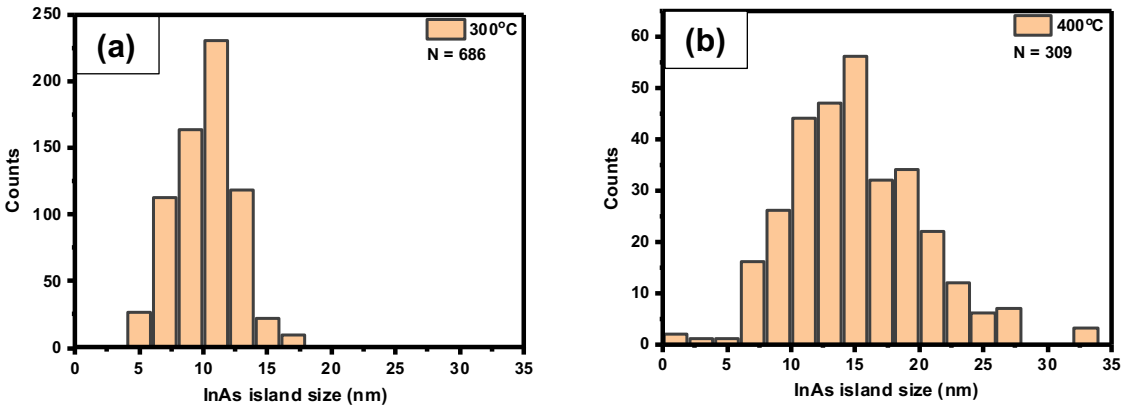

Fig. 6.2. Size distribution of InAs islands formed on SAH templates for 300°C (a) and 400°C (b) respectively. The average island diameter and island density amount to 10 ± 2 nm and $2021/\mu m^2$ for 300°C and to 15±5 nm and $170/\mu m^2$ for 400°C.

At the highest growth temperature 450°C, the GaAs pillars are found to be totally devoid of InAs islands, as seen in Fig. 6.1 (d). The high In adatom desorption rate at this temperature prevents any stable formation of nuclei. HAADF-STEM images and EDS analysis (Figs. 6.3 and 6.4) confirm the above observations. Only a weak In signal is detected over GaAs pillars due to its lower In desorption rate, as indicated by HAADF-STEM and STEM-EDS line scan analysis in Fig. 6.3. The STEM-EDS scan line A-B in Fig. 6.3(a) results in the quantitative EDS profile shown in Fig. 6.3(b), the error bars indicated in this profile were calculated using the formula for 3σ error, $3\sigma = 3/\sqrt{N} \cdot C_i^p$ for an element P and data point i, where N is the number of counts at i. The formula is based on Gaussian statistics, owing to the Gaussian nature of EDS spectra [7] as seen in Fig. 6.3(c).

A good correspondence between the quantitative EDS data of Fig. 6.3(b) and the counts in Fig. 6.3(d) is observed. At lower counts, such as at outside the GaAs pillar the error values increase and an equi-atomic distribution of Ga, As and a lack of In are observable on the body of the pillar. Yet another proof for the same observation comes from the spectrum image (SI) shown in Fig. 6.3(e). The SI image is a slice through the 3D data cube described in section 3.3.2.3, viewed from the energy-distance axis (y-axis in Fig. 3.4(c)). In this 2D representation, the intensity of the yellow lines shows the number of counts detected for the corresponding X-Ray energy. The EDS spectrum in Fig. 6.3(c), corresponding to the dotted line in Fig. 6.3(e) shows one of the 81 spectra used to create the SI image, captured over a length of 39.5 nm at 0.49 nm intervals.

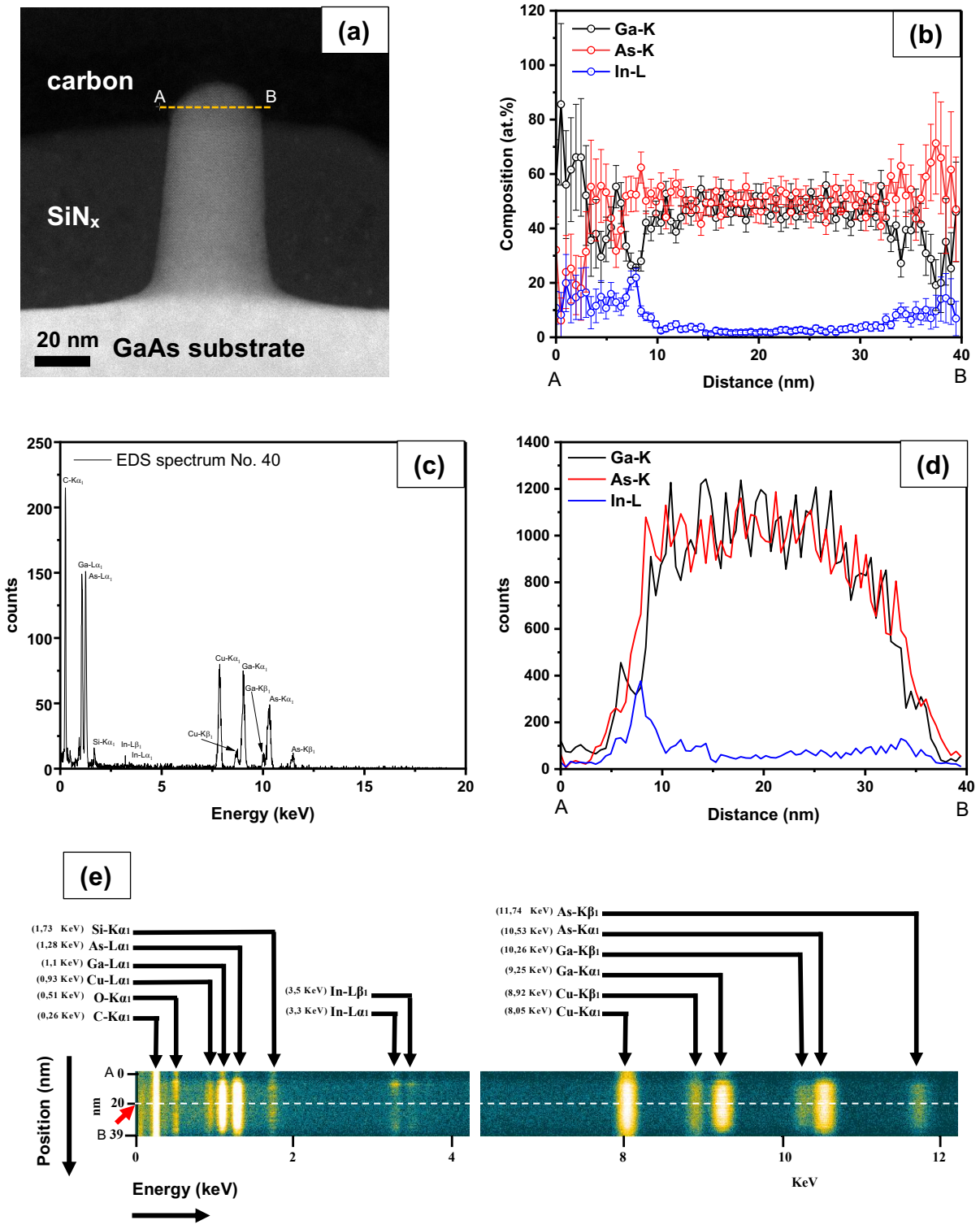

Fig. 6.3. A GaAs nanopillar embedded in the SAH template, with top exposed is shown in (a) after MBE growth at T_{sub} = 450°C. The HAADF-STEM-EDS line profile marked using orange dotted line in (a) is plotted for In, Ga and As in (b) with 3σ error bars calculated using signal counts for the same profile, shown in (d). (c) An EDS spectrum of a selected data point in the line profile (a), corresponding to the dotted white line in (e). The EDS signal counts for Ga, As and In of line scan profile (a) are shown in (d). The EDS spectrum image corresponding to (b) is shown in (e) indicating In presence only at pillar edges. The starting and ending points of the line scan, A and B respectively are indicated in the images where necessary.

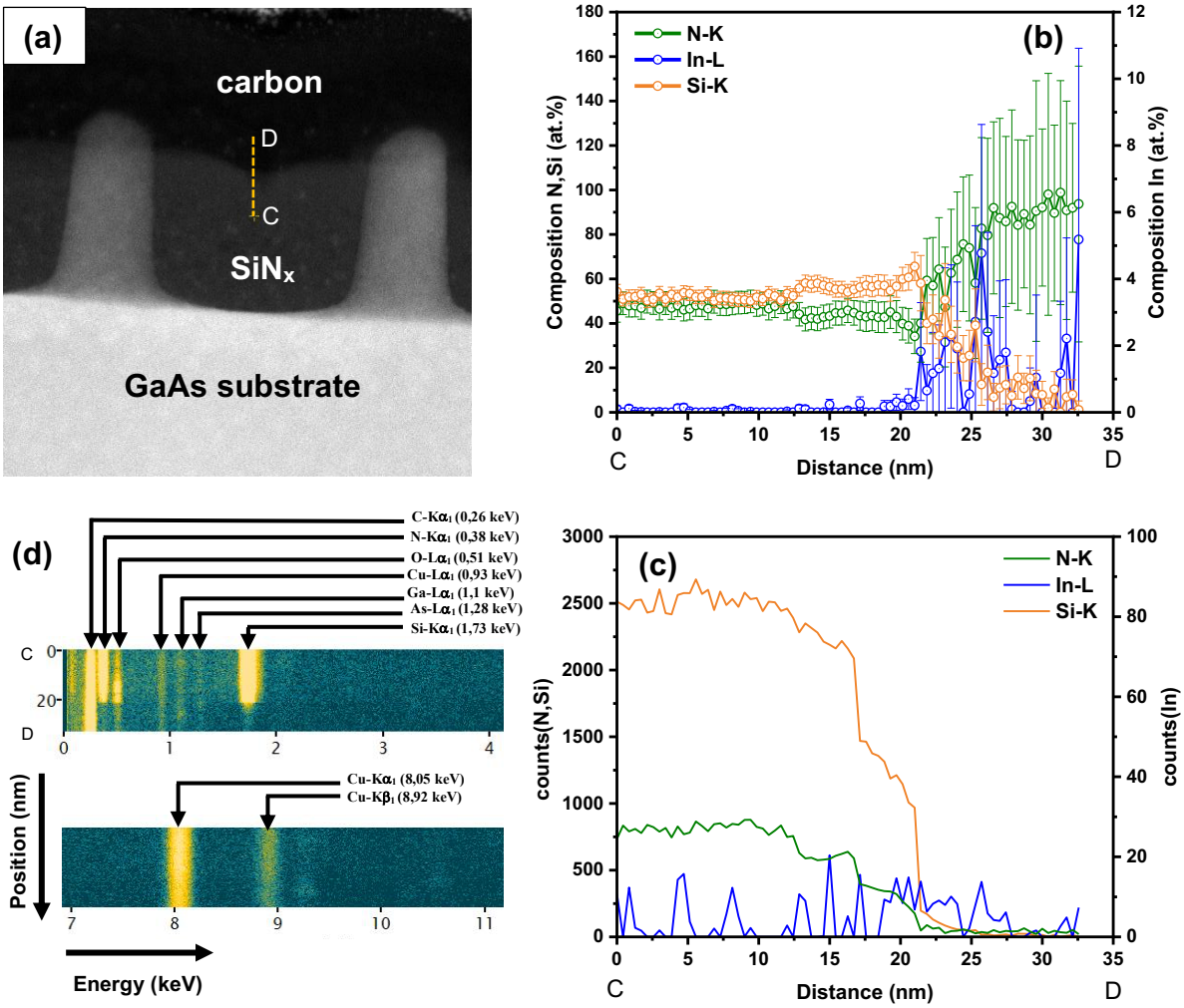

Fig. 6.4. A GaAs nanopillar embedded in the SAH template, with top exposed is shown in (a) after MBE growth at T_{sub} = 450°C. The HAADF-STEM-EDS line profile marked using orange dotted line in (a) is plotted for N, In and Si in (b) with 3σ error bars calculated using signal counts for the same profile, shown in (c). In (d) the EDS spectrum image corresponding to (b) is shown. The starting and ending points of the line scan are indicated by C and D respectively in the images where necessary.

No detectable amount of In was found also on the SiN_x mask as seen in Fig. 6.4, here the spectrum image (SI) in Fig. 6.4 (d) shows the absence of In signals corresponding to In-Lα_1 and In- Lβ_1 (compare with Fig. 6.3(e) for reference), a graphical representation of X-Ray counts corresponding to N-K, Si-K and In-L are plotted in Fig. 6.4(c) and the quantitative analysis of the same along the line C-D , represented in Fig. 6.4(b) confirms the absence of In. The line STEM-EDS profiles were captured over a length of 33 nm at a sampling interval of 0.42 nm.

Upon closer observation, the pillar tops also show evidence of possible crystallographic etching at their edges. A reason for this is the field concentration at pillar edges during the late stages of RIE of SiN_x masks by fluorine ions [8,9]. Evidence for this is shown using a pillar in Fig. 6.5 (a) and (b). The pillar top clearly exhibits a faceted top, indicating material removal from the edges. Further, the analysis of lattice plane spacings of HAADF-STEM images from the pillar edges reveals the presence of the non-polar {110} type of planes indicated in Fig. 6.5 (c) using a white arrow. The indexed fast Fourier transform (FFT) image of Fig. 6.5(c), shown in Fig. 6.5(f) was used to calculate the inverse Fourier transform (IFFT) image using the diffraction spots corresponding to the {022} planes. The average interplanar spacing estimated using DigitalMicrogrpah software [10] form Fig. 6.5(f) using the integrated intensity of the line profile shown matched the theoretical value of the {022} planes in GaAs. A schematic of the GaAs crystal lattice viewed along the $[1\bar{1}0]$ direction showing the {110} plane stacking is shown to show the equivalence of the {022} and {110} planes.

HAADF-STEM images of an InAs island grown at the lowest growth temperature of 300°C are displayed in Fig. 6.6(a) and (b). The enhanced intensity due to HAADF Z-contrast shows that the InAs island has grown mainly from the pillar edge to the side. It contains rotational twin boundaries (RTB) due to local fluctuations in the formation energies [11]. One of the RTB is highlighted in the inset of Fig. 6.5(b). Some of the InAs islands which have nucleated on the SiN_x mask at this low deposition temperature, as mentioned above are also visible.

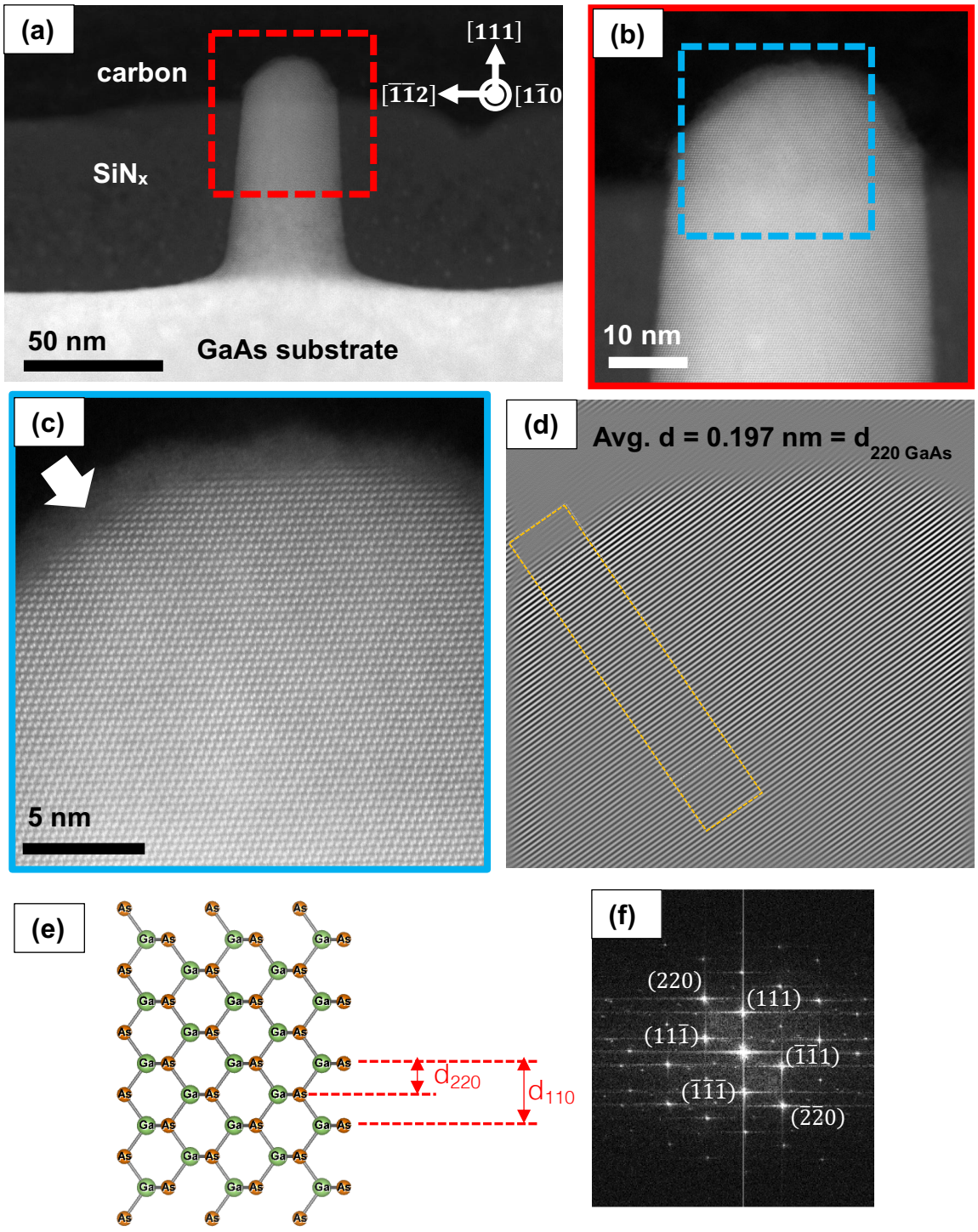

Fig. 6.5. (a) A GaAs nanopillar embedded in the SiNx film, with the top exposed, after MBE growth at T_{sub} = 450°C. The pillar top is shown at higher magnifications in (b) and (c). (d) is an inverse Fourier transform of (c) created by Bragg filtering (022) reflections in the FFT image in (f), showing the (002) planes. (e) is a crystallographic model of the {110} plane stacking in GaAs, viewed the [1$\bar{1}$0] direction.

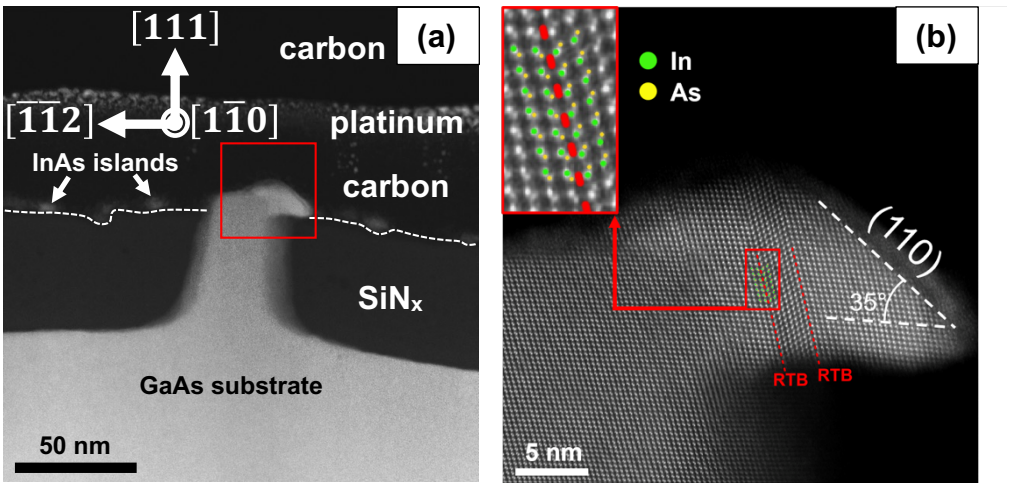

Fig. 6.6. The various protective layers surrounding a GaAs nanopillar with InAs island grown at 300°C is shown in (a). A high magnification HAADF-STEM image of the InAs island with rotational twin boundaries marked with red dotted lines is shown in (b). The Atomic configuration across the RTB is shown in the inset. Formation of the (110) type of facet is also shown for the InAs islands using white dotted lines.

For T_{sub} = 400°C, the InAs islands appear slightly larger than for T_{sub} = 300°C and are found to be extended along the in-plane ⟨11$\bar{2}$⟩ direction (Fig. 6.5(a) vs 6.6(a)). Fig. 6.6 shows HAADF-STEM images of one such InAs island formed on top of a GaAs nanopillar. A closer inspection of Fig. 6.7(a) in Fig. 6.7(b) reveals that the initial portion of the InAs island crystallized in the ZB phase and the extended arm growing on the (11$\bar{1}$) or (111)B plane is found to crystallize in the WZ phase, as demonstrated by the fast Fourier transform (FFT) pattern analysis in Fig. 6.7 (c) – (e). Additionally, the WZ portion and the WZ/ZB interface are found to consist of numerous stacking faults on the (0001) basal plane. These observations give hints on the switching of crystal growth from ZB to the WZ phase. Such a transition between the polytypes has been reported in literature during the growth of InAs nanowires to take place via the formation of multiple rotational twins [11-13]. However, no such features have been observed in the present case.

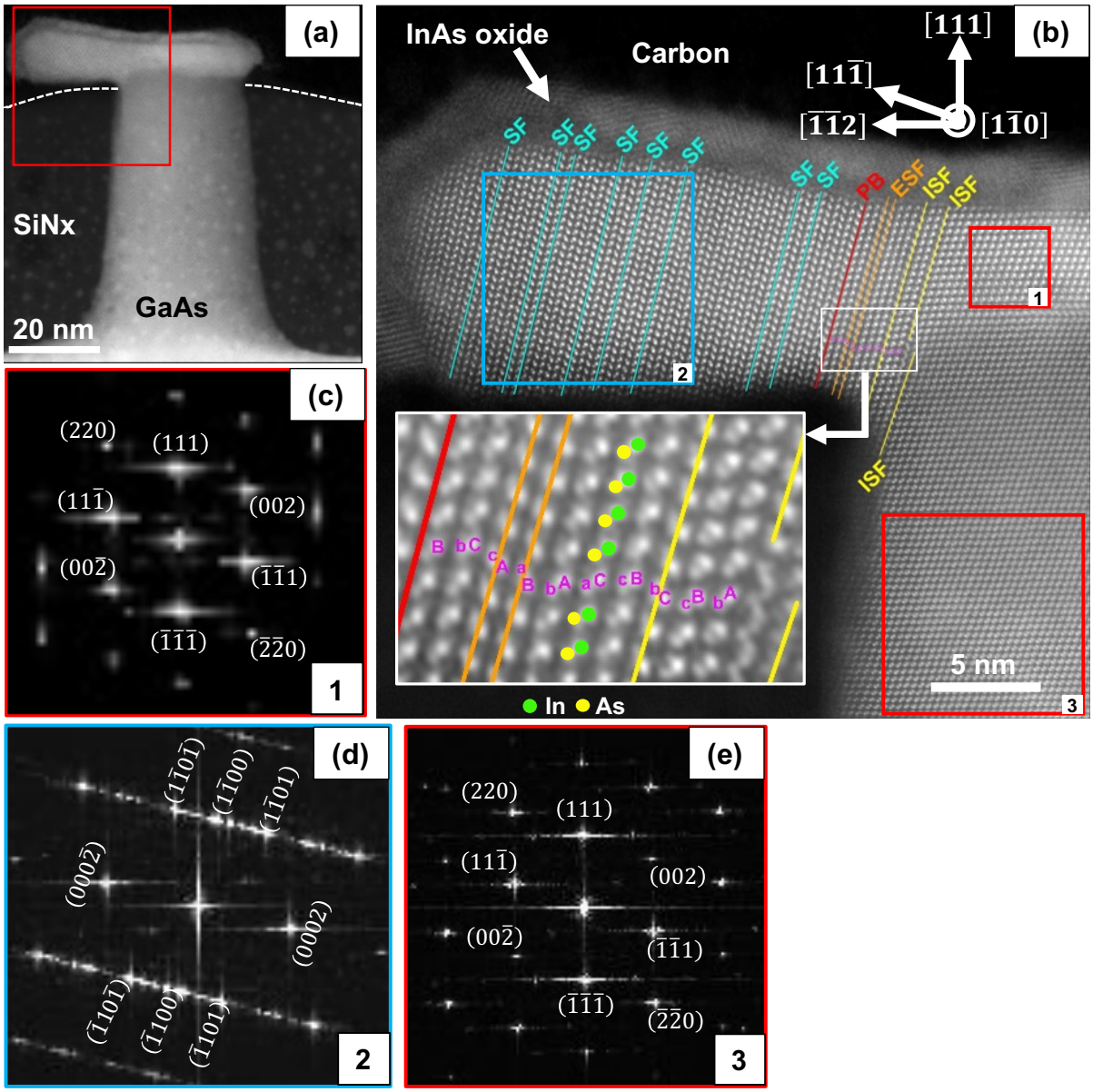

Fig. 6.7. (a) HAADF-STEM image of a GaAs nanopillar being part of an SAH substrate InAs deposition at 400°C. (b) is high resolution HAADF-STEM of the InAs island with defects clearly marked. The inset in (b) shows the atomic configuration at the interface separating the WZ and ZB phases. (c), (d) and (e) are FFT images corresponding to regions 1 (InAs ZB), 2 (InAs WZ) and 3 (GaAs ZB) marked in (b).

In droplet formation under As-rich conditions, similar to those employed here, has clearly been demonstrated and proven using detailed SEM investigations [14] and in-situ time resolved synchrotron x-ray diffraction experiments [15]. According to these studies, In droplet formation by In adatom agglomeration on substrate occurs within a short duration of opening the In shutter. In the present study, such In droplets could

form either due to the direct impingement or migration of In adatoms onto GaAs pillar tops. Once formed, the InAs growth occurs via the vapour liquid solid (VLS) type of mechanism, where initially the ZB segment forms on the pillar tops due to its lower energy [1].

The WZ portion starts to form when liquid In starts to crystallize within a junction having thickness lower than ≈ 20 nm which favors WZ formation [16]. An additional factor promoting this is the V/III ratio dependent contact angle between the GaAs pillar top and the In liquid droplet. In-situ TEM based MBE studies of self-catalyzed GaAs nanowire growth indicate the favorability of WZ phase for a narrow contact angle range between 100 - 125° [17,18] under As-rich conditions. Similar As-rich conditions can be expected to prevail towards the end of the MBE growth experiments in the present study where the As flux is provided even after the In source is shut. The In droplet volume and concentration shrinks along with the retraction and stabilization of a contact angle favoring the WZ phase formation [1]. The WZ phase nucleates with its (0001) basal plane aligned with the $(11\bar{1})$ ZB-InAs due plane matching. Remarkably, these optimum conditions of contact angle, In liquid volume and supersaturation seem to occur at a very narrow temperature window.

During the growth at T_{sub} = 425°C, the formation of defect-free InAs island on the GaAs nanopillars is observed, shown in Fig. 6.8 (a) and in Fig. 6.8 (b) at higher magnification. A GPA based mean dilatation map (Fig. 6.8(c)) derived from Fig. 6.8(b) and the line profile in Fig. 6.8 (d), corresponding to the marked ROI in 6.8 (c), show complete strain relaxation of both lattices. Here the strain relaxation is facilitated by the island's edge position and surface strain relaxation [2,19]. The broadening of the transition zone in the dilatation profile can be attributed to the overlap of InAs and GaAs lattices long the beam direction. Additionally, the strain maps show no influence of the surrounding SiN_x hard mask on the strain state of the GaAs nanopillar top or the heterointerface.

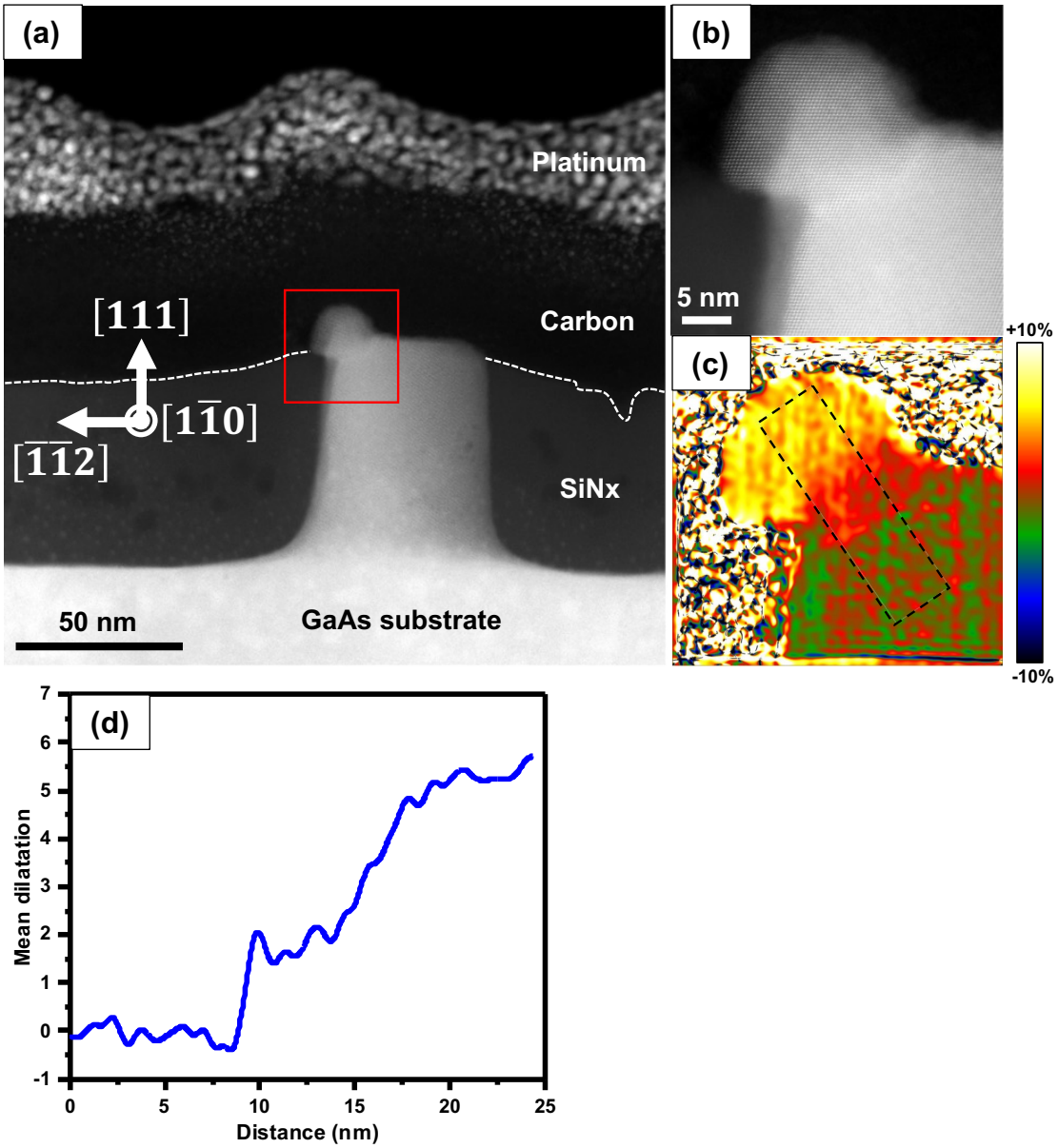

Fig. 6.8. (a) HAADF-STEM image of a SiN_x embedded GaAs nanopillar after InAs deposition at 425°C . The sample was covered with protective films of carbon and a Pt-C compound after MBE for FIB specimen preparartion. (b) High resolution HAADF-STEM image of the InAs island (red square in (a)) showing the defect-free InAs lattice. (c) GPA mean dilatation strain, $\Delta_{xy} = 1/2\ (\varepsilon_{xx} + \varepsilon_{yy})$ map of (b). (d) Mean dilatation profile from the region marked in (c) showing the complete strain relaxation in InAs.

6.2 Summary

1.) InAs heteroepitaxy on a SAH template developed for achieving site specific growth on GaAs(111)A nanopillar tops was carried out at temperatures between 300 and 450°C at a growth rate 0.011 nm/s and with a fixed deposited thickness of 2 nm.

2.) InAs formation on both the SiNx hard mask and pillar tops are observed at temperatures less than or equal to 400°C. For the highest substrate temperature of 450°C the InAs islands were completely absent due to In adatom desorption.

3.) At 400°C, InAs islands containing both ZB and WZ phases are observed. This is ascribed to the formation of a possible liquid In phase. The WZ segment is assumed to be formed when the contact angle of liquid In is in the range 100 – 125°, under As rich conditions during growth while the In droplet has a size of less than 20 nm.

4.) Completely defect free InAs islands are formed at 425°C, free from constrains of the SAH template, with efficient surface strain relaxation.

References

1) T. Riedl, V.S. Kunnathully, A.K. Verma, T. Langer, B. Büker, A. Hütten, D. Reuter and J.K.N. Lindner, "Selective area heteroepitaxy of InAs nanostructures on nanopillar-patterned GaAs(111)A", J. Appl. Phys., 132 (2022) 185701

2) T. Riedl, V.S. Kunnathully, A. Trapp, T. Langer, D. Reuter and J.K.N. Lindner, "Strain-driven InAs island growth on top of GaAs(111) nanopillars", Phys. Rev. Mater., 4 (2022) 014602

3) C.A. Schneider, W.S. Rasband and K.W. Eliceiri, "NIH Image to ImageJ: 25 years of image analysis", Nat. Methods, 9 (2012) 671.

4) S.C. Lee and S.R.J. Brueck, "Nanoscale Patterned Growth Assisted by Surface Out-Diffusion of Adatoms from Amorphous Mask Films in Molecular Beam Epitaxy", Cryst. Growth Des., 16 (2016) 3669.

5) F. Allegretti, M. Inoue and T. Nishinaga, "In-situ observation of GaAs selective epitaxy on GaAs(111)B substrates", J. Crsyt. Growth, 146 (1995) 354.

6) P. Aseev, A. Fursina, F. Boekhout, F. Kriek, J.E. Sestoft, F. Borsoi, S. Heedt, G. Wang, L. Binci, S. Marti-Sanchez, T. Swoboda, R. Koops, E. Uccelli, J. Arbiol, P. Krogstrup, L.P. Kouwenhoven and P. Caroff, "Selectivity map for molecular beam epitaxy of advanced III-V quantum nanowire networks", Nano Lett., 19 (2019) 218.

7) D. B Williams and B.C. Carter, "Transmission electron microscopy: A textbook for electron microscopy", Springer (2009)

8) W.-C. Tian, J.W. Weigold and S.W. Pang, "Comparison of Cl_2 and F^- based dry etching for high aspect ratio Si microstructures etched with an inductively coupled plasma source", J. Vac. Sci. Technol. B, 18 (2000) 1890

9) B. Chang, G.A.E. Anand, X. Liu, H. Jansen, L. Romano and A. Han,"Field enhancement effect in reactive ion etching – a novel mechanism for plasma processing and plasma diagnostics", Mater. Des., 254 (2025) 114144

10) Gatan Inc., DigitalMicrograph software: https://www.gatan.com/products/tem-analysis/digitalmicrograph-software

11) P. Caroff, K.A. Dick, J. Johansson, M.E. Messing, K. Deppert and L. Samuelson,"Controlled polytypic and twin-plane superlattices in III-V nanowires", Nat. Nanotechnol, 4 (2009) 50

12) L. Güniat, P. Caroff and A.F. i Morral, "Vapor Phase Growth of Semiconductor Nanowires: Key Developments and Open Questions", Chem. Phys. Rev., 119 (2019) 8958

13) M. Koguchi, H. Kakibayashi, M. Yazawa K. Hiruma and T. Katsuyama,"Crystal Structure Change of GaAs and InAs Whiskers from Zinc-Blende to Wurtzite Type", Jpn. J. Appl. Phys., 13 (1992) 2061

14) Th Graph, T. Rieger, Ch Blömers, Th Schapers, D. Grützmacher and M.I. Lepsa, "Self-catalyzed VLS grown InAs nanowires with twinning superlattices", NanoTech., 24 (2013) 335601

15) A. Biermanns, E. Dimakis, A. Davydok, T. Sasaki, L. Geelhar, M. Takahasi and U. Pietsch, "Role of liquid indium in the structural purity of wurtzite InAs nanowires that grow on Si(111)", Nano Lett., 14 (2014) 6878

16) T. Akiyama, K. Sano, N. Nakamura and T. Ito, "An Empirical Potential Approach to Wurtzite–Zinc-Blende Polytypism in Group III–V Semiconductor Nanowires", Jpn. J. Appl. Phys., 45 (2006) L275

17) F. Panciera, Z. Baraissov, G. Patriarche, V. G. Dubrovskii, F. Glas, L. Travers, U. Mirsaidov, and J.-C. Harmand "Phase Selection in Self-catalyzed GaAs Nanowires", Nano Lett. 20, (2020) 1669

18) T. Dursap, M. Vettori, C. Botella, P. Regreny, N. Blanchard, M. Gendry, N. Chauvin, M. Bugnet, A. Danescu, and J. Penuelas, "Wurtzite phase control for self-assisted GaAs nanowires grown by molecular beam epitaxy", NanoTech., 32, (2021) 155602

19) T. Riedl, V.S. Kunnathully, A. Trapp, T. Langer, D. Reuter and J.K.N. Lindner, “Size-Dependent Strain Relaxation in InAs Quantum Dot on Top of GaAs(111)A Nanopillars”, Adv. Mater. Interfaces, 9 (2022) 2102159

Chapter 7
Conclusions and outlook

7.1 Conclusions

The present thesis deals with the heteroepitaxial growth of InAs on nanostructured GaAs (111)A surfaces using molecular beam epitaxy (MBE). Nanosphere lithography and reactive ion etching were used in conjunction to create nanopillar patterned GaAs(111)A substrates. By using 220 nm polystyrene spheres, mono and double layer patterns were deposited on the substrate. The spheres were annealed to create round or rounded triangular interstices approximately 30 nm in diameter, later used to define Ni hard mask patterns on the substrates. Reactive ion etching of the substrates through the Ni hard mask patterns yields hexagonal arrays of nanopillars with average diameter of 28 or 31 nm and pitches of 129 or 228 nm for mono and double layer masks, respectively. By achieving this on areas of approximately 10 cm^2 the fundamentals were laid to explore full potential of nano-heteroepitaxy on compliant substrates.

InAs MBE growth parameters on nanopillar patterned substrates are varied to study growth on pillar tops and between the pillars. Temperatures in the range 150 – 410°C, growth rates 0.011 nm/s and deposited thicknesses 15, 5 and 2 nm were probed. It was observed that only at the lowest growth temperature of 150°C InAs islands form on the pillar tops, while at higher deposition temperatures, the InAs was found to form facetted hillocks around the pillar bases. An optimum parameter for the formation of InAs islands on the pillar tops set defined by temperature, growth rate and deposited thickness, 150°C, 0.011 nm/s and 15 nm respectively was identified based on microstructural analysis of the deposits using SEM and AFM. Further, microstructural analysis using (S)TEM was performed to access the crystal quality. Misfit dislocations with Burgers vector $\vec{\boldsymbol{b}} = a/2[\bar{1}01]$ were observed along with stacking fault defects. In order to reduce and suppress misfit dislocations in the InAs islnads , lower InAs deposited nominal thicknesses of 5 and 2 nm were explored. At 2 nm of deposited nominal InAs thickness, dislocation free InAs islands with a width and height of 6 nm atop the 25 nm diameter GaAs(111)A pillars were synthesized. A

Stranski- Krastanov type of growth where InAs islands form on a few atomic layers thick InAs wetting layer was observed. Molecular statics simulations of exemplary InAs islands performed in collaboration with Dr. Thomas Riedl for the various thicknesses revealed the increasing contribution of surface strain relaxation towards the accommodation of misfit strain as InAs island size was reduced. The studies also explain the preference of InAs islands to nucleate on pillar edges due to more efficient strain relaxation resulting from a competition between strain energy and surface energy.

At elevated growth temperature InAs growth was concentrated at the pillar bases where due to curvature and kink position effects resulting in localized, pyramidal dislocation containing films. In order to enable also nanoheteroepitaxial growth at higher temperatures, a selective area heteroepitaxy (SAH) template exposing only GaAs pillar tops (≈ 17 nm) embedded in silicon nitride was developed. MBE growth of InAs was performed upon such substrates in temperature range 300 – 450°C at a growth rate of 0.011 nm/s and with an deposited thickness a 2 nm. Perfect selectivity of InAs growth exclusively on the exposed GaAs pillar tops was achieved at 425°C, resulting from a balance between adatom adsorption and desorption. The resulting InAs islands were defect free and strain free. At the highest growth temperature of 450°C, bare GaAs tops resulted from the complete adatom desorption. At 300°C and 400°C, islands formed both on nanopillars and the SiN_x hard mask due to lower desorption, with a higher areal density on the hard mask at the lower growth temperature. At 400°C, the InAs islands showed a tendency to crystallize in the wurtzite phase towards the later growth stages, which is assumed to be due to a combination of surface energy, As concentration and contact angle related effects. Such InAs islands are believed to form via a localized vapor liquid solid type of mechanism due to formation of In droplets during the initial stages of MBE.

7.2 Outlook

The study presented in this thesis demonstrates the possibility to employ nanosphere lithography as a tool to fabricate nanostructures that enable possibilities to realize selective area heteroepitaxy. Additionally, the formation of Stranski-Krastanov type InAs islands on GaAs(111)A surfaces is unique to this work.

The majority of current work is focused on structural characterizations. The optical properties of the InAs islands, however, have not yet been probed. Photoluminescence measurements would open a new avenue for research.

Additionally, for the SAH templates only the monolayer patterned areas have been structurally characterized using (S)TEM. The double layer patterned areas with lower pillar density yield InAs islands which are more vertical and thicker. This is observable when comparing SEM images and AFM topography scans of InaAs islands at monolayer and double layer patterned areas seen in Fig. 7.1. Also, the greater extent of pillar top coverage by the InAs islands increases the probability of strain partitioning at the pillar tops and should therefore be investigated.

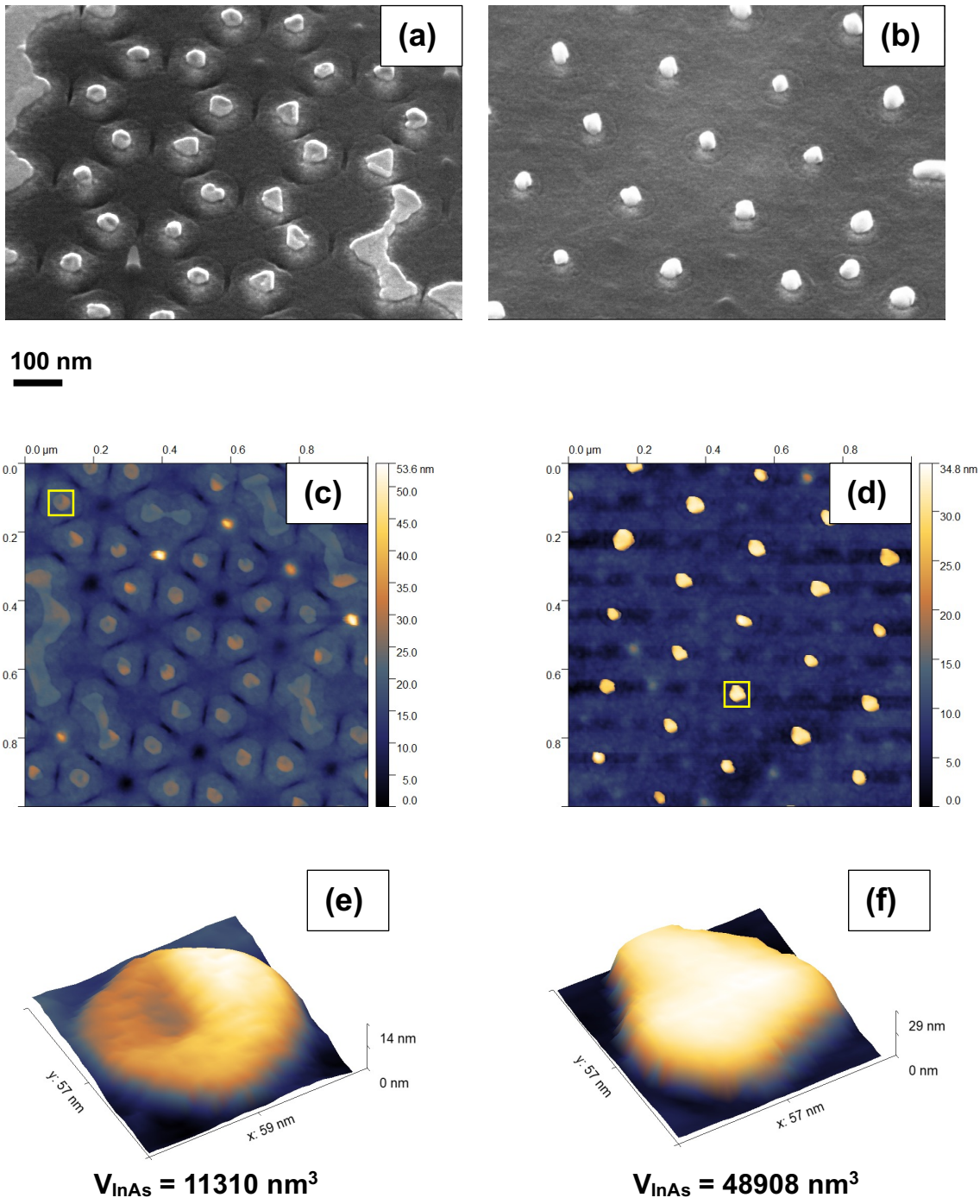

Fig. 7.1. 45° tilted view SEM images of SAH templates after depositing 2 nm of InAs at a growth rate of 0.011nm/s, captured at ML (a) and DL (b) areas, respectively. (c) and (d) are AFM surface topography scans of ML (c) and DL (d) patterned areas in which the regions of interest marked with yellow squares are analysed for the InAs island volume InAs, the values of which are mentioned below the respective higher magnification cut out volumes in (e) and (f).

Appendix-A1
Linear elasticity

The lattice misfit strain at semiconductor heterointerfaces is known to impact properties such as band structure, band gap and mobility. This section provides a brief review of elasticity theory in solids. The concepts presented here aid in the appreciation of the origins, measurement and representation of strain a the InAs/GaAs heterointerface. Majority of the concepts presented here have been adapted from references [1,2,43]. Linear elasticity is applicable when deformations are very small compared to the lattice parameter of the materials involved.

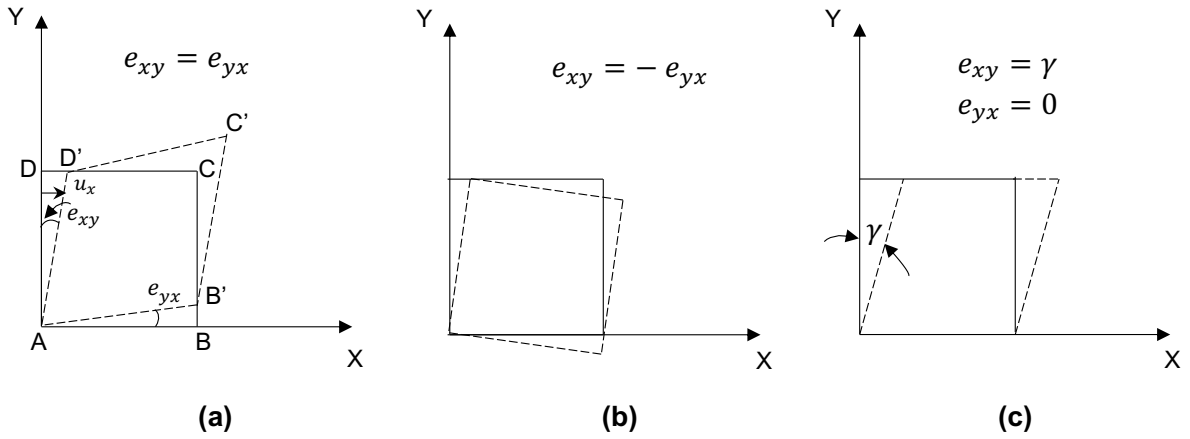

Fig. A1.1 The various modes of deformation due to shear and rotation. (a) Pure shear with no rotation (b) pure rotation with no shear (c) pure shear due to displacement along one the x-axis.

A1.1 The strain tensor

Suppose a point Q = (x_1, x_2, x_3) within a semiconductor heterostructure is displaced to Q = (x_1', x_2', x_3') because of lattice mismatch strains. The resulting lattice distortion can be represented by a displacement vector u with components u_x, u_y and u_z along the three principal axes. For solids that are elastic, the displacements are linear with distance. Under these conditions, the relative distortion of the lattice along the X-axis, $\partial u_x/\partial x = e_{xx}$ and the corresponding displacement is given by $u_x = e_{xx}x$. Extending this argument to the three axes, the displacement equations can be written as:

$$u_x = e_{xx}x + e_{xy}y + e_{xz}z$$

$$u_y = e_{yx}x + e_{yy}y + e_{yz}z$$

$$u_z = e_{zx}x + e_{zy}y + e_{zz}z \quad \text{A1-1}$$

$$u_i = e_{ij}x_j \quad \text{A1-2}$$

Note: According to the standard convention for representing stresses (σ_{ij}) and strains (ε_{ij}), the first index, "i" represents the plane normal and the second index "j" represents the direction upon which stress or strain acts. This convention is essential for a lucid representation of stress and strain tensors.

displacements and remaining six components with i $\neq$ j to displacements arising from shear strains and lattice rotation. In Fig. A1.1 (a), the square element ABCD when subjected to shear causes line AD to displace to AD′. Here, the corresponding displacement u_x is proportional to distance long the y-axis, from Fig. A1.1 (a)

$$e_{xy} = \frac{DD'}{DA} = \frac{\partial u_x}{\partial x} \quad \text{A1-3}$$

Similarly, angular distortion along the x-axis results in,

$$e_{yx} = \frac{BB'}{AB} = \frac{\partial u_y}{\partial x} \quad \text{A1-4}$$

By convention, shear rotations are positive when a body rotates towards positive axes because of distortions. Two other possibilities of lattice displacement are lattice rotation and simple shear, represented in Fig. A1.1 (b) and (c). Fig. A1.1(b) shows that the equal and opposite components e_{xy} and -e_{yx} cancel out one another thus, pure rotation does not result in shape change. Simple shear, γ_{ij} on the other, defined as the total angular change from a right-angle causes shape change as seen in Fig. A1.1 (c).

$$\gamma_{xy} = \frac{\partial u_x}{\partial y} + \frac{\partial u_y}{\partial x}$$

$$\gamma_{xz} = \frac{\partial u_z}{\partial x} + \frac{\partial u_x}{\partial z}$$

$$\gamma_{yz} = \frac{\partial u_z}{\partial y} + \frac{\partial u_y}{\partial z} \quad \text{A1-5}$$

γ_{ij} is also called engineering strain and $\gamma_{ij} = 2\,\varepsilon_{ij}$, because $\gamma_{xy} = \gamma_{yx}$.

The relative displacement tensor e_{ij} can conveniently be represented in the form of the matrix,

$$e_{ij} = \begin{vmatrix} e_{xx} & e_{xy} & e_{xz} \\ e_{yx} & e_{yy} & e_{yz} \\ e_{zx} & e_{zy} & e_{zz} \end{vmatrix} = \begin{vmatrix} \frac{\partial u_x}{\partial x} & \frac{\partial u_x}{\partial y} & \frac{\partial u_x}{\partial z} \\ \frac{\partial u_y}{\partial x} & \frac{\partial u_y}{\partial y} & \frac{\partial u_y}{\partial z} \\ \frac{\partial u_z}{\partial x} & \frac{\partial u_z}{\partial y} & \frac{\partial u_z}{\partial z} \end{vmatrix} \quad \text{A1-6}$$

The e_{ij} components contain both strain and rotational components, these are separated using a postulate of tesor theroy. According to which, any second-rank tensor can be decomposed into symmetric (ε_{ij}) and ant-symmetric (ω_{ij}) components. Here, $e_{ji} = e_{ij}^{\mathrm{T}}$ (transpose of e_{ij})

$$e_{ij} = \frac{1}{2}\left(e_{ij} + e_{ji}\right) + \frac{1}{2}\left(e_{ij} - e_{ji}\right) \quad \text{A1-7}$$

$$e_{ij} = \left(\varepsilon_{ij} + \omega_{ji}\right) \quad \text{A1-8}$$

where,

$\varepsilon_{ij} = \frac{1}{2}\left(\frac{\partial u_i}{\partial x_j} + \frac{\partial u_j}{\partial x_i}\right)$ is called the strain tensor

$\omega_{ij} = \frac{1}{2}\left(\frac{\partial u_i}{\partial x_j} - \frac{\partial u_j}{\partial x_i}\right)$ is called the rotation tensor

$$\varepsilon_{ij} = \begin{vmatrix} \varepsilon_{xx} & \varepsilon_{xy} & \varepsilon_{xz} \\ \varepsilon_{yx} & \varepsilon_{yy} & \varepsilon_{yz} \\ \varepsilon_{zx} & \varepsilon_{zy} & \varepsilon_{zz} \end{vmatrix} = \begin{vmatrix} \frac{\partial u_x}{\partial x} & \frac{1}{2}\left(\frac{\partial u_x}{\partial y} + \frac{\partial u_y}{\partial x}\right) & \frac{1}{2}\left(\frac{\partial u_x}{\partial z} + \frac{\partial u_z}{\partial x}\right) \\ \frac{1}{2}\left(\frac{\partial u_x}{\partial y} + \frac{\partial u_y}{\partial x}\right) & \frac{\partial u_y}{\partial y} & \frac{1}{2}\left(\frac{\partial u_y}{\partial z} + \frac{\partial u_z}{\partial y}\right) \\ \frac{1}{2}\left(\frac{\partial u_x}{\partial z} + \frac{\partial u_z}{\partial x}\right) & \frac{1}{2}\left(\frac{\partial u_y}{\partial z} + \frac{\partial u_z}{\partial y}\right) & \frac{\partial u_z}{\partial z} \end{vmatrix}$$

A1-9

$$\omega_{ij} = \begin{vmatrix} \omega_{xx} & \omega_{xy} & \omega_{xz} \\ \omega_{yx} & \omega_{yy} & \omega_{yz} \\ \omega_{zx} & \omega_{zy} & \omega_{zz} \end{vmatrix} = \begin{vmatrix} 0 & \frac{1}{2}\left(\frac{\partial u_x}{\partial y} - \frac{\partial u_y}{\partial x}\right) & \frac{1}{2}\left(\frac{\partial u_x}{\partial z} - \frac{\partial u_z}{\partial x}\right) \\ \frac{1}{2}\left(\frac{\partial u_y}{\partial x} - \frac{\partial u_x}{\partial y}\right) & 0 & \frac{1}{2}\left(\frac{\partial u_y}{\partial z} - \frac{\partial u_z}{\partial y}\right) \\ \frac{1}{2}\left(\frac{\partial u_z}{\partial x} - \frac{\partial u_x}{\partial z}\right) & \frac{1}{2}\left(\frac{\partial u_z}{\partial y} - \frac{\partial u_y}{\partial z}\right) & 0 \end{vmatrix}$$

A1-10

The general strain equation reads,

$$u_i = \varepsilon_{ij} x_j + \omega_{ij} x_j \qquad \text{A1-11}$$

A1.2 Hooke's law

The strains within in a semiconductor material resulting in stresses can be derived with the help of a *constitutive equation* due to Robert Hooke called the Hooke's law. According to the Hooke's law, the stress and strain are linearly related for a material being strained within its elastic limit. The general form of Hooke's law reads:

$$\sigma_{ij} = \mathrm{C}_{ijkl} \varepsilon_{kl} \qquad \text{A1-12}$$

where, $\mathrm{C_{ijkl}}$ is a fourth order tensor called compliance comprising 81 components. The inverse relation of equation A1-12 is:

$$\varepsilon_{ij} = \mathrm{S}_{ijkl} \sigma_{kl} \qquad \text{A1-13}$$

where, $\mathrm{S_{ijkl}}$ is the fourth order tensor called stiffness. Both stiffness and compliance tensors contain 81 components, they can be reduced to 36 considering only non-zero terms and symmetry of crystalline solids. For highly symmetric crystals such as cubic and hexagonal, this number is further reduced to 21, due to which the Hooke's law can be expressed as:

$$\begin{bmatrix} \sigma_{xx} \\ \sigma_{yy} \\ \sigma_{zz} \\ \tau_{yx} \\ \tau_{zx} \\ \tau_{xy} \end{bmatrix} = \begin{bmatrix} \mathrm{C}_{11} & \mathrm{C}_{12} & \mathrm{C}_{12} & 0 & 0 & 0 \\ \mathrm{C}_{12} & \mathrm{C}_{11} & \mathrm{C}_{12} & 0 & 0 & 0 \\ \mathrm{C}_{12} & \mathrm{C}_{12} & \mathrm{C}_{11} & 0 & 0 & 0 \\ 0 & 0 & 0 & \mathrm{C}_{44} & 0 & 0 \\ 0 & 0 & 0 & 0 & \mathrm{C}_{44} & 0 \\ 0 & 0 & 0 & 0 & 0 & \mathrm{C}_{44} \end{bmatrix} \begin{bmatrix} \varepsilon_{xx} \\ \varepsilon_{yy} \\ \varepsilon_{zz} \\ \varepsilon_{yz} \\ \varepsilon_{zx} \\ \varepsilon_{xy} \end{bmatrix} \qquad \text{A1-14}$$

where, C_{11}, C_{12} and C_{44} are the three independent stiffness components.

A spatial representation of normal (σ_{ij}) , shear stresses (τ_{ij}) and strains (ε_{ij}) is presented in Fig. A1.2.

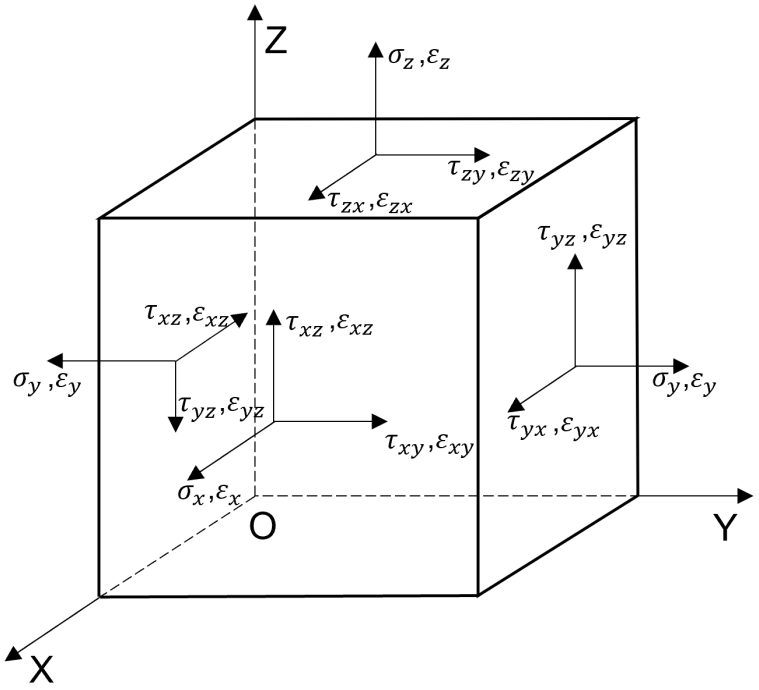

Fig. A1.2 Components of three-dimensional stress and strain.

A1.3 Elastic constants

Some of the important elastic properties used in the constitutive equations defining stress and strain of a deformed material at a point are described in this section.

Young's modulus, Y

The Young's modulus of a material is defined as the ratio of uniaxial stress to strain.

$$\text{Young's modulus} = \text{Y} = \frac{\text{uniaxial stress}}{\text{uniaxial strain}} \qquad \text{A1-15}$$

Biaxial modulus, E′

The biaxial state of stress at semiconductor heterointerfaces are more conveniently related by the biaxial modulus.

$$\text{Biaxial modulus} = \text{E}' = \frac{\text{biaxial stress}}{\text{biaxial strain}} = \text{C}_{11} + \text{C}_{12} - \frac{2\,\text{C}_{12}^2}{\text{C}_{11}} \qquad \text{A1-16}$$

Shear modulus, G

Shear modulus or the rigidity modulus is defined as the ratio of shear stress to shear strain.

$$\text{Shear modulus} = \text{G} = \frac{\text{shear stress}}{\text{shear strain}} = \frac{(\text{C}_{11} - \text{C}_{12})}{2} \qquad \text{A1-17}$$

Poisson ratio, υ

The ratio of transverse contraction to longitudinal elongation is called the Poisson ratio.

$$\text{Poisson ratio} = \upsilon = -\frac{\text{transverse stress}}{\text{longitunial strain}} = \frac{C_{12}}{(C_{11} + C_{12})} \qquad \text{A1-18}$$

the Poisson ratio of most semiconductors lies close to 0.3.

Biaxial relaxation constant, R_B

The biaxial relaxation constant which is the analogue of Poisson's ratio under biaxial loading under plane strain conditions is defined as:

$$\text{Biaxial relaxation constant} = R_B = -\frac{\text{in-plane strain}}{\text{out-of-plane strain}} = \frac{2C_{12}}{C_{11}} \qquad \text{A1-19}$$

Appendix-A2

The theory of nanoheteroepitaxy

This section describes the theoretical background of nanoheteroepitaxy in detail which is necessary for appreciating the applicability and limitations of this model. All the information presented here has been formulated based on [72] and [73].

Luryi and Suhir's model forms the precursor for the NHE model. It assumes an epilayer restricted to the seed pad of diameter 2*l*, making rigid contact with the non-complaint substrate. The edges of the seed pads are located at -l and +l along the y-axis with respect to the origin O, through which the z-axis passes perpendicular to the substrate surface. A total epilayer thickness, h, resulting from the coalescence or merger of films from adjacent seed pads is considered. These details are described in Fig. A2.1. The separation between adjacent seed pads is assumed large enough to prevent interactions between their strain fields. Under these conditions, the in-plane stress, $\sigma_{\parallel}$ is be expressed as:

$$\sigma_{\parallel} = \frac{Y_{epi}}{1-\upsilon_{epi}}\, \varepsilon_{epi}\, \chi(y,z) e^{-z\pi/2l} \ , \qquad \text{A2-1}$$

where Y_{epi}, ε_{epi} and υ_{epi} are the Young's modulus, strain and Poisson ratio of the epilayer. The lateral stress distribution is described by the function $\chi(x,y)$ whose value depends on h_e, the effective range of stress along the z-axis.

$$\chi(y,z) = \begin{cases} 1 - \frac{\cosh(ky)}{\cosh(kl)} \ ; & Z \le h_e \\ 1 \ ; & Z \ge h_e \end{cases} \qquad \text{A2-2}$$

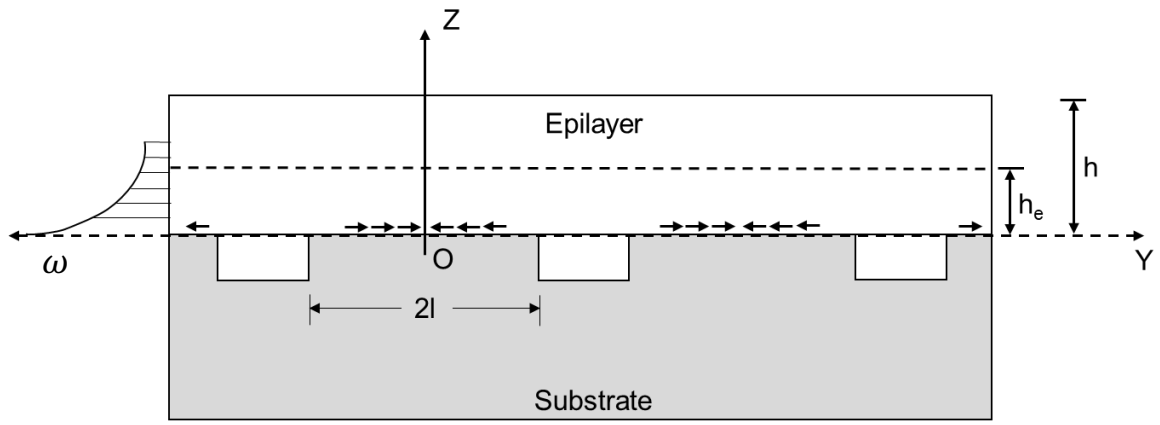

Fig. A2.1 An illustration of the model system considered by Luryi and Suhir, depicting the epilayer thickness, h , the effective height, h_e and the strain profile $\omega(0,z)$ normal to one of the seed pads, towards the left is shown.

The Interfacial compliance parameter k in equation A2-2 is described as

$$k = \left[\frac{3}{2}\left(\frac{1-\upsilon}{1+\upsilon}\right)\right]^{1/2} \frac{1}{h_e} = \frac{\xi}{h_e} \quad \text{A2-3}$$

The strain energy density of the epilayer which is maximum at y=0 is expressed as

$$\omega(y,z) = \frac{1-\upsilon}{Y}\ {\sigma_{\parallel}}^2 \quad \text{A2-4}$$

Integration of ω(y, z) over the entire film thickness yields the strain energy density per unit area, E_s , described as

$$E_s = \int_0^h \omega(0,z)dz = \frac{Y}{1-\upsilon}\ f^2\ h_e \quad \text{A2-5}$$

Due to the negligible contribution of χ to the integral in equation A2-5, its value described by the top line of equation A2-2 was extended to all values of z by Luryi and Suhir. The second part of equation A2-5 yields the expression for h_e as:

$$h_e = h\left\{\left[1 - \operatorname{sech}\left(\frac{\xi l}{h_e}\right)\right]^2 \left[1 - e^{(-\pi h/l)}\right]\frac{l}{\pi h}\right\} = h\left[\phi\left(\frac{l}{h}\right)\right]^2 \quad \text{A2-6}$$

The right-hand side of equation A2-6 describes the reduction factor $\phi(l/h)$, $\phi \longrightarrow 1$ for $l \gg h$ and $\phi \propto (l/h)^{1/2}$ that is $h_e \approx h$ when $l \gg h$ and for $l \ll h$, $\phi \longrightarrow 0$ thus,

$$h_e \approx \frac{1}{h}\left[1 - \operatorname{sech}(\xi h)\right]^2 \quad \text{A2-7}$$

An expression for estimating critical thickness, $h_c^l(f)$, needed for triggering plastic relaxation can be derived from A2-5 and A2-6 as

$$h_c^l(f) = h_c\left[\phi\ (l/h_c^l)f\right]$$

here, h_c is the critical thickness predicted for planar substrates using either People and Bean or Matthew's and Blakeslee expression. The terms $\phi\ (l/h_c^l)$ and f are thickness dependent reduction factor [L-S] and lattice misfit respectively.

Zubia and Hersee extended the above results to include substrate compliance effects which is necessary for the appropriation of total strain between the two layers. Under such assumptions, the total misfit strain, f of the substrate-epilayer system at a coherent interface can be expressed as:

$$f = \varepsilon_{epi} + \varepsilon_{sub}\ , \quad \text{A2-8}$$

where ε_{epi} and ε_{sub} are the portioned strains of epilayer and substrate. Considering the balance of forces at the interface,

$$\sigma_{epi}h_{epi} + \sigma_{sub}h_{sub} = 0 \quad \text{A2-9}$$

The in-plane stress, $\sigma_{\parallel}$ is related to the in-plane strain by the relation,

$$\sigma_{\parallel} = \frac{\mathrm{Y}}{1-\upsilon}\varepsilon \qquad \text{A2-10}$$

By substituting the values corresponding to Young's moduli and Poisson ratios of epilayer and substrate, the corresponding stresses σ_{epi} and σ_{sub} can be arrived at, which are:

$$\sigma_{epi} = \frac{\mathrm{Y}_{epi}}{1-\upsilon}\,\varepsilon_{epi} \text{ and } \sigma_{sub} = \frac{\mathrm{Y}_{sub}}{1-\upsilon}\,\varepsilon_{sub} \qquad \text{A2-11 and A2-12}$$

The equations A2-8, A2-9 and A2-10 when solved yield the expressions for partitioned strains of epilayer and substrate which shows a dependence on the ratio h_{epi}/h_{sub}:

$$\varepsilon_{epi} = \frac{f}{1+\left(\mathrm{K}\frac{h_{epi}}{h_{sub}}\right)} \text{ and } \varepsilon_{epi} = \frac{f}{1+\left(\frac{1}{\mathrm{K}}\frac{h_{sub}}{h_{epi}}\right)}, \qquad \text{A2-13 and A2-14}$$

where the parameter K is described as:

$$K = \frac{\mathrm{Y}_{epi}}{(1-\upsilon_{epi})}\frac{(1-\upsilon_{sub})}{\mathrm{Y}_{\mathrm{sub}}} \qquad \text{A2-15}$$

Following the same approach as Luryi and Suhir, the stresses in the epilayer and nanopatterned substrate with diameter 2l are expressed as

$$\sigma_{epi}(y,z) = \frac{\mathrm{Y}_{epi}}{1-\upsilon_{epi}}\,\varepsilon_{epi_0}\,\chi(y,z)e^{-z\pi/2l} \qquad \text{A2-16}$$

and

$$\sigma_{sub}(y,z) = \frac{\mathrm{Y}_{sub}}{1-\upsilon_{sub}}\,\varepsilon_{sub_0}\,\chi(y,z)e^{-z\pi/2l} \qquad \text{A2-17}$$

where ε_{epi_0} and ε_{sub_0} are the partitioned epilayer and substrate strains at the interface. The conditions of static equilibrium are now adopted assuming that lateral stress distribution is uniform up until sample edges, where it drops to zero.

$$\int_0^{h_{epi}} \sigma_{epi}(z)dz + \int_{-h_{sub}}^{0} \sigma_{sub}(z)\,dz = 0 \qquad \text{A2-18}$$

The above integration when solved yields the relations for the in-plane interfacial partitioned strains for the nanoscale epilayer island and substrate

$$\varepsilon_{epi,0} = \frac{f}{1+\left(K\frac{\left(1-e^{\left(-\pi h_{epi}/2l\right)}\right)}{\left(1-e^{\left(-\pi h_{sub}/2l\right)}\right)}\right)} \qquad \text{A2-19}$$

and

$$\varepsilon_{sub,0} = \frac{f}{1+\left(\frac{1}{K}\frac{\left(1-e^{\left(-\pi h_{sub}/2l\right)}\right)}{\left(1-e^{\left(-\pi h_{epi}/2l\right)}\right)}\right)} \qquad \text{A2-20}$$

The total areal strain energy of the system can now be described as earlier by the Luryi and Suhir approach as

$$E_s(y) = \int_0^{h_{epi}} \omega_{epi}(y,z)dz + \int_{-h_{sub}}^{0} \omega_{sub}(y,z)dz \quad \text{A2-21}$$

When the above integration is performed setting y=0, it yields the maximum areal strain energy densities for epilayer and substrate

$$E_{epi} = \frac{Y_{epi}}{1-\upsilon_{epi}} \varepsilon_{epi,0}^2 \left[1 - \operatorname{sech}(k_{epi}l)\right]^2 \frac{l}{\pi} \left[1 - e^{-(\pi h_{epi}/l}\right] \quad \text{A2-22}$$

$$E_{epi} = \frac{Y_{sub}}{1-\upsilon_{sub}} \varepsilon_{sub,0}^2 \left[1 - \operatorname{sech}(k_{sub}l)\right]^2 \frac{l}{\pi} \left[1 - e^{-(\pi h_{sub}/l}\right] \quad \text{A2-23}$$

By comparing the form of the above equations with that of strain energy on planar substrates,

$$E = \frac{Y}{1-\upsilon} \varepsilon^2 h \quad \text{A2-24}$$

the effective layer thickness for the epilayer and substrate can be extracted,

$$h_{eff} = \left[1 - \operatorname{sech}(k_{epi}l)\right]^2 \frac{l}{\pi} \left[1 - e^{-(\pi h_{epi}/l}\right] \quad \text{A2-25}$$

and

$$h_{sub} = \left[1 - \operatorname{sech}(k_{sub}l)\right]^2 \frac{l}{\pi} \left[1 - e^{-(\pi h_{sub}/l}\right] \quad \text{A2-26}$$

Equations A2-22 and A2-23 can now be rewritten as

$$E_{epi} = \frac{Y_{epi}}{1-\upsilon_{epi}} \varepsilon_{epi,0}^2 h_{epi}^{eff} \quad \text{A2-27}$$

and

$$E_{sub} = \frac{Y_{sub}}{1-\upsilon_{sub}} \varepsilon_{sub,0}^2 h_{sub}^{eff} \quad \text{A2-28}$$

Combining the above expressions gives the total coherent strain energy of the substrate/epilayer system, this can be written as

$$E_{coh.}^{Total} = E_{epi} + E_{sub} \quad \text{A2-29}$$

If this value exceeds the areal strain energy of a dislocation, $E_{Disl.}$ placed at the middle of the heterointerface. Zubia and Hersee had used the areal strain energy expression of a screw dislocation, expressed as

$$E_D = \frac{Gb^2}{4\pi(1-\upsilon)W_D} \ln\left(\frac{R}{b}\right) \quad \text{A2-30}$$

Where R represent the distance between the dislocation line and the free surface, usually taken as epilayer thickness, h and W_D is the dislocation width. However, it is

known that screw dislocations cannot relieve misfit strain at the heterointerface. A general expression for a mixed dislocation, the use of which is more pragmatic can be expressed as

$$E_{Disl.} = \frac{1}{5}\frac{G_{sub}G_{epi}b}{2\pi\,(G_{sub}+G_{epi})}\left(\cos^2\theta + \frac{\sin^2\theta}{1-\upsilon_{dep}}\right)\left(1+\ln\frac{R}{b}\right), \qquad \text{A2-31}$$

where G_{sub} and G_{epi} are the shear moduli of substrate and epilayer respectively, b and θ are the magnitude of Burger vector and the angle between dislocation line and its Burgers vector respectively. Here, R denotes the distance of the dislocation line from the nearest free surface, this value is usually taken as the epilayer thickness, h. The effective dislocation width in this case is taken as 5 times the magnitude of the Burgers vector.

Appendix-3

Practical considerations during SAH template fabrication

A few key practical aspects were followed to successfully realize the above results and these are described here in the best possible detail. Firstly, a wafer $1/3^{rd}$ was nanopillar patterned and overgrown by SiN_x film. The progress of film penetration to reveal the pillar tops is thus made possible by cleaving smaller slices, a final cleave is made to yield a wafter $1/6^{th}$ as shown in Fig. A3.1(b). The intermediate stages are distinguishable by the variation in the SiN_x film's color which results from interference as seen in Fig. A3.1(a). Another important aspect is the careful bonding and debonding of the substrate to the stainless steel 316L block. Towards this end an acetone soluble wax with a flow temperature of 74°C marketed by Ted Pella Inc. under the name Crystalbond 509 was used. Pieces of this wax were melted over the 316L steel block placed over a hot plate maintained at 100°C, the SiN_x/GaAs(111)A wafer $1/3^{rd}$ is placed over these droplets and gently moved with a tweezer to spread the wax underneath. The substrate attaches to the steel block upon cooling and re-solidification of the glue. This array makes it amenable for safe handling of wafer during the planarization step. After planarization the substrate is dethatched from the steel block by reheating the arrangement using the hotplate again. Once detached, the residues below the substrate surface are dissolved by swabbing with lint free paper dipped in acetone.

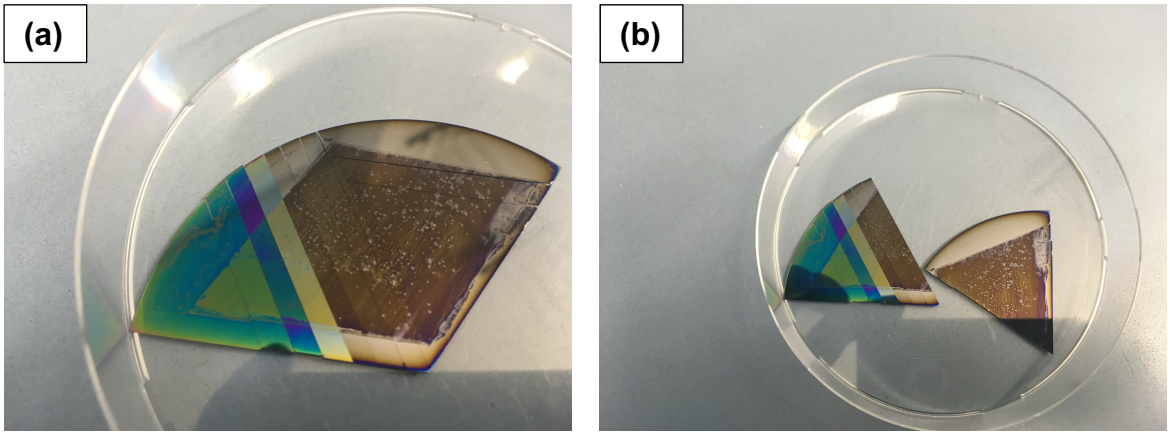

Fig. A3.1 (a) and (b) are the actual images of a SiN_x film deposited nanopillar patterned GaAs(111)A substrate after various stages of surface preparation. (a) shows a full wafer $1/3^{rd}$ whereas (b) shows the two wafer $1/6^{th}$s' resulting from cleaving. The transition of color form blue to brown results from change of SiN_x film thickness.

Additionally, the films take up the profiles of the pillars upon which they grow and form depressions when the growth fronts of nearest neighboring pillars meet. Film thickness measured from pillar base to the crest of undulations amounted to approximately 285nm of which 90nm accounted for the surface waviness.

Appendix-A4

Growth reports

In this chapter the growth sheets of the MBE grown samples listed in Chapter 4, Table 4.3 are presented. The growth sheet numbers A0618, A0643, A0668, A0698, A0740, A0771, A0793, A0874, A0904, A1100, A1120, A1132 correspond to InAs MBE growth runs performed on nanopillar patterned GaAs(111)A substrates whereas growth sheets A1216, A1271, A1338 and A1697 were performed on the GaAs(111)A nanopillar patterned substrates with SiN_x selective area heteroepitaxy growth masks.

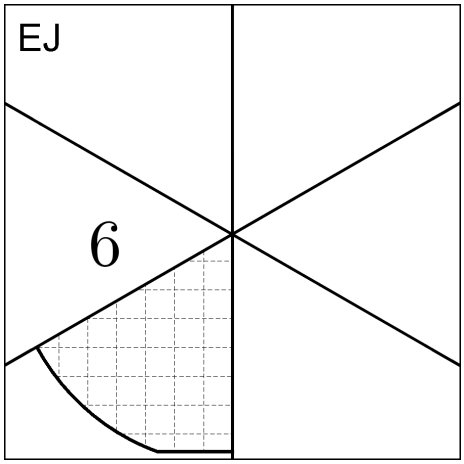

Sample: **A0618**

Material: GaAs:Si

Orientation: (111)A

Wafer: W3-S4

Rotation: 10

Pressure (mBar): 9.43×10^{-9}

Date: 30.11.2017

File: a0618.asl

		300K	77K	4.2K	1K
dark	μ [cm^2 / Vs]				
	n [cm^{-2}]				
illum	μ [cm^2 / Vs]				
	n [cm^{-2}]				

Layer	*Loop*	*T [°C]*	*Dur. [s]*	*Thickn. [nm]*
InAs		410.0	1353.4	15

growth rate

InAs 0.011 nm/s

Comment

InAs on prepatterned GaAs nanopillars

As_VP = 50%
p_As approx. 2.5e-5

HS for >2h @250°C
AH-Cleaning at 350°C for 15 min

(Grown by A. Trapp)

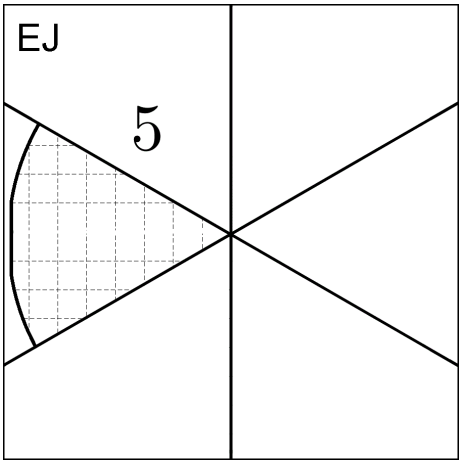

Sample: **A0643**

Material: GaAs

Orientation: (111)A

Wafer: W3-S2

Rotation: 10

Pressure (mBar): 3.38×10^{-8}

Date: 10.01.2018

File: a0643.asl

		300K	77K	4.2K	1K
dark	μ [cm^2 / Vs]				
	n [cm^{-2}]				
illum	μ [cm^2 / Vs]				
	n [cm^{-2}]				

Layer	*Loop*	*T [°C]*	*Dur. [s]*	*Thickn. [nm]*
InAs		350.0	1353.4	15

growth rate

InAs 0.011 nm/s

Comment

InAs on prepatterned GaAs nanopillars

As_VP = 50%
p_As = 2.53e-5

HS for >2h @300°C
AH-Cleaning at 350°C for 3 min

(Grown by A. Trapp)

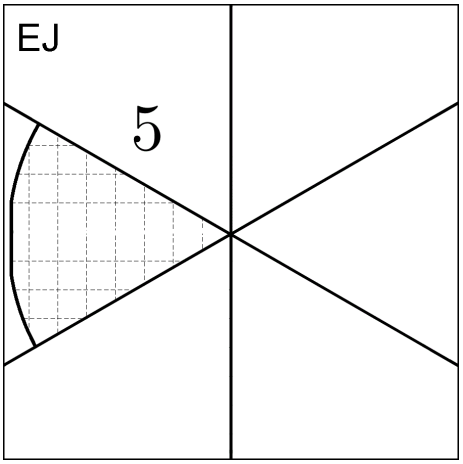

Sample: **A0668**

Material: GaAs

Orientation: (111)A

Wafer: W6-S2

Rotation: 10

Pressure (mBar): 6.04×10^{-9}

Date: 29.01.2018

File: a0668.asl

		300K	77K	4.2K	1K
dark	μ [cm^2 / Vs]				
	n [cm^{-2}]				
illum	μ [cm^2 / Vs]				
	n [cm^{-2}]				

Layer	*Loop*	*T [°C]*	*Dur. [s]*	*Thickn. [nm]*
InAs		300.0	1353.4	15

growth rate

InAs 0.011 nm/s

Comment

InAs on prepatterned GaAs nanopillars

As_VP = 50%
p_As = 2.53e-5

HS for >2h @300°C
AH-Cleaning at 350°C for 3 min

(Grown by A. Trapp)

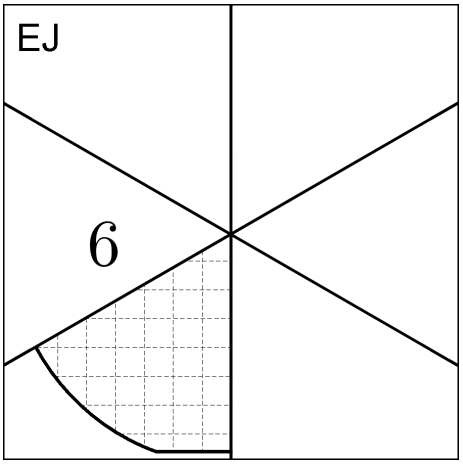

Sample: **A0698**

Material: GaAs:Si

Orientation: (111)A

Wafer: W6-S3

Rotation: 10

Pressure (mBar): 9.41×10^{-9}

Date: 14.02.2018

File: a0698.asl

		300K	77K	4.2K	1K
dark	μ [cm^2 / Vs]				
	n [cm^{-2}]				
illum	μ [cm^2 / Vs]				
	n [cm^{-2}]				

Layer	*Loop*	*T [°C]*	*Dur. [s]*	*Thickn. [nm]*
InAs		300.0	136.4	15

growth rate
InAs 0.11 nm/s

Comment
InAs on prepatterned GaAs nanopillars

As_VP = 50%
p_As = 2.41e-5

HS for >2h @300°C
AH-Cleaning at 350°C for 3 min

(Grown by A. Trapp)

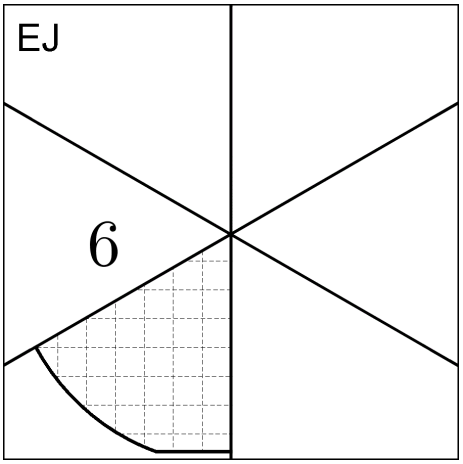

Sample: **A0740**

Material: GaAs:Si

Orientation: (111)A

Wafer: W7-S3

Rotation: 10

Pressure (mBar): 3.86×10^{-9}

Date: 12.04.2018

File: a0740.asl

		300K	77K	4.2K	1K
dark	μ [cm^2 / Vs]				
	n [cm^{-2}]				
illum	μ [cm^2 / Vs]				
	n [cm^{-2}]				

Layer	*Loop*	*T [°C]*	*Dur. [s]*	*Thickn. [nm]*
InAs		150.0	1353.4	15

growth rate

InAs 0.011 nm/s

Comment

InAs on prepatterned GaAs nanopillars

As_VP = 50%
p_As = 2.35e-5

HS for >2h @300°C
AH-Cleaning at 350°C for 3 min

(Grown by A. Trapp)

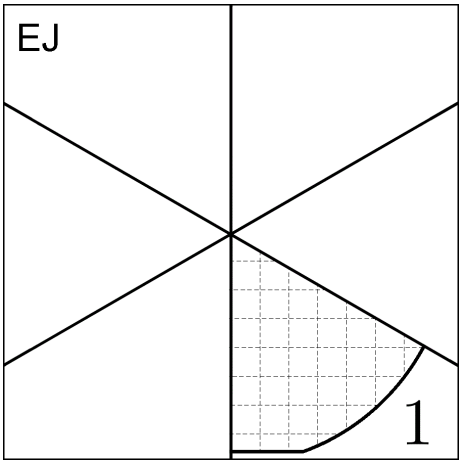

Sample: **A0771**

Material: GaAs

Orientation: (111)A

Wafer: W8-S4

Rotation: 10

Pressure (mBar): 4.45×10^{-9}

Date: 16.05.2018

File: a0771.asl

		300K	77K	4.2K	1K
dark	μ [cm^2 / Vs]				
	n [cm^{-2}]				
illum	μ [cm^2 / Vs]				
	n [cm^{-2}]				

Layer	*Loop*	*T [°C]*	*Dur. [s]*	*Thickn. [nm]*
InAs		150.0	452.4	5

growth rate

InAs 0.011 nm/s

Comment

InAs on prepatterned GaAs nanopillars

As_VP = 15%
p_As = 2.29e-5

HS for >2h @300°C
AH-Cleaning at 350°C for 3 min

(Grown by A. Trapp)

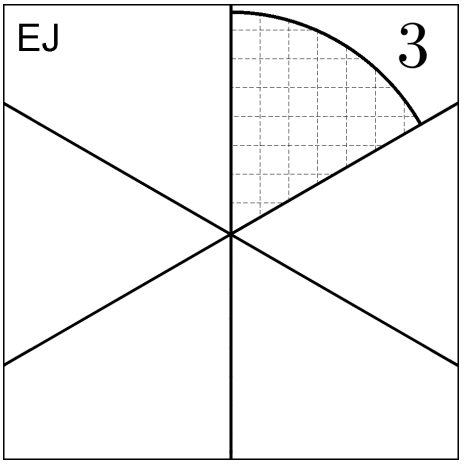

Sample: **A0793**

Material: GaAs

Orientation: (111)A

Wafer: W8-S6

Rotation: 10

Pressure (mBar): 2.34×10^{-10}

Date: 13.06.2018

File: a0793.asl

		300K	77K	4.2K	1K
dark	μ [cm^2 / Vs]				
	n [cm^{-2}]				
illum	μ [cm^2 / Vs]				
	n [cm^{-2}]				

Layer	*Loop*	*T [°C]*	*Dur. [s]*	*Thickn. [nm]*
InAs		150.0	180.4	2

growth rate

InAs 0.011 nm/s

Comment

InAs on prepatterned GaAs nanopillars

As_VP = 30%
p_As = 2.30e-5

HS for >2h @300°C
AH-Cleaning at 350°C for 3 min

(Grown by A. Trapp)

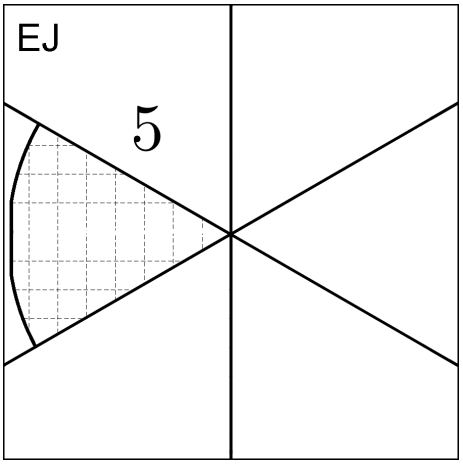

Sample: **A0874**

Material: GaAs

Orientation: (111)A

Wafer: W10-S5

Rotation: 10

Pressure (mBar): 4.63×10^{-8}

Date: 12.09.2018

File: a0874.asl

		300K	77K	4.2K	1K
dark	μ [cm^2 / Vs]				
	n [cm^{-2}]				
illum	μ [cm^2 / Vs]				
	n [cm^{-2}]				

Layer	*Loop*	*T [°C]*	*Dur. [s]*	*Thickn. [nm]*
InAs		300.0	1365.4	15

growth rate

InAs 0.011 nm/s

Comment

InAs on prepatterned GaAs nanopillars

As_VP = 30%
p_As = 2.31e-5

HS for 2h @300°C
AH-Cleaning at 350°C for 3 min

(Grown by A. Trapp)

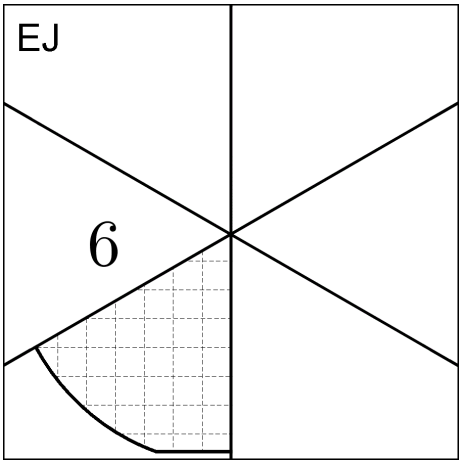

Sample: **A0904**

Material: GaAs

Orientation: (111)A

Wafer: W12_S6

Rotation: 10

Pressure (mBar):

Date: 29.10.2018

File: a0904.asl

		300K	77K	4.2K	1K
dark	μ [cm^2 / Vs]				
	n [cm^{-2}]				
illum	μ [cm^2 / Vs]				
	n [cm^{-2}]				

Layer	*Loop*	*T [°C]*	*Dur. [s]*	*Thickn. [nm]*
InAs		150.0	452.4	5

growth rate

InAs 0.011 nm/s

Comment

InAs on prepatterned GaAs nanopillars

As_VP = 50%
p_As = 2.17e-5

HS for >2h @300°C
AH-Cleaning at 350°C for 3 min

(Grown by T. Langer)

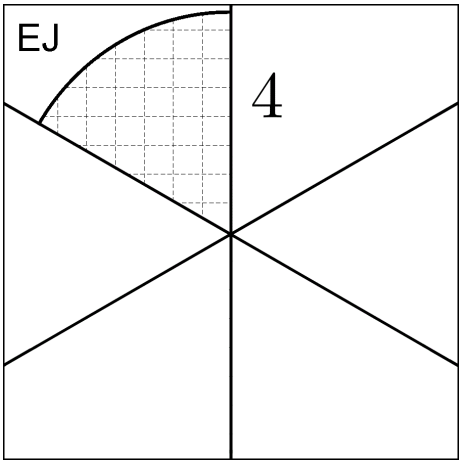

Sample: **A1100**

Material: GaAs

Orientation: (100)

Wafer: W15_S4

Rotation: 10

Pressure (mBar):

Date: 19.06.2019

File: a1100.asl

		300K	77K	4.2K	1K
dark	μ [cm^2 / Vs]				
	n [cm^{-2}]				
illum	μ [cm^2 / Vs]				
	n [cm^{-2}]				

Layer	*Loop*	*T [°C]*	*Dur. [s]*	*Thickn. [nm]*
InAs		150.0	181.8	2

growth rate

InAs 0.011 nm/s

Comment

InAs on prepatterned GaAs nanopillars

As_VP = 30%
p_As = 2,45E-5

HS for >1h @300 °C
AH-Cleaning at 350 °C for 3 min

(Grown by T. Langer)

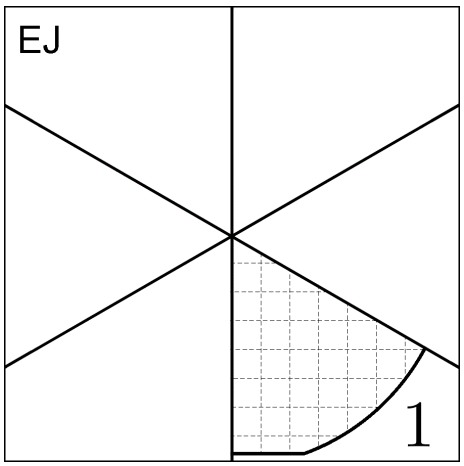

Sample: **A1120**

Material: GaAs

Orientation: (100)

Wafer: W14_S1

Rotation: 10

Pressure (mBar):

Date: 09.07.2019

File: a1120.asl

		300K	77K	4.2K	1K
dark	μ [cm^2 / Vs]				
	n [cm^{-2}]				
illum	μ [cm^2 / Vs]				
	n [cm^{-2}]				

Layer	*Loop*	*T [°C]*	*Dur. [s]*	*Thickn. [nm]*
InAs		200.0	1363.6	15

growth rate

InAs 0.011 nm/s

Comment

InAs on prepatterned GaAs nanopillars

As_VP = 30%
p_As = 2,46E-5

HS for >1h @300 °C
AH-Cleaning at 350 °C for 3 min

(Grown by T. Langer)

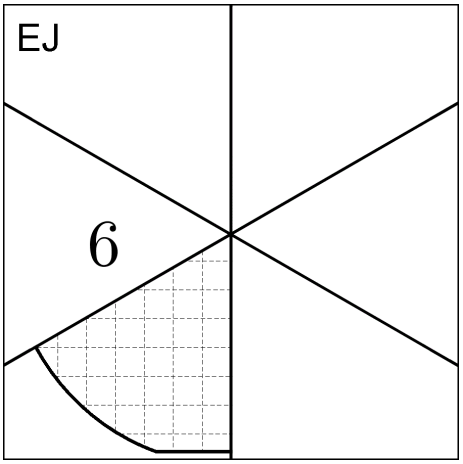

Sample: **A1132**

Material: GaAs

Orientation: (100)

Wafer:

Rotation: W15_S6

Pressure (mBar):

Date: 16.07.2019

File: a1132.asl

		300K	77K	4.2K	1K
dark	μ [cm^2 / Vs]				
	n [cm^{-2}]				
illum	μ [cm^2 / Vs]				
	n [cm^{-2}]				

Layer	*Loop*	*T [°C]*	*Dur. [s]*	*Thickn. [nm]*
InAs		250.0	1363.6	15

growth rate

InAs 0.011 nm/s

Comment

InAs on prepatterned GaAs nanopillars

As_VP = 30%
p_As = 2,30E-5

HS for >1h @300 °C
AH-Cleaning at 350 °C for 3 min

(Grown by)

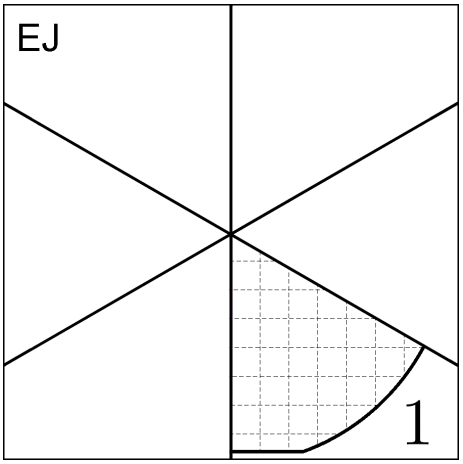

Sample: **A1216**

Material: GaAs

Orientation: (111A)

Wafer: W14-S2-3

Rotation: 10

Pressure (mBar):

Date: 02.12.2019

File: a1216.asl

		300K	77K	4.2K	1K
dark	μ [cm^2 / Vs]				
	n [cm^{-2}]				
illum	μ [cm^2 / Vs]				
	n [cm^{-2}]				

Layer	*Loop*	*T [°C]*	*Dur. [s]*	*Thickn. [nm]*
InAs		300.0	181.8	2

growth rate

InAs 0.011 nm/s

Comment

InAs on prepatterned GaAs nanopillars

As_VP = 19.2%
p_As = 2.31E-5

AH-Cleaning at 350°C for 3 min

(Grown by A. Verma)

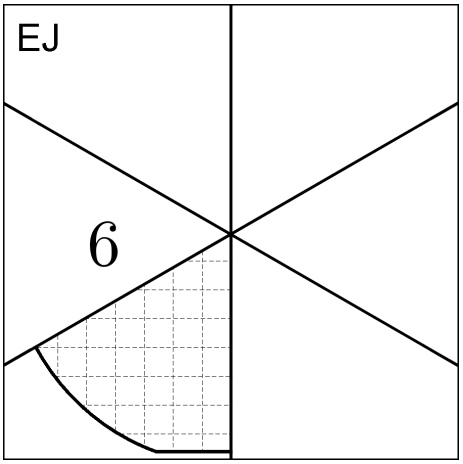

Sample: **A1271**

Material: GaAs

Orientation: 111A

Wafer: W16-S2-3

Rotation: 10

Pressure (mBar):

Date: 20.12.2019

File: a1271.asl

		300K	77K	4.2K	1K
dark	μ [cm^2 / Vs]				
	n [cm^{-2}]				
illum	μ [cm^2 / Vs]				
	n [cm^{-2}]				

Layer	*Loop*	*T [°C]*	*Dur. [s]*	*Thickn. [nm]*
InAs		450.0	181.8	2

growth rate

InAs 0.011 nm/s

Comment

InAs on prepatterned GaAs nanopillars

As_VP = 25%
p_As = 2.32E-5

HS for >1h @300°C
AH-Cleaning at 350°C for 3 min

(Grown by A. Verma)

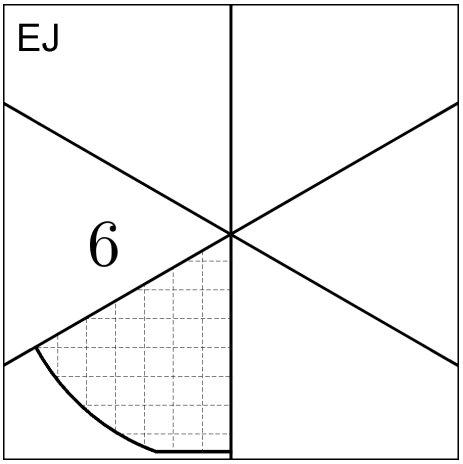

Sample: **A1338**

Material: GaAs

Orientation: (100)

Wafer: W17S3-2

Rotation: 10

Pressure (mBar):

Date: 31.01.2020

File: a1338.asl

		300K	77K	4.2K	1K
dark	μ [cm^2 / Vs]				
	n [cm^{-2}]				
illum	μ [cm^2 / Vs]				
	n [cm^{-2}]				

Layer	*Loop*	*T [°C]*	*Dur. [s]*	*Thickn. [nm]*
InAs		400.0	181.8	2

growth rate

InAs 0.011 nm/s

Comment

InAs on prepatterned GaAs nanopillars

As_VP = 19.2%
p_As = 2.32E-5

AH-Cleaning at 350°C for 3 min

(Grown by A. Verma)

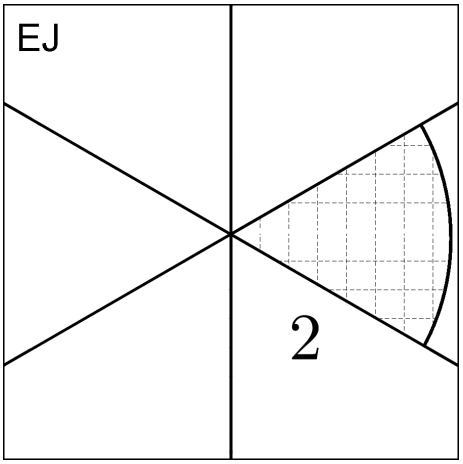

Sample: **A1697**

Material: GaAs

Orientation: (100)

Wafer: SW2_S32

Rotation: 10

Pressure (mBar):

Date: 02.11.2020

File: a1697.asl

		300K	77K	4.2K	1K
dark	μ [cm^2 / Vs]				
	n [cm^{-2}]				
illum	μ [cm^2 / Vs]				
	n [cm^{-2}]				

Layer	*Loop*	*T [°C]*	*Dur. [s]*	*Thickn. [nm]*
InAs		425.0	181.8	2

growth rate

InAs 0.011 nm/s

Comment

(Grown by T. Langer)

List of figures

List of tables

List of publications

In-peer reviewed journals

1) Selective area heteroepitaxy of InAs nanostructures on nanopillar-patterned GaAs(111)A, T. Riedl, V.S. Kunnathully, A.K. Verma, T. Langer, D. Reuter, B Büker, A. Hütten and J.K.N. Lindner, J. Appl. Phys., 132 (2022), 185701.

2) Size-dependent Strain Relaxation in InAs Quantum Dots on top of GaAs(111)A Nanopillars, T. Riedl, V.S. Kunnathully, A. Trapp, T. Langer, D. Reuter and J.K.N. Lindner, Adv. Mater. Interfaces, 9(2022), 2102159.

3) InAs heteroepitaxy on nanopillar-patterned GaAs(111)A, Vinay S. Kunnathully, T. Riedl, A. Trapp, T.Langer, D. Reuter and J.K.N. Lindner, J. Cryst. Growth, 537 (2020), 125597.

4) Characterization of PS-PMMA Interfaces in Microphase Separated Block Copolymer Thin Films by Analytical (S)TEM, J. Bürger, V.S. Kunnathully, D. Kool, J.K.N. Lindner and K. Brassat, Nanomaterials, (10) 1 (2020), 141.

5) Strain-Driven InAs Island Growth on top of GaAs (111) Nanopillars, T. Riedl, V.S. Kunnathully, A. Trapp,T. Langer, D. Reuter and J.K.N. Lindner, Phys. Rev. Mater., 4 (2020), 014602

6) Computational design of model Re/Ru bearing Ni-Based superalloys, K.V. Vamsi, K.N. Goswami, K.S.Vinay, S.K. Verma, R. Balamuralikrishnan, N. Das, D. Banerjee and S. Karthikeyan, MATEC Web of conferences 14 (2014), 17007.

Conference contributions

1) J. Bürger, V.S. Kunnathully, T. Riedl and J.K.N. Lindner, "Atomic electric fields in InAs measured by scanning transmission electronmicroscopy", 14th international conference on Physics of Advanced Materials (ICPAM-14), 8–15 September, Dubrovnik, Croatia (2022)

2) V. Kunnathully, A. Trapp, T.Riedl, T. Langer, D. Reuter and J. K. N. Lindner, "InAs heteroepitaxyonnano-pillarpatterned GaAs(111)A", DGKK Workshop 2018, Paderborn (2018).

3) T. Riedl, V.Kunnathully, A. Trapp, T. Langer, D. Reuter and J. K. N. Lindner, "Relaxation of misfit in nanoscale InAs growths atop GaAs(111)A nanopillars", DGKK Workshop 2018, Paderborn (2018).

4) V. Kunnathully, T. Riedl, A. Trapp, D. Reuter and J. K. N. Lindner, "Defect Formation in InAs Nanoislands Heteroepitaxially Grown on Nanopillar-Patterned GaAs(111)A", 19th International Conference on Extended Defects in Semiconductors, Thessaloniki (2018).

5) V. Kunnathully, T. Riedl, A. Karlisch, D. Reuter, and J. K. N. Lindner: 'InAs heteroepitaxy on GaAs patterned by nanosphere lithography'. E-MRS Fall Meeting. Warsaw (2017)

6) T. Riedl, V. Kunnathully, A. Karlisch, D. Reuter, N. Weber, C. Meier, R. Schierholz, and J. K. N. Lindner, "Morphology, structure and enhanced PL of molecular beam epitaxial $In_{0.2}Ga_{0.8}As$ layers on nanopillar patterned GaAs", E-MRS Spring Meeting. Strasbourg (2017)

Acknowledgements

Here, I would like to thank all the people and organizations who have contributed towards making this thesis possible.

First and foremost, my heartfelt thanks to **Prof. Jörg K. N. Lindner**, for giving me the opportunity to work in his research group (Nanopatterning Nanoanalysis Photonic Materials or NNP) at Department of Physics, Paderborn University for establishing a state of the art (S)TEM at the Paderborn University, for proofreading my papers and Ph.D. thesis and providing very detailed comments to bringing out the best from it and for providing me with mental support whenever I needed it the most. I am also equally indebted to **Dr. Thomas Riedl** for being my mentor, for guiding me into the realm of semiconductor processing with care to minute details and for performing the molecular statics simulations in this thesis without which a quantitative understanding of the strain relaxation mechanisms would have been impossible.

I am also very much grateful to **Dr. Dirk Reuter** and his research group (Optoelectronic materials and devices or OMD) at Department of Physics, Paderborn University for performing the MBE growth of my samples in this context I would like to thank **Dr. Alexander Trapp**, **Dr. Tobias Henksmeier**, **Timo Langer** and **Dr. Akshay Kumar Verma**. The other students form his group **Dr. Nand Lal Sharma**, **Dr. Viktoryia Zolatanosha**, **Mario Littmann**, **Pascal Mahler**, **Binamra Shrestha** and **Dr. Stepan Shvarko** for valuable discussions on MBE and plesant working conditions and to lab engineer **Bastian Aisenbrey** for always being there to help me. I also thank the Prof. Reuter for letting me use his AFM apparatus.

Coming back to the NNP, I have had the opportunity to work with many amazing colleagues over the years, I would like to firstly thank lab engineer **Werner Sievers** for guiding me through the lab and providing me with all the technical and mental support when evever I required. The other lab engineers who were equally of help that I want thank are **Yannick Lang** and **Julian Sulikowski** for supporting most of my experiemtnal set-ups. I also thank the secretary for NNP, **Nina Prante** for her support with procurement of various consumables and equipment. I thank **Dr. Julius**

Bürger for providing me with the best STEM alingments without which many of the images in this thesis might have no looked shap enough, **Dr. Katharian Brassat** for being a good mentor, **Dr. Maja Groll** for valuable TEM related discussions, **Michael Kismann** and **Werner Ridder** for TEM specimen preparation. I also thank **Jithin Varghese**, **Harikrishnan Venugopal**, **Dr. Sara Arceiz-Casas**, **Dr. Annika Stelhorn Tim Baumgarten** , **Felix Lohmeyer**, **Jana Freibel** and **Alexander Stratmann** and **Daniel Kool** for being good colleagues with whom I meaningful conversations.

I also thank the group of **Prof. Andreas Hütten** and **Dr. Björn Büker** (Thin films and physics of nanostructures or TFPN), Department of Physics, Bielefeld University for helping with the FIB-TEM specimen prparation. I also thank **Prof. Miko Schaper** (Chair for Materials Science), Departement of Mechanical Engineering, Paderborn University, for letting me use the vibromet polishing machine for the planarization of silicon nitride hard-masks, **Prof. Thomas Zentgraf** and his students **Dr. Basudeb Sain** and **Dr. Bernhard Reineke** of the Ultrafast Photonics group, Department of Physics, Paderborn University for helping me use the carbon sputtering unit. Also, special thanks to the group (Nanophotonics and Nanomaterials) of **Prof. Cedrik Meier** and his students **Dr. Nils Weber**, **Dr. Sandro Hoffmann** and **Ruth Volmert** at the, Departement of Physics, Paderborn University for guiding me with the use of reactive ion etching (RIE) equipment.

I also thank the German science foundation or Deutsche Forschungsgemeinschaft (DFG) for funding the work of this project though the project numbers Ri2655/1-1 and Li449/16-1

And most importantly, I thank my parents and my sister for their support always.

Declaration of plagiarism

I, Vinay Kunnathully Sathees Kumar (Matriculation number: 7065721) hereby declare that the Ph.D. thesis titled **"InAs heteroepitaxy on nanopillar patterned GaAs(111)A surfaces"** was carried out under the guidance of Prof. Jörg K. N. Lindner and Dr. Thomas Riedl at the Department of Physics in the University of Paderborn, Paderborn, Germany. The literature sources, works and contributions of investigators that have directly or indirectly contributed to this thesis have been sincerely acknowledged to the best of my knowledge. Additionally, no form of artificial intelligence-based aids has been used for generating the contents of this thesis, except for translation of the abstract from English language to German language using OpenAI: GPT-5.4-Thinking provided by central IT and media services, Paderborn University.

Further, I declare that this thesis has not formed the basis for awarding a diploma, degree, membership or associateship or similar titles in any university or institute of higher education.

I am aware that the respective work can be considered as a "fail" in the event of a false declaration.

(Signature)

Vinay S. Kunnathully

Paderborn, (date)